STUDY OF X RAY EMISSION FROM

SOLAR ACTIVE REGIONS

by

JOHN P. PYE, B.Sc.

A THESIS

SUBMITTED TO THE UNIVERSITY OF LEICESTER

FOR THE DEGREE OF DOCTOR OF PHILOSOPHY

OCTOBER 1976

DEPARTMENT OF PHYSICS
UNIVERSITY OF LEICESTER

DEDICATION

TO

MY WIFE

LYDIA

AND

MY PARENTS

WILLIAM & DOROTHY PYE

QUOTATIONS

"These (the first solar ultraviolet) rocket spectra are certainly fascinating. My first look at one gives me a sense that I was seeing something that no astronomer could expect to see unless he was good and went to heaven!"

(H.N. Russell, May 1947, in L. Goldberg, 1974).

"The pioneers have roughly explored the Sun and an army of settlers is trying to make a living of it. .... In 1950 one could describe the Sun as follows:

'The Sun is a thermally radiating gaseous sphere'.

In 1970 I would describe the Sun in a more complicated manner:

'The Sun is a rotating magnetic plasma with a complex transient XUV, optical, radio and cosmic ray spectrum'."

(M. Kuperus, 1974).

J.P.Pye Ph.D. Thesis

ERRATA

p.17, line 9: "anistropy" should read "anisotropy".

p.17, line 18: "$v_j^{\ 2}$" should read "$\overline{v_j^{\ 2}}$".

p.23, line 5: "conductivity " should read "conductivity σ ".

p.31, line 12: "$\bar{g}(z,T_e, \lambda)$" should read "$\bar{g}_{ff}(z,T_e, \lambda)$".

p.32, lines 23 and 25: "$\bar{g}_{ff}$" should read "$\bar{g}_{fb}$".

p.51, line 24: "that" should read "than".

p.86, line 12: "region 12624" should read "regions 12624 and 12628".

p.87, line 17: "12628" should read "11621".

p.104, line 13: "Ly " should read "Lyα".

Table 4.4, column 4: "8.75" should read "8.75$^{a)}$ ".

p.124, line 1 : "and is 0.0 0.1" should read "and is $\sim 0.0 \rightarrow 0.1$".

p.127, line 7: "ective" should read "active".

p.131, line 26: "n=3 2" should read "n=3$\rightarrow$2".

p.144, line 17: "sp^5" should read "$2p^5$".

p.150, line 30: "(see Table 6.4 for " should read "(see Table 6.4) for ".

p.164, line 5: "$2p^5 3s$" should read "$2p^4 3s$".

p.79 Table 4.1 should be Table 4.11a

p.115 centre $R \leq R_a$

$n_e \geq n_e^*$

SUMMARY

A study of the X-ray emission from solar coronal active regions is presented. The observations were made with two instruments: (1) a collimated Bragg crystal spectrometer with high spectral resolution ($400 \lesssim \lambda/\Delta\lambda \lesssim 1000$) and moderate spatial resolution (about 3 arc min), and (2) a grazing incidence telescope which obtained broad wavelength-band images with high spatial resolution (about 2 arc sec). Chapter 1 gives a brief review of the relevant physics, with particular emphasis on the Sun's soft X-ray emission (i.e. $1 \lesssim$ wavelength, $\lambda \lesssim 25$ Å). The plasma and atomic physics required to interpret the X-ray observations are summarised in Chapter 2.

The instruments used in this work were the (sounding) rocket-borne Leicester Mk. 3 Bragg spectrometer, and the American Science and Engineering (ASE) X-ray telescope S-054, aboard the Skylab Apollo Telescope Mount. The instruments and data analysis techniques are described in Chapter 3.

The data are interpreted in terms of thermal emission from an optically thin plasma. In Chapter 4, coronal active region models, are derived, of electron density and emission measure ($n_e^2\Delta V$) as a function of electron temperature and spatial location. Abundances are derived for the elements oxygen, neon, sodium, magnesium, aluminium, silicon, iron and nickel in the solar corona.

Chapters 5, 6 and 7 describe observations and interpretation of spectra of ions belonging to particular isoelectronic sequences, namely: Chapter 5, the Helium-like ions O VII, Ne IX and Mg XI; Chapter 6, the Neon-like ions Fe XVII and Ni XIX, Chapter 7, Fluorine-like Fe XVIII and Oxygen-like Fe XIX.

CONTENTS

Frontispiece

SKYLARK SL1206 LAUNCH
WOOMERA, S. AUSTRALIA
0535 UT 26 NOVEMBER 1973

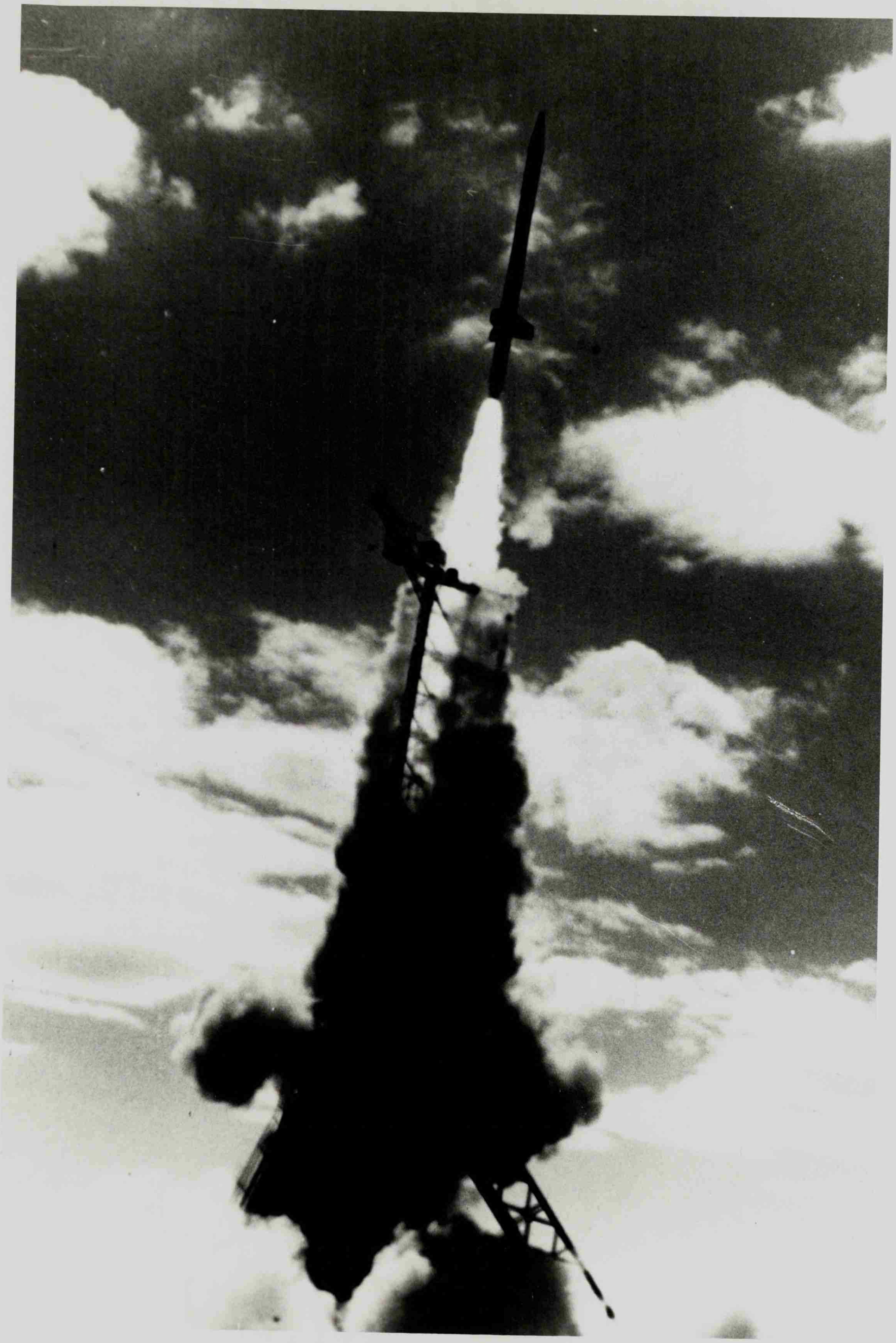

Chapter 1

REVIEW OF SOLAR PHYSICS AND SOLAR SOFT X-RAY EMISSION

1.1 Introduction

The Sun is a nearly spherical high temperature ($\sim 10^4$-10^7K) plasma containing a magnetic field. The physical conditions of temperature, density and elemental composition, combined with the interactions between the plasma and the magnetic field, produce many and varied phenomena. The Sun emits electromagnetic (e.m.) and particle radiation (cosmic rays) over a wide range of energies. The only method available, to obtain information on the processes occurring in the Sun, is the study of its radiation; similar techniques are used for the diagnosis of physical conditions in laboratory plasmas and other astrophysical plasmas.

The solar e.m. emission extends over most of the spectrum (see Figure 1.1), from radio to gamma rays. This thesis is concerned with the observation, analysis and interpretation of soft X-radiation (mainly in the range below 25Å) from solar active regions. Since X-rays cannot penetrate the Earth's atmosphere, it is necessary to carry the observing instrumentation to an altitude ($\gtrsim$140 km for wavelengths $\lesssim$25 Å) where the atmospheric absorption is negligible. Therefore, the experiments are launched into space, either on a ballistic sounding rocket or an orbiting satellite. At photon energies $\gtrsim$ 20 keV observations may be made from balloon-borne experiments.

In order to analyse and interpret the data in terms of the physical conditions and processes occurring in the solar plasma, it is first necessary to consider the relevant background material. To this end, the present chapter and Chapter 2 will review: solar physics, solar soft X-ray emission, plasma physics, and atomic processes. It is not intended to give an exhaustive coverage of each subject, but rather to summarize selected topics as a basis for the work that follows. References to published works which provide a broader treatment of each area, are given.

Observations of the Sun, in addition to providing information on solar processes are also useful in the fields of plasma and atomic physics, since there exist, in the Sun, physical conditions which cannot be reproduced on Earth.

1.2 Solar Structure

As already mentioned in Section 1.1 the Sun is a nearly spherical high temperature ($\sim 10^4$–10^7 K) plasma, much of which contains a magnetic field. The solar plasma consists of (by number of atoms) approximately 90% hydrogen, 10% helium, and 1% admixture of heavier elements, mainly carbon, nitrogen, oxygen, neon, magnesium, silicon, sulphur and iron. Nuclear fusion reactions in the central core of the Sun are its basic energy source. The reactions are maintained by the high temperature ($\sim 10^7$ K) and density ($\sim 10^{26}$ cm^{-3}) in the core; these necessary conditions are supplied by the exothermic reactions themselves and by the gravitational self-attraction of the solar gas, the latter process having been responsible for the initial fulfilment of these requirements during the early evolution of the Sun.

The energy generated in the core is transported outwards by radiation and then by convection, until it reaches the visible surface of the Sun, the photosphere, to be radiated into space. It is convenient and conventional to divide the observable Solar atmosphere into three layers; these are (extending outwards), the photosphere, the chromosphere and the corona. The photospheric spectrum (according to which the Sun is classified as a type G2 star) closely approximates to that of a blackbody at 6000 K, with some absorption (Fraunhofer) lines. At the top of the photosphere, the temperature reaches a minimum ($\sim$4000 K) and then increases outward to a coronal value $\sim 10^6$ K. The layer just above the temperature minimum is called the chromosphere, from its dominant visible emission, the red Hα line (λ6563 Å).

The outermost layer of the solar atmosphere, the corona, extends from a height of about 3000 km above the photosphere out to many solar radii. The high temperatures $\sim 10^6$ K are maintained over this large range of distances, but the density drops rapidly, in the outward direction. Because of the high temperature most of the coronal emission is in the soft X-ray band; conversely, the only region of the solar atmosphere to emit X-rays is the corona. Moreover, the density gradient restricts significant X-ray emission to the inner part of the corona ($\lesssim 10^5$ km above the photosphere) where the electron density is $\sim 10^8$–10^{10} cm^{-3}. The energy required to heat the chromosphere and corona is supplied by the dissipation of mechanical waves, generated in the sub-photospheric convection zone (see e.g. Stein and Leibacher, 1974).

The solar structure and typical values of important parameters for different parts of the Sun, are summarized in Figures 1.2 to 1.7 and Tables 1.1 and 1.2. More detailed discussions of the Sun and its atmosphere are given in the texts by Zirin (1966), Gibson (1973), that edited by Macris (1971), and the review by Howard (1972).

1.3 Solar Activity

The presence of a magnetic field in the solar plasma introduces a "preferred" direction (see Section 2.3). Localized concentrations of the magnetic field, termed "active regions", extend from below the photosphere out into the corona. The anisotropy due to the magnetic field, is responsible for the features observed, in emission or absorption, in different parts of the spectrum from radio to X-rays, and associated with active regions. These features (some of which are shown in Figures 1.3 and 1.4) include sunspots, plages, loops, filaments and prominences. Figure 1.8 shows a schematic diagram of an active region, relating these phenomena to the magnetic field configuration. It is generally accepted that the magnetic field is concentrated (and hence active regions formed) by the "winding-up", due to the Sun's differential rotation, of the sub-photospheric field lines which are "frozen" (see Section 2.3.3) into the plasma (Babcock, 1960, 1961; Leighton, 1969; Parker, 1970). The suggested operation of this mechanism is illustrated in Figure 1.9. The rotation period of the photosphere varies from about 26 days at the equator to about 37 days at the poles. The Babcock-Leighton model also helps to explain the following observations:

(1) The solar activity (as measured by numbers and sizes of active regions and the emission at different wavelengths) varies in a cyclic manner with a period of about 11 years (see Figure 1.10).

(2) At the start of a cycle, active regions appear at high latitudes (about $\pm 30^{\circ}$). In the course of the cycle, they emerge progressively closer to the equator and often fade away entirely at the end of the cycle (see Figure 1.11).

(3) Active regions appear in a bipolar configuration with the polarity of the leading portion (with respect to solar rotation) being opposite in the northern and southern hemispheres.

(4) The polarity of the leading portion in each hemisphere reverses with each eleven year cycle (see Figure 1.12).

The lifetime of a typical active region is of the order of a solar rotation; a typical 'life history' is given in Table 1.3.

Active regions are the sites of solar flares; these are transient events involving a sudden release of energy, which is observed as emission throughout the electromagnetic and particle spectrum (see Figure 1.13). It is thought (e.g. Zirin, 1966, 1974) that the flare energy is supplied by restructuring of the active region magnetic field. Flares may last from a few minutes to several hours.

1.4 The Coronal Soft X-ray Emission

Due to the high temperature of the corona most of its radiation is at soft X-ray wavelengths, from about 1 to 100 Å. The spectrum consists of line emission from highly ionized atoms and continuum emission due to free-free (thermal bremsstrahlung), free-bound (radiative recombination) and two-photon decay processes (see Section 2.4 .3.2). Two assumptions which are usually made in the analysis of coronal X-ray observations are: (1) the corona is optically thin at X-ray wavelengths, (2) for non-flare observations, the plasma is in an equilibrium state, i.e. time independent equations may be used. Taking typical values of coronal parameters ($T_e \sim 10^6$ K, $n_e \sim 10^9$ cm^{-3}, path length $\sim 10^9$-10^{10}cm) and referring to the discussion in Sections 2.3.2 and 2.4.3 shows that these assumptions should generally be valid.

At wavelengths less than 25 Å the coronal spectrum is dominated by the lines of hydrogen- and helium-like ions of oxygen, neon, magnesium, silicon and sulphur, and of neon-like iron. These lines are only produced efficiently at temperatures $\gtrsim 1.5 \times 10^6$ K and so are true coronal lines, free from confusion with the radiation from the lower temperature layers of the solar atmosphere. The instrument normally used to obtain high resolution solar spectra below 25 Å has been the Bragg crystal spectrometer. Grazing incidence diffraction gratings have also been employed, but to a much more limited extent. Mechanical collimators are often used to restrict the observations to a particular portion of the corona. An example of the X-ray spectrum obtained by a collimated crystal spectrometer, is shown in Figure 1.14 (from Parkinson, 1971a).

The highest spatial resolution observations of the X-ray corona have been obtained by grazing-incidence reflection telescopes, with the images recorded on photographic film. Broadband filters are used to give some spectral information. Figure 1.4 shows an example of such a photograph (from Vaiana et al., 1973a). These high resolution images show that the X-ray emitting plasma traces out the coronal magnetic field configuration; this is understandable, since the magnetic field is frozen into the plasma and the magnetic pressure is much greater than the thermal gas pressure (see Section 2.3.3). Vaiana et al. (1973b) have identified six classes of coronal structure observable in the X-ray photographs: (1) active regions, (2) active region interconnections, (3) large loop structures associated with unipolar magnetic regions, (4) coronal holes, (5) coronal bright points, (6) the structures surrounding filament cavities. Examples of these features are shown in Figure 1.4.

In order to establish correctly the coronal plasma parameters, observations having both high spatial and high spectral resolution are required. To date, technological and sensitivity constraints have prevented the construction and use of a true X-ray spectroheliometer, that is, an instrument capable of obtaining high spatial resolution images with a high resolution spectrum for each image picture element. Therefore, the instruments which have so far been used have had either high spectral resolution with a moderate spatial resolution (mechanically collimated Bragg crystal spectrometers) or high spatial resolution with low spectral resolution (grazing-incidence telescopes with broadband filters). The development of these techniques is well illustrated by the example of the X-ray Astronomy Group at Leicester University, which has concentrated on the design, construction and use of Bragg crystal spectrometers, while, in contrast, at American Science and Engineering (ASE) the main emphasis has been on the development of grazing-incidence X-ray telescopes, The terms "high" and "low" resolution will be quantified later.

In a few cases, simultaneous spectra and images have been obtained by using separate spectrometers and telescopes (Davis et al., 1975; present work, Chapter 4). These observations show that, when deriving coronal plasma parameters from the data, it is necessary to have both high spectral and high spatial resolution measurements, in order to avoid possible misinterpretation and ambiguity. Several research groups are now in the course of designing X-ray spectroheliometers of the sort mentioned earlier, employing grazing-incidence imaging optics and a spectrometer (either Bragg crystal or grazing-incidence diffraction grating) arranged along the same optical path (NASA-GSFC, 1974, 1975; Davis, 1974).

Further information on observations of the coronal X-radiation, their analysis and interpretation, instrumentation, historical background and earlier work may be found in the reviews by Neupert (1969, 1971), Pounds (1970), Doschek (1972, 1975), Walker (1972, 1974, 1975), Doschek and Meekins (1973), Vaiana et al. (1973, 1975), Culhane and Acton (1974), Vaiana and Tucker (1974) and Parkinson (1975a, 1975b). Reviews of the instrumentation are given by Giacconi et al. (1969), Gursky and Schwartz (1974), Underwood (1974) and Acton (1975). Fawcett (1974) has reviewed the classification of spectral lines observed from plasmas at coronal temperatures.

Here, we present a review of the solar X-ray astronomy programme at Leicester University. Vaiana et al. (1973, 1974) have reviewed the solar X-ray astronomy programme at ASE; the progress in coronal X-ray imaging techniques, since the early 1960's, is demonstrated by the photographs in Figure 1.15.

1.5 The Solar X-ray Astronomy Programme at Leicester University

The X-ray Astronomy Group of the Physics Department, Leicester University has been actively engaged in solar X-ray astronomy since the joint University College London (UCL)/Leicester experiment aboard Ariel I launched in April 1962. Subsequently, collaborative experiments with UCL have been flown on the satellites ESRO 2, OSO IV and OSO V. The X-ray spectroheliograph aboard OSO V, launched in January 1969, continued to work well up to the satellite's shut-down in mid-1975 (on the successful launch of OSO VIII). The solar X-ray maps obtained by this experiment are published in "Solar Geophysical Data". All the above experiments employed broadband proportional counter detector systems.

In addition to the satellite work there has been a continuous programme of sounding rocket experiments, most of them using the Skylark rocket. Early payloads included proportional counter spectrometers and pin-hole cameras with photographic film recording. Since 1966 however, the primary instrument used on Skylark flights has been the plane, scanning, Bragg crystal spectrometer, to perform high resolution X-ray spectrometry of solar active regions, in the wavelength range below 25 Å.

The objectives in observing the coronal soft X-ray emission with high spectral resolution, may be summarized as follows:

(1) The diagnosis of coronal plasma parameters (e.g. temperature, density, emission measure (n_e^2V), element abundances), in order to further our knowledge of the physical processes which occur in the corona.

(2) Atomic Spectroscopy. The conditions in the coronal plasma - low density ($n_e \sim 10^9$ cm^{-3}), high temperature ($T_e \sim 10^6$ K), and relatively steady state ($\sim$hours to days, for non-flaring sources) - cannot be reproduced on Earth, and hence the corona is a useful spectroscopic X-ray light source, particularly for the observation of forbidden transitions (e.g. the magnetic dipole $1s^2.{}^1S_0 - 1s2s.{}^3S_1$ in He-like ions, and the magnetic quadrupole $2p^6.{}^1S_0 - 2p^53s.{}^3P_2$ in Ne-like ions). The measurements of the line spectrum yield valuable atomic data, such as wavelengths, energy levels, and excitation rates, and provide comparisons with theoretical models for the ions observed.

The Leicester crystal spectrometer flights are listed in Table 1.4. The increasing resolution and sensitivity achieved by successive instruments, are illustrated by the spectra shown in Figure 1.16.

Most of the spectra recorded by the Leicester instruments from 1966 to 1973 were from non-flaring active regions. The first flights (SL304, SL305, S41) confirmed earlier observations and theoretical predictions, that the solar soft X-ray spectrum is dominated by line emission, mainly from H- and He-like O, Ne, Mg, Si, and Ne-like Fe. They also showed that, in agreement with pin-hole camera X-ray photographs, the bulk of the X-ray emission originated in coronal active regions, and that the active regions contained, in general, a multi-temperature plasma ($T \sim 1.5 \times 10^6$ K up to $\sim (6-8) \times 10^6$ K) (Evans et al., 1967; Evans and Pounds, 1968; Batstone et al., 1970; Evans, 1970). All these early flights viewed the whole Sun, and hence when more than one active region was present, the slightly different angle subtended by each, at the crystal, gave rise to spectra that were shifted relative to each other. This problem was solved by restricting the field of view of each spectrometer with a collimator (of the multiple-grid type). The first experiment of this type to be designed was S69 (a second generation (Mk. 2) instrument), with a field of view of 4 arc min x 4 arc min FWHM (full width at half maximum) (Evans, 1970; Parkinson, 1971a,b); although it was not flown until a few weeks after SL804, the first flight of the third generation (Mk. 3) spectrometer.

The Mk. 3 instrument is the present generation of Leicester crystal spectrometer and its design reflects the experience gained from the earlier experiments. It has been successfully flown and recovered three times: SL804 (24 November 1970), SL1101 (30 November 1971), SL1206 (26 November 1973). The payload consists of three plane, scanning, Bragg crystal spectrometers, covering between them the wavelength range 4 to 23 Å, and collimated to 3 arc min x 3 arc min FWHM. It is discussed in more detail in Chapter 3. The observations and data analysis from flights of the Mk. 3 spectrometer, up to the start of the work covered by this thesis, will now be reviewed. The flight programme in each case was to obtain high resolution X-ray spectra (from 4 to 23 Å) of two active regions. The observing time for each region was about 2½ min, divided up so that the crystals performed a "fast" scan through a Bragg angle range of $\sim 35^{\circ}$ in about 1 min, and a "slow" scan through $\sim 5^{\circ}$ in the remaining 1½ min. The slow scan was made to coincide with the observation, on each crystal, of the $n = 2 \rightarrow 1$ lines of the He-like ions O VII, Ne IX, Mg XI (n is the principal quantum number).

(a) SL804 was launched from Woomera, S. Australia at 2213 UT on 24 November 1970.

OBSERVATIONS:

Due to an unknown attitude error the experiment appears to have viewed an area of "quiet" corona. 18 sec after the start of observations the detector window of the KAP spectrometer failed. 206 sec after launch the spectrometer drive motor stopped, thus the second active region was not observed.

88 min before the SL804 flight, an Aerobee 150 rocket carrying an ASE grazing-incidence X-ray telescope, was launched from White Sands, New Mexico. The experiment worked correctly, and obtained X-ray images in various wavelength bands. From these, it appears that SL804 probably observed large scale "quiet" coronal structures and possibly a coronal bright point.

DATA ANALYSIS:

Due to the low intensities and the failure of the KAP spectrometer, only a few spectral lines were observed, namely:

the $n = 2 \rightarrow 1$ resonance, intercombination and forbidden lines of Ne IX and Mg XI, and the $\lambda\lambda$12.12, 12.26 Å lines of Fe XVII. These data were, however, sufficient to yield a coronal model of emission measure and electron temperature, and a value for the relative abundance of iron (Parkinson, 1971a; Parkinson et al., 1972).

(b) SL1101 was launched from Woomera, S. Australia at 0529 UT on 30 November 1971.

OBSERVATIONS:

The active regions observed were McMath 11621 and 11619. An attitude error of 14° in roll meant that the centres of the active regions were not viewed at maximum collimator efficiency. All spectrometers worked correctly and returned good data, throughout the observing time.

Near to the time of the SL1101 flight, X-ray spectroheliograms were obtained by the OSO-5 and OSO-7 satellites, and ground based observations were made by the Carnarvon Solar Observatory, W. Australia.

DATA ANALYSIS:

The spectra had a higher resolution and sensitivity than any previously obtained, resulting in the observation of many hitherto unobserved weak lines and the separation of a large number of lines which had, in previous data, been seriously blended. The results of the analysis of region 11621 are summarized as follows (from Parkinson, 1972, 1973a, 1975c):

(1) Intensities and wavelengths were measured for 98 lines, and identifications proposed for 62 of these. Many of the lines were observed for the first time.

(2) The intensities of the $n = 2 \rightarrow 1$ resonance lines of O VII, VIII, Ne IX, X, Mg XI were used to construct a thermal model of emission measure versus electron temperature.

(3) Comparison of the measured and predicted wavelengths and intensities of the satellites to the He-like ions Ne IX and Mg XI, showed good agreement.

(4) All eight of the known $n = 3 \rightarrow 2$ transitions in Fe XVII were observed for the first time, and their measured relative intensities were in substantial agreement with those predicted by current theoretical models.

(5) Several members of the resonance series 1s - np in H- and He-like O, Ne, Mg were observed, and their measured and calculated intensities were shown to be in reasonable agreement.

(6) Relative abundances were derived for the elements O, Ne, Na, Mg, Fe, Ni.

(7) Effective oscillator and collision strengths were derived from the observations, for the identified transitions.

(8) Where the same spectral line was observed on more than one crystal, the intensities derived from the data, by using the crystal integrated reflectivity measurements of Leigh and Evans, were consistent.

The spectrum of region 11619 is analysed in the present work, together with the spectra of regions 12624 and 12628, observed by SL1206. The Leicester Bragg spectrometers and the data obtained until the end of 1970, are the subject of the theses by Evans (1970) and Parkinson (1971a).

Table 1.1 Relative Values of Kinetic and Magnetic Energy Density in the Sun (Zirin, 1966)

Place	$n(cm^{-3})$	$T(deg)$	$B(gauss)$	$nkT\left(\frac{erg}{cm^3}\right)$	$B^2/8\pi\left(\frac{erg}{cm^3}\right)$
Photosphere (quiet)	10^{15}	6000	1	800	0.04
Photosphere (active)	10^{15}	6000	50	800	100
Sunspot	10^{15}	4000	1000	500	40,000
Chromosphere (quiet)	10^{13}	7000	1	10	0.04
Chromosphere (network facula)	10^{13}	20,000	50	30	100
Corona	10^{9}	10^{6}	50	.014	100

Table 1.2 Characteristic length and time scales for coronal structures

($n_e = 10^9 cm^{-3}$, $T = 2 \times 10^6$ K, B = 5G)

(Vaiana and Tucker, 1974)

Mean interparticle distance ($\propto N^{-1/3}$)	$\sim 10^{-3}$ cm
Debye shielding length $\lambda(\propto T^{1/2}N^{-1/2})$	$\sim 10^{-1}$ cm
Electron gyro radius $R_L(\propto T^{1/2} B^{-1})$	$\sim 10^{-2}$ cm
Collision mean free path $\lambda_C(\propto T^2 N^{-1})$	$\sim 10^{7}$ cm
Characteristic length of coronal structure L_C	$\sim 10^{9}$ cm
X-ray line absorption mean free path λ_a	$\gtrsim 10^{11}$ cm
Period of plasma oscillation $t_p(\propto N^{-1/2})$	$\sim 10^{-9}$ s
Electron gyro period ($\propto B^{-1}$)	$\sim 10^{-8}$ s
Ionization time $t^I(\propto T^{-1/2} N^{-1}Z^4)$	$\sim 10^{3}$ s
Recombination time $t_R(\propto T^{1/2} N^{-1} Z^{-1})$	$\sim 10^{3}$ s
Conduction cooling time $t_{cc}(\propto L_c^2 NT^{-5/2})$ ($L_c=10^{10}$ cm)	$\sim 10^{4}$ s
Radiation cooling time $t_{Rc}(\propto TN^{-1})$	$\sim 10^{4}$ s

Table 1.3 Life history of a typical active region (Brandt, 1966)

DAY	SPOTS	MAGNETIC REGION	FACULAE	FLARES	PROMINENCES (Filaments)	CORONAL REGIONS
1	Spots may originate a few hours after faculae appear, but usually only pores.	Assumes bipolar character.	Systematic alignment of chromospheric fine structure around area which becomes bright facular speck. Speck develops east-west orientation.			Green patch forms after spots appear. Parallels facular development. Same extent as facular region.
2	West end of facular regions shows first *p* spot.	Characteristic dimension magnetic region $\backsim$50,000 km.	Area increases in size and brightness.	First signs of activity.	Small, unstable filaments appear around faculae.	Green line increases.
5	*f* spot appears at east end of faculae; other small spots in between; main spots are continually separating.			Flares between *f* and *p* spots.	Sunspot prominences appear.	
11	Maximum development.	Field irregular and variable.	Size and brightness increases; dimensions $\backsim 10^5$ km.	Peak of flare activity.		Yellow-line brightness with flare activity.

DAY	SPOTS	MAGNETIC REGION	FACULAE	FLARES	PROMINENCES (Filaments)	CORONAL REGIONS
27	Usually only *p* spot remains; the f spot disappears by being "bridged" by bright, normal photosphere.	Magnetic flux reaches maximum.	Facular area still increases in size.	Flares rare.	Stable filament forms on poleward side of facular area, makes angle of some 40° with meridian and points toward *p* spot.	Maximum green-line brightness.
54	No spots.		Brightness decreases and area cut in half by filament.		Filament now $\backsim 10^5$ km in length and starting to swing toward east-west orientation.	Green line decreases in brightness.
81		Field strength declines.	Area constant, dissolves into bright facular network (still brighter than normal chromosphere).		Length increases and orientation continues toward east-west.	
108			Faculae dissolved.		Maximum length achieved and nearly east-west (parallel to equator).	
135		Area occupies one-twentieth of disk.	CA undetectable in photosphere or chromosphere except for some fine structure oriented around filament.		Length decreases; prominence starts poleward migration.	
162–270		BMR fills one-fifth of disk and changes into UMR.			Filament changes structure and joins polar crown filaments.	Coronal streamers, associated with UMR.*

* Note: East and west are as the Sun is seen from the Earth.

Table 1.4 Leicester University solar sounding rocket (Skylark) experiments - plane, scanning, Bragg crystal spectrometers

Launch date (dy/mth/yr)	Experiment serial no.[a)]	Instrument Mark no.	Collimation FWHM(arc min)	Crystals	Wavelength range (Å)	Total area each crystal (cm^2)	Publications[b)]
5/5/1966	SL304	1	none	KAPx2	11-23	1	1,2
8/8/1967	SL305	1	none	EDDT Beryl	3.5-8 7.5-15	1	3
22/11/1968	S41	2	none	LiF NaCl ADP KAP	1.5-3.5 2.2-4.0 4.5-9.5 9.0-22.0	12	4,9
24/11/1970	SL804	3	3x3	ADP Gypsum KAP	4-9.4 7-13.9 9-23	100	5,7
6/12/1970	S69	2b	4x4	EDDT ADP Gypsum KAP	3.5-8 4-9.4 7-13.9 9-23	12	5,6,7
30/11/1971	SL1101	3	3x3	ADP Gypsum KAP	4-9.4 7-13.9 9-23	100	8,10,11,12,13,14
26/11/1973	SL1206	3	3x3	ADP Gypsum KAP	4-9.4 7-13.9 9-23	100	14

Footnotes to Table 1.4

a) Serial nos. : SL- were launched from Woomera, by SRC as part of the British National Space Research Programme.

S- were launched from Sardinia, by ESRO.

b) References:

1) Evans et al. (1967)
2) Evans and Pounds (1968)
3) Batstone et al. (1970)
4) Evans (1970)
5) Parkinson (1971a)
6) Parkinson (1971b)
7) Parkinson et al. (1972)
8) Parkinson (1972)
9) Parkinson (1973c)
10) Parkinson (1973a)
11) Parkinson (1975a)
12) Parkinson (1975b)
13) Parkinson (1975c)
14) Present work

FIGURES

Chapter 1

1.11 Sunspot 'butterfly' diagram, showing the latitude variation of sunspot occurrence with the solar activity cycle (Kiepenheuer, 1959).

1.12 Idealized reversal of polar and sunspot polarities with the advancement of the solar cycle (Gibson, 1973).

1.13 Schematic representation of the sequence of events in the radiation from a flare (Kane, 1974).

1.14 X-ray spectrum of a solar active region (McMath 11060) obtained on 6 December 1970 by a collimated Bragg crystal spectrometer flown on a Skylark rocket (flight S69) by the University of Leicester. These data are not corrected for the variation in instrument sensitivity with wavelength, but clearly illustrate the dominance of line emission in this spectral region. Identities of the parent ions for the stronger lines are indicated (Parkinson, 1971a).

1.15 X-ray photographs of the solar corona, illustrating the progress in solar X-ray imaging. (Vaiana et al., 1973b).

a 15 October 1963, the first X-ray image of the Sun made with a grazing incidence telescope.

b 17 March 1965, electroformed nickel mirror with resolution about 30 arc sec.

c 8 June 1968, Kanigen-coated beryllium mirror with resolution about 2 arc sec.

d 8 April 1969, similar instrumentation to c.

e 4 November 1969, similar instrumentation to c.

f 7 March 1970, similar instrumentation to c.

g 24 November 1970, similar instrumentation to c.

h 8 March 1973, quartz mirror with resolution better than 2 arc sec.

1.16 (Leicester University) X-ray spectra of solar coronal active regions, illustrating the progress in solar X-ray (Bragg crystal) spectrometry. The same spectral region ($\lambda \sim 9$ Å) is shown in each case. The spectral lines are the Mg XI $n = 2 \rightarrow 1$ transitions and their satellites.

a 8 August 1967, beryl crystal, uncollimated, flight SL305 (Batstone et al., 1970).

b 22 November 1968, ADP crystal, uncollimated, flight S41 (R. Batstone, private communication in Parkinson, 1975a).

c 6 December 1970, ADP crystal, collimated (4 x 4 arc min, FWHM)^2, flight S69 (Parkinson, 1971b).

d 30 November 1971, ADP crystal, collimated (3 x 3 arc min, FWHM)^2, flight SL1101 (Parkinson, 1972).

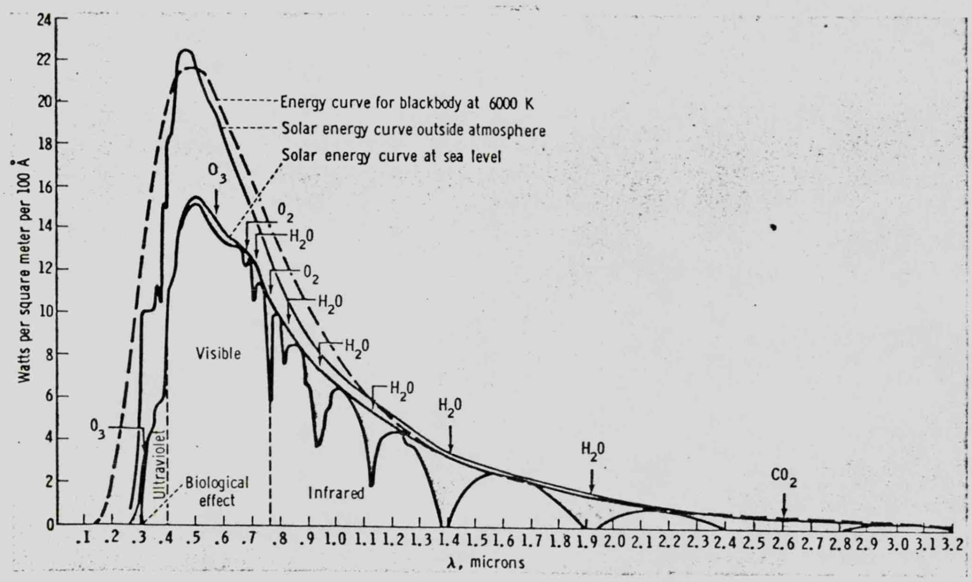

Fig. 1.1.a.

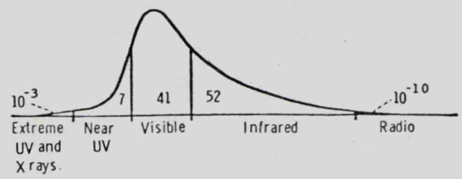

Fig. 1.1.b.

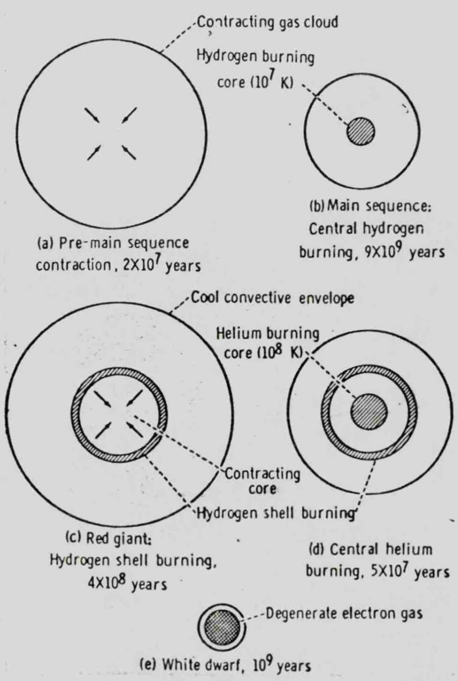

Fig. 1.2.

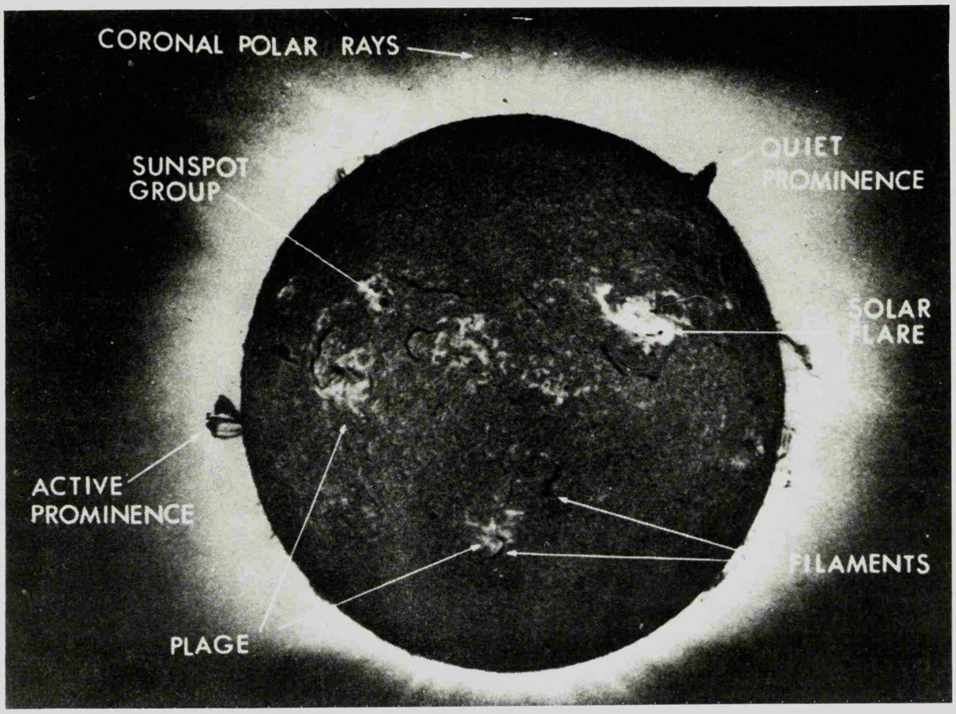
CORONAL POLAR RAYS
SUNSPOT GROUP
QUIET PROMINENCE
SOLAR FLARE
ACTIVE PROMINENCE
FILAMENTS
PLAGE

Fig. 1.3.

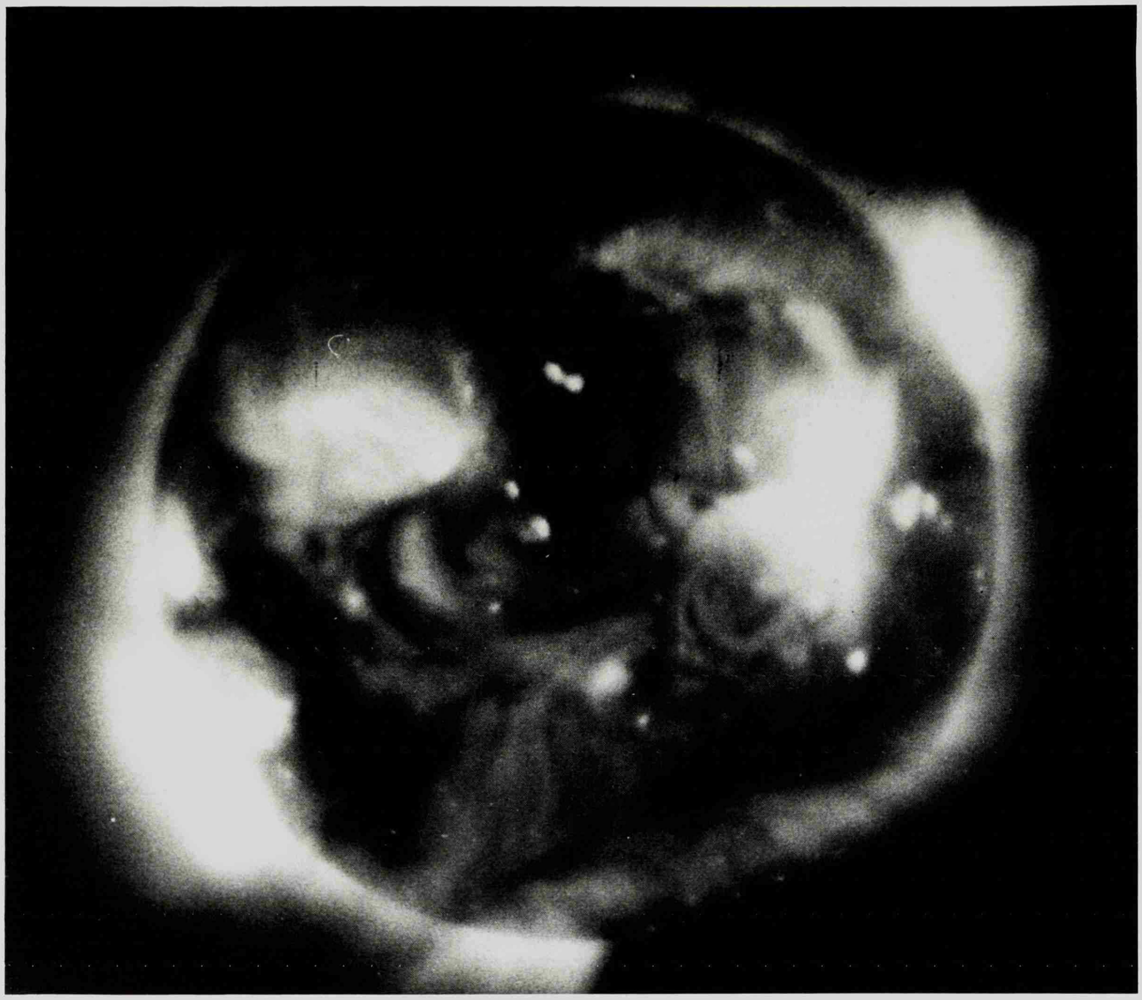

Fig. 1.4.a.

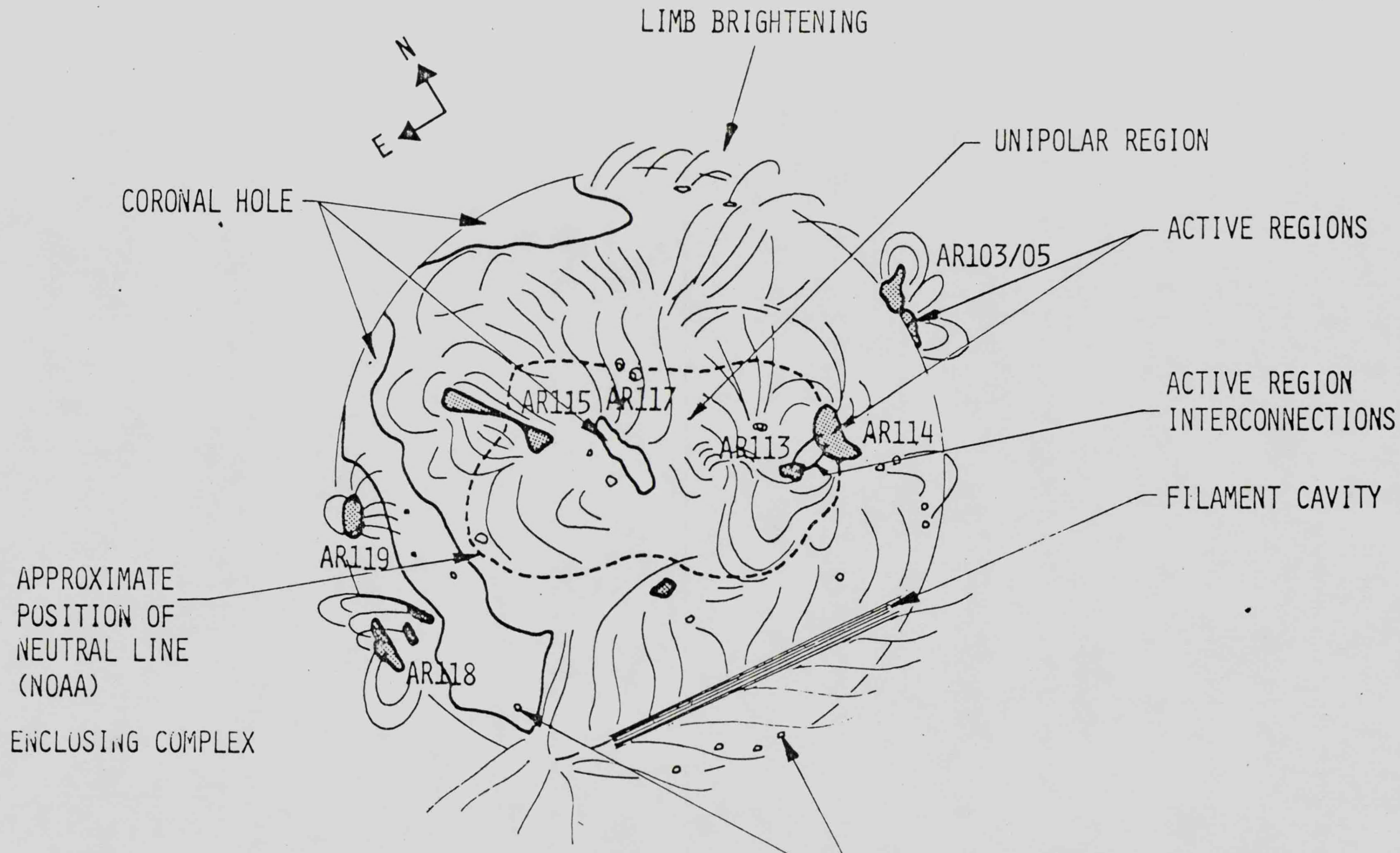
LIMB BRIGHTENING
N
E
UNIPOLAR REGION
CORONAL HOLE
ACTIVE REGIONS
AR103/05
ACTIVE REGION
INTERCONNECTIONS
AR115
AR117
AR113
AR114
FILAMENT CAVITY
AR119
APPROXIMATE
POSITION OF
NEUTRAL LINE
(NOAA)
AR118
ENCLOSING COMPLEX
BRIGHT POINTS

Fig. 1.4.b.

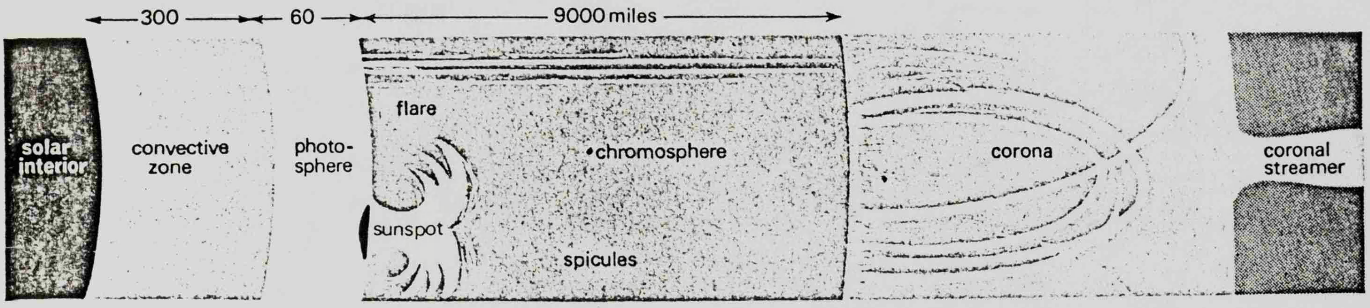

Fig. 1.5.a.

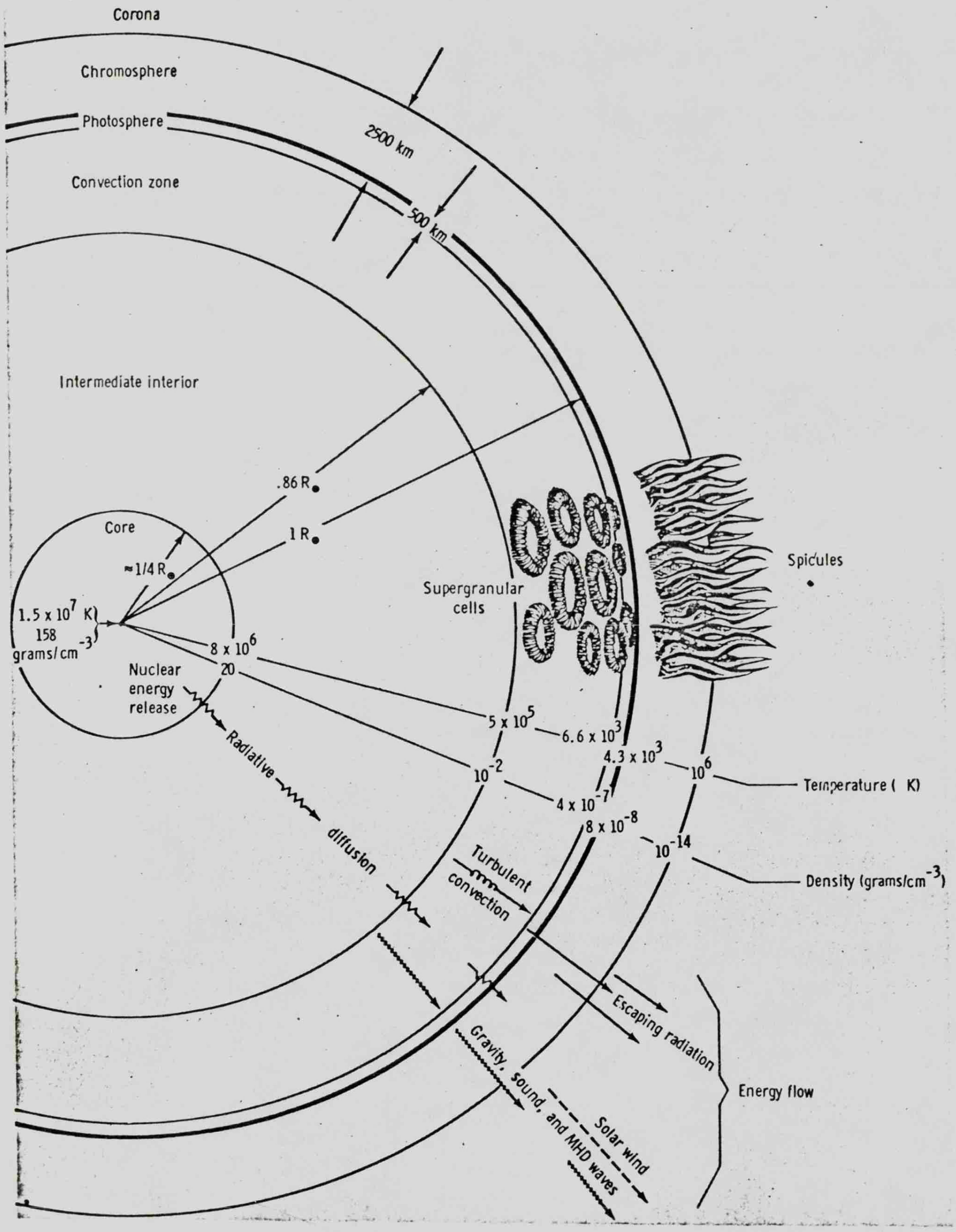

Fig. 1.5.b.

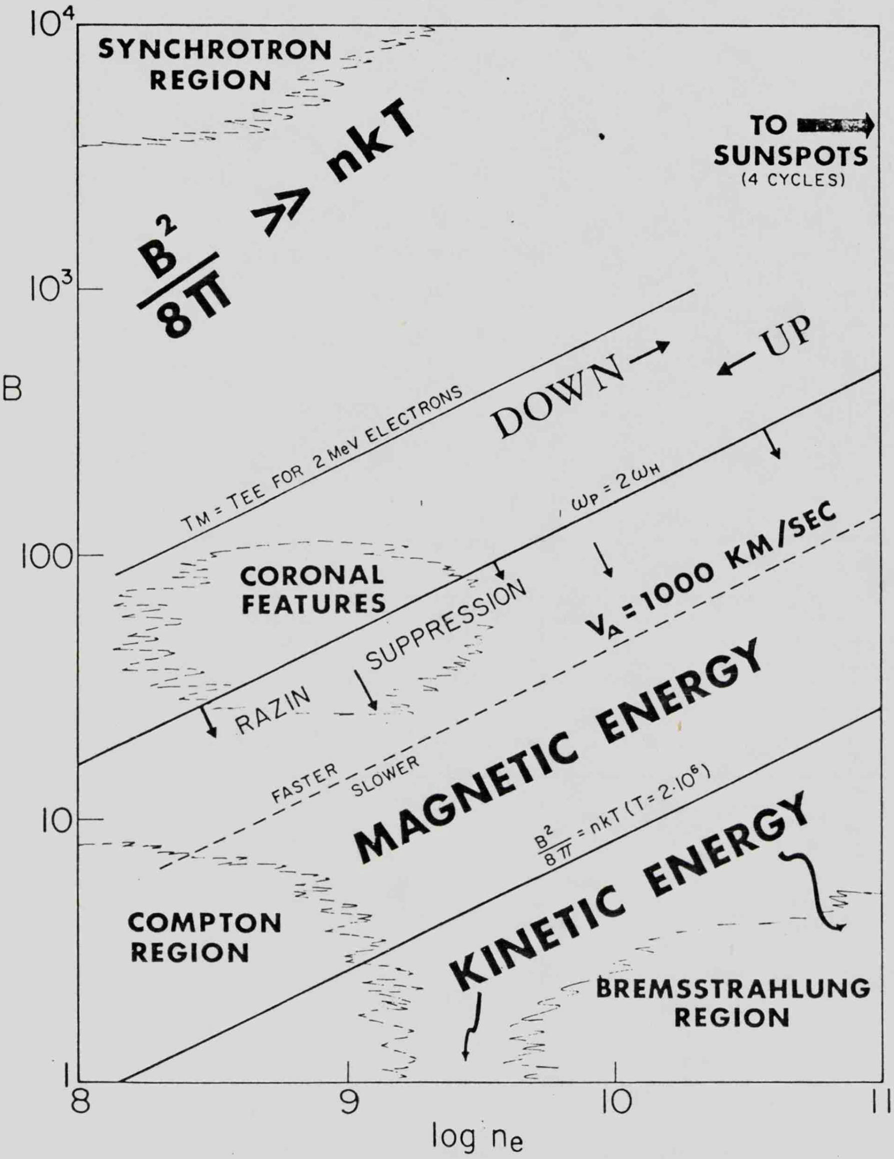

A GUIDE TO SOLAR PHYSICAL PROCESSES

The two physical parameters of greatest importance in solar physical processes are the magnetic field B and the electron density n_e. These quantities govern the mode by which energetic electrons lose energy. If B is large and n_e small, synchrotron emission (upper left corner) is the dominant mode. For small B and large n_e (lower right corner) bremsstrahlung is dominant. When both B and n_e are small (lower left), electrons interact primarily with photons to lose energy by inverse Compton processes.

The lowest diagonal line is the locus of values in which the magnetic and thermal energy densities are equal in a two million degree plasma. Below this line the kinetic energy dominates – above it the magnetic energy dominates. The dashed diagonal line indicates the locus of values for which the Alfvén velocity $V_A = 1000$ km/s. Above the line the velocity is faster and below the line slower. The third diagonal line is the locus of values for which $\omega_p = 2\omega_H$. Above this line the plasma does not seriously interfere with the spectrum and intensity of synchrotron and gyro-synchrotron emission. Below the line the Razin effect results in a suppression of lower frequencies of synchrotron emission. The top diagonal line is the locus of values for which the decay time for the energy loss by a 2 MeV electron is the same for synchrotron emission as for bremsstrahlung. Although the four diagonal lines represent four different physical parameters, a time, a frequency, a velocity, and an energy density, the slope of all lines is 0.5. This points out the fundamental fact that whereas the electron density enters into physical processes in a linear way, it is the square of the magnetic field which plays the analogous physical role in such processes.

Several geometrical features are also shown on the graph. Sunspots (upper right) with values of $n_e \sim 10^{15}$ and $B \sim 10^{3-4}$ are not on the graph. 'Up' and 'down' refer to vertical directions in the solar atmosphere. Up is associated with decreasing values of B and n_e. The region encompassed by coronal densities is shown in the left-center section of the graph. The graph is also available as a multi-colored 35 mm slide.

Fig. 1.5.c.

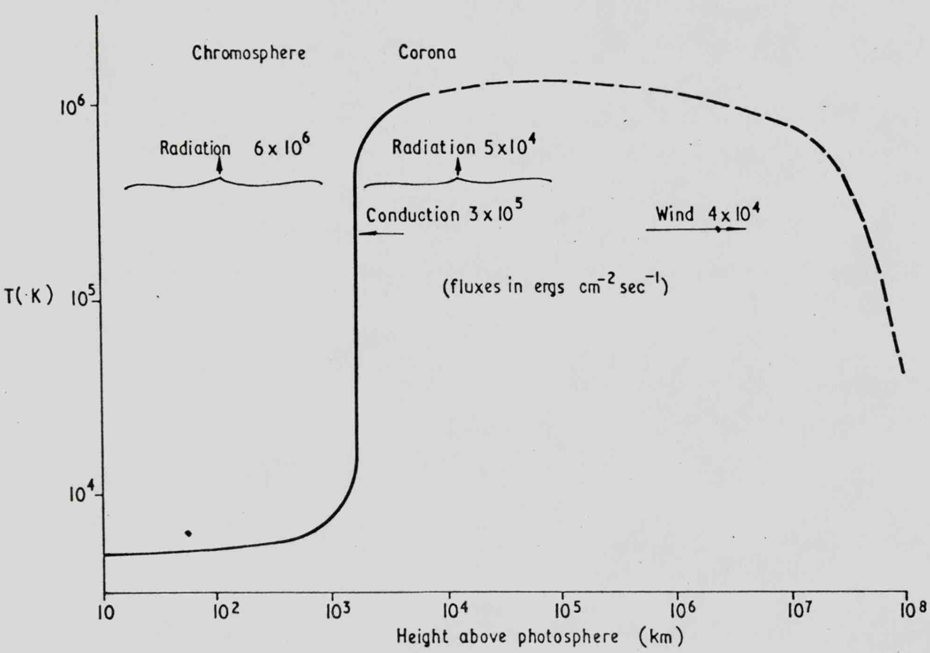

Chromosphere
Corona
Radiation 6 x 10^6
Radiation 5x10^4
Conduction 3 x 10^5
Wind 4 x 10^4
(fluxes in ergs cm^-2 sec^-1)
T(°K)
Height above photosphere (km)

Fig. 1.6.

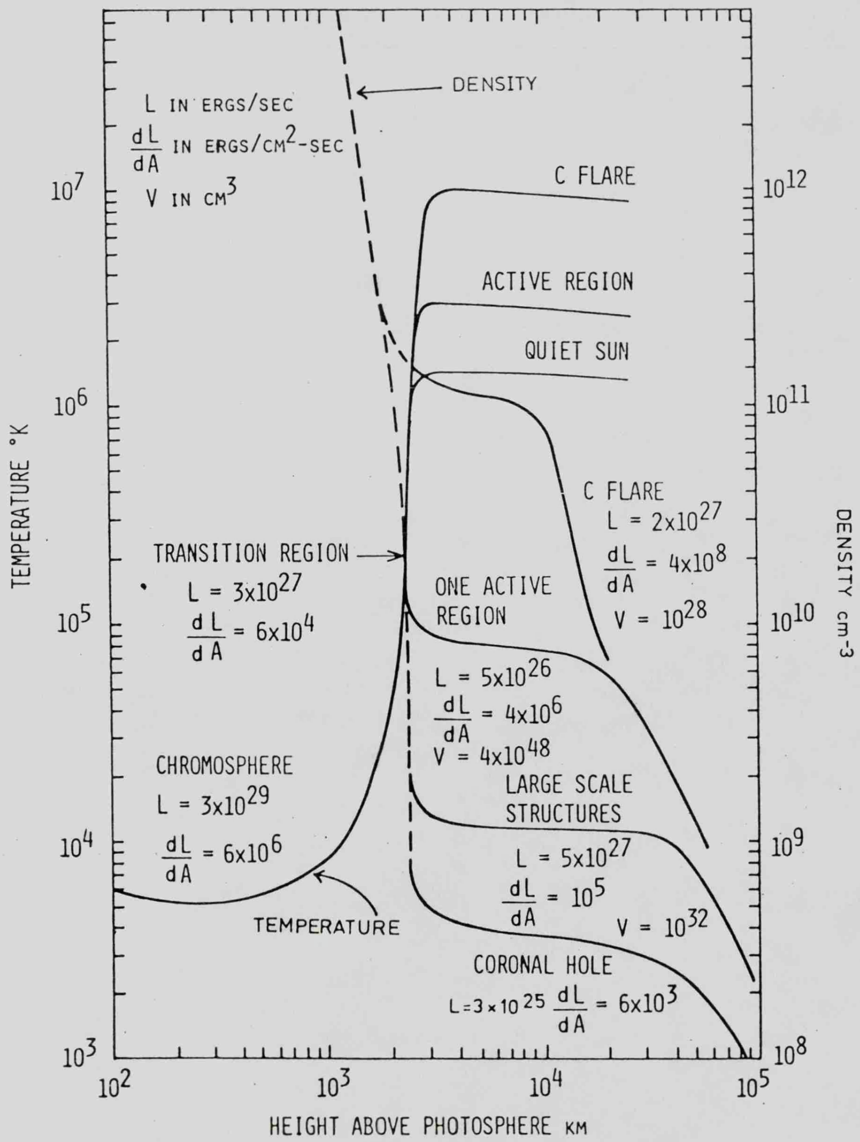

DENSITY
L IN ERGS/SEC
dL/dA IN ERGS/CM^2-SEC
V IN CM^3
C FLARE
ACTIVE REGION
QUIET SUN
C FLARE
L = 2x10^27
dL/dA = 4x10^8
V = 10^28
TRANSITION REGION
L = 3x10^27
dL/dA = 6x10^4
ONE ACTIVE REGION
L = 5x10^26
dL/dA = 4x10^6
V = 4x10^48
LARGE SCALE STRUCTURES
L = 5x10^27
dL/dA = 10^5
V = 10^32
CHROMOSPHERE
L = 3x10^29
dL/dA = 6x10^6
TEMPERATURE
CORONAL HOLE
L=3x10^25 dL/dA = 6x10^3
TEMPERATURE °K
DENSITY cm-3
HEIGHT ABOVE PHOTOSPHERE KM

Fig. 1.7.

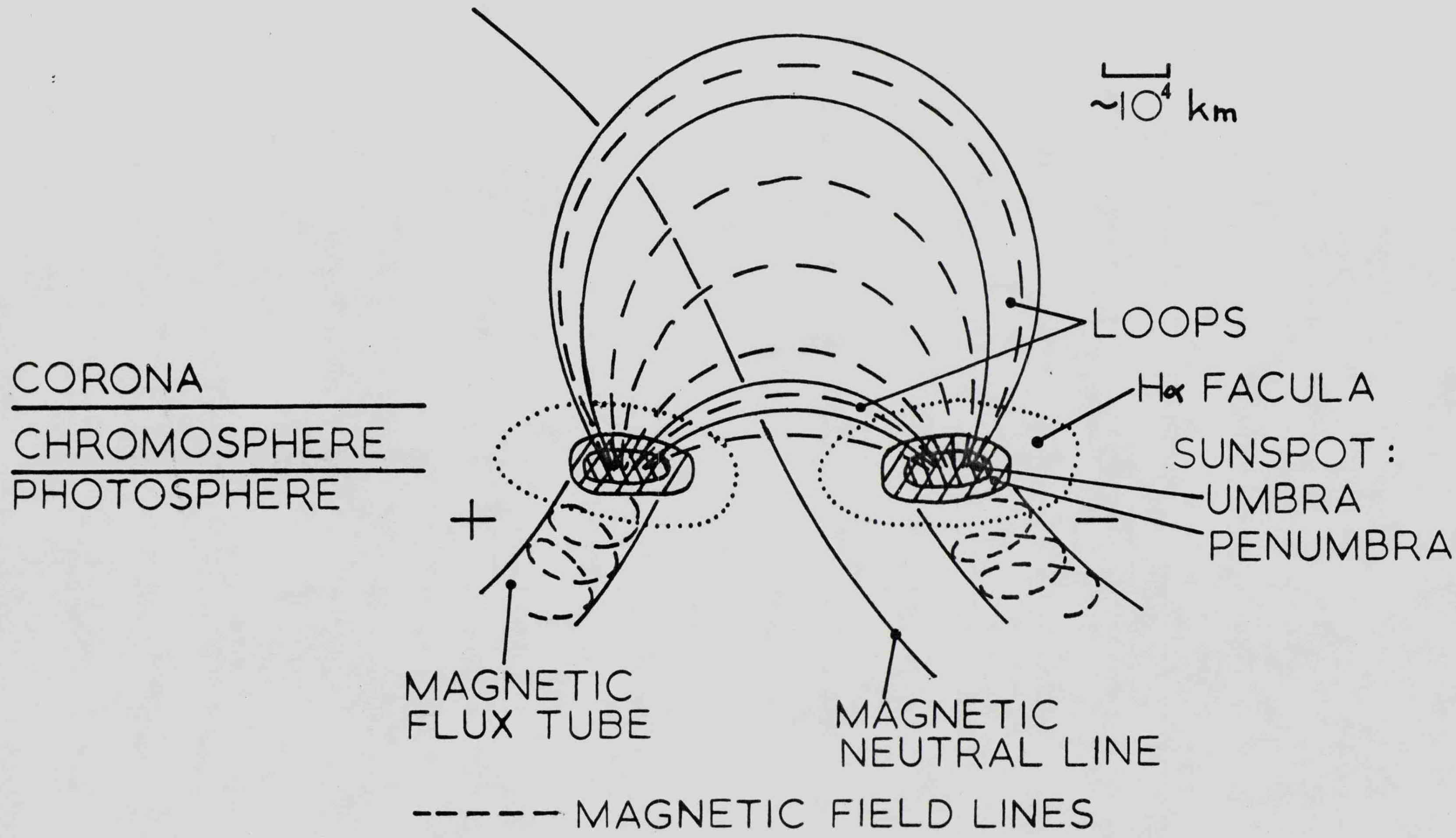
~10⁴ km
CORONA
CHROMOSPHERE
PHOTOSPHERE
LOOPS
Hα FACULA
SUNSPOT:
UMBRA
PENUMBRA
+
−
MAGNETIC
FLUX TUBE
MAGNETIC
NEUTRAL LINE
----- MAGNETIC FIELD LINES

Fig. 1.8.

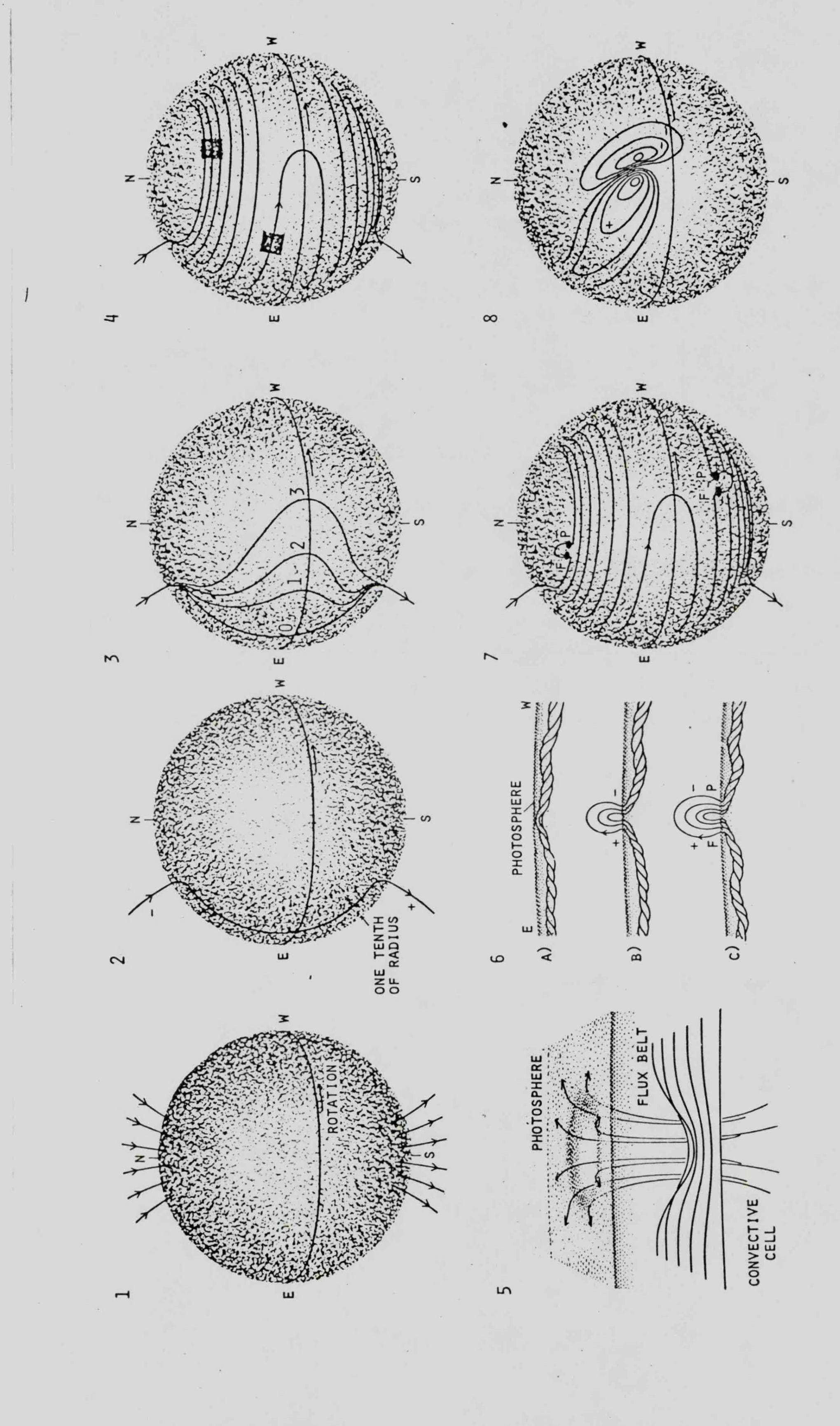

1
2
3
4
5
6
7
8
N
S
E
W
ROTATION
ONE TENTH OF RADIUS
PHOTOSPHERE
FLUX BELT
CONVECTIVE CELL
A)
B)
C)

Fig. 1.9.

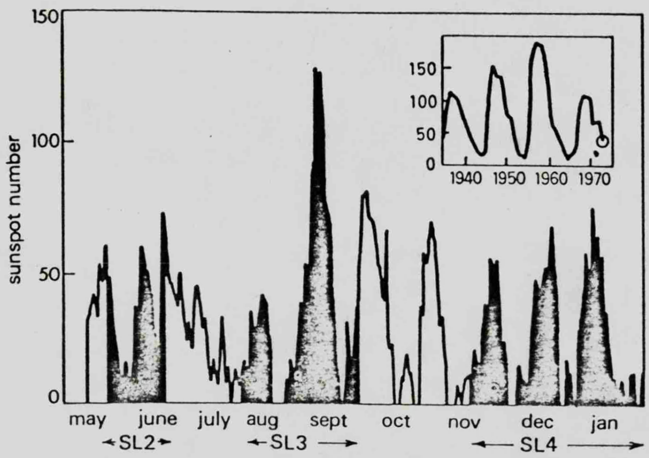

Fig. 1.10.

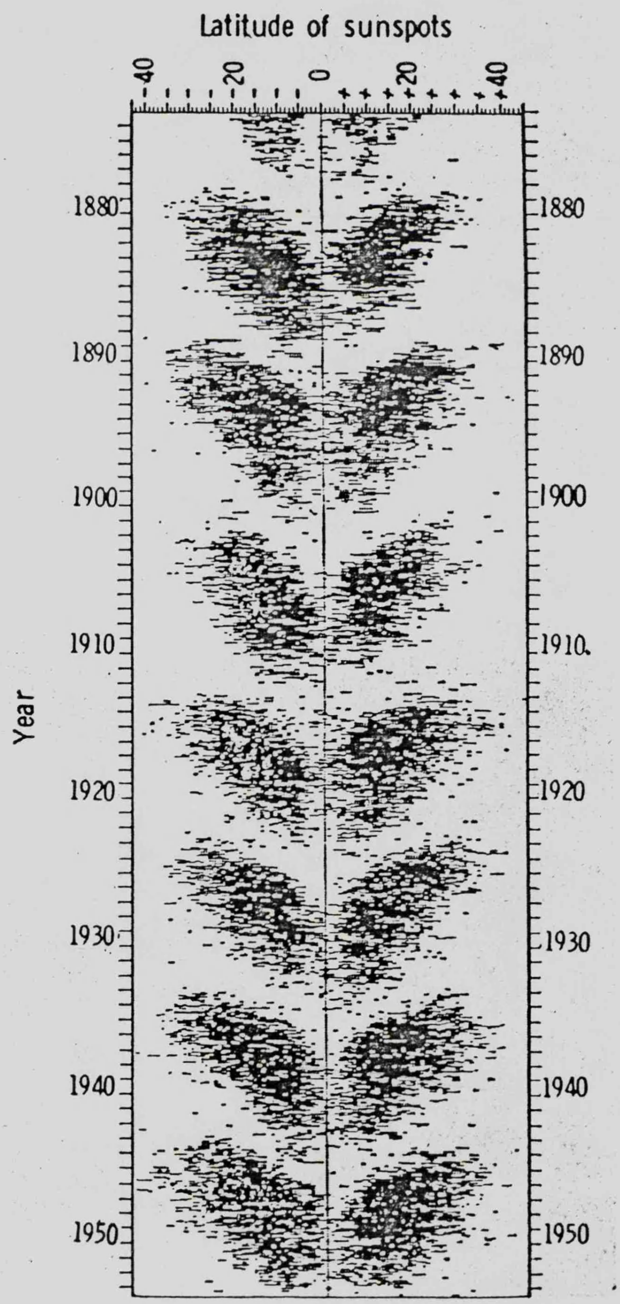

Fig. 1.11.

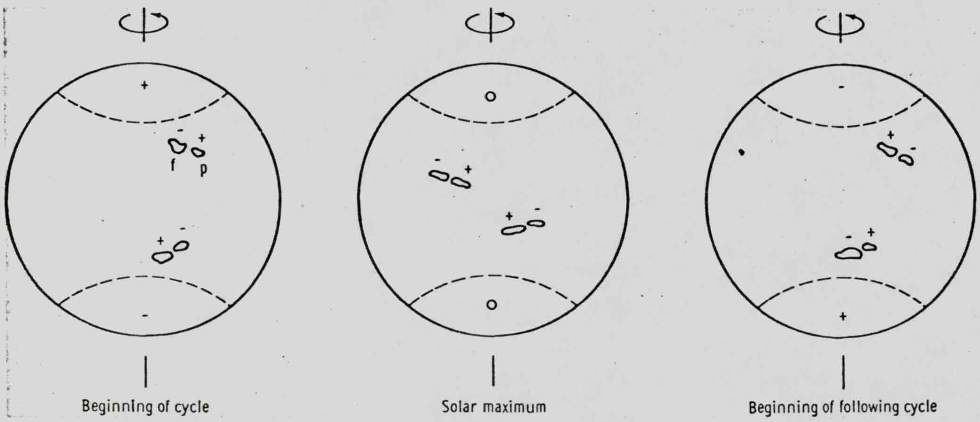

Fig. 1.12.

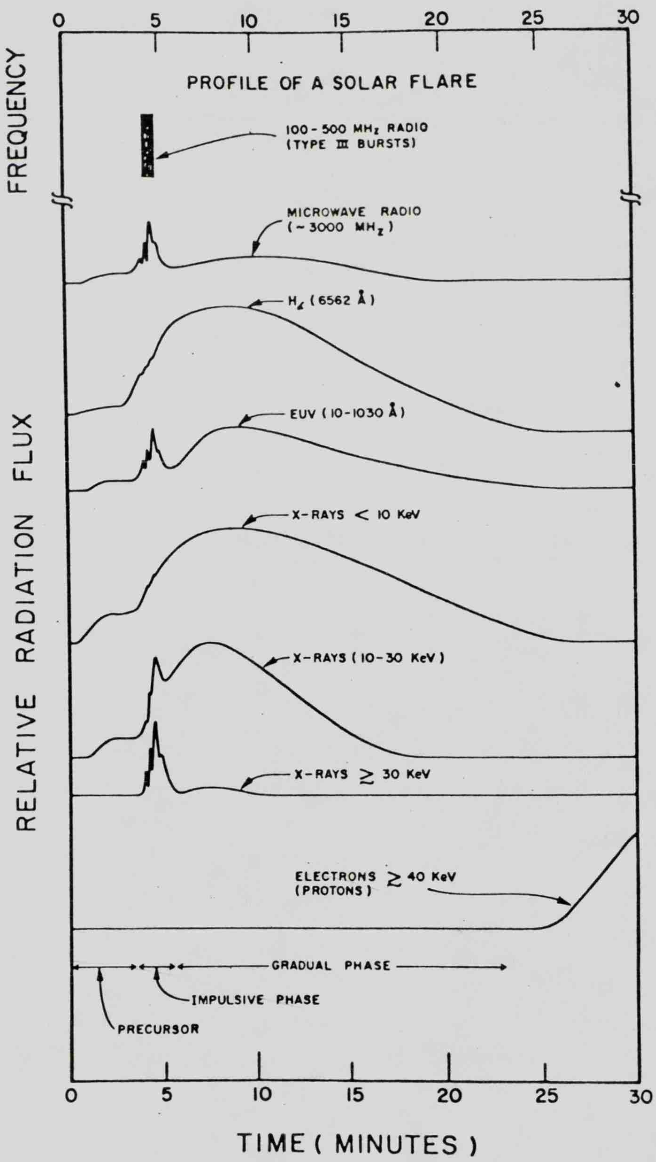

Fig. 1.13.

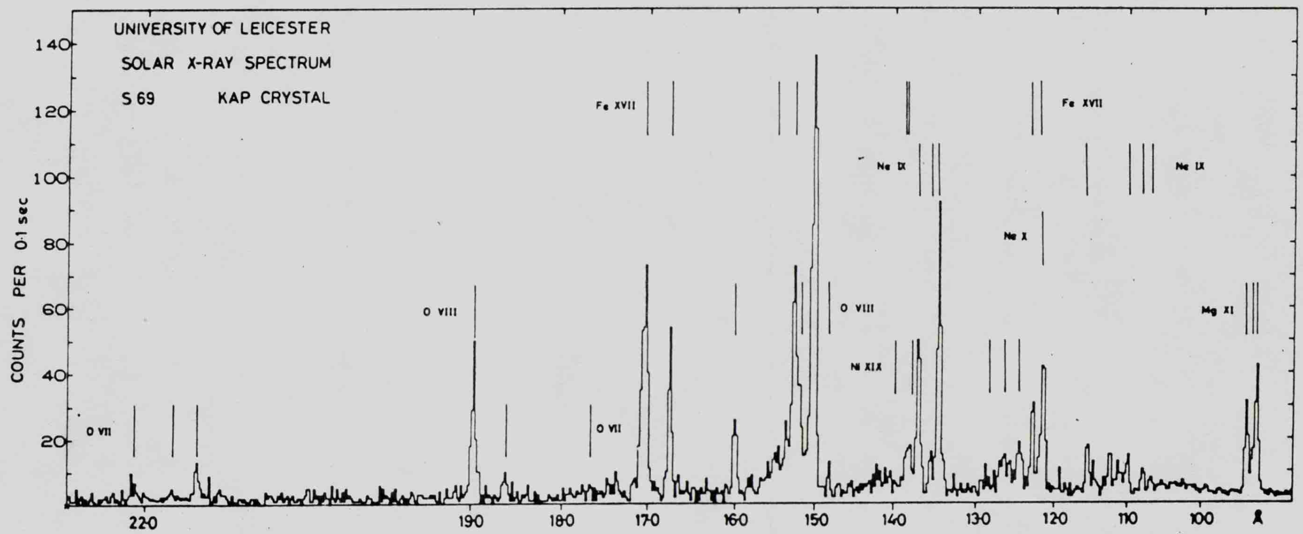
UNIVERSITY OF LEICESTER
SOLAR X-RAY SPECTRUM
S 69 KAP CRYSTAL
COUNTS PER 0·1 sec
Fe XVII
Ne IX
Ne X
O VIII
Ni XIX
Mg XI
O VII
Å

Fig. 1.14.

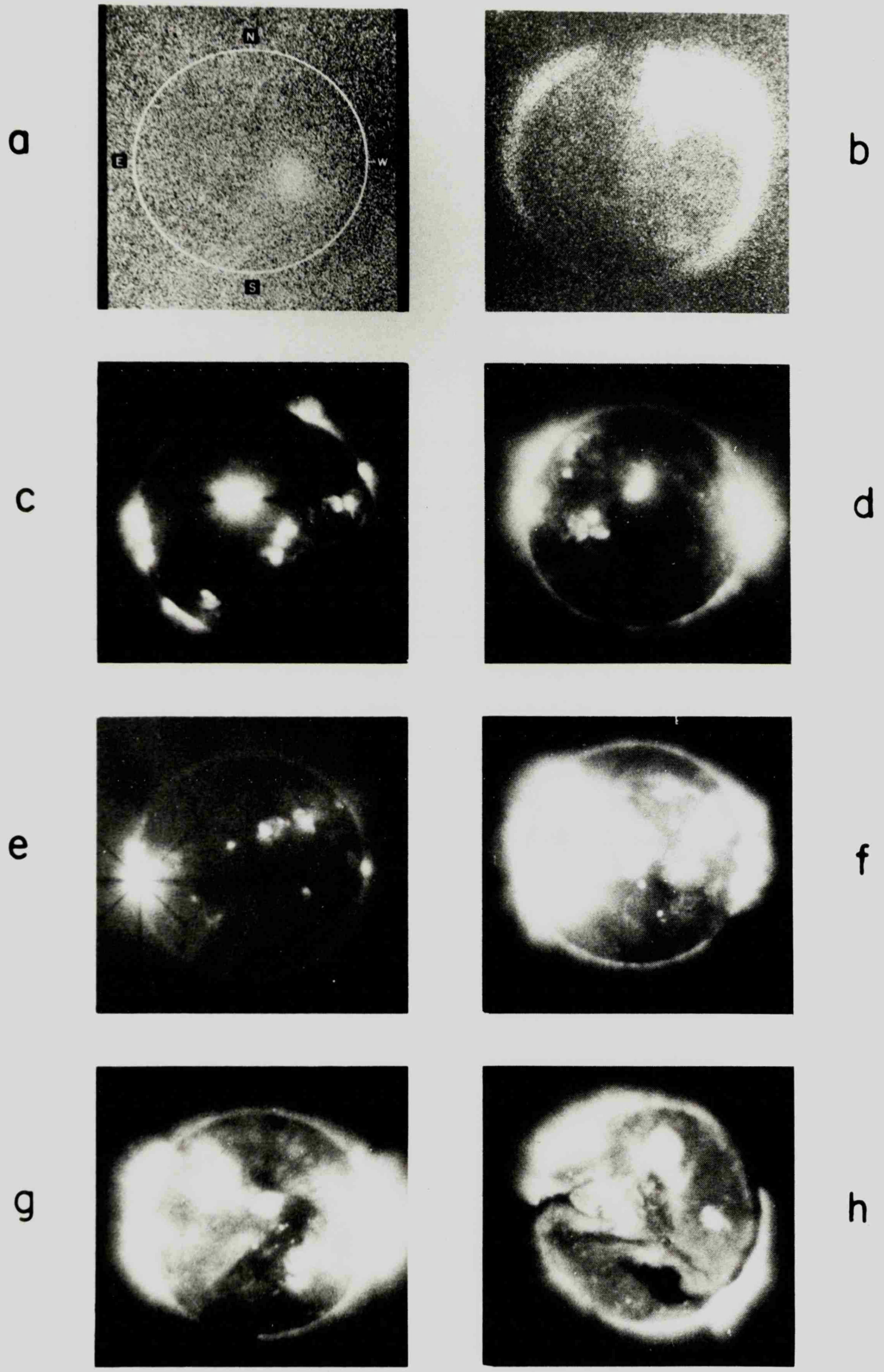

Fig. 1.15.

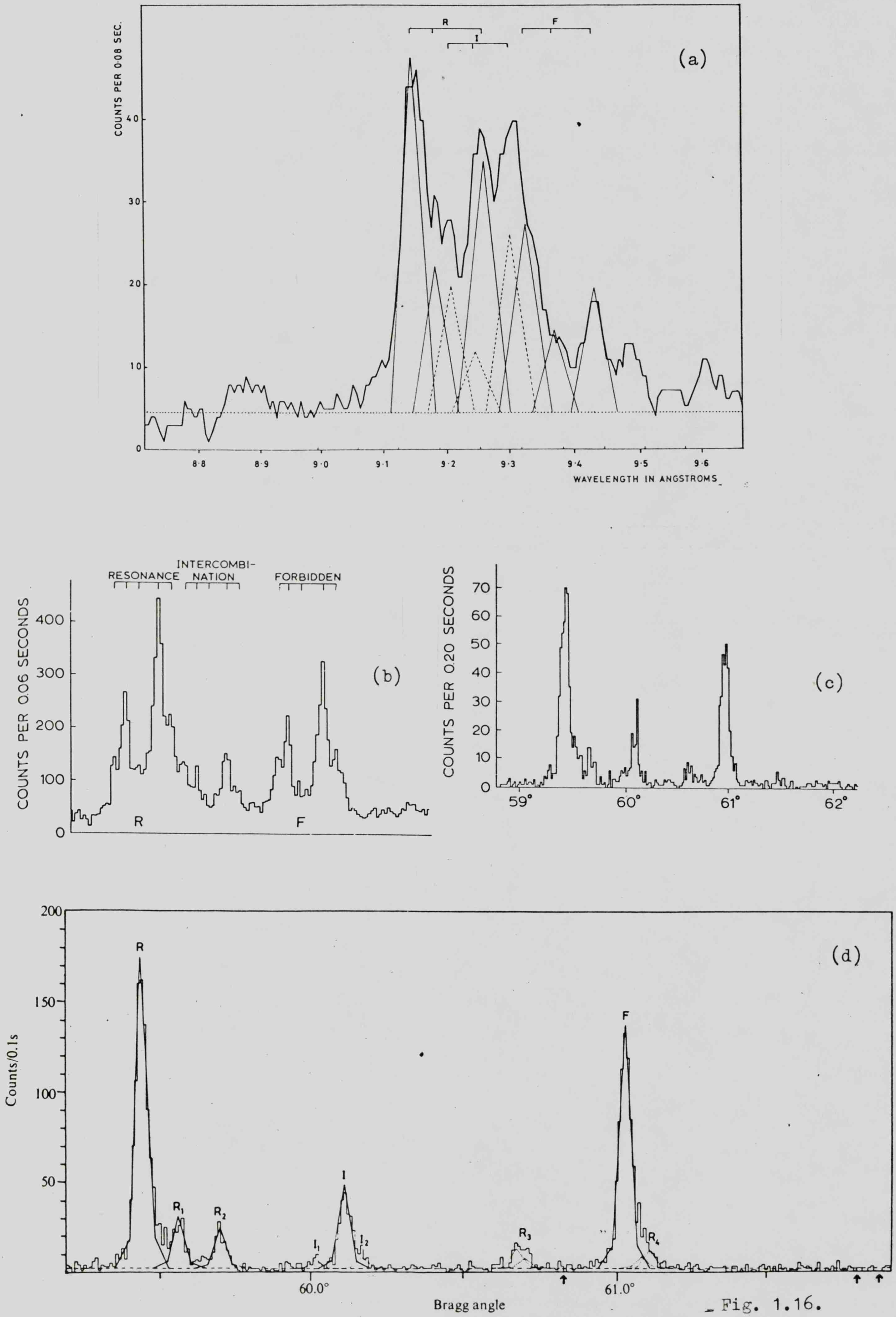

(a)
COUNTS PER 0·08 SEC.
R
I
F
WAVELENGTH IN ANGSTROMS
8·8
8·9
9·0
9·1
9·2
9·3
9·4
9·5
9·6
(b)
COUNTS PER 0.06 SECONDS
RESONANCE
INTERCOMBI-NATION
FORBIDDEN
R
F
(c)
COUNTS PER 0.20 SECONDS
59°
60°
61°
62°
(d)
Counts/0.1s
R
R_1
R_2
I_1
I
I_2
R_3
F
R_4
60.0°
61.0°
Bragg angle

Fig. 1.16.

Chapter 2

REVIEW OF PLASMA AND ATOMIC PHYSICS

2.1 Introduction

This chapter reviews those aspects of plasma and atomic physics required for the analysis and interpretation of the observations of solar active region X-radiation, presented in this thesis.

2.2 Measurable Parameters of a Photon Beam

The only way in which the properties and behaviour of the Sun can be measured is by observation of the solar photon and particle emission. For any beam of photons the physical quantities or parameters which may, in principle, be measured by an observer (where observer is taken to include the measuring device) are:

(1) Direction of arrival

(2) Time of arrival

(3) Wavelength or frequency (or photon energy)

(4) Intensity (number of photons or energy in the beam incident on unit area per unit time)

(5) Polarization (measurement of the orthogonal amplitude components in the e.m. wave)

For a complete description of the incident beam, the intensity and polarization must be specified as a function of direction, time and wavelength. The smallest detectable value or change in value of one of these quantities, is termed the sensitivity or resolution of the measuring instrument with respect to that quantity.

In order to calculate, from the measurements, the values of the parameters at the source of the emission it is necessary to use other information (from experiment or theory) to allow for modification of the parameters by the measuring instrument and in the distance between source and instrument. An attempt can then be made to interpret these figures in terms of parameters (e.g. temperature) of the source, which may be compared with theoretical models in an attempt to understand the mechanisms occurring in the source.

The instruments that have recorded the data which are analysed in the present work have measured the intensity of the solar soft X-ray spectrum as a function of direction (i.e. position on the solar disk), wavelength and time, with varying sensitivity and resolution.

2.3 Plasma Physics

A plasma may be defined as "a system containing mobile charged particles". Its behaviour is determined mainly by electric and magnetic effects, and on a macroscopic scale it is electrically neutral. The latter is a consequence of the electrostatic attraction between particles of opposite charge. The solar plasma is a gas which is ionized due to its high temperature. The main constituent is hydrogen, and in most cases the plasma may be considered as a fully ionized hydrogen gas containing a magnetic field. The magnetic field causes some of the physical properties of the plasma to be anisotropic, and their values parallel ($/\!/$) and perpendicular ($\perp$) to the magnetic field vector must be evaluated separately.

Spitzer (1962) covers most of the important aspects of fully ionized gases in general, while Kaplan et al., (1974) review the plasma physics of the solar atmosphere. Summaries of those topics in plasma physics important for the Sun are given by Zirin (1966) and Meyer (1971). Extensive use has been made of these references in preparing the present section.

2.3.1 Properties of Plasmas

The properties of a plasma may be defined as the sum of the properties of its constituents. For example, the density is given by:

$$\rho = \sum_j \rho_j \tag{2.1}$$

$$n = \sum_j n_j \tag{2.2}$$

$$\rho_j = n_j m_j \tag{2.3}$$

where: ρ = total mass density of the plasma

ρ_j = mass density of constituent j

n = total number density of the plasma

n_j = number density of constituent j

m_j = mass of a particle of constituent j .

The rectangular Cartesian coordinate system used in the following discussion is shown in Figure 2.1. Note that the labels x, 1, $\parallel$ are equivalent, and similarly y, 2, $\perp$ and z, 3, $\perp$.
The magnetic field vector $\underline{B}$ is taken parallel to the z axis.

It is usual to assume that each constituent of the plasma may be considered as a set of structureless particles. If all the particles of constituent j are in equilibrium, the distribution of their velocities in a particular coordinate i, is Maxwellian with a mean $\overline{v_{ji}^2}$, and a kinetic temperature T_{ji} may be assigned to the constituent, where:

$$\tfrac{1}{2}m_j\overline{v_{ji}^2} = \tfrac{1}{2}kT_{ji} = E_{T_{ji}}/n_j \qquad (2.4)$$

where $\overline{v_{ji}^2}$ = mean square kinetic velocity of constituent j, in coordinate i

k = Boltzmann constant

T_{ji} = kinetic temperature of constituent j, in coordinate i

$E_{T_{ji}}$ = thermal energy of constituent j, in coordinate i, per unit volume.

If the density is low, collisions will be infrequent and anisotropy in the plasma, caused for example by a magnetic field or mass streaming, will lead to different velocity distributions in each coordinate, i.e.:

$$\tfrac{1}{2}m_j\overline{v_{j/\!/}^2} = \tfrac{1}{2}kT_{j/\!/} = E_{T_{j/\!/}}/n_j \quad , \qquad (2.5)$$

$$\tfrac{1}{2}m_j\overline{v_{j\perp}^2} = kT_{j\perp} = E_{T_{j\perp}}/n_j \quad . \qquad (2.6)$$

Where, however, there are many collisions, the velocity distributions will be the same in all directions and:

$$\tfrac{1}{2}m_j\overline{v_j^2} = \frac{3kT_j}{2} = E_{T_j}/n_j \qquad (2.7)$$

where: $\overline{v_j^2}$ = total mean square velocity of constituent j

T_j = kinetic temperature of constituent j

E_{T_j} = total thermal kinetic energy of constituent j, per unit volume.

In a collision dominated equilibrium situation the kinetic temperatures of all the constituents will be equal.

The pressure of a gas may be defined as the rate of momentum transfer across unit surface area, by the particles. It is a tensor $\underline{\underline{P}}$ given by:

$$\underline{\underline{p}} = \begin{pmatrix} p_{11} & p_{12} & p_{13} \\ p_{21} & p_{22} & p_{23} \\ p_{31} & p_{32} & p_{33} \end{pmatrix} = (p_{ik}) \tag{2.8}$$

where: $$p_{ik} = \sum_j \rho_j \, \bar{v}_{ji} \bar{v}_{jk} \; . \tag{2.9}$$

In most cases the off-diagonal terms vanish, as there are as many negative as positive contributions, leaving:

$$\underline{\underline{p}} = \begin{pmatrix} p_{11} & 0 & 0 \\ 0 & p_{22} & 0 \\ 0 & 0 & p_{33} \end{pmatrix} = \begin{pmatrix} p_1 & 0 & 0 \\ 0 & p_2 & 0 \\ 0 & 0 & p_3 \end{pmatrix} = (p_i) \tag{2.10}$$

where: $$p_i = \sum_j \rho_j \, \overline{v_{ji}^2} \; . \tag{2.11}$$

Hence, in the presence of a magnetic field:

$$\underline{\underline{p}} = \begin{pmatrix} p_\perp & 0 & 0 \\ 0 & p_\perp & 0 \\ 0 & 0 & p_\parallel \end{pmatrix} \tag{2.12}$$

where: $$p_\parallel = \sum_j \rho_j \, \overline{v_{j\parallel}^2} \tag{2.13}$$

$$p_\perp = \sum_j \rho_j \, \overline{v_{j\perp}^2} \; . \tag{2.14}$$

For the isotropic case, or if collisions are frequent, the pressure p_i in any direction i is:

$$p_i = \tfrac{1}{3} \sum_j \rho_j \, \overline{v_j^2} \; . \tag{2.15}$$

The magnetic pressure p_m and the magnetic energy per unit volume E_m, are given by:

$$P_m = E_m = B^2/(8\pi) \qquad \text{(c.g.s.- e.s. units)}$$
$$= B^2/(2\mu_0) \qquad \text{(S.I. units)} \tag{2.16}$$

where: μ_0 = permeability of free space .

The thermal conductivity of a fully ionized hydrogen plasma parallel to, or in the absence of a magnetic field is:

$$K = 1.84 \times 10^{-5}\ T^{5/2}/\ln\Lambda \qquad \text{erg(sec cm K)}^{-1} \tag{2.17}$$

In a strong magnetic field the conductivity perpendicular to the field is greatly reduced, heat is conducted only by the ions, and the thermal conductivity is:

$$K_{\perp} = 1.48 \times 10^{-17}\ n_H^2 \ln\Lambda\,/(T^{\frac{1}{2}}B^2) \quad \text{erg(sec cm K)}^{-1} \tag{2.18}$$

provided: $10^5 T^{3/2} B/(n_H \ln\Lambda) \gg 1$

where: n_H = hydrogen number density (cm^{-3})

$\ln\Lambda$ is given in Table 2.1.

The electrical conductivity of a fully ionized hydrogen plasma, parallel to, or in the absence of a magnetic field is:

$$\sigma = 1.53 \times 10^{-4}\ T^{3/2}/\ln\Lambda \qquad \text{ohm cm} . \tag{2.19}$$

The electrical conductivity perpendicular to a strong magnetic field is:

$$\sigma_{\perp} = 7.75 \times 10^{-5} T^{3/2}/\ln\Lambda \qquad \text{ohm cm} . \tag{2.20}$$

2.3.2 Characteristic Timescales, Frequencies and Distances in Plasmas

There are many characteristic motions and timescales in a plasma, especially in the presence of a magnetic field. Only those which are relevant to the present work will be considered here.

If a charged particle moves in a magnetic field such that it has a component of velocity perpendicular to the field vector $\underline{B}$, its motion projected on to the plane perpendicular to $\underline{B}$ will be along a circular path (this follows from the Lorentz force law). This motion is known as the gyration, cyclotron or Larmor motion. The corresponding angular frequency ω_g and radius r_g, are given by:

$$\omega_{gj} = q_j B/(m_j c) \qquad \text{(c.g.s.- e.s. units)} \qquad (2.21)$$

$$= q_j B/m_j \qquad \text{(S.I. units)}$$

$$r_{gj} = v_{j\perp}/\omega_{gj} \qquad (2.22)$$

where: q_j = charge of particle j

m_j = mass of particle j

c = velocity of light in vacuo .

The particle species j are normally electrons and positive ions (including protons).

A natural electrostatic mode of vibration of a plasma is the oscillation of the electrons relative to the proton centre of mass. The frequency of oscillation is called the plasma frequency ω_p, and the corresponding length scale is the Debye length λ_D.

$$\omega_{pe} = (4\pi n_e e^2/m_e)^{\frac{1}{2}} \qquad \text{(c.g.s.- e.s. units)} \qquad (2.23)$$

$$= (n_e e^2/(\varepsilon_o m_e))^{\frac{1}{2}} \qquad \text{(S.I. units)}$$

$$\lambda_D = (kT_e/(4\pi n_e e^2))^{\frac{1}{2}} \qquad \text{(c.g.s.- e.s. units)} \qquad (2.24)$$

$$= (\varepsilon_o kT_e/(n_e e^2))^{\frac{1}{2}} \qquad \text{(S.I. units)}$$

$$= v_{the}/\omega_{pe}$$

$$= \left[\frac{\text{(kinetic energy of electrons)}}{\text{(potential energy of electrons)}}\right]^{\frac{1}{2}} n_e^{-\frac{1}{3}}$$

where: subscript e denotes electrons

v_{the} = thermal velocity of electrons

e = electron charge

ε_o = permittivity of free space.

There are characteristic times which may be associated with various processes in the plasma e.g. achievement of a Maxwellian distribution, equipartition of energy, radiative and conductive cooling, and which provide a measure of the relative speed of these processes and an approximate value for the timescale on which they occur.

A definition often used for the characteristic relaxation time t_x of a physical quantity x by a particular process, is that given by the exponential (e)-folding time, i.e. the time for x to rise to a factor e, or fall to a factor e^{-1}, of its original value x_0. If x varies exponentially with time, the e-folding time is:

$$x_0/(dx/dt)_{t=0} \quad .$$

However, this expression is often also used as the relaxation time in the more general case of x(t).

Formulae for some of the more important relaxation times are given below and in Section 2.4.3, namely:

$$t_D = v^3 A_D^{-1} \left[\emptyset\left(\frac{v}{v_f}\right) - G\left(\frac{v}{v_f}\right)\right]^{-1} \tag{2.25}$$

$$t_E = v^3 \left[4A_D G\left(\frac{v}{v_f}\right)\right]^{-1} \tag{2.26}$$

$$t_c = 11.4A^{\frac{1}{2}} T^{3/2}(nZ^4 \ln\Lambda)^{-1} \quad \text{sec} \tag{2.27}$$

$$t_{sl} = 2kT_f v \left[\left(1 + \frac{m}{m_f}\right) \quad A_D m_f G \left(\frac{v}{v_f}\right)\right]^{-1} \qquad (2.28)$$

$$t_{eq} = (T_f - T)/(dT/dt) \qquad (2.29)$$

$$= 5.87 \; AA_f \left[n_f Z^2 Z_f^{\,2} \ln\Lambda\right]^{-1} \left[\frac{T}{A} + \frac{T_f}{A_f}\right]^{3/2} \quad \text{sec}$$

where: t_D, the deflection time = the time in which the field particles deflect the test particles by 90^0.

t_E, the energy exchange time = the time in which the r.m.s. energy change of the test particles equals their original energy.

t_c, the self-collision time = t_D (and t_E) for particles of one kind interacting with themselves.

t_{sl}, the slowing down time = the relaxation time for the mean velocity of the test particles.

t_{eq}, the thermal energy equipartition time = the energy relaxation time between test and field particles, where both have a Maxwellian velocity distribution.

A_D, the diffusion constant = $\dfrac{8\pi e^4 n_f Z^2 Z^2{}_f \ln\Lambda}{m^2}$

A = atomic weight

G and (Ø − G) are given in Table 2.2,

subscript f denotes field particles,

unsubscripted variables refer to test particles.

The thermal conduction cooling time t_{cc} is:

$$t_{cc} = 3n_e kT_e/(dF_c/dl) \qquad (2.30)$$

where: F_c, the conducted flux = energy conducted/unit area /unit time

$= KT_e^{5/2} dT_e/dl$.

Culhane et al. (1970) give the following approximation for t_{cc}:

$$t_{cc} \approx 1.25 \times 10^{-10} n_e l^2 / T_e^{5/2} \text{ sec} \qquad (2.31)$$

where: l = length of magnetic flux tube containing plasma (cm).

2.3.3 Balance of Gas and Magnetic Pressures

The electrical conductivity σ (Equation 2.19), in a hot highly ionized plasma is very high, and Ohm's law reduces to:

$$\underline{E} = \underline{j}/\sigma \approx 0 \ . \qquad (2.32)$$

Using one of Maxwell's equations gives:

$$\frac{\partial \underline{B}}{\partial t} = -\underline{\nabla} \times \underline{E} \approx 0 \qquad (2.33)$$

where: $\underline{E}$ = electric field vector

$\underline{j}$ = electric current density vector.

That is, the time rate of change of the magnetic field vector is zero, and so the field is constant along a trajectory of a volume element of gas - the magnetic field is "frozen" into the gas. Whether the gas or the magnetic pressure is dominant is determined by the ratio:

$$\beta = \frac{P_\perp}{P_m} \qquad (2.34)$$

where: $P_\perp$ = gas pressure perpendicular to $\underline{B}$, and includes, when present, the pressure due to macroscopic or turbulent gas motion of mean velocity $\overline{v_{T\perp}}$, i.e.

$$P_\perp = nkT + \tfrac{1}{2}\rho \overline{v_{T\perp}}^2 \ . \qquad (2.35)$$

If $\beta > 1$ motions of the gas will tend to push around the magnetic field.

If $\beta < 1$ motions of the magnetic field will tend to push around the gas.

2.4 Atomic Processes in Plasmas

In order to analyse and interpret observations of the coronal X-radiation, it is necessary to be able to compare them with theoretical models for the emission mechanisms. Since (a) the corona is optically thin to X-rays; (b) the dominant radiation present in the corona is the photospheric emission, which corresponds approximately to that from a blackbody at 6000 K; (c) coronal particle temperatures are $\sim 10^6$ K; it follows that, in the corona, matter and radiation are uncoupled, i.e. there is negligible exchange of energy between them. Also, for many transitions (in particular those of interest here) collisional de-excitation is negligible compared with radiative decay, under coronal conditions (see Section 2.4.3.3). Hence, in general, neither complete (CTE) nor local (LTE) thermodynamic equilibrium applies in the corona. However, CTE and LTE are briefly discussed here to provide an introduction for the theoretical atomic models necessary to describe coronal conditions.

2.4.1 Complete Thermodynamic Equilibrium (CTE)

There are three conditions which must be satisfied for a system to be in a state of CTE:

(1) Thermal equilibrium, i.e. there are no finite temperature differences between the system and its surroundings, or between any two parts of the system.

(2) Mechanical equilibrium, i.e. there are no finite unbalanced forces acting upon, or exerted by, the system.

(3) Chemical equilibrium, i.e. the internal structure and composition of the system are constant in space and time.

Hence, the macroscopic parameters (e.g. temperature) of the system are time independent, and it may be noted that these criteria imply conservation of mass and energy in the system.

From these conditions and the application of statistical mechanics, it follows (e.g. Spitzer, 1962; Zemansky, 1968) that, for the various forms of energy in the system (in this case a plasma):

(a) The kinetic energy of the particles (atoms, ions and free electrons) is given by Maxwell's equation for the distribution of energies.

(b) The distribution of population densities over the excited states of the atoms and ions is given by the Boltzmann equation.

(c) The distribution of densities of ionization stages of the atoms and ions is given by the Saha equation.

(d) The radiation energy is given by the Planck equation.

The derivations of these distributions do not require a knowledge of either the energy transfer mechanisms or the rates of the processes.

For a system in CTE the "Principle of Detailed Balancing" applies. This states that the probability per unit time of any process equals the probability per unit time of its reverse.

2.4.2 Local Thermodynamic Equilibrium (LTE)

There are many cases where a plasma exhibits some of the properties of the state of CTE, but not all the conditions for CTE are fulfilled. If the plasma is not in CTE but is, by some criteria, sufficiently close to it, then the plasma is said to be in LTE. There is no precise definition of LTE, but normally the following relaxations are made to the conditions for CTE (Wilson, 1962; Griem, 1964, McWhirter, 1965; Zirin, 1966)

(1) Some of the radiation energy is allowed to escape from the plasma, and hence the spectral intensity distribution is not, in general, given by Planck's function.

(2) The plasma parameters (e.g. temperature, density, chemical composition) are allowed to vary in space and time. The time variations however, are sufficiently slow that the free electron energy distribution is still given by Maxwell's equation, and the excitation and ionization energy distributions for the bound electrons by the Boltzmann and Saha equations, respectively.

The time variations must be slow enough and the radiation losses small enough, that detailed balancing still occurs for collisional processes. The spectroscopy of LTE plasmas has been discussed by Griem (1964), McWhirter (1965) and Zirin (1966). Suitable criteria for the existence of LTE are given by Wilson (1962), Griem (1964) and McWhirter (1965). For the excitation and ionization distributions to be given by the Boltzmann and Saha equations, respectively, these authors derive the condition:

$$n_e \gtrsim 10^{12} X_i^3 T_e^{\frac{1}{2}} \qquad (2.36)$$

where: n_e = electron density (cm^{-3})

X_i = ionization potential of the ion under consideration (eV)

T_e = electron temperature (K).

This is a necessary, but not sufficient, condition for LTE.

Since, in the solar corona $T_e \sim 10^6$ K, $n_e \sim 10^9$ cm^{-3}, $\ln\Lambda \sim 20$, and for the coronal ions to be discussed in the present work $X_i \gtrsim 739$ eV (the value for O VII), it follows that LTE does not hold in this case. Atomic models appropriate to coronal conditions are discussed below.

2.4.3 Atomic Processes in the Solar Corona (Non-LTE)

When deriving atomic models applicable to the solar corona, it is necessary to take account of the individual processes which may, at least potentially, populate and depopulate each energy level (both bound and free). A summary is given in Table 2.3 (after Zirin, 1966). It is found that in many practical cases only a few of the mechanisms are important and need to be considered. Woolley and Allen (1948), and Elwert (1952, 1961) laid the foundations for theoretical calculations of the spectrum of coronal-type plasmas.

We are concerned here with the radiation emitted when an electron makes a transition (in energy) in the field of an atom (either neutral or ionized). The intensity of radiation leaving the plasma, from a particular transition, depends upon (e.g. McWhirter, 1965):

(a) the number of electrons in the upper level of the transition i.e. the upper level population,

(b) the atomic probability of the transition,

(c) the probability of the photons produced escaping from the plasma without being re-absorbed.

In most of the cases to be considered here, the value of process (c) is practically unity i.e. the plasma is optically thin.

Most of the models which have been proposed require that the free electron energy distribution is Maxwellian. In order for this to be true, the following three criteria must be fulfilled (Wilson, 1962):

$$t_{ee} \ll t_{ff},\ t_h,\ t_{part} \qquad (2.37)$$

where: t_{ee} = electron-electron relaxation time (see Section 2.3.2)

t_{ff} = energy decay time for thermal Bremsstrahlung (see Section 2.4.3.2)

t_h = energy heating time

t_{part} = particle containment time.

Since:

$$t_{ee} = 0.3T_e^{1.5}/(n_e \ln\Lambda) \quad (2.38)$$

the first criterion reduces to (Wilson, 1962):

$$T_e \ll 5 \times 10^{11} \ln\Lambda \quad K \quad . \quad (2.39)$$

As $\ln\Lambda \sim 10$, it is expected that this condition should be satisfied in any practical case. The second criterion is expected normally to be satisfied, except possibly in the case of some flares (see for example Sturrock, 1973; Datlowe et al. 1974; Van Beek et al. 1974, for characteristic timescales in solar flares). Since the coronal plasma is confined by the magnetic field due to freezing-in of the field lines and the dominance of the magnetic pressure ($\beta \ll 1$), the third criterion should be satisfied, with the possible exception of some energetic flare events. The work of Stevens (1974) also supports this conclusion.

2.4.3.1 Ionization Balance

One of the factors required in the determination of the upper level population of a transition, is the number of ions to which the particular transition is due. The time rate of change of number density, of an ion X_z, with net charge z, is (e.g. McWhirter, 1965):

$$\frac{dn_z}{dt} = n_e(n_{z-1}Q_{z-1} + n_{z+1}\alpha_{z+1}) - n_e n_z(Q_z + \alpha_z) \quad (2.40)$$

where: n_z = number density of ion of net charge z

Q_z = total rate coefficient for ionization from X_z to X_{z+1}.

α_z = total rate coefficient for recombination from X_z to X_{z-1} .

Kafatos and Tucker (1972) give characteristic timescales for ionization (t_I) and recombination (t_R) of a hydrogenic ion of nuclear charge Z:

$$t_I \sim 50T_7^{-\frac{1}{2}}n_9^{-1}(Z/10)^4\exp\left[1.6(Z/10)^2/T_7\right] \quad \text{sec} \qquad (2.41)$$

$$t_R \sim 1000T_7^{\frac{1}{2}}/\left[n_9(Z/10)\right] \quad \text{sec} \qquad (2.42)$$

where:

$$T_7 = T_e/10^7 \text{ K}$$
$$n_9 = n_e/10^9 \text{ cm}^{-3} .$$

A more general expression for the characteristic relaxation time to the steady state (t_s) is given by McWhirter (1965):

$$t_s = \left[n_e(Q_{z_s-1} + \alpha_{z_s})\right]^{-1} \qquad (2.43)$$

where z_s is the net charge of the last ion to be formed in the plasma as it approaches ionization equilibrium. Under such conditions $Q_{z_s-1} \sim \alpha_{z_s} \sim 10^{-12}$ cm^3 sec^{-1} (McWhirter, 1965; Jordan, 1969, 1970; Summers, 1974).

For ionization equilibrium:

$$\frac{dn_z}{dt} = 0$$

and Equation 2.40 reduces to:

$$\frac{n_{z+1}}{n_z} = \frac{Q_z}{\alpha_{z+1}} . \qquad (2.44)$$

For coronal conditions Q and α are given by (Jordan,1969):

$$Q = Q_c + Q_a , \qquad (2.45)$$
$$\alpha = \alpha_r + \alpha_d \qquad (2.46)$$

where the subscripts r, d, c, a, indicate radiative recombination, dielectronic recombination, electron collisional ionization, and autoionization respectively. Equations 2.40 or 2.44 may be solved for (n_z/n_E), the abundance of each ion stage relative to the total element abundance. For ionization equilibrium, ionic abundances have been calculated by Jordan (1969, 1970), Allen and Dupree (1969), Cox and Tucker (1969), Landini and Fossi (1972), and Summers (1972, 1974), covering all the solar abundant elements and also many of low abundance. Doschek (1972), Kafatos and Tucker (1972), Doschek and Meekins (1973), and Phillips et al. (1974) have studied the time dependent ionization of some hydrogen- and helium-like ions in model and actual flare events. Landini et al. (1973) have investigated ionization and recombination in a plasma having a non-thermal (power law) electron energy distribution, while McWhirter and Wilson (1974) have calculated the effect on the ionization, of a sound wave propagating through a plasma.

2.4.3.2 Atomic Spectra

We are concerned here with the intensity of radiation as a function of wavelength (i.e. the spectral intensity), emitted by the coronal plasma. There are three types of electron radiative de-excitation transition, which must be considered for the coronal soft X-ray spectrum; these are: (a) free-free, (b) free-bound, and (c) bound-bound. It will be assumed here, that the electron energy distribution is Maxwellian, i.e. the emission is "thermal". Both thermal and non-thermal X-ray emission (and absorption) processes in astrophysical plasmas, are reviewed by Blumenthal and Tucker (1974). Since most of this thesis is concerned with the analysis of line emission spectra arising from bound-bound transitions, this topic will be discussed in more detail than the other radiative processes.

(a) FREE-FREE EMISSION

Free-free (or bremsstrahlung) radiation is emitted when a free electron is accelerated in the Coulomb field of an ion. A free electron of energy W_i encounters an ion of net charge z and emits a photon of energy $(W_i - W_f)$ while making a transition to another free state W_f. For a Maxwellian electron distribution, the process is termed thermal bremsstrahlung, and a continuous spectrum is produced, which is given by (Culhane, 1969):

$$\frac{d^3E_{ff}}{dtdVd\lambda} = 7.15 \times 10^{-47}\exp(-hc/(\lambda kT_e))n_e n_H \times \left[\sum_{Z,z}\left\{A_Z z^2 \bar{g}_{ff}(z,T_e,\lambda)\right\}\right] \quad (2.47)$$

where: $\frac{d^3E_{ff}}{dtdVd\lambda}$ = intensity of thermal bremsstrahlung, at earth distance, per unit wavelength interval, produced by unit volume of the corona (erg cm^{-2} sec^{-1} $Å^{-1}$)

T_e = electron temperature (K)

λ = wavelength (Å)

n_e = electron number density (cm^{-3})

n_H = hydrogen number density (cm^{-3})

A_Z = abundance of element X_Z, relative to hydrogen $= n_X/n_H$

z = net charge of ion $X_{Z,z}$ of element X_Z

$\bar{g}_{ff}(z,T_e,\lambda)$ = temperature averaged free-free hydrogenic Gaunt-factor.

Karzas and Latter (1961) have computed and tabulated $\bar{g}_{ff}$.

The characteristic cooling time t_{ff} of a plasma, by thermal bremsstrahlung is (e.g. Blumenthal and Tucker, 1974):

$$t_{ff} \approx 10^{11} n_e^{-1} T_e^{\frac{1}{2}} \quad \text{sec.} \quad (2.48)$$

(b) FREE-BOUND EMISSION

If a free electron of energy W_i encounters an ion of net charge z and makes a transition to a bound state (principle quantum number, n) of ionization energy $-I_{z-1,n}$, the electron is said to have recombined with the ion. A photon of energy $(W_i + I_{z-1,n})$ is emitted, and the process is termed radiative recombination. The spectral distribution is continuous, with discontinuities (edges) at photon energies $I_{z-1,n}$, and is given by (Culhane, 1969):

$$\frac{d^3E_{fb}(Z,z,n)}{dtdVd\lambda} = 12.02 \times 10^{-44} T_e^{-3/2} \lambda^{-2} n_e n_H A_Z n_z n_Z^{-1} \chi^2_{Z,z-1,n} n \left(\frac{S_n}{2n^2}\right)$$

$$\times \; \bar{g}_{fb}(z,n,\lambda) \exp\left[-\left\{(hc/\lambda) - \chi_{Z,z-1,n}\right\}/(kT_e)\right]$$

(2.49)

where: $\frac{d^3E_{fb}(Z,z,n)}{dtdVd\lambda}$ = intensity of recombination radiation, at earth distance, per unit wavelength interval, produced by unit volume of the corona, and due to recombination to level n of ion (Z,z) (erg cm^{-2} sec^{-1} Å^{-1})

$\chi_{Z,z-1,n}$ = ionization potential from level n of ion (Z,z-1) (eV)

n_z = number density of ion (Z,z)

n_Z = number density of element Z

$\left(\frac{S_n}{2n^2}\right)$ = unoccupied fraction of the n shell in ion (Z,z)

$\bar{g}_{fb}(z,n,\lambda)$ = hydrogenic recombination Gaunt factor averaged over l states for each level.

Karzas and Latter (1961) have computed and tabulated $\bar{g}_{fb}$.

(c) BOUND-BOUND EMISSION

When an electron makes a radiative transition from one bound energy level E_i, to another of lower energy E_j, the energy emitted is simply:

$$E_{ij} = E_i - E_j = hc/\lambda_{ij} \quad . \tag{2.50}$$

In most cases of interest, the whole of the energy E_{ij} is in the form of a single photon of wavelength λ_{ij}. The spectral distribution of such radiation is known as a discrete or line spectrum; since, in the absence of any perturbing factors (taken here to include the 'natural line width' due to the Uncertainty Principle), the spectrum for any given pair of levels i and j, would be a Delta function at photon energy E_{ij}. It is possible in some instances, however, for the upper level to decay radiatively by the emission of two photons, of energies E_{iv} and E_{vj}, where:

$$E_{iv} + E_{vj} = E_{ij} \tag{2.51}$$

and the subscript v represents a "virtual" energy level which may be anywhere between i and j. Hence, the resulting spectrum is a continuum. Two-photon decay may be an important process in the depopulation of certain metastable states, in particular, the two-photon transitions $2s.{}^2S_{\frac{1}{2}} - 1s.{}^2S_{\frac{1}{2}}$ and $1s2s.{}^1S_0 - 1s^2.{}^1S_0$ in H- and He-like ions respectively, are thought to contribute to the coronal soft X-ray continuum spectrum (e.g. Tucker and Koren, 1971; Walker, 1972). According to Tucker and Koren:

$$\frac{dP_{2\gamma}(Z,z)}{dVd\lambda} = 4\,\mathcal{E}_{21}(Z,z)\,\lambda^{-1}\left(\frac{\lambda_T}{\lambda}\right)^3\left[1-\left(\frac{\lambda_T}{\lambda}\right)\right] \tag{2.52}$$

where: $\lambda_T = hc/E_{ij}$

$\frac{dP_{2\gamma}(Z,z)}{dVd\lambda}$ = power emitted per unit wavelength interval, by unit volume, and due to one of the above mentioned two-photon transitions in the ion (Z,z)

$\mathcal{E}_{21}(Z,z) \quad = \mathcal{E}(Z,z,1s.^2S_{\frac{1}{2}} - 2p.^2P_{\frac{1}{2},3/2})$

for $2s.^2S_{\frac{1}{2}} \rightarrow 1s.^2S_{\frac{1}{2}}$ in H-like ions.

$= \mathcal{E}(Z,z,1s^2.^1S_0 - 1s2p.^1P_1)$

$+ \mathcal{E}(Z,z,1s^2.^1S_0 - 1s2p.^3P_{1,2})$

$+ \mathcal{E}(Z,z,1s^2.^1S_0 - 1s2s.^3S_1)$

for $1s2s\,^1S_0 \rightarrow 1s^2.^1S_0$ in He-like ions.

$\mathcal{E}(Z,z,L)$ = power emitted per unit volume by the line transition L in ion (Z,z).

Since it is to be considered in some detail, the subject of spectral line intensities will be discussed separately, in Section 2.4.3.3.

(d) THE CORONAL SOFT X-RAY SPECTRUM

To summarize, the coronal soft X-ray spectrum contains contributions from several atomic processes; the discrete spectrum arises from line emission, the continuous spectrum from thermal bremsstrahlung, radiative recombination, and two-photon decay. A number of authors (Culhane, 1969; Landini and Fossi, 1970; Tucker and Koren, 1971; Mewe, 1972a; Walker, 1972) have given results for the theoretical coronal soft X-ray spectrum. Examples of these calculations are illustrated in Figures 2.2 and 2.3, from which may be seen the relative importance of the different emission processes as a function of wavelength and temperature.

2.4.3.3 Spectral Line Emission - The Population and Depopulation of Excited States.

In order to calculate the intensity of a particular spectral line from an ion, it is necessary to determine the energy level populations of the ion. The time rate of change of the population density $\dot{n}_i$ (cm^{-3}) of a state i can be expressed as a function of all the other states j (McWhirter, 1965; Gabriel and Jordan, 1972):

$$\frac{dn_i}{dt} = \sum_{j \neq i} n_j R_{ji} - n_i \sum_{j \neq i} R_{ij} \qquad (2.53)$$

where: ij denotes a transition from i to j, i.e. $i \rightarrow j$

R_{ij} = total probability per unit time of a transition from state i to state j (sec^{-1}).

In the most general case, each coefficient, R, is comprised of a summation of transition rates due to many different processes (see Table 2.3). Usually however, in practice, only a few of these terms are important in determining the intensity of a specific transition, and the relevant ones will be considered further when particular transitions are discussed.

For the time dependent case, the set of simultaneous differential equations formed by stating Equation 2.53 for each level, must be solved. However, in a low density plasma such as that in the corona, the characteristic time, t_{ex}, for the population of an excited state to establish itself, is much shorter than the ionization state relaxation time (Equations 2.41, 2.42, 2.43) (McWhirter, 1965), and hence:

$$\frac{dn_i}{dt} \approx 0.$$

Usually, a good approximation for t_{ex} is (McWhirter, 1965):

$$t_{ex} = \left[\sum_{j<i} A_{ij} \right]^{-1} \qquad (2.54)$$

where: A_{ij} = spontaneous radiative transition probability (sec^{-1}).

Equation 2.53 now reduces to the time independent solution:

$$n_i = \left(\sum_{j \neq i} n_j R_{ji} \right) / \left(\sum_{j \neq i} R_{ij} \right) \qquad (2.55)$$

The population density n_i is, in general, a function of the plasma parameters, such as temperature, density, and elemental and ionic abundances. Assuming that the plasma is optically thin to the wavelength λ_{ij}, the energy emissivity ε (erg cm^{-3} sec^{-1}), and energy intensity I(erg cm^{-2} sec^{-1}), of any spectral line ij, for constant plasma parameters, are given by (e.g. Gabriel and Jordan, 1972):

$$\varepsilon_{ij} = n_i A_{ij} E_{ij} \tag{2.56}$$

$$I_{ij} = (4\pi L^2)^{-1} \int_V \varepsilon_{ij} dV \tag{2.57}$$

where: L = distance from the source to the observer (cm)

V = emitting volume visible to observer (cm^3)

E_{ij} = photon energy (erg).

The emissivity and intensity may be expressed in photon units (photons cm^{-3} sec^{-1} and photons cm^{-2} sec^{-1}, respectively) by dividing the right-hand side of Equation 2.56 by E_{ij}.

For many lines in the coronal spectrum, especially resonance transitions (i.e allowed electric dipole transitions), the dominant population and depopulation mechanisms for the upper level i, are electron collisional excitation from the ground state g and spontaneous radiative decay of the excited state, respectively. This is known as the "optically thin corona model" (McWhirter, 1965), and under equilibrium conditions:

$$n_e n_g C_{gi} = n_i \sum_{l<i} A_{il} \tag{2.58}$$

where C is the collisional excitation rate coefficient, defined below.

2.4.3.4 Collisional Transition Rates

In the following discussion collisional transitions caused by electron impact are considered; but the same arguments apply in general to collisional transitions due to other particles, such as protons and ions. However, proton and ion excitation from a level j to a level i ($i > j$), is only important when kT is large compared with the excitation energy ($E_i - E_j$) of the transition (Walker, 1972).

The collisional rate coefficient C for a particular transition $j \rightarrow i$, is related to the collision cross-section Q by:

$$C = \langle vQ \rangle = \int_{E_0}^{\infty} vQf(E)dE \qquad (2.59)$$

where: C = collisional rate coefficient ($cm^3 \ sec^{-1}$)

Q = collision cross-section (cm^2)

v = electron velocity

$f(E)$ = the energy distribution function of the electrons

E = electron energy

E_0 = threshold energy for excitation = energy difference between the two levels, $E_i - E_j$, = 0 for de-excitation.

In most practical cases, f(E) is a Maxwellian distribution with an electron temperature T_e.

Q may be expressed in terms of the collision strength Ω (a dimensionless quantity):

$$\Omega = Qw_1E/(\pi a_0^{\ 2}) \qquad (2.60)$$

where: a_0 = Bohr radius (cm)

w_1 = statistical weight of the initial level

= $2J + 1$

J = inner quantum number of the level

and E is in Rydberg.

An exact evaluation of Q is difficult, and one of the simpler approximations, often used for optically allowed transitions is the Bethe or $\bar{g}$ approximation (Van Regemorter, 1962):

$$Q = \frac{8\pi}{\sqrt{3}} \cdot \frac{f}{EE_0} g \pi a_o^2 \qquad (2.61)$$

where: f = absorption oscillator strength

g = Gaunt factor

and E, E_0 are in Rydberg.

g is proportional to the probability that the colliding electron undergoes a free-free transition from energy E_i to energy E_j (Van Regemorter, 1962).

The absorption oscillator strength, f_{ji} is related to the spontaneous radiative transition probability, A_{ij} (sec^{-1}), by the expression (Wiese et al., 1966):

$$f_{ji} = 1.4992 \times 10^{-16} \lambda_{ij}^2 (w_j/w_i) A_{ij} \quad . \qquad (2.62)$$

Substituting Equation 2.61 in Equation 2.60 gives:

$$\Omega = \frac{8\pi}{\sqrt{3}} \frac{f w_1 g}{E_0} \quad . \qquad (2.63)$$

Combining Equations 2.59 and 2.61 gives:

$$C = 8\sqrt{\frac{\pi}{3}} (ha_o/m) f\bar{g} (E_0 T_e^{\frac{1}{2}})^{-1} \exp(-E_0/T_e) \qquad (2.64)$$

with E_0 and T_e in Rydberg, or:

$$C = 1.70 \times 10^{-3} f\bar{g} (E_0 T_e^{\frac{1}{2}})^{-1} \exp\left[-E_0/(kT_e)\right] \qquad (2.65)$$

where E_0 is now in eV and T_e in K.

$\bar{g}$ is the temperature averaged value of the Gaunt factor, namely:

$$\bar{g} = \exp\left[E_0/(kT_e)\right] \int_{E_0/kT_e}^{\infty} g \exp(-x) dx \qquad (2.66)$$

g and $\bar{g}$ are tabulated by Van Regemorter (1962), who finds that for positive ions and $E/(kT_e) > 1$, $\bar{g}$ tends to the value of g at threshold i.e.

$$\bar{g}\ (E > kT_e) \approx g\ (E_0) \approx 0.2 \quad .$$

This expression is good to a factor 3 (Gabriel and Jordan, 1972).

Equations 2.59 and 2.60 may be combined to give C in terms of Ω:

$$C = 1.36\ w_1^{-1} T_e^{-3/2} \int_{E_0}^{\infty} \Omega \exp\left[-E/(kT_e)\right] dE. \qquad (2.67)$$

If Ω is taken to be constant at some mean value $\bar{\Omega}$, Equation 2.67 becomes:

$$C = 8.65 \times 10^{-6} w_1^{-1} T_e^{-\frac{1}{2}} \bar{\Omega} \exp\left[-E_0/(kT_e)\right]. \qquad (2.68)$$

Thus, the collisional rate coefficient C, may be expressed in terms of either $\bar{g}$ and f, or Q, Ω or $\bar{\Omega}$.

Collisional excitation and de-excitation processes between two levels i and j (j is the upper level), are related by the following expressions:

$$C_{ji} = C_{ij} \frac{w_i}{w_j} \exp\left[E_{ij}/(kT_e)\right] \qquad (2.69)$$

$$Q_{jiE'} = Q_{ijE} \frac{w_i}{w_j} \frac{E}{E'} \qquad (2.70)$$

$$\Omega_{jiE'} = \Omega_{ijE} \qquad (2.71)$$

where: $E' = E - E_{ij}$

w_i, w_j = statistical weights of levels i, j respectively.

The calculation of electron impact excitation rates and cross-sections is reviewed by Moiseiwitsch and Smith (1968) and Bely and Van Regemorter (1970); while their measurement is reviewed by Moiseiwitsch and Smith (1968) and Gabriel and Jordan (1972). Collisional excitation rates for some cases of interest to the present work, are discussed in Section 4.2.

2.4.3.5 Spectral Line Broadening and Shift

Examination of the formulae for the wavelength changes caused by physical processes in the source (e.g. Gabriel et al., 1962; Zirin, 1966; Allen, 1973; Gibson, 1973) shows that the only phenomenon likely to be significant for the coronal plasma, at X-ray wavelengths, is the Doppler effect, which is given by the expression:

$$\lambda_1 - \lambda = \Delta\lambda = \frac{v}{c}\lambda \tag{2.72}$$

where: v = line-of-sight velocity of radiating source relative to observer (measured in direction away from observer)

λ = measured wavelength of a given spectral line for $v = 0$

λ_1 = measured wavelength of the spectral line for velocity v

$\Delta\lambda$ = Doppler wavelength shift.

If there is a distribution of line-of-sight velocities v, then this will appear as a broadening in the profile of the spectral line rather than a simple wavelength shift. For the case of emitting ions, having a Maxwellian velocity distribution with temperature T_i, the Doppler broadening is given by:

$$\Delta\lambda_D/\lambda = 7.16 \times 10^{-7} \sqrt{T_i/M} \tag{2.73}$$

where: $\Delta\lambda_D$ = full-width-at-half-maximum (FWHM) of the Doppler broadened line profile (Å)

T_i = ion temperature (K)

M = atomic mass number of ion (a.m.u.).

2.4.3.6 Optical Depth

So far in the present work it has been assumed that the plasma is optically thin at the wavelengths of interest. In order to test this assumption, expressions for the optical depth τ due to the important types of photon absorption and scattering are given below (derived from Wilson, 1962; Blumenthal and Tucker, 1974). It is assumed that the plasma is spatially uniform.

$$\tau = \chi D \tag{2.74}$$

$$\tau_r = 8.33 \times 10^{-21} f \lambda^2 D n_i / \Delta\lambda_D \tag{2.75}$$

$$\tau_{pi} = 10^{-17} \varepsilon D n_i / (X_i \bar{g}_{fb} p) \tag{2.76}$$

$$\tau_{ff} = 3.11 \times 10^{-38} \bar{g}_{ff} \lambda^2 D n_e^2 T_e^{-3/2} \tag{2.77}$$

$$\tau_{es} = 6.67 \times 10^{-26} D n_e \tag{2.78}$$

where: χ = linear absorption coefficient (cm^{-1})

τ_r = optical depth for resonance line absorption at the centre of a Doppler broadened line profile

τ_{pi} = optical depth for photo-ionization

τ_{ff} = optical depth for free-free (thermal Bremsstrahlung) absorption

τ_{es} = optical depth for (Thomson) electron scattering

D = line of sight dimension of the plasma (cm)

n_i = number density of the absorbing ion (cm^{-3})

ε = number of optical electrons

$\bar{g}$ = temperature averaged Gaunt factor (~ 1)

p = quantum number of the ground state

X_i = ionization potential (eV).

The relative importance of the various optical depth effects can be seen by substituting typical values for coronal conditions into Equations 2.74 to 2.78. For example, considering the O VII resonance line λ 21.60 Å and the following values:

$$T_i = T_e = 2 \times 10^6 \text{ K}$$

$$n_e = 10^9 \text{ cm}^{-3}$$

$$D = 10^9 \text{ cm}$$

$$n_i = \frac{n_i}{n_O} \cdot \frac{n_O}{n_H} \cdot \frac{n_H}{n_e} \cdot n_e = (0.5) \times (5 \times 10^{-4}) \times (0.8) \times (10^9) \text{ cm}^{-3} = 2 \times 10^5 \text{cm}^{-3}$$

gives: $\tau_r = 0.1$

$\tau_{pi} = 7 \times 10^{-6}$

$\tau_{ff} = 5 \times 10^{-18}$

$\tau_{es} = 7 \times 10^{-7}$.

Hence it is found that the only mechanism likely to cause any significant opacity to X-rays in the coronal plasma, is that of resonance line absorption.

The calculation of the intensity of radiation leaving an optically thick plasma, requires the solution of the equation of radiative transfer. In most cases, this involves analytical or numerical approximations (e.g. McWhirter, 1965; Zirin, 1966). However, for resonance line absorption, the fate of the absorbed photon may be examined from the ratio (e.g. Loulergue and Nussbaumer, 1974):

$$y = A_{jl} / \sum_i R_{ji} \qquad (2.79)$$

where: j = upper level of the resonance line

l = lower level of the resonance line.

If y = 1 (i.e. $\sum_i R_{ji} = R_{jl} = A_{jl}$), the absorbed photon is re-emitted at the same wavelength but may be scattered into a different direction. Provided the plasma is spatially uniform the total observed intensity will be the same as the optically thin case. (For a broadened line the intensity must be integrated over the line profile). If $y < 1$, the observed intensity will generally be less than in the optically thin situation.

2.4.3.7 Summary of Diagnostic Techniques for the Coronal Plasma

Listed below, are the plasma diagnostic techniques which may be used to interpret coronal soft X-ray observations. The theoretical basis and application of these methods will be discussed in the appropriate chapters.

The symbols used have the following meaning:

T_e, electron temperature

T_i, ion temperature

n_e, electron number density

A_Z, (= n_Z/n_H) abundance of an element relative to hydrogen

f , absorption oscillator strength

V , emitting volume

l , line-of-sight path length

T_{eff}, effective line-of-sight temperature

S , (= $\int_V n_e^2 dV$), volume emission measure

Y , (= $\int_l n_e^2 dl$), line-of-sight emission measure

I(j), absolute intensity of spectral line j

E_j, incident energy in focal plane/picture element/cm^2/sec, for filter j.

(a) USING SPECTRAL LINES:

(1) T_e derived from I(Lyα)/I(Lyβ) in H-like ions (Hutcheon and McWhirter, 1973).

(2) T_e derived from I (satellite, dielectronic recombination)/ I (resonance) in He-like ions (Gabriel, 1972a; Bhalla et al., 1975).

(3) T_z (indicates ionization balance) derived from I (satellite, inner-shell excitation)/I (resonance) in He-like ions (Gabriel, 1972a; Bhalla et al., 1975).

(4) n_e derived from I (forbidden)/I (intercombination) in He-like ions (Gabriel and Jordan, 1972, 1973).

(5) S derived from I (n = 2 $\rightarrow$ 1 resonance) in H- and He-like ions (Batstone et al., 1970; Parkinson, 1975c).

(6) A_Z derived from I, given S and f (Parkinson, 1975c).

(7) f_{eff} derived from I, given S and A_Z (Parkinson, 1975c).

(8) T_i derived from thermal Doppler broadening of spectral line profile (Zirin, 1966).

(9) Macroscopic velocities derived from Doppler shift or broadening of line (Zirin, 1966).

NOTE: Methods (8) and (9) cannot be applied to the present data due to insufficient spectral resolution and precision.

(b) USING BROADBAND IMAGES:

(1) T_{eff} derived from E_i/E_j (Vaiana et al., 1973; Davis et al., 1975).

(2) Y derived from E_i and T_{eff} (Vaiana et al., 1973; Davis et al., 1975).

(3) n_e derived from I and Y (Vaiana et al., 1973; Davis et al., 1975; present work Chapter 4).

Table 2.1 Values of $\ln\Lambda$ (Spitzer, 1962)

T, °K	Electron Density n_e, cm^{-3}								
	1	10^3	10^6	10^9	10^{12}	10^{15}	10^{18}	10^{21}	10^{24}
10^2	16.3	12.8	9.43	5.97					
10^3	19.7	16.3	12.8	9.43	5.97				
10^4	23.2	19.7	16.3	12.8	9.43	5.97			
10^5	26.7	23.2	19.7	16.3	12.8	9.43	5.97		
10^6	29.7	26.3	22.8	19.3	15.9	12.4	8.96	5.54	
10^7	32.0	28.5	25.1	21.6	18.1	14.7	11.2	7.85	4.39
10^8	34.3	30.9	27.4	24.0	20.5	17.0	13.6	10.1	6.69

Table 2.2 Values of $G(x)$ and $\Phi(x)-G(x)$ (Spitzer, 1962)

x	0.0	0.1	0.2	0.3	0.4	0.5	0.6	0.7	0.8	0.9
$G(x)$	0	.037	.073	.107	.137	.162	.183	.198	.208	.213
$\Phi(x) - G(x)$	0	.075	.149	.221	.292	.358	.421	.480	.534	.584
x	1.0	1.1	1.2	1.3	1.4	1.5	1.6	1.7	1.8	1.9
$G(x)$	.214	.211	.205	.196	.186	.175	.163	.152	.140	.129
$\Phi(x) - G(x)$	.629	.669	.706	.738	.766	.791	.813	.832	.849	.863
x	2.0	2.5	3.0	3.5	4.0	5.0	6.0	7.0	8.0	10.0
$G(x)$	.119	.080	.056	.041	.031	.020	.014	.010	.008	.005
$\Phi(x) - G(x)$	.876	.920	.944	.959	.969	.980	.986	.990	.992	.995

Table 2.3 Atomic Processes (Zirin, 1966)

Process	*Incoming*	*Outgoing*	*Rate*
Absorption	photon + atom	excited atom	$u_\nu B_{mn} N_m$
Spontaneous Emission	excited atom	photon + atom	$N_n A_{nm}$
Induced Emission	photon + excited atom	2 photons + atom	$u_\nu B_{nm} N_n$
Free–Free Emission (Bremsstrahlung)	electron + ion	electron (lower energy) + ion + photon	$N_e N_i A_{\kappa\kappa'}$
Free–Free Absorption	photon + electron + ion	electron (higher energy) + ion	$N_e N_i B_{\kappa'\kappa} u_\nu$
Photoionization	photon + atom	ion + electron	$u_\nu N_m B_{m\kappa}$
2-Body Recombination	electron + ion	photon + atom (may be excited)	$N_e N_i A_{\kappa m}$
Collisional Excitation	electron + atom	electron (lower energy) + excited atom	$N_m N_e C_{mn}$
Collisional De-excitation	electron + excited atom	electron (higher energy) + atom	$N_n N_e C_{nm}$
Collisional Ionization	electron + atom	2 electrons + ion	$N_m N_e C_{m\kappa}$
3-Body Recombination	2 electrons + ion	electron + atom	$N_e^2 N_i C_{\kappa m}$
Dielectronic Recombination	electron + excitable ion	photon + excited atom	$N_e N_i A_\kappa^d$
Dielectronic Absorption or Autoionization	photon + excited atom	ion + electron (via autoionization)	$N_n u_\nu B_\kappa^d$

Footnotes to Table 2.3

Explanation of symbols:

A = Einstein transition probability coefficient for emission

B = " " " " " absorption

C = Collisional rate coefficient

N = Number density

u_ν = Radiation energy density at frequency ν

Subscripts:

e denotes electron

i denotes state of ionization

m,n denote bound energy levels in an ion

χ, χ' denote continuum energy levels

Pairs of subscripts go from first to second e.g. A_{nm} = A from $n \rightarrow m$.

Superscripts:

d denotes dielectronic process.

FIGURES

Chapter 2

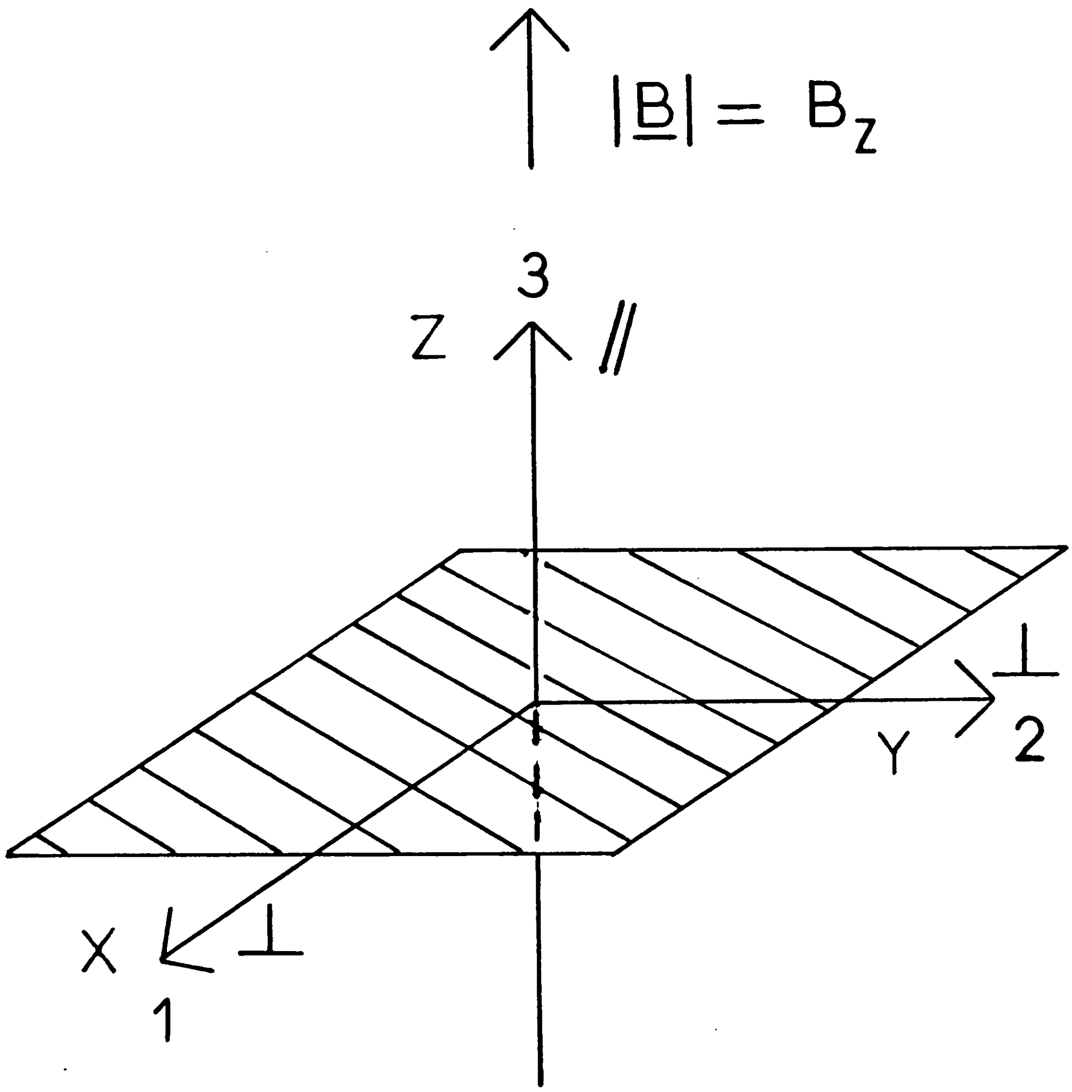

Fig. 2.1.

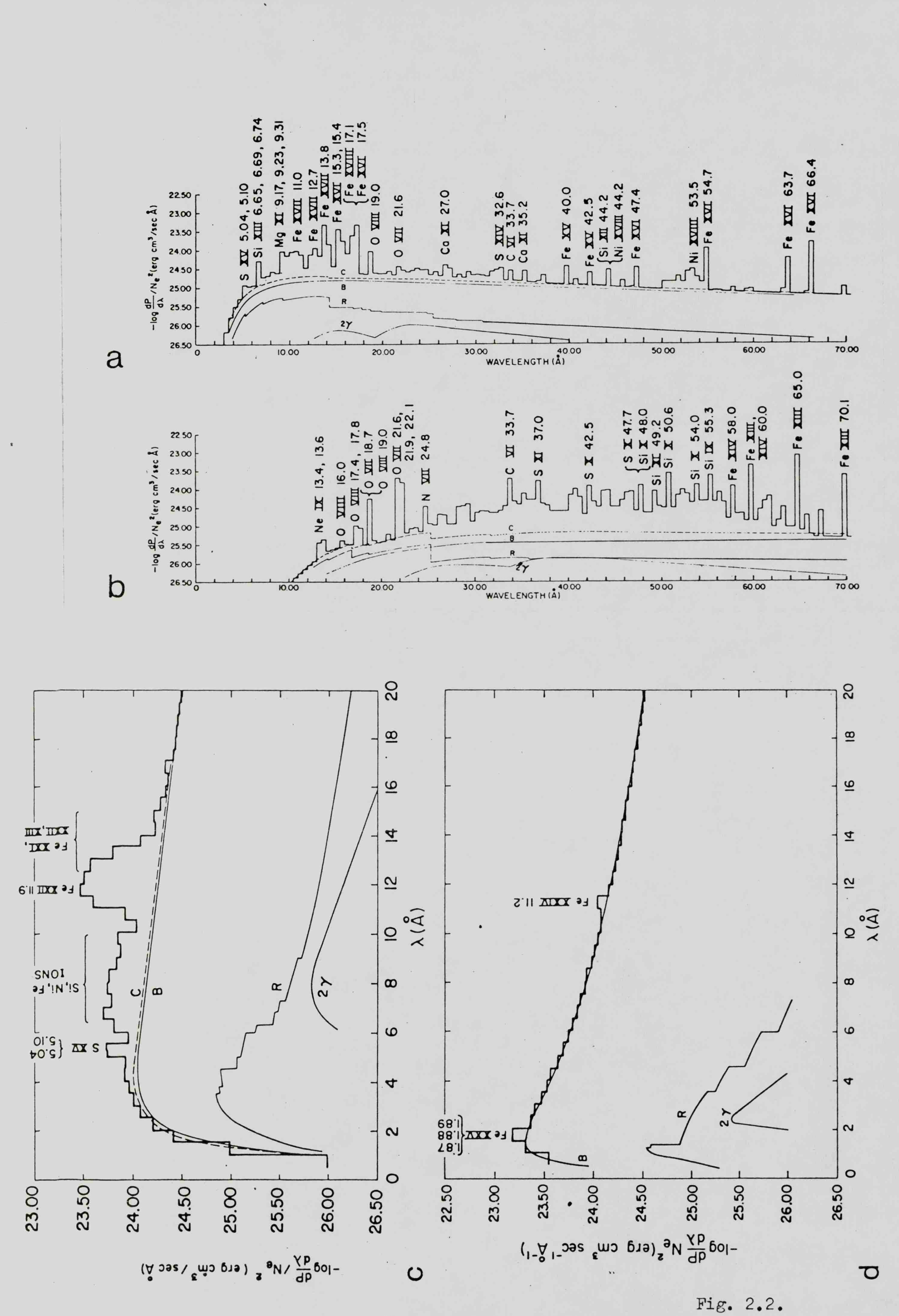
a
b
c
d
WAVELENGTH (Å)
WAVELENGTH (Å)
λ (Å)
λ (Å)
$-\log \frac{dP}{d\lambda}/N_e^2$ (erg cm^3/sec Å)

Fig. 2.2.

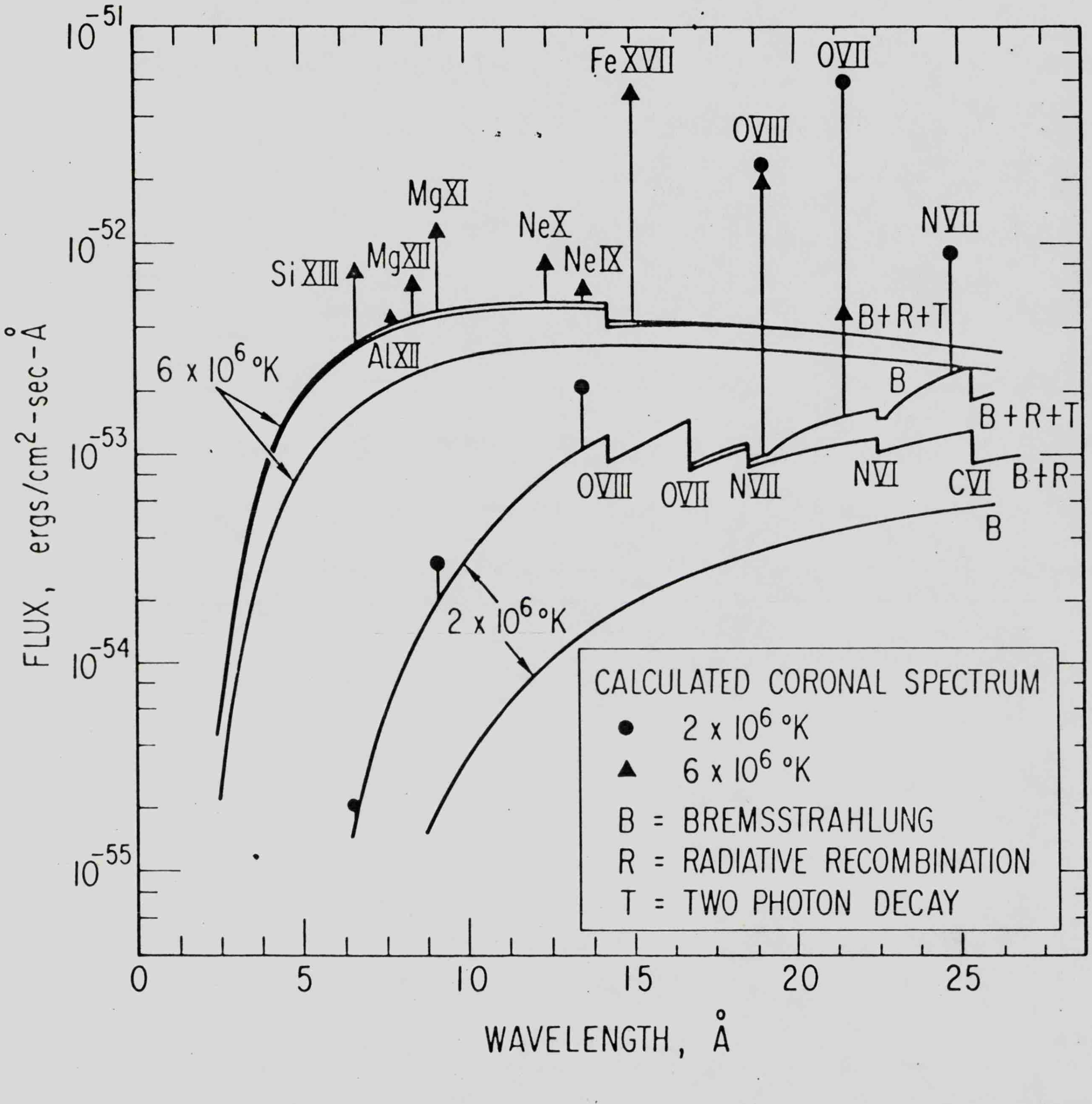
CALCULATED CORONAL SPECTRUM
2 x 10^6 °K
6 x 10^6 °K
B = BREMSSTRAHLUNG
R = RADIATIVE RECOMBINATION
T = TWO PHOTON DECAY
FLUX, ergs/cm²-sec-Å
WAVELENGTH, Å
6 x 10^6 °K
2 x 10^6 °K
Fe XVII
O VII
O VIII
N VII
Mg XI
Ne X
Ne IX
Mg XII
Si XIII
Al XII
B+R+T
B
B+R
N VI
C VI
10^-51
10^-52
10^-53
10^-54
10^-55
0
5
10
15
20
25

Fig. 2.3.

Chapter 3

THE SL1101/SL1206 AND S-054 EXPERIMENTS

3.1 Introduction

Of the solar X-ray data presented in this thesis, most of the spectra were obtained by the Leicester Mk.3 spectrometer on flights SL1101 and SL1206, and the images by the ASE X-ray telescope S-054 aboard the NASA Skylab Apollo Telescope Mount (ATM). In this chapter, these instruments and the associated data reduction and analysis methods are described, together with the observing programmes performed by the experiments. Details of the design and construction of the instrument are given by Evans (1970) and Parkinson (1971a) for the Leicester spectrometer, and by Vaiana et al. (1974) for the ASE telescope. Here, the emphasis will be placed on discussing those instrument parameters whose values are required in the data reduction and analysis.

3.2 The Elements of an X-ray Astronomy Experiment

Gursky (1970) has listed the basic elements of any X-ray astronomy instrument, namely:

(1) Collimator (e.g. slits, grids, wires, focussing optics) to determine the arrival direction of the photons relative to the instrument axes.

(2) Beam conditioner (e.g. filters, Bragg crystal, diffraction grating, polarizer) to isolate particular components of the photon beam e.g. wavelength ranges, polarization directions.

(3) Detector (e.g. proportional counter, scintillation counter, solid state detector, channel multiplier) to register the arrival of the photons.

(4) Signal processor (amplifiers, background rejection circuits, pulse height analysers, analogue to digital converters,

scalers, synchronization circuits) to obtain the data in a form suitable for subsequent reduction and analysis.

In order to complete the experiment, the following are also required:

(5) Carrier vehicle (satellite, rocket, balloon) to lift the instrument above the heavy X-ray attenuation of the Earth's atmosphere.

(6) Attitude sensor (e.g. sun sensor, star sensor, magnetometers, inertial platform) to determine the instrument orientation relative to external references.

(7) Telemetry system to transmit the processed scientific data (and usually "housekeeping" data e.g. monitor and calibration values) to the receiving and recording stations on the ground.

This list may be extended further to include the data reduction and analysis:

(8) Data reduction and analysis:

(a) Calibration of the recorded data e.g. conversion of counts to intensity, and voltages to Bragg angle to wavelength.

(b) Deconvolution of the instrument response function from the data.

(c) Search for, and attempt to identify statistically significant features in the data (e.g. cosmic X-ray sources, solar active regions, spectral lines).

(d) Interpretation of the data in terms of physical models (e.g. emission mechanisms, emission measure/temperature models).

Similar schemes can be used to describe most experiments for the detection of e.m. and particle radiation. The essential elements of an X-ray astronomy experiment are shown schematically in Figure 3.1.

3.3 The SL1101 and SL1206 Experiments

3.3.1 Instrumentation

The Leicester Mk.3 instrument, flown on SL804, SL1101 and

SL1206, consisted of three plane scanning Bragg crystal spectrometers, covering between them the wavelength range 4 to 23 Å. The crystals were mounted on a single rotation shaft, but could be biased in Bragg angle relative to each other. The field of view of each spectrometer was restricted to 3 arc min FWHM by square hole multiple-grid collimators (Evans, 1970; Parkinson, 1971a). The multigrid collimator has the advantage over the conventional slit collimator, that grazing-incidence reflections are eliminated and hence the area selected for observation can be isolated more effectively. The three crystals used (their lattice planes and approximate lattice spacings, 2d) were ADP (ammonium dihydrogen phosphate, 101 plane, 2d $\approx$ 10.6 Å), gypsum (020 plane, 2d $\approx$ 15.2 Å) and KAP (potassium acid phthalate, 001 plane, 2d $\approx$ 26.6 Å), the dimensions of each being about 13.6 x 6.7 cm. The diffracted photons were detected by proportional counters containing 2 cm atmos. of 90:10 argon:methane with aluminium coated polypropylene windows. In both SL1101 and SL1206 flights the ADP and gypsum spectrometers had counter windows of 6μ polypropylene plus 1000 Å aluminium. The counter window for the KAP spectrometer on SL1101 was 4μ polypropylene plus 1000 Å aluminium, and on SL1206 was 4μ polypropylene plus 2000 Å aluminium. The background counting rate was reduced by means of an anticoincidence system on the rear of each detector and by a single channel analyser, which only accepted detector pulses within a height range corresponding approximately to the wavelength range scanned by the appropriate crystal. The effective collecting area of each spectrometer, taking into account all geometrical factors such as transmission of the collimator and detector window support, but not allowing for wavelength-dependent factors such as crystal reflectivity and detector efficiency, was about 15 cm^2.

If a beam of parallel monochromatic radiation of wavelength λ, is incident at a glancing angle θ, on a set of parallel crystal planes, the radiation diffracted from each crystal plane will interfere constructively and hence produce an efficiently reflected beam at a glancing angle θ, provided that Bragg's law:

$$n\lambda = 2d \sin\theta \tag{3.1}$$

is approximately satisfied. d is the interplanar spacing and n an integer (n = 1 in the present work). The term "approximately" is used because: (1) the reflected beam has significant intensity over a finite angular range; and (2) the peak reflectivity (i.e. the peak diffracted intensity) does not, in general, occur at precisely the angle given by Equation 3.1 (see Sections 3.3.3.1 and 3.3.3.2). The important parameters of the crystal diffraction curve (or 'rocking curve') are illustrated by Figure 3.2.

The measure of crystal reflectivity that is usually determined and required, is the integrated reflectivity R, which may be defined as (e.g. Van Speybroeck, 1972):

$$R = \int_{\theta} P(\theta, \lambda)\, d\theta = E\omega/I_o \tag{3.2}$$

where: the incident beam is parallel and monochromatic

$P(\theta, \lambda)$ = probability of Bragg reflection for incident angle θ

ω = $d\theta/dt$

= crystal rotation rate

E = total energy reflected by the crystal as it scans through the spectral line.

I_o = incident energy per unit time.

Hence, the measured intensity of a spectral line is related to the instrument parameters and the number of counts recorded for the line by the equation:

$$I = 10^8 \, hc\omega N/(\lambda AR \varepsilon) \qquad (3.3)$$

where:

I = absolute energy intensity of the spectral line (erg cm^{-2} sec^{-1})

h = Planck's constant (erg sec)

c = speed of light in vacuo (cm sec^{-1})

ω = crystal rotation rate (rad sec^{-1})

N = number of counts recorded for the line in one scan of the crystal

λ = wavelength of the line (Å)

A = net collecting area of the spectrometer (cm^2)

R = crystal integrated reflectivity (rad)

ε = photon detection efficiency of the proportional counter.

Photon intensity may be obtained by multiplying the right-hand side of Equation 3.3 by:

$$\lambda \, / \, (10^8 hc).$$

The crystal reflectivities were obtained from the measurements of Leigh and Evans (1975) whose results are shown in Figure 3.3. The proportional counter detection efficiencies were calculated from the mass absorption coefficients of Leroux (1963) and are shown in Figure 3.4. The crystal rotation rates used were:
1.1×10^{-2} rad sec^{-1} (SL1101 and SL1206 'fast' scans),
1.6×10^{-3} rad sec^{-1} (SL1101 'slow' scans) and
1.0×10^{-3} rad sec^{-1} (SL1206 'slow' scans).

The angular position of the crystals was determined with a 14-bit optical shaft encoder, allowing accurate calculation of absolute wavelengths, with an uncertainty, in general, of about $\pm$ (0.001 - 0.003) Å (see Section 3.3.3.2).

The principle of the spectrometer is outlined in Figure 3.5, while Figure 3.6 shows the Leicester Mk. 3 instrument itself. In addition to the spectrometers, the payload carried a white-light cine camera and an array of X-ray pin-hole cameras, to assist in post-flight determination of the spectrometer pointing positions. This information was also derived from the output signal of the Marconi attitude control unit (ACU) sun sensor.

3.3.2 Observations

SL1101 was launched at 0529 UT on 30 November 1971 and SL1206 at 0535 UT on 26 November 1973, both on sun-stabilised Skylark sounding rockets from Woomera, S. Australia. The latter flight was part of a collaborative observing programme with ASE who obtained X-ray photographs of the Sun with the S-054 ATM X-ray telescope simultaneously with the Leicester observations (see Section 3.4). Two active regions were observed on each flight. Unless it is otherwise stated, all active regions will be referred to by their McMath calcium plage number. Observations from one of the active regions (region 11621) viewed during flight SL1101 have already been reported by Parkinson (1972, 1973a, 1975c). The results reported here are from SL1101 observations of region 11619 (near S10 W35) and SL1206 observations of region 12624 (near S10 W28) and 12628 (near S11 E19).

The experiment pointing positions are known to an accuracy of about $\pm$ ($\frac{1}{2}$ to 1) arc min and the pointing stability was better than $\pm$ 10 arc sec.

Region 12624 was observed about 60 minutes after the peak of an importance-N class C0 flare. Regions 11619 and 12628 were non-flaring at the time of the observations. All three active regions had bipolar magnetic configurations and were close to maximum development(Solar Geophysical Data, 1972, 1974).

The Skylark rocket provides around 5 minutes observing time above 120 km; thus each active region was viewed for about two and a half minutes, divided so that the crystals performed a fast scan through a Bragg angle range of $\sim 35^{\circ}$ in 1 minute and a slow scan through $\sim 5^{\circ}$ in the remaining $1\frac{1}{2}$ minutes. The slow-scan was made to coincide with the simultaneous observation on each crystal at a Bragg angle of about 60° (arranged by appropriate biasing), of the $n = 2 \rightarrow 1$ resonance, intercombination and forbidden lines and satellite lines to the He-like ions O VII (on KAP), Ne IX (on gypsum) and Mg XI(on ADP). The full range of Bragg angles was scanned once for each active region; then for the second region observed on each flight, the spectrometers began another fast scan which was terminated by the vehicle re-entering the Earth's atmosphere.

The data covers the spectral range 4 to 23 Å, and many emission lines are observed. The identified transitions include those from H-like O, Ne and Mg; He-like O, Ne, Na, Mg, Al and Si; Ne-like Fe and Ni; and F-like Fe. In addition, there are a number of lines which are unidentified or only tentatively classified. Emission lines from ions corresponding to high active region temperatures, e.g. Mg XII and Fe XVIII, are relatively more intense in region 12624 than in the other active regions and this aids the identification of some spectral lines. In particular, there are about ten lines in the 13-14 Å range which only appear in the data from region 12624; these are discussed further, in Section 7.2. These enhanced intensities suggest that this region contains an observable quantity of plasma at higher temperatures, as might be expected from a decaying flare. This is confirmed by a model of emission measure as a function of temperature, derived by a method similar to that of Batstone et al. (1970) (see Section 4.3).

3.3.3 Data Reduction and Analysis Methods

One of the author's first tasks was the design and implementation of a data reduction and analysis system for the SL1206 observations. This took the form of a suite of computer programs written in FORTRAN IV. The computers used were the University of Leicester Computing Laboratory ICL 4130 (prior to December 1974) and CDC Cyber 72 (since December 1974).

The Skylark Type T29C telemetry used on the flights, was an amplitude modulated, 24 channel time-multiplexed system. The multiplexor sampling frequency was 84 sec^{-1} and the spectrometer data sampling frequency was set equal to this frequency and synchronised with it. Thus the fundamental resolution time of the experiment was 1/84 i.e. 0.012 sec, and this interval will be referred to as a "data frame" or "integration period". For each data frame, the spectral data from the experiment takes the form of recorded counts per integration period for each spectrometer channel and the current shaft encoder position. Monitor and calibration voltages are also present. When the data is recorded at the receiving station the time is added.

The final reduced database consists of a number ($\sim 10^4$) of time sequential data frames, where each data frame contains:

(1) Time from launch, in seconds (correct to three decimal places). Launch time is taken as the Instrumentation Timing Datum (ITD).

(2) Shaft encoder position, indicated by a number between 0 (for 0^o) and 4096 (for 90^o).

(3) Counts per integration period for each of the three spectrometer channels.

The information is stored on a magnetic tape suitable for reading on a digital computer.

The reduction of the telemetered data to the final database is done by a FORTRAN IV computer program MTREDUCE. All subsequent analysis is performed on this database and a number of programs have been developed for this purpose. These include programs for calibration, fitting spectral line profiles, and display of the spectra as tables and graphs. In order to optimise the signal to noise ratio and the resolution for a particular section of data, the counts per integration period may be summed into counts per bin, where a "bin" is an integral number of data frames. For example, the spectrum shown in Figure 3.7 has 16 integration periods per bin or histogram step. The wavelength and intensity calibrations of the data are discussed in Sections 3.3.3.2 and 3.3.3.3 below.

3.3.3.1 Deconvolution of the Observed Spectrum

The observed spectrum is a convolution of the source spectral and spatial intensity distributions, the collimator transmission profile andthe crystal rocking curve, with the superposition of a background due mainly to cosmic ray events and specular reflection from the crystals. Since, apart from recombination edges, the continuum contribution to the spectral distribution is a slowly varying function of wavelength (compared to the line contributions; see Section 2.4.3.2), this may also be taken as a superposed background when considering the line spectrum, as in the present work. In order to obtain the best estimates of line intensity and wavelength it is necessary to deconvolve the observed spectrum by fitting the expected profile to each line feature in the data. This procedure becomes of particular importance where two or more lines are blended together. The choice of the profile will now be discussed.

The resolving power $\lambda/\Delta\lambda$ of the SL1101 and SL1206 spectra is in the range 400 to 2000, but even at a resolving power $\sim$ 2000 some of the lines are blended. In such cases the procedure is to find, by computational trial and error, the least squares fit of a synthesised profile to the data. The first trial profile is synthesised using the best available prior knowledge of the number of component lines likely to exist in the blend, their (most probable) wavelengths, and their most probable intensities. The program then finds the best fit with relative line wavelengths and intensities as parameters. In this profile synthesis each component is represented by the instrument wavelength response function. This latter is not usually known from prior information (see below). Therefore any given line blend is studied, using, as the instrument response profile, the profile of a nearby unblended line (or lines) in the spectrum. This approach requires that the instrument profile be the same for different transitions. Hence, the contributions to the net instrument profile have been considered as follows.

The contributions to the wavelength profile emitted by the plasma are summarised by Allen (1973). In coronal active regions all these line broadening processes are expected to be negligible compared with the instrument profile, with the possible exception of thermal Doppler broadening of lines from low Z(12 - 14) ions recorded with the ADP spectrometer. With this exception, this is the justification for the use of a nearby unblended profile in the analysis of blends. This method is also normally justified for the ADP spectrometer, since nearby lines in this case are usually due to transitions in the same ion, for instance, the Mg XI lines around 9.2 Å (see Figure 3.7).

The instrument spectral resolution may be examined by inspection of the first differential of the Bragg equation (Equation 3.1):

$$\Delta\lambda = 2d\cos\theta.\Delta\theta \quad \text{or} \quad \lambda/\Delta\lambda = (\tan\theta)/\Delta\theta \;. \quad (3.4)$$

The glancing angle θ to the crystal can be determined only to an accuracy corresponding to the angular size of the source. This is defined by the convolution of the field of view function of the collimator and the source brightness distribution. The Skylark vehicle allows the instrument only about 300 seconds of observing time, so that the spectrum must be scanned at speeds $d\theta/dt$ in the range 10^{-2} to 10^{-3} rad sec^{-1} in order to obtain suitable spectral coverage. Given the restriction of these scan speeds, it then follows that, with the instrument aperture limited to the order of 50 cm^2 by the vehicle diameter (44 cm), the field cannot be restricted to much less than 3 x 3 (arc min)^2 if there is to be sufficient signal strength to justify the corresponding resolution. Since this is of the same order as the size of coronal active regions (see Section 4.5) the convolute of the two effects is not known. Hence, the profile used for deconvolution must, in general, be extracted from the data itself. This profile may be tested for consistency with the range of line widths expected from consideration of the collimator field of view, the crystal diffraction curve, and where known from independent measurement, the source brightness distribution.

It is convenient to use some analytic expression for the line profile to be fitted to the data. In the case of the fast spectral scans a triangular profile is generally used, namely:

$$y = y_0 \left[1 - \left(|x - x_0| \right)/\Delta x_{\frac{1}{2}}\right] \quad \text{if } |x - x_0| \leqslant \Delta x_{\frac{1}{2}} \qquad (3.5)$$

$$y = 0 \qquad \text{if } |x - x_0| > \Delta x_{\frac{1}{2}}$$

where: y = profile height at position x

y_0 = profile peak height

x_0 = position of the profile peak

$\Delta x_{\frac{1}{2}}$ = FWHM of the profile.

This simple function normally fits the fast scan spectra with sufficient accuracy, compared with the statistical uncertainties in the data. The slow scan spectra have greatly increased sensitivity and resolution compared with the fast scans; the line profiles are consequently fitted with smooth curves having extended wings. This empirical function is given by:

$$y = \alpha G(x) + (1 - \alpha)L(x) \qquad (3.6)$$

where: $G(x)$ = Gaussian function

$= y_0 \exp \left[-\ln 2 \left\{2(x - x_0)/\Delta x_{\frac{1}{2}}\right\}^2\right]$

$L(x)$ = Lorentzian function

$= y_0/\left[1 + \left\{2(x - x_0)/\Delta x_{\frac{1}{2}}\right\}^2\right]$

α = shape factor (usually, $\alpha \approx 0.6$).

This curve is known as a Gauss-Lorentz linear combination (Fraser and Suzuki, 1970). The shape factor α controls the ratio of the area under the profile wings to that in the core. Other authors (e.g. Doschek et al., 1971; Parkinson, 1972, 1975c) have used various empirical formulae to represent the line profile.

The background level is obtained from regions of each spectral scan which are believed to be free from line-emission.

In order for an observed feature in the spectrum to be classed as a spectral line, it must satisfy the following criteria:

(1) The shape must be consistent with the profiles discussed above.

(2) The recorded counts must be statistically significant at the 4σ level, i.e. $N \geqslant 4\sqrt{B}$, where B is the background count over the line profile.

The conditions that must be fulfilled for a line to be classified as a particular transition in a specific ion, are:

(1) The measured wavelength must agree with the calculated or laboratory measured wavelength to within the estimated uncertainties.

(2) The measured intensity must be approximately consistent with the predicted intensity (if a reliable calculation is available).

3.3.3.2 Calibration of the Wavelength Scale.

A very good approximation to the wavelength scale of a correctly operated Bragg spectrometer may be written in the form:

$$\lambda = \left[2(d_T - \delta d)/n\right] \sin \theta \qquad (3.7)$$

where:

$$d_T = d_{18}\left[1 + \alpha(T - 18)\right] \qquad (3.8)$$

and: θ = glancing angle (to the lattice planes) of a monochromatic X-ray beam (wavelength λ) at which the diffracted power is at maximum

d_{18} = lattice period at $18^{\circ}C$

α = crystal linear expansion coefficient in a direction orthogonal to the lattice planes

T = crystal temperature in $^{\circ}C$

δd is a function of wavelength which may be obtained from calculation or measurement.

In order to use Equation 3.7 to assign a wavelength scale to a coronal X-ray spectrum, d and $\delta d(\lambda)$ must be precalibrated and an angle measuring device in the flight spectrometer must be correctly adjusted so that the glancing angle θ is measured between the principal axis of the collimator and the crystal lattice planes.

The precision necessary for these operations may be estimated as follows. The resolving power of the equipment is about 2000 in favourable parts of the spectrum (e.g. ADP crystal at $\lambda \sim 9$ Å). This is then set by the response profile of the input collimator, at nominally 3 arc min. The sensitivity of the measurements is sufficient to determine the position of the peak of the stronger recorded lines to a small fraction of this profile width. For this reason the data can be usefully sampled at very small increments of θ ; the sample period is about 2.5 arc seconds in the case of SL1206. In final data presentation an optimum bin size may then be selected in units of $\Delta\theta$ = 2.5 arc sec. Figure 3.7 shows a small sample of the SL1206 data binned at 16 sample periods, i.e. at increments in θ of 40 arc seconds; the positions of the peaks of several of the lines may be measured to a precision of one bin. Thus, the precision of θ measurement is required to be at least as good as, say $\pm$ 20 arc sec; a corresponding precision is then also required in the calibration of d_{18}, α , T and $\delta d(\lambda)$.

The first effect to be considered will be that of crystal temperature. The linear expansion coefficient for ADP, gypsum, and KAP are known to be about (17, 30, 40) x 10^{-6} $^{o}C^{-1}$ respectively (Bertin, 1970; Blake and Wick, 1973). In the case of a Skylark launch the rocket may be open to local weather at the launch tower for several hours before ignition, and internal instrumentation temperatures have been found to vary between about 0 and 60° C according to the influence of air temperature, solar heating and internal electrical dissipation (Evans, 1975). The crystal temperature may be expected to change during flight also; changes of a few $^{\circ}$C have been measured (Evans, 1975). The result of this is a change in the wavelength calibration up to the order of one part per thousand, which is far outside present tolerance. Clearly therefore, absolute calibration via Equation 3.7 requires in-flight measurement of the crystal temperature.

To the precision required, α and $\delta d(\lambda)$ may be regarded as fixed for given crystal species and need not be calibrated for each sample. This may not, however, be true of d_{18}. In the laboratory programme at Leicester, measurements of d_{18} have not yet been accumulated on sufficient crystal samples to exclude the possibility of a significant sample spread in lattice period (Evans, 1975).

The question of the correct in-flight measurement of the glancing angle θ poses several difficulties. One problem is the high cost of commercial devices capable of continuous automatic electronic measurement of angle resolved to a few arc seconds. Given such a device, a problem occurs on installation when the scale zero of the angle encoder must be adjusted (or at least located) so as to refer to the glancing angle of the collimator axis to the crystal lattice planes. The angular location of the lattice planes with respect to the crystal optical surface is in general not known to $\pm$ 20 arc sec. The only satisfactory answer to this problem is to observe the same spectral feature at θ and (π - 2θ) by the procedure of zero error cancellation (Evans, 1975).

The procedure for calibration via direct use of equation 3.7 with prior determination of all parameters is thus an expensive and tedious matter. The conditions have therefore been examined, which must be met for effective self-calibration of the wavelength scale by use of reference lines recognisable in the coronal spectrum. Equation 3.7 may be rewritten as:

$$\lambda = 2d_{eff} \sin \theta \tag{3.9}$$

where d_{eff} is regarded as an unknown free parameter. A value may be calculated for $2d_{eff}$ for any feature in the recorded spectrum whose wavelength is known and for which a θ value is measured. The value found for d_{eff} at any data point will be influenced by the actual lattice period at the crystal temperature, the dispersion terms at wavelength λ, the zero error in measurement of θ (due perhaps to an offset between crystal planes and crystal optical surface) and other errors in the recorded value of θ due to imperfect behaviour of the angle encoder. Assuming the availability of a set of suitably placed reference lines through a spectral scan, $2d_{eff}$ may be plotted against λ and a best-fit interpolation may be used to find the wavelength of any other feature in the spectrum. Figure 3.8 shows the plot of $2d_{eff}$ for the KAP scans of the SL1206 flight; the $2d_{eff}$ for the other scans show a similar behaviour. The figure shows details of the choice of reference lines, their known wavelengths and cites the sources of these wavelengths. It appears that, <u>provided there is no rapid change in the value of $2d_{eff}$ between the pair of reference lines used in a given wavelength estimation</u>, then indeed wavelengths are generally available to about $\pm$ 0.002 Å. Note that, because of the condition underlined above, accurate wavelengths cannot be found by this method if they lie in the neighbourhood of an absorption edge of a constituent element of the crystal. This is due to the rapid variation in the dispersion terms $\delta d(\lambda)$ in such cases (Evans, 1975). The relevant absorption edges and the crystals to which they apply, are as follows:

ADP: phosphorus K λ5.8 Å

gypsum: calcium K λ3.5 Å, sulphur K λ5.0 Å

KAP: potassium K λ3.5 Å, oxygen K λ23.2 Å.

However, all the spectral lines observed in the SL1101 and SL1206 data lie in the wavelength range 6.6 to 22.1 Å, and hence the above criterion should be satisfied for these spectra.

Although the procedure as above can be implemented quite independently of special procedures in alignment of the crystals etc., it is the normal practice at Leicester to include correct adjustment of the angle encoder in the preparation of the instrument. The complete sequence of spectrometer alignment is then as follows (Evans, 1975):

(1) Measure angle between crystal lattice and optical surface. This is done by the two-reflection method as described by Schnopper (1962). The method is not very sensitive (final uncertainty is about 1 arc min) and is only used to exclude the possibility of gross error. Enough measurements have been accumulated on crystal samples from the main suppliers to Leicester University (Nuclear and Silica Products Ltd.), that there is now sufficient confidence in their production tolerances that this operation is only made on an occasional sample basis.

(2) Define spectrometer direction of look. An optical flat is permanently fixed to the forward-looking face of the instrument. The orthogonal to this flat is defined as the

principal axis of the instrument. A high resolution autocollimator is mounted (axis vertical) on a good grade surface table so that its axis may be translated whilst maintaining its angular position to $\pm$ 2 arc sec. The spectrometer is mounted firmly on the floor beside the surface table. The autocollimator is adjusted in position to observe the spectrometer master reference and the return is zeroed. A standard angle gauge (say, $30^{\circ}00'00'' \pm 2''$) is placed on the crystal and the autocollimator axis is translated to view the top of the angle block. The spectrometer θ-control motor is operated to bring the autocollimator return to zero. The casing of the angle encoder is rotated so that the output signal is exactly $30^{\circ} \pm$ one least significant bit (LSB).

(3) The input X-ray beam collimator is now installed and the autocollimator again moved over the surface table to view the reference mirror of the collimator principal axis. The collimator mounting is then adjusted to zero the return in the autocollimator.

The net result of these operations is that the vehicle ACU can be used to correctly direct the spectrometer to view any local region of the sun if the angular relationship between the instrument reference mirror and the ACU sun-sensor principal axis is known. In addition, the shaft encoder is correctly zeroed to read Bragg angle θ.

Experience has shown that if these adjustments are correctly made, then use of the known crystal period from the literature (e.g. Bearden and Huffman , 1962; Wyckoff, 1965; Adler, 1967), in Equation 3.7, gives all features occurring within about

2 - 3 arc min of the expected angle, i.e. an absolute wavelength scale is established to about 1 part in 1000. Given this satisfactory starting point the reference lines are then used to refine the calibration to about 1 part in 20,000.

One further significant economy may be made. In the above discussion, it has been assumed that the glancing angle is measured to the required precision of 1 part in 20,000, and the need for a 20 arc sec resolution angle encoder is implied, at a cost of several thousand pounds sterling. In fact, the instrument is equipped with a 14 bit (LSB = 1' 19") device at a cost of a few hundred pounds. The reason for this is that although a low resolution (14 bit) encoder will typically be constructed to $\pm$ 1 LSB absolute accuracy, the errors in the locations of the transitions between ones and zeroes in the least significant track will be almost all long period errors arising from eccentric mounting of the disc and ovality in the track (Evans, 1975). Small angular differences may then be read to much better precision than one LSB by linear interpolation between the times of LSB transitions. This operation requires the condition thatthe main bearings, drive gearing and control system be of sufficient quality to maintain $d\theta/dt$ adequately constant. Temperature stability of the angular position of the transition points cannot be expected and this is believed to be the reason for the lack of reproducibility between the scans shown on Figure 3.8. The worst case disagreements between the scans are in fact less than $\pm$ 1 LSB and this is within the manufacturer's specification for the angle encoder.

Each rèference line used in the wavelength calibration is required to satisfy the following conditions (in addition to the identification criteria given in Section 3.3.3.1):

(1) The uncertainty in the theoretical wavelength must be $\lesssim \pm$ 0.001 Å.

(2) The line must be resolvable from any other known lines in the data.

It is found from the literature that the only transitions fulfilling criterion (1) are the lines of H- and He-like ions.

The reference wavelengths for H-like ions are effectively exact and are taken from the tables of Garcia and Mack (1965). These tables show that for H-like ions with nuclear charge $Z \leqslant 20$, the two components of the Lyman α 1S - 2P line are separated by a wavelength difference of 0.005 to 0.006 Å, approximately independent of Z. The relative intensities of these components are expected to be proportional to the statistical weights of their upper levels under coronal conditions (Hutcheon and McWhirter, 1973). These components are not resolved in the present spectra and it is assumed that the wavelength of the peak of the observed line corresponds to the statistically weighted mean wavelength. The same procedure is followed for the Lyman β and γ lines, where the splittings are much smaller.

Wavelengths for He-like ion lines are taken from the calculations of Ermolaev and Jones (1974). The uncertainty claimed for these (as deduced by summing the uncertainties given for each component term in the expression for the appropriate energy level values) is about 1 part in 10^5. These wavelengths have been checked as far as possible by comparing them with the precision measurements of resonance $1s^2.\,^1S_0 - 1s\,np.\,^1P_1$ lines of He-like ions with $8 \leqslant Z \leqslant 13$ reported by Tyrén (1940), Flemberg (1942) and Blake (1970). The root mean square difference between the calculated and measured values is about 6 parts in 10^5, which is comparable with the uncertainty in measurement. In only one case

(Flemberg's measurement of the F VIII $1s^2.{}^1S_0$ - $1s\,2p.{}^1P_1$ line) does the discrepancy exceed 1 part in 10^4. However this measurement differs from the results of Tyrén and Blake, which are mutually consistent and within 5 parts in 10^5 of the calculated values. Thus, the calculated wavelengths of Ermolaev and Jones (1974) have been accepted as standards good to at least $\pm$ 0.001 Å in the interval 7 to 22 Å.

Those observed lines which satisfy the criteria given above, are listed in Table 3.1, together with the reference wavelengths and derived values of $2d_{eff}$ for each spectral scan. The values of $2d_{eff}$ between the reference points, are calculated by linear interpolation or weighted least squares method; fitting a second or higher order polynomial makes no significant difference. In the data, there are several unresolvable blends where the wavelengths of the individual components are accurately known from calculation or laboratory measurement; these features may be used to test the consistency of the wavelength calibration. For example, on the KAP fast scans, the O VIII Lyβ line at 16.006 Å (Garcia and Mack, 1965) cannot be resolved from the Fe XVIII $2p^5.{}^2P_{3/2}$ - $2p^4({}^3P)3s.\ {}^4P_{3/2}$ line reported at 16.003 Å by Feldman et al. (1973). The measured wavelengths for the peak of this blend are 16.006, 16.004 and 16.003 Å, for regions 11619, 12628, and 12624 respectively, and thus are in good agreement with the known wavelengths of the components.

It will be seen in later chapters, that using the calibration method described above, the measured wavelengths of identified lines in the SL1101 and SL1206 spectra in many cases agree with calculations and laboratory measurements to within 0.002 to 0.003 Å.

3.3.3.3 Calibration of Spectral Line Intensity

For convenience in evaluation, Equation 3.3 may be rewritten as:

$$I = S_e N \quad \text{erg cm}^{-2}\ \text{sec}^{-1} \tag{3.10}$$

where $S_e = 10^8\ hc\omega/(\lambda A R \varepsilon)$ erg cm^{-2} sec^{-1} cnt^{-1}. (3.11)

S_e is defined as the instrument energy sensitivity and contains all the instrumental parameters required for the conversion of recorded counts to line intensity. A computer program SPREFF has been written to calculate the sensitivity of each spectrometer as a function of wavelength. The input values to the program are ω, the detector window and gas thickness (for the calculation of ε), R as a tabulated function of λ (the program performs a linear interpolation between the given points), the geometrical factors required for the calculation of A as a function of Bragg angle θ, the nominal value of crystal 2d and the wavelength range and step size over which S_e is to be calculated. The output of the program is a tabulation of S_e, A, R and ε as a function of wavelength; also printed is the instrument photon sensitivity:

$$S_p = S_e \lambda/(10^8\ hc) \quad \text{ph cm}^{-2}\ \text{sec}^{-1}\ \text{cnt}^{-1}. \tag{3.12}$$

Figures 3.9 and 3.10 show the energy sensitivity as a function of wavelength, for each spectrometer scan. For Bragg angles less than about 30^o and greater than about 55^o, the geometrical area A starts to decrease; at small Bragg angles the reduction is due to the crystal not filling the photon beam from the collimator, and at large Bragg angles it is caused by the detector mounting cutting into the beam from the collimator.

The uncertainties in the instrument parameters used to derive the measured spectral line intensities, are estimated to be:

$\delta R/R \lesssim \pm 5\%$

$\delta \varepsilon/\varepsilon \lesssim \pm 15\%$

$\delta A/A \lesssim \pm 15\%$

$$\delta\omega/\omega \lesssim \pm 1\% \quad .$$

The uncertainty in crystal integrated reflectivity R has been estimated from the agreement between measurements made on several samples of each crystal material and the experimental uncertainty on the data for each sample (Leigh and Evans, 1975; Hall and Evans, 1975). The uncertainty in the photon detection efficiency ε has been obtained by comparing the mass absorption coefficients of Leroux (1963) with the more recent values of Veigele (1973), and from the estimated uncertainty in the average thickness of the detector window. The uncertainty in the geometrical collecting area A has been determined from measurements of the relevant dimensions on the spectrometer (Watson, 1975; present work). An upper limit to the uncertainty in crystal rotation rate ω has been established from examination of the flight data.

The upper limit uncertainties given above are, in general, estimates of the systematic errors involved, and hence in many cases, the actual accuracy achieved is much higher than is implied by these figures. For example, the relative intensities of nearby lines observed by the same crystal will, in general, be more accurate than their absolute intensities. This must be taken into account when considering the reliability of the measured line intensities and quantities derived from them (e.g. temperature and emission measure).

The uncertainty δN in the number of counts N recorded for a spectral line, is calculated from the expression (e.g. Bertin, 1970):

$$(\delta N)^2 = N + 2B \tag{3.13}$$

where B is the background count over the line profile.

In order to estimate the total uncertainty for a particular case, the various error terms are combined in a linear or quadratic manner, according to whether the dominant uncertainties are systematic or random, respectively.

When quoting the measured intensity of a spectral line, the following definitions will apply in this thesis, unless otherwise stated;

(a) A measured upper limit intensity is derived from the actual number of counts (minus background) recorded at the expected position of the spectral line.

(b) The uncertainty of a measured intensity (either statistically significant or upper limit) is the standard deviation calculated from the statistical uncertainties in the crystal integrated reflectivity and in the counts recorded for the spectral line and the background.

In determining the measured intensity of a spectral line via Equation 3.3 (or 3.10), no allowance is made for atmospheric absorption. In general, the right-hand sides of Equations 3.3 and 3.11 must be divided by the atmospheric transmission at wavelength λ and altitude h. However, for the SL1101 and SL1206 spectra presented here, the effect of atmospheric absorption is estimated to be less than 10% at all wavelengths (i.e. $\lambda \lesssim 22$ Å) and less than 5% for $\lambda \lesssim 15$ Å. These figures are derived from the known flight trajectories of the vehicles and the calculated atmospheric transmission of Henke and Elgin (1970).

3.4 The S-054 Experiment

3.4.1 Instrumentation

The primary instrument in the ASE ATM S-054 experiment is an X-ray telescope assembly with a photographic film detection system. The telescope optios is a nested pair of coaxial confocal grazing-incidence mirrors of paraboloid-hyperboloid (Wolter type 1) design and diameters 23 and 31 cm. The mirror surface is Kanigen, a nickel-phosphorous alloy, deposited on a beryllium support structure. The principles of the optical system are shown in Figure 3.11. The S-054 experiment is shown in Figures 3.12 and 3.13. The geometrical collecting area of the instrument is 42 cm^2 and its focal length 213 cm, giving an image scale of 0.001 cm per arc sec. The spatial resolution is $\sim$2 arc sec.

The overall wavelength range of the instrument is 2 - 60 Å. Spectral information is normally obtained by the use of broadband filters, of which there are six, each one having a different wavelength response. Details of the filters are given in Table 3.2. In order to provide the necessary dynamic range of detection sensitivity the photographic exposure time may be varied from $\frac{1}{4}$ to 256 sec, in increments of a factor 4. Spectral resolution may also be achieved by the use of a normal-incidence transmission diffraction grating with resolving power $\lambda/\Delta\lambda \sim 50$ at 7 Å. Since this technique produces dispersed overlapping images, it is used mainly for observations of very bright compact features, such as flares.

In addition to the main telescope system, the S-054 experiment contains several ancillary instruments to provide monitoring facilities for the Skylab crew, and attitude information.

3.4.2 Observations

The Skylab space station was launched into a near-circular Earth orbit of about 430 km altitude, on 14 May 1973. Three manned missions were performed: 25 May to 22 June 1973, 28 July to 25 September 1973 and 16 November 1973 to 8 February 1974. At the time of the SL1206 observations, S-054 obtained a sequence of coronal X-ray images using filters 1, 2 and 3, and a full range of exposure times.

The S-054 images show that region 12628 was extended by about 6 arc min on the disk, its bipolar closed loop structure being clearly visible, while region 12624 was much more compact, $\sim$1 arc min across. Region 12624 was observed about 60 minutes after the peak of an importance -N, class C0 flare; the flare activity is evident in both the spectra and photographs. Region 12628 was not flaring at the time of the SL1206 observations, but produced an importance 1B flare about 15 minutes afterwards, the onset being recorded by S-054.

3.4.3 Data Reduction and Analysis Methods

The quantity measured in an X-ray exposure through a given filter is the photographic density at any given point on the film. The film density is converted into energy deposited per unit area per unit time and the effect of the telescope point response function (shown in Figure 3.14) is removed by deconvolution. For an optically thin, steady state plasma, the deconvolved deposited energy for filter i, is related to the physical parameters of the observed region by the equation (Vaiana et al., 1973b):

$$E_i = \left[A/(4\pi f^2)\right] \int_l \int_\lambda \int_{T_e} p\left[\lambda, T_e(l)\right] . \eta_i(\lambda) . \left[n_e(l)\right]^2 . dT_e \, d\lambda \, dl \tag{3.14}$$

where: E_i = deconvolved deposited energy per unit area per unit time per picture element, for filter i (erg cm^{-2} sec^{-1} picture $element^{-1}$)

A = effective collecting area of telescope (cm^2) $\approx$ 15 cm^2 for S-054.

f = focal length of telescope (cm)

l = distance along line-of-sight (cm)

$\eta_i(\lambda)$ = filter transmission and telescope reflectivity at wavelength λ

$p[\lambda, T_e(l)]$ = power emitted at wavelength λ by unit line-of-sight emission measure at electron temperature T_e (erg sec^{-1} cm^5) .

$p\left[\lambda, T_e(l)\right]$ is determined from a theoretical model for the coronal X-ray spectrum (currently a modified version of the Tucker and Koren (1971) calculations), and $\eta(\lambda)$ is obtained from laboratory calibrations.

Equation 3.14 may be rewritten as

$$E_i = \left[A/(4\pi f^2)\right] . \int_{T_e} F_i(T_e)\, Y(T_e)\, dT_e \qquad (3.15)$$

where: $Y(T_e) = \int_l \left[n_e(l)\right]^2 dl$

= line-of-sight emission measure at electron temperature T_e (cm^{-5})

$F_i(T_e) = \int_\lambda p\left[\lambda, T_e(l)\right]\eta_i(\lambda)\, d\lambda$

= Filtered Spectrum Integral (FSI).

If the plasma along the line-of-sight is isothermal, Equation 3.15 reduces to:

$$E_i = \left[A/(4\pi f^2)\right] . F_i(T_e) . Y(T_e) . \qquad (3.16)$$

Since in this case, $\left[A/(4\pi f^2)\right] . Y(T_e)$ is constant for all filters:

$$R_{ij}(T_e) = E_i/E_j = F_i(T_e)/F_j(T_e) \qquad (3.17)$$

where $R_{ij}(T_e)$ the Sp ectral Hardness Index (SHI), is a function of temperature only, for any two filters i and j. In the more realistic case of Equation 3.15, the temperature derived from the SHI represents a weighted average of the true temperature distribution along the line-of-sight, and will be termed the effective or line-of-sight temperature T_{eff}. The effective line-of-sight emission measure is then:

$$Y_{eff} = (4\pi f^2/A) . E_i/F_i(T_{eff}) . \qquad (3.18)$$

For the S-054 telescope, the constant:

$$A/(4\pi f^2) = 2.631 \times 10^{-5} .$$

The film density is digitised by a scanning microdensitometer with an aperture equivalent to 2 arc sec x 2 arc sec on the film. The image is then stored as an array of numbers on magnetic computer tape. The ASE Solar Physics Group have developed a suite of computer programs for the processing of this data. They are written mainly in PL/I for the IBM 360/370 computers at ASE. The facilities available include array manipulation to perform analysis similar to that described above and image display in the form of tabulations, contour plots and cross-sections. The author has used these programs in the analysis of the S-054 images obtained at the time of the SL1206 flight, and in the correlation of the images with the SL1206 spectra. These results are presented in Chapter 4.

The response of the film to incident radiation is wavelength dependent and hence, in general, varies with the temperature of the observed plasma. This effect may be represented, in the film density to energy conversion, by a parameter $a\mu(T_e)$, which may be determined from laboratory measurements. It is convenient, in the initial film density to energy conversion to set $a\mu(T_e) = 1$ and then include the actual values of $a\mu(T_e)$ with the temperature functions $F_i(T_e)$ and $R_{ij}(T_e)$ as follows:

$$F'_i(T_e) = F_i(T_e) . a\mu_i(T_e) \tag{3.19}$$

$$Q_{ij}(T_e) = R_{ij}(T_e) . a\mu_i(T_e)/a\mu_j(T_e) \tag{3.20}$$

$$E_i = E_i^o/a\mu_i(T_e) \tag{3.21}$$

where: E_i^o = deposited energy, using $a\mu(T_e) = 1$

E_i = true deposited energy

and $F'_i(T_e)$ and $Q_{ij}(T_e)$ are the effective values of FSI and SHI respectively, to be used in analysing the image arrays of E_i^o. In the quantitative analysis given in Chapter 4, the images used were obtained through filters 1 and 3. The values of $\eta_i(\lambda)$, $F'_i(T_e)$ and $Q_{ij}(T_e)$ for these filters, are plotted in Figures 3.15 to 3.17.

Gerassimenko (1975) estimates that the uncertainty in the film density to energy conversion is $\sim 20\%$ for filters 1 and 3.

Table 3.1.a SL1101 and SL1206 wavelength calibrations: $2d_{eff}$ versus wavelength for the ADP spectrometers

Ion	Transition[a]	Reference wavelength (Å)[b]	$2d_{eff}$ (Å) Active region no. 11619[c]	12628[d]	12624[d]
Fast scan:					
Si XIII	R	6.648		10.652	10.660
	I	6.688		10.662	10.664
	F	6.740		10.653	10.658
Mg XI	4R	7.473			10.655
Al XII	R	7.757			10.655
Mg XI	3R	7.850			10.652
Al XII	F	7.872			10.656
Mg XII	Lyα	8.421		10.645	10.656
Slow scan:					
Mg XI	R	9.169	10.647	10.648	10.650
	I	9.231	10.648	10.648	10.648
	F	9.314	10.647	10.648	10.648

Table 3.1b SL1101 and SL1206 wavelength calibrations : $2d_{eff}$ versus wavelength for the gypsum spectrometers

Ion	Transition[a]	Reference Wavelength(Å)[b]	$2d_{eff}$(Å) Active region no. 11619[c]	12628[d]	12624[d]
Fast scan:					
Al XII	R	7.757		15.216	15.219
Mg XI	3R	7.850	15.236	15.218	15.230
Mg XII	Lyα	8.421		15.211	15.218
Mg XI	R	9.169	15.247	15.208	15.220
	I	9.231	15.239	15.209	15.211
	F	9.314	15.234	15.207	15.215
Ne X	Lyβ	10.239		15.204	15.213
Ne IX	4R	11.000	15.217	15.200	15.207] e)
Na X	R	11.003	15.220	15.204	15.211]
Ne IX	3R	11.547	15.213	15.202	15.213
Ne X	Lyα	12.134	15.217	15.201	15.202
Slow scan:					
Ne IX	R	13.447	15.205	15.201	15.203
	I	13.553	15.206	15.202	15.202
	F	13.699	15.207	15.201	15.202

Table 3.1c SL1101 and SL1206 wavelength calibrations : $2d_{eff}$ versus wavelength for the KAP spectrometers

Ion Transition[a]		Reference wavelength(Å)[b]	$2d_{eff}$ (Å)		
			Active region no.		
			11619[c]	12628[d]	12624[d]
Fast scan:					
Mg XI	R	9.169	26.785	26.698	26.740
	F	9.314	26.782	26.682	26.736
Ne IX	R	13.447	26.700	26.655	26.670
	F	13.699	26.692	26.657	26.674
O VIII	Lyγ	15.176	26.683	26.650	26.663
O VII	3R	18.628		26.633	26.641
O VIII	Lyα	18.969	26.639	26.632	26.637
Slow scan:					
O VII	R	21.601	26.628	26.623	26.632
	F	22.098	26.632	26.622	26.624

Footnotes to Table 3.1

a) Lyα, β, γ $= 1s.^2S_{\frac{1}{2}} - np.^2P_{\frac{1}{2},\frac{3}{2}}$, n = 1,2,3, respectively.

nR $= 1s^2.^1S_0 - 1snp.^1P_1$, n = 2,3,4,etc.

('R' implies '2R').

I $= 1s^2.^1S_0 - 1snp.^3P_1$.

F $= 1s^2.^1S_0 - 1snp.^3S_1$.

b) H-like ions : Garcia and Mack (1965)

He-like ions: Ermolaev and Jones (1974)

c) SL1101

d) SL1206

e) Unresolvable blend in present data.

Table 3.2 S-054 Filters

Filter no.	Material[a)]	Spectral passband(s) (Å)[b)]
1	13μ Be	3.5-17
2	3μ Teflon	3.5-14, 19-23
3	none	3.5-36, 44-60
4	5.7μ Parylene	3.5-19, 44-47
5	51μ Be	3.5-11
6	25μ Be	3.5-14

a) plus 1μ Polypropylene + 3000 Å Al.

b) 1% transmission and 3.5 Å mirror cutoff.

3.16 S-054 filtered spectrum integral (FSI) for filters 1 and 3. F_{Vi} is the volume effective FSI, F_i' is the line-of-sight effective FSI (defined in the text), A is the telescope effective collecting area, and ΔA is the area of a picture element in the telescope focal plane (courtesy of ASE).

3.17 S-054 effective spectral hardness index (defined in the text) for filters 1 and 3 (courtesy of ASE).

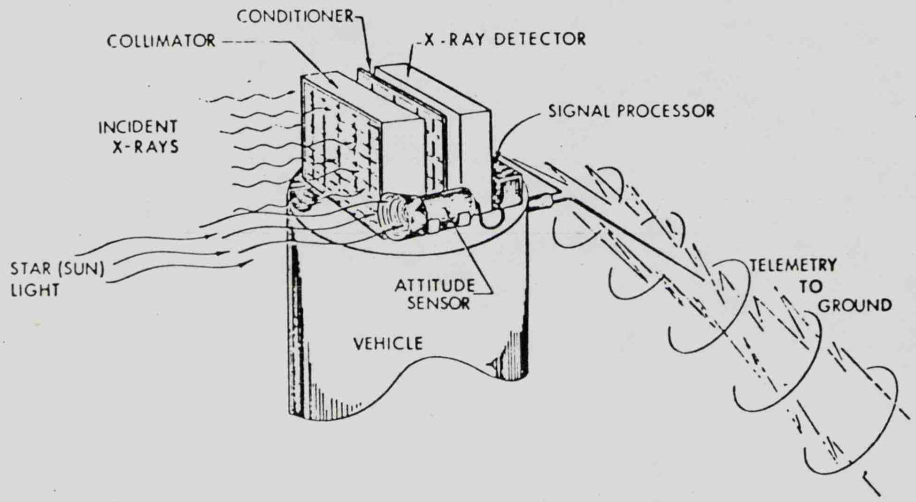
CONDITIONER
COLLIMATOR
X-RAY DETECTOR
INCIDENT
X-RAYS
SIGNAL PROCESSOR
STAR (SUN)
LIGHT
ATTITUDE
SENSOR
TELEMETRY
TO
GROUND
VEHICLE

Fig. 3.1.

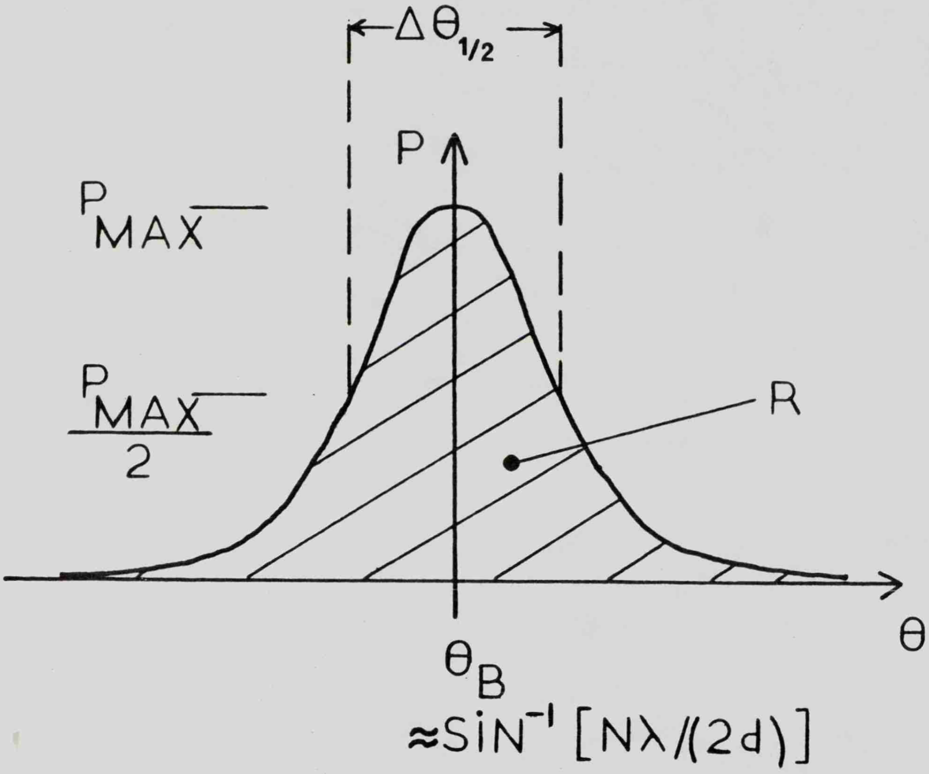

$\Delta\theta_{1/2}$
P
P_{MAX}
$\frac{P_{MAX}}{2}$
R
θ
θ_B
$\approx \sin^{-1}[N\lambda/(2d)]$

Fig. 3.2.

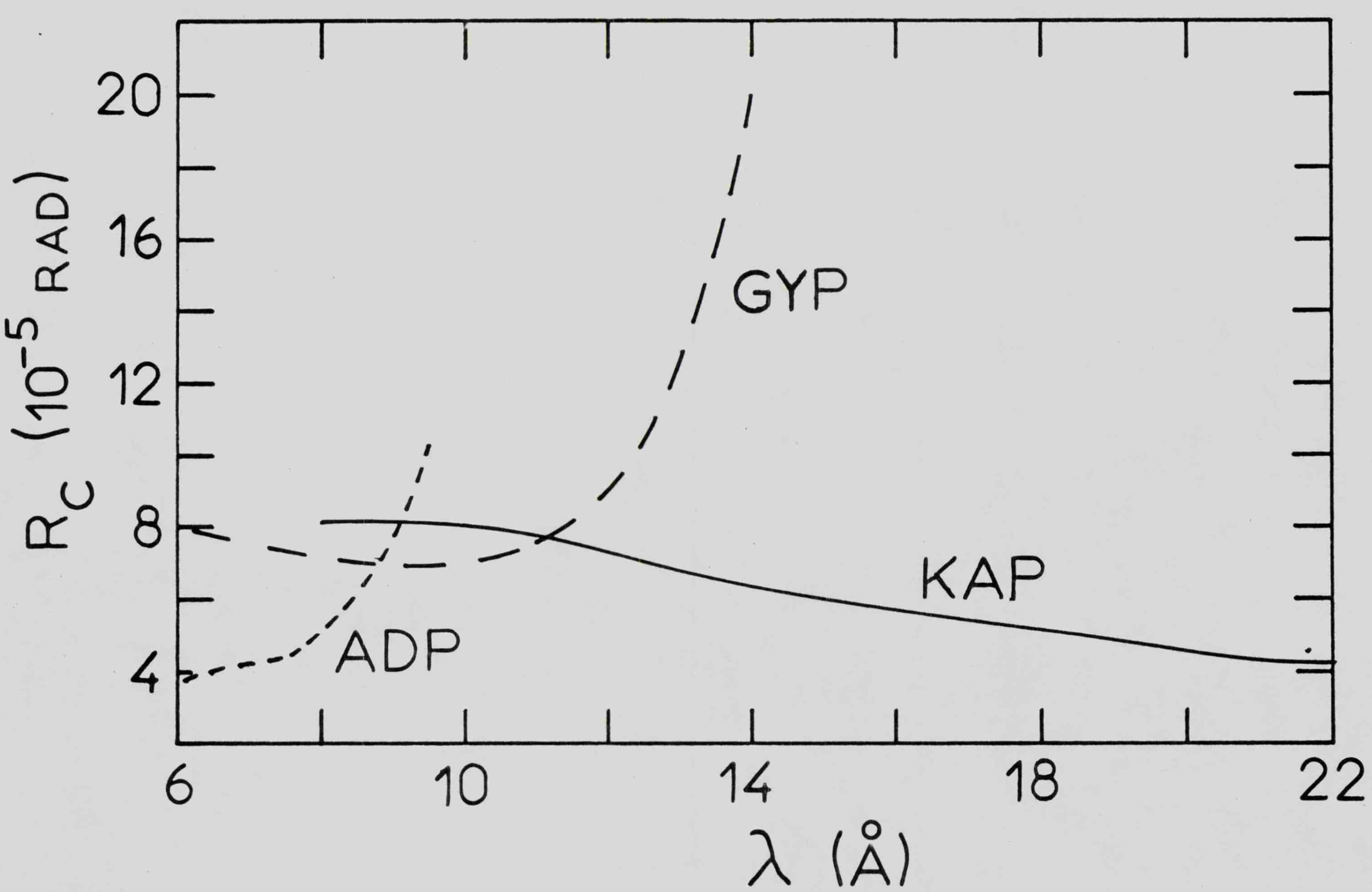

Fig. 3.3.

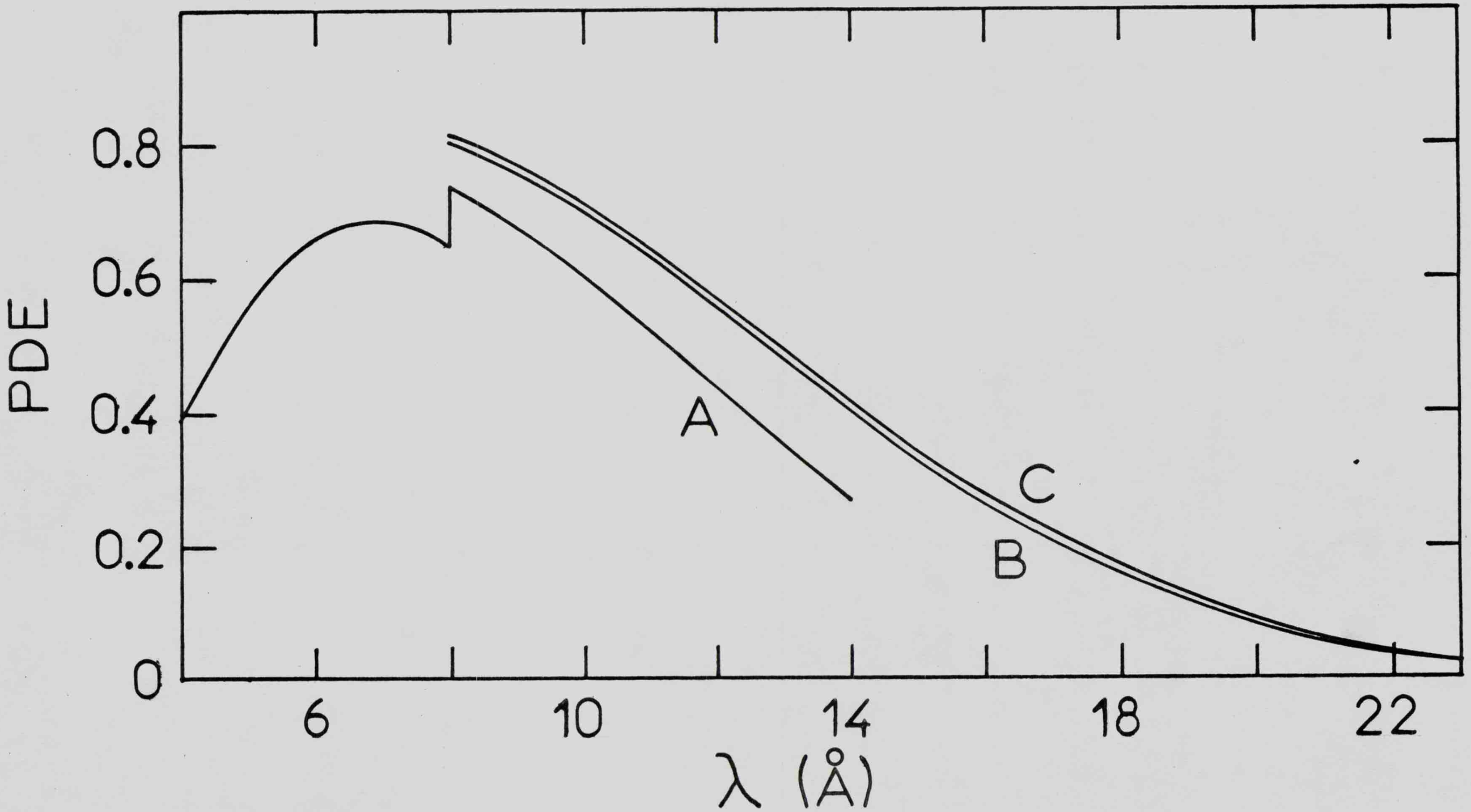

Fig 3.4.

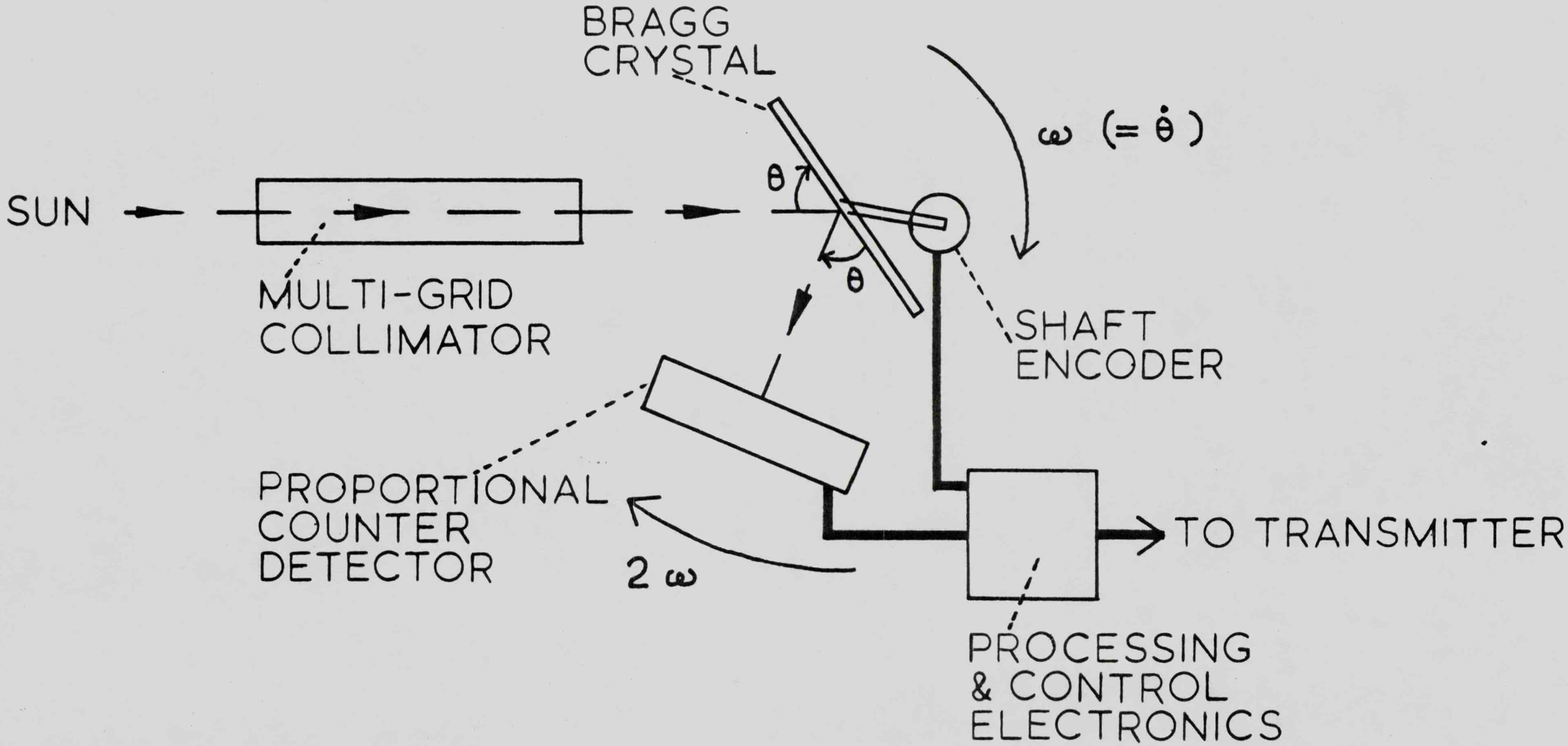
SUN
MULTI-GRID
COLLIMATOR
BRAGG
CRYSTAL
θ
θ
ω (= θ̇)
SHAFT
ENCODER
PROPORTIONAL
COUNTER
DETECTOR
2 ω
PROCESSING
& CONTROL
ELECTRONICS
TO TRANSMITTER

Fig. 3.5.

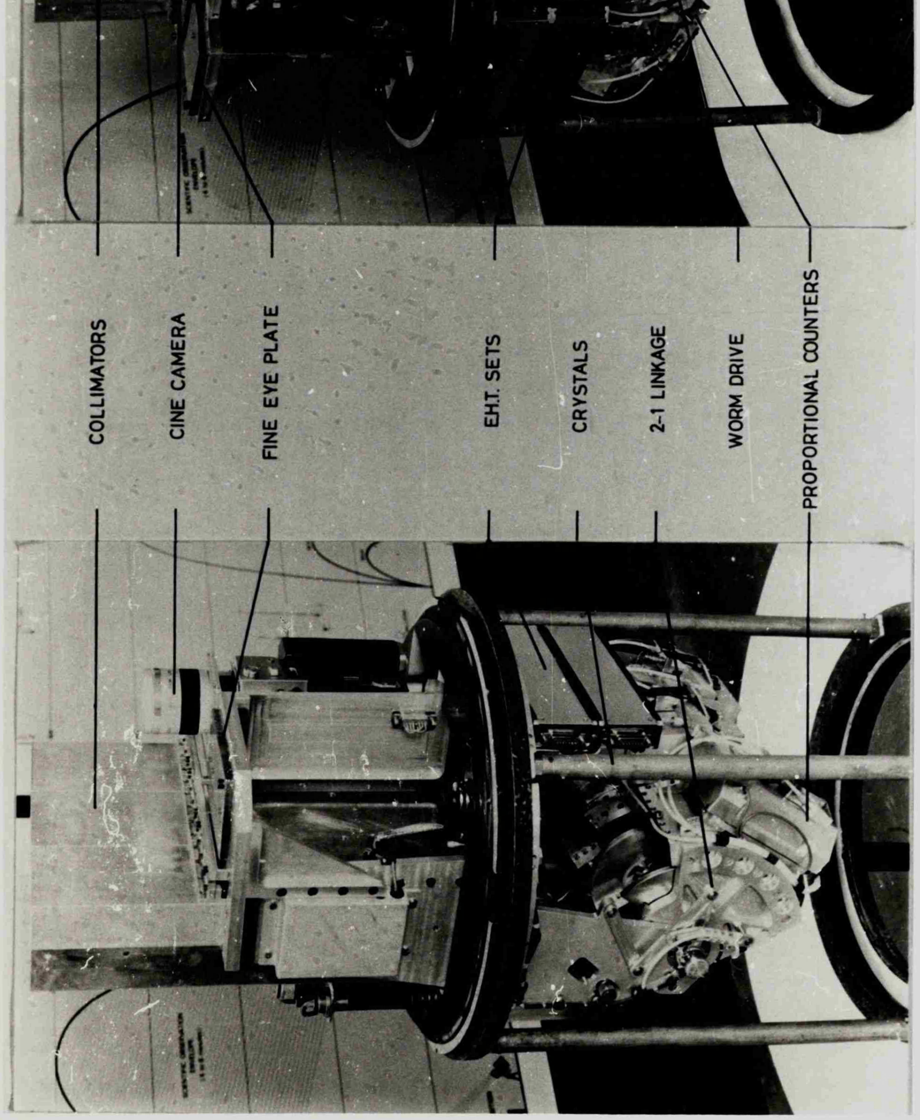
COLLIMATORS
CINE CAMERA
FINE EYE PLATE
E.H.T. SETS
CRYSTALS
2-1 LINKAGE
WORM DRIVE
PROPORTIONAL COUNTERS

Fig. 3.6.

Fig. 3.7.

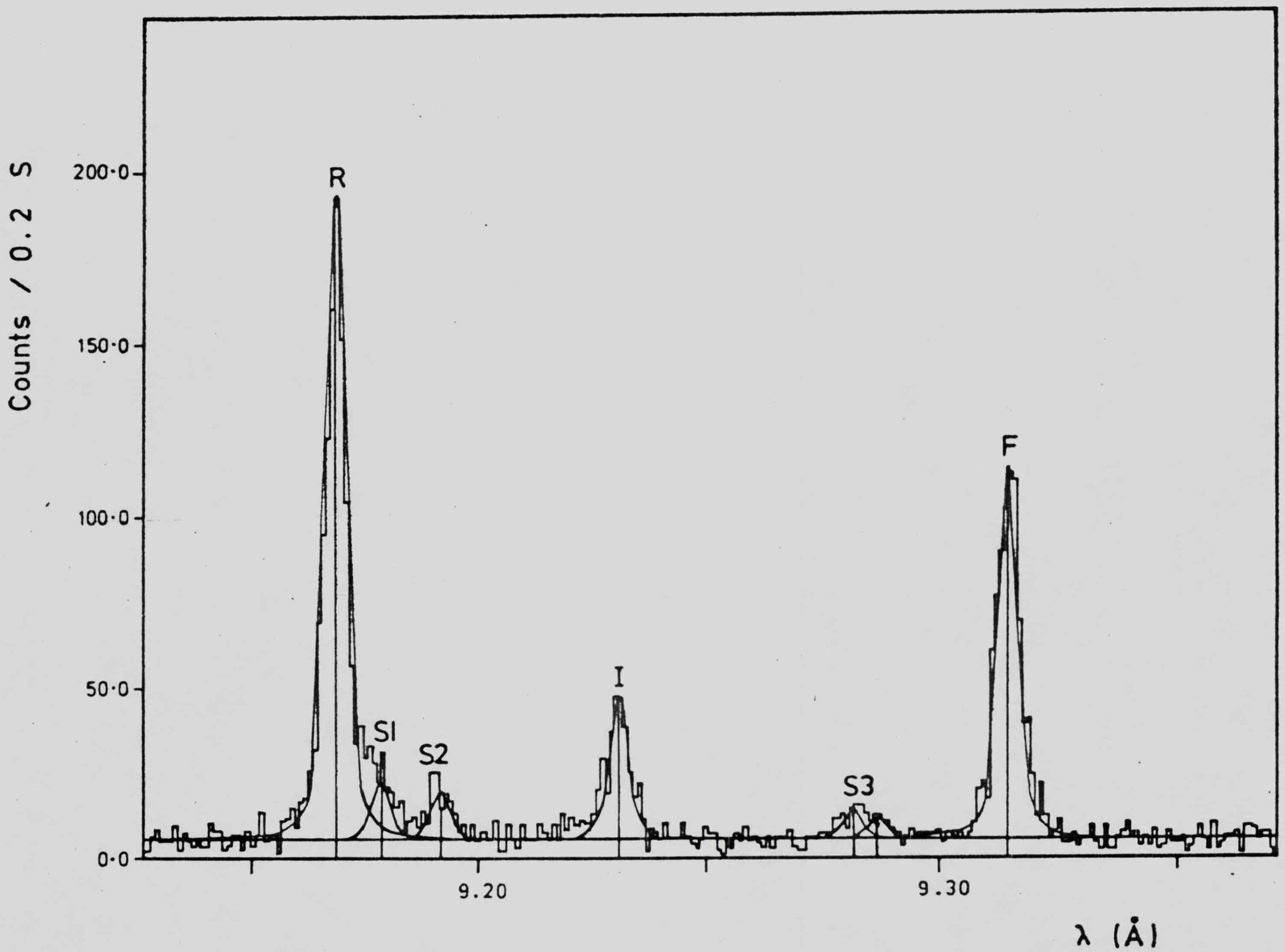

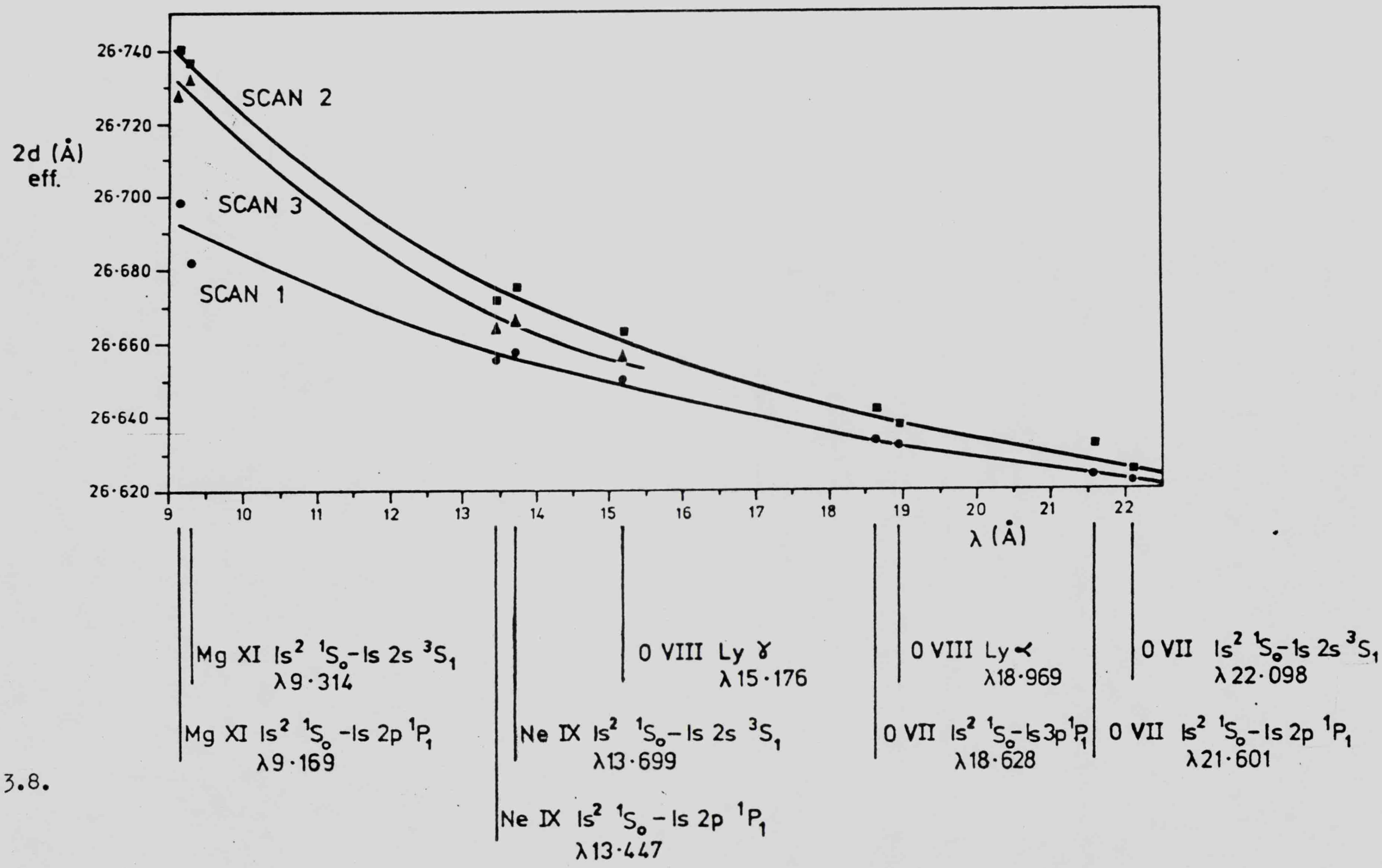

2d (Å) eff.
26·740
26·720
26·700
26·680
26·660
26·640
26·620
SCAN 2
SCAN 3
SCAN 1
9
10
11
12
13
14
15
16
17
18
19
20
21
22
λ (Å)
Mg XI 1s² ¹S₀–1s 2s ³S₁ λ9·314
Mg XI 1s² ¹S₀–1s 2p ¹P₁ λ9·169
Ne IX 1s² ¹S₀–1s 2s ³S₁ λ13·699
Ne IX 1s² ¹S₀–1s 2p ¹P₁ λ13·447
O VIII Ly γ λ15·176
O VIII Ly α λ18·969
O VII 1s² ¹S₀–1s 3p ¹P₁ λ18·628
O VII 1s² ¹S₀–1s 2s ³S₁ λ22·098
O VII 1s² ¹S₀–1s 2p ¹P₁ λ21·601

Fig. 3.8.

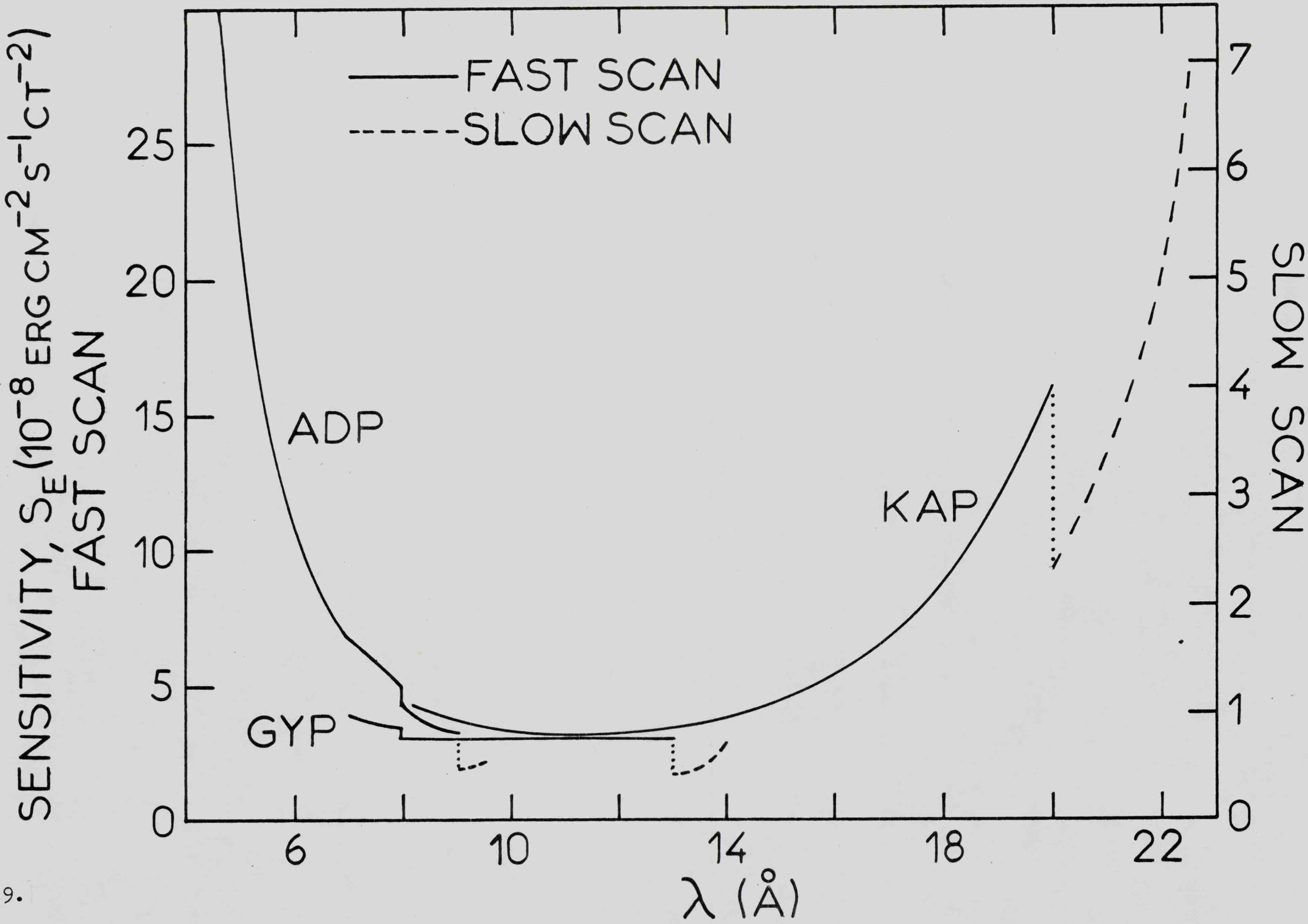

FAST SCAN
SLOW SCAN
SENSITIVITY, S_E (10^-8 ERG CM^-2 S^-1 CT^-2)
FAST SCAN
SLOW SCAN
ADP
GYP
KAP
λ (Å)
0
5
10
15
20
25
6
10
14
18
22
0
1
2
3
4
5
6
7

Fig. 3.9.

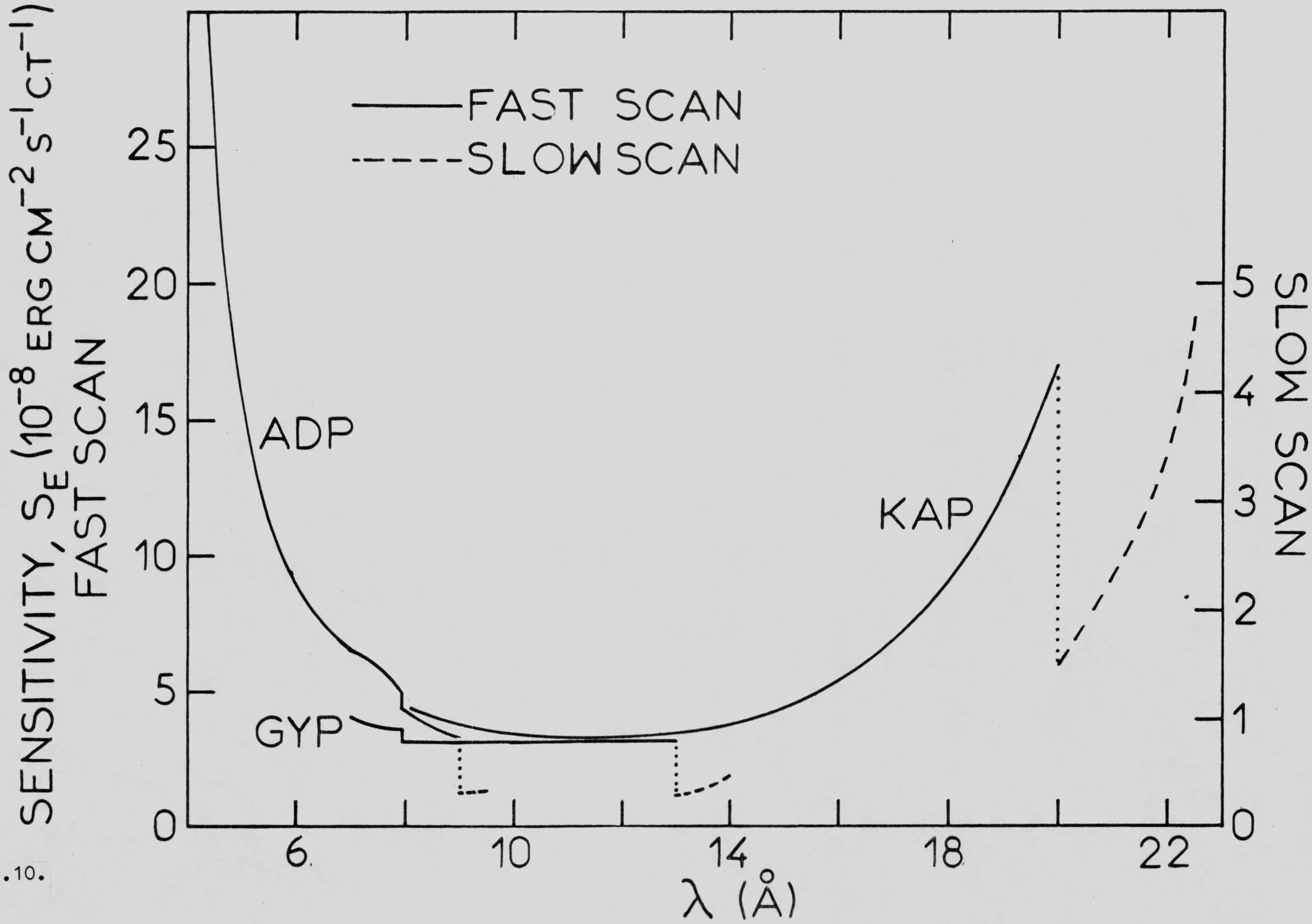

SENSITIVITY, S_E (10^{-8} ERG CM^{-2} s^{-1}CT^{-1})
FAST SCAN
25
20
15
10
5
0
FAST SCAN
SLOW SCAN
ADP
GYP
KAP
6
10
14
18
22
λ (Å)
SLOW SCAN
5
4
3
2
1
0

Fig. 3.10.

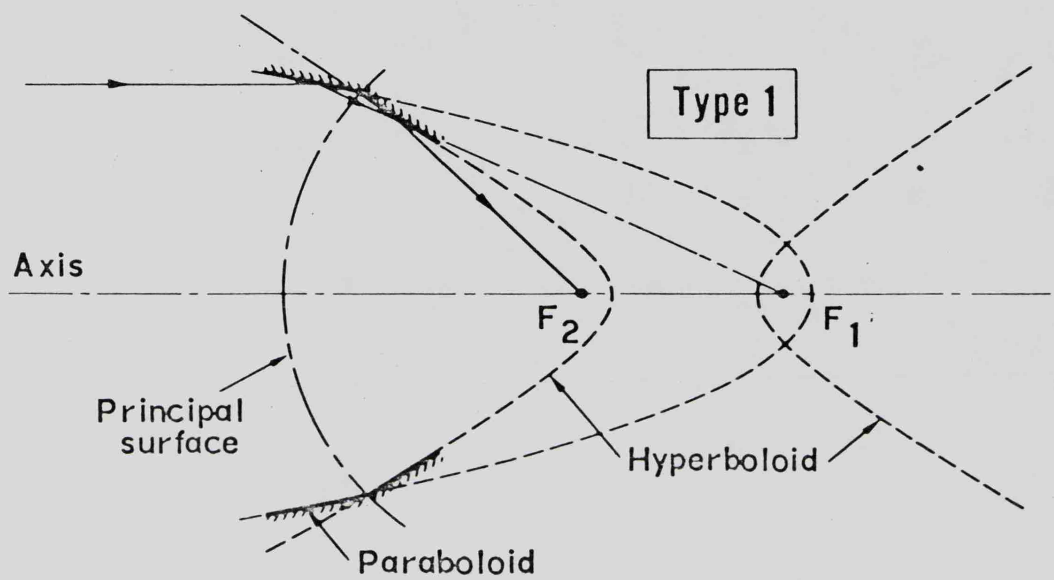
Type 1
Axis
F_2
F_1
Principal surface
Hyperboloid
Paraboloid

Fig. 3.11.

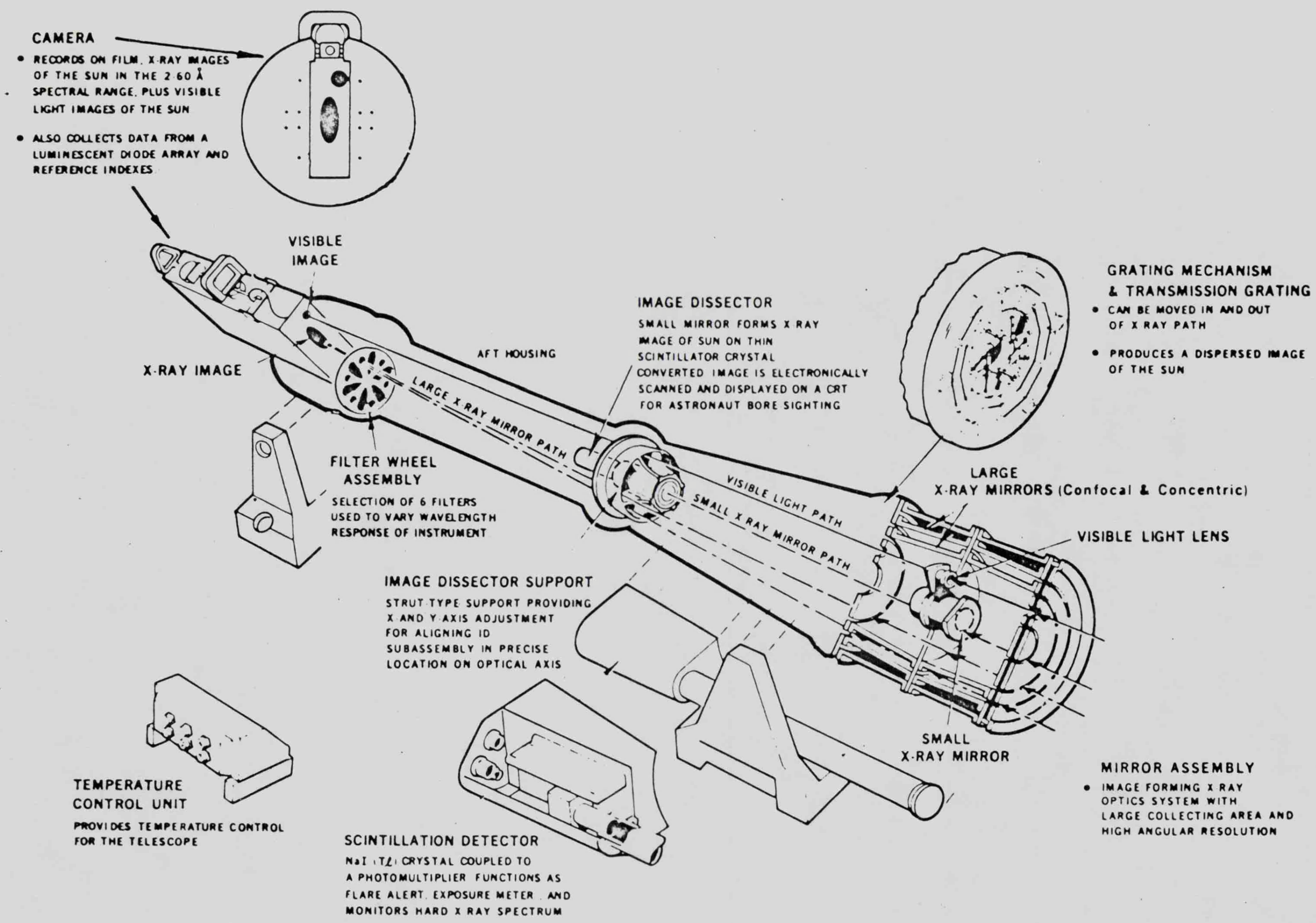
CAMERA
• RECORDS ON FILM, X-RAY IMAGES OF THE SUN IN THE 2-60 Å SPECTRAL RANGE, PLUS VISIBLE LIGHT IMAGES OF THE SUN
• ALSO COLLECTS DATA FROM A LUMINESCENT DIODE ARRAY AND REFERENCE INDEXES
VISIBLE IMAGE
X-RAY IMAGE
AFT HOUSING
LARGE X-RAY MIRROR PATH
FILTER WHEEL ASSEMBLY
SELECTION OF 6 FILTERS USED TO VARY WAVELENGTH RESPONSE OF INSTRUMENT
IMAGE DISSECTOR
SMALL MIRROR FORMS X RAY IMAGE OF SUN ON THIN SCINTILLATOR CRYSTAL CONVERTED IMAGE IS ELECTRONICALLY SCANNED AND DISPLAYED ON A CRT FOR ASTRONAUT BORE SIGHTING
VISIBLE LIGHT PATH
SMALL X RAY MIRROR PATH
GRATING MECHANISM & TRANSMISSION GRATING
• CAN BE MOVED IN AND OUT OF X RAY PATH
• PRODUCES A DISPERSED IMAGE OF THE SUN
LARGE X-RAY MIRRORS (Confocal & Concentric)
VISIBLE LIGHT LENS
IMAGE DISSECTOR SUPPORT
STRUT TYPE SUPPORT PROVIDING X AND Y AXIS ADJUSTMENT FOR ALIGNING ID SUBASSEMBLY IN PRECISE LOCATION ON OPTICAL AXIS
SMALL X-RAY MIRROR
MIRROR ASSEMBLY
• IMAGE FORMING X RAY OPTICS SYSTEM WITH LARGE COLLECTING AREA AND HIGH ANGULAR RESOLUTION
TEMPERATURE CONTROL UNIT
PROVIDES TEMPERATURE CONTROL FOR THE TELESCOPE
SCINTILLATION DETECTOR
NaI (Tl) CRYSTAL COUPLED TO A PHOTOMULTIPLIER FUNCTIONS AS FLARE ALERT, EXPOSURE METER, AND MONITORS HARD X RAY SPECTRUM

Fig. 3.12.

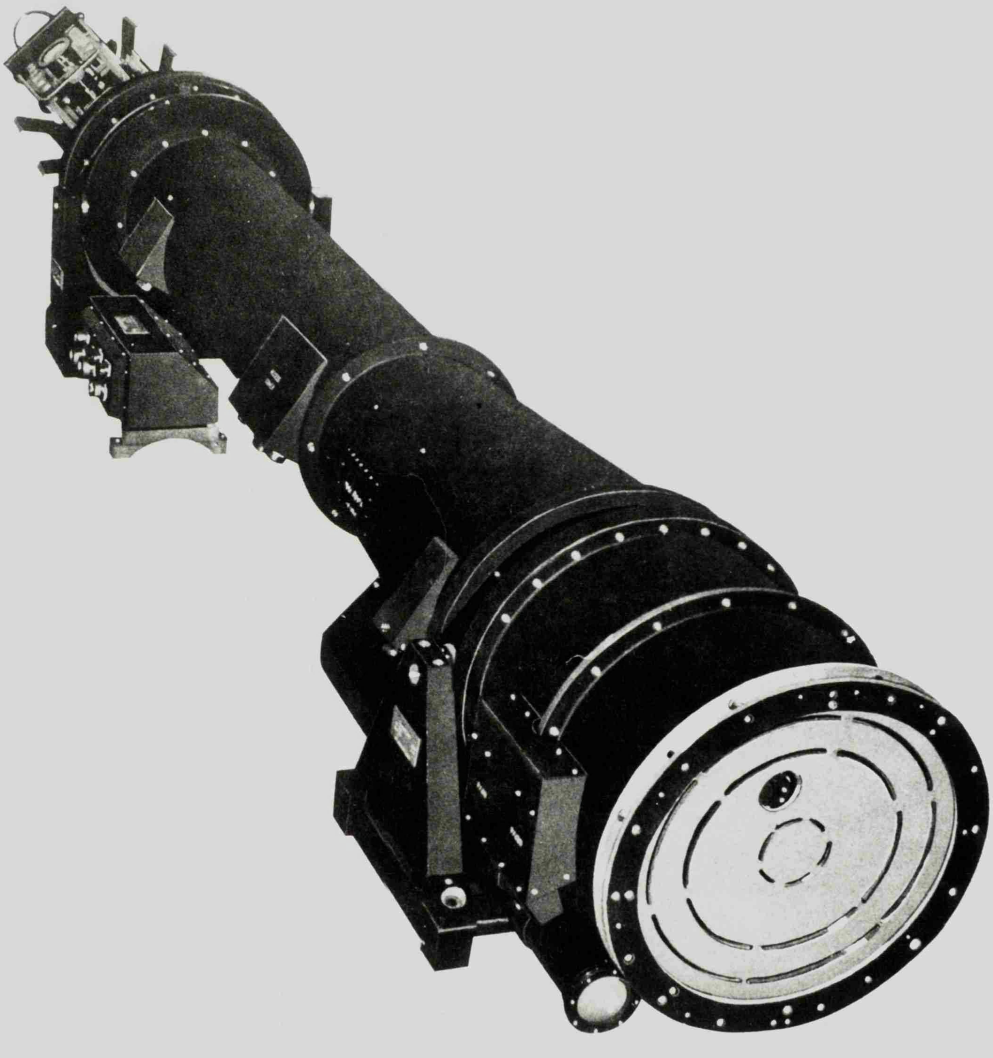

Fig. 3.13.

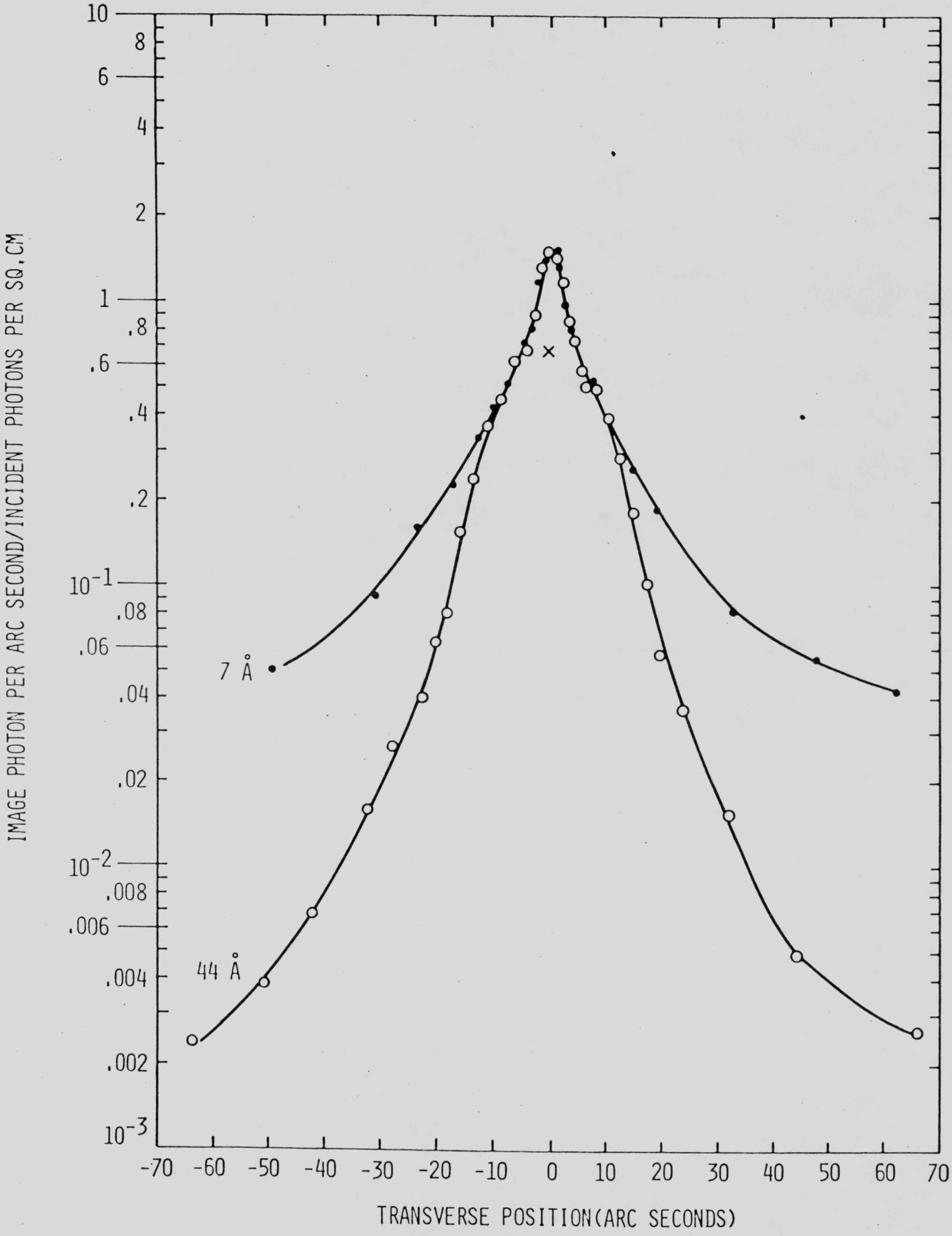
IMAGE PHOTON PER ARC SECOND/INCIDENT PHOTONS PER SQ.CM
10
8
6
4
2
1
.8
.6
.4
.2
10^{-1}
.08
.06
.04
.02
10^{-2}
.008
.006
.004
.002
10^{-3}
7 Å
44 Å
-70
-60
-50
-40
-30
-20
-10
0
10
20
30
40
50
60
70
TRANSVERSE POSITION(ARC SECONDS)

Fig. 3.14.

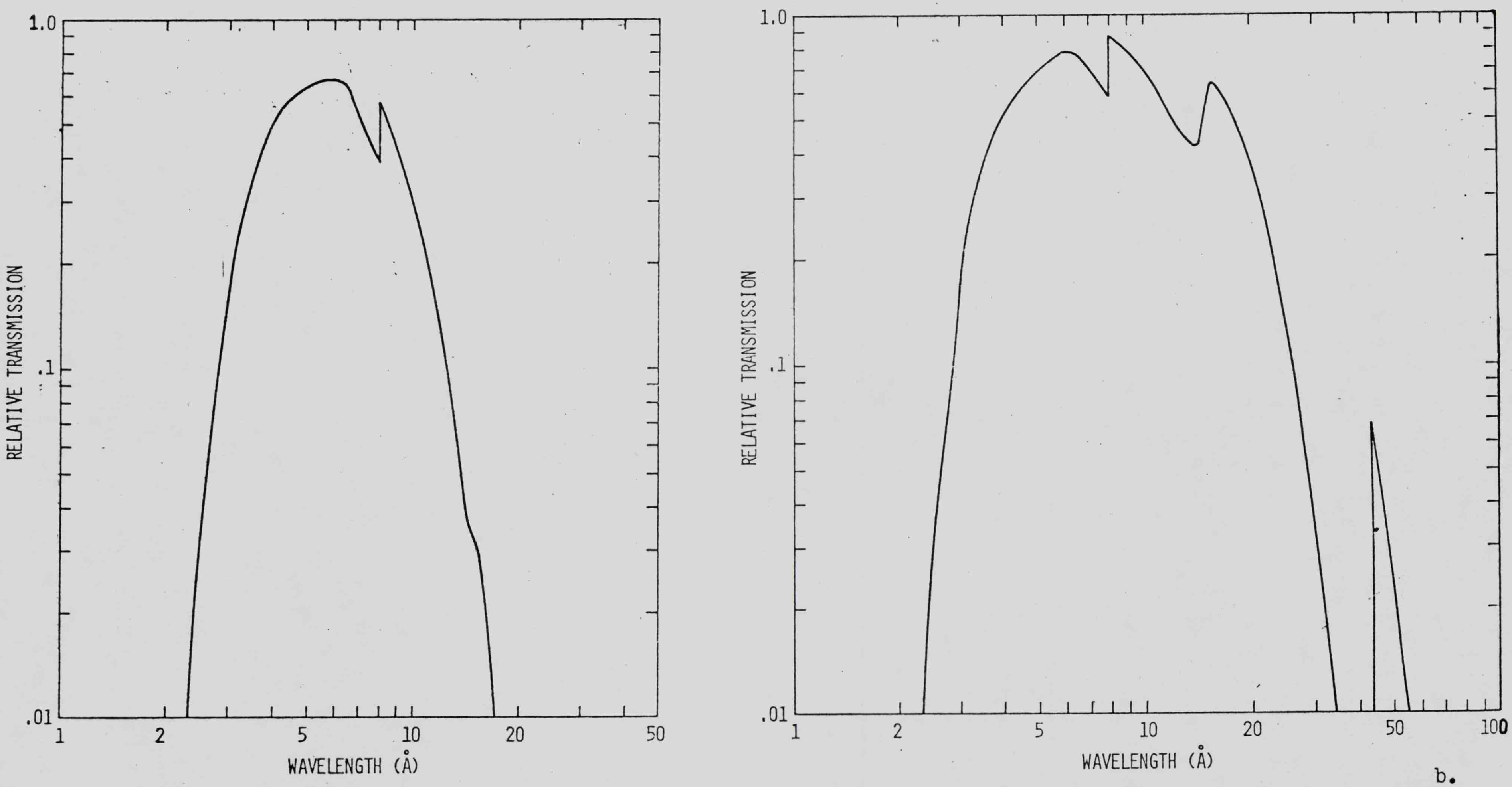
1.0
.1
.01
RELATIVE TRANSMISSION
1
2
5
10
20
50
WAVELENGTH (Å)
a.
1.0
.1
.01
RELATIVE TRANSMISSION
1
2
5
10
20
50
100
WAVELENGTH (Å)
b.

Fig. 3.15.

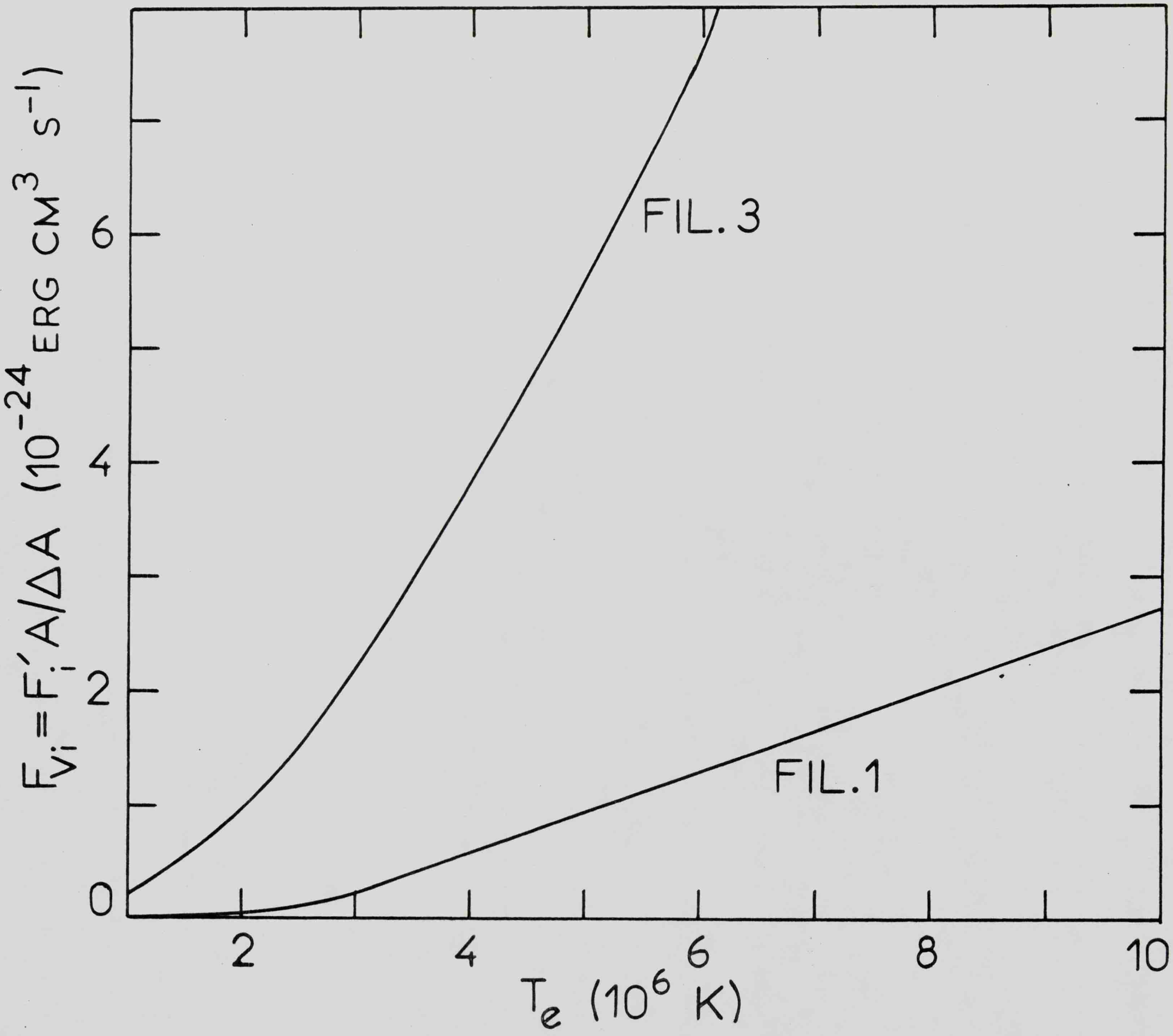

Fig. 3.16.

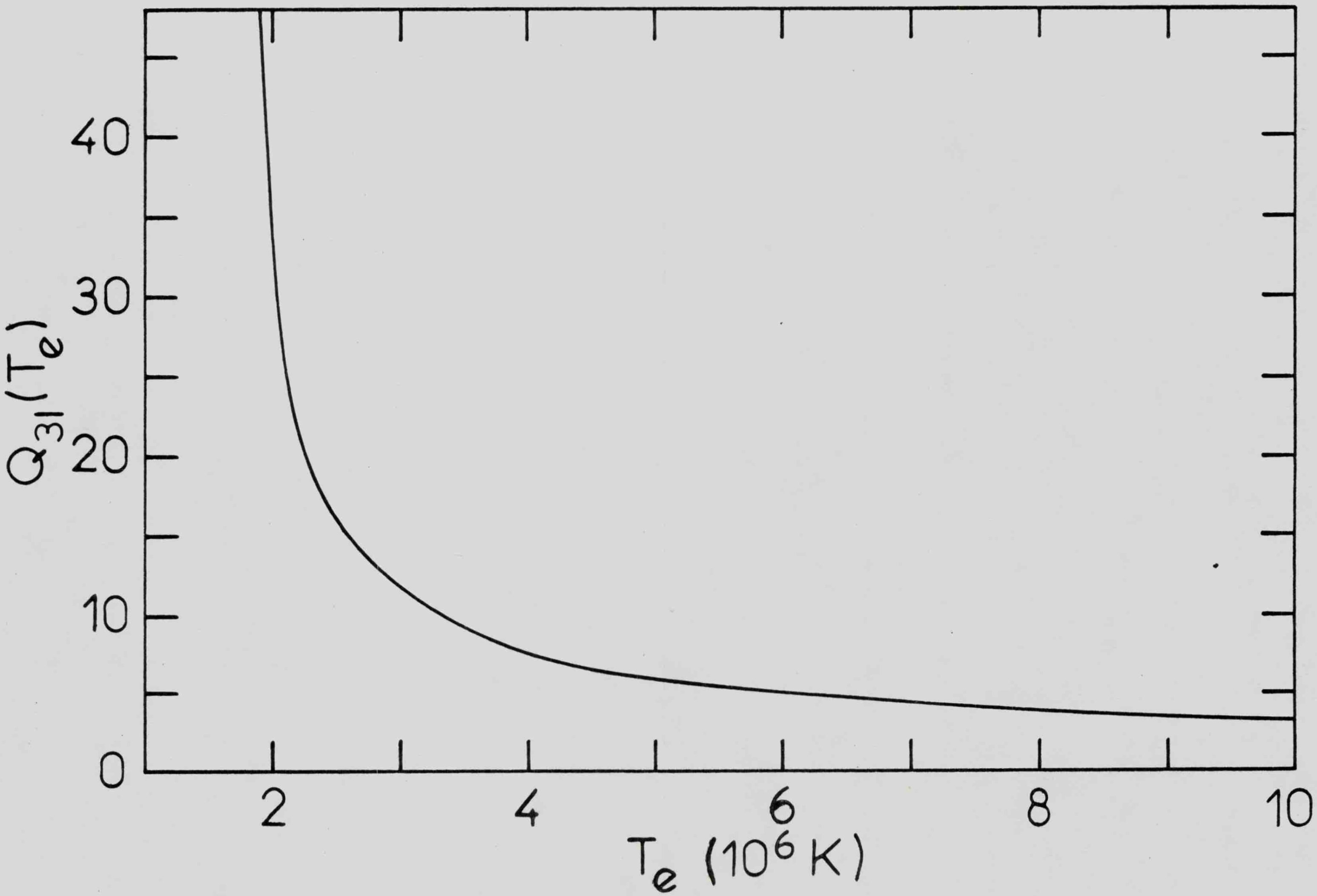

Fig. 3.17.

Chapter 4

CORONAL ACTIVE REGION MODELS FROM X-RAY OBSERVATIONS

4.1 Introduction

The previous chapters have emphasised the importance of X-ray observations in the diagnosis of the high temperature coronal plasma. Some of the diagnostic techniques for the interpretation of X-ray spectral line intensities will now be discussed and applied, with particular reference to the SL1101 and SL1206 data from regions 11619, 12628 and 12624. The subject areas to be covered are:

(1) Interpretation of absolute spectral line intensities in terms of a coronal model of volume emission measure ($\int_V n_e^2 dV$) against electron temperature.

(2) Comparison of coronal models from Leicester observations over the period 1966 to 1973.

(3) Correlation of the SL1206 spectra and S-054 images for regions 12628 and 12624.

(4) Determination of chemical element abundances in the corona, from relative and absolute line intensities.

Other diagnostic methods, such as determination of electron temperature and ionization balance from intensities of satellite lines to the He-like resonance lines, are discussed in thè appropriate chapters.

4.2 Coronal Emission Measure/Temperature Models

In general, the observed plasma must be assumed to be multi-thermal, and the method of determining the temperature structure consists of obtaining the "best-fit" (by some criteria, such as χ^2) of the calculated to the measured line intensities, using the emission measure $S(T_e)$ as a function of electron temperature as the free variable. The description of $S(T_e)$ may take the form of either:

(1) an analytic empirical expression containing several free parameters (Chambe, 1971; Walker, 1972; Phillips, 1975), or

(2) a set of mean values, each corresponding to a finite temperature interval (Evans and Pounds, 1968; Batstone et al., 1970; Beigman and Vainshtein, 1971; Parkinson, 1975c).

The first method offers the advantage of a continuous distribution of emission measure with temperature, but has the disadvantage that it may introduce erroneous features or constraints. The second method has the drawback that the emission measure is averaged over finite temperature intervals, but it does not impose any other constraints on the distribution; it may also be noted that the finite "resolution" of this model (i.e. the width of the temperature steps) simply reflects the fact that a finite number of observations (i.e. spectral line intensities) are used in its construction, and each of these observations may originate from a finite range of temperatures. It is this method that will be used in the present work to derive active region models; more specifically the technique employed will be that first formulated by Batstone et al. (1970) and revised by Parkinson (1975c).

In deriving an expression relating the intensity of a spectral line to atomic and plasma parameters, the following assumptions will be made:

(1) The free electron energy distribution is Maxwellian.

(2) The plasma is in ionization equilibrium.

(3) Optical depth effects are negligible.

(4) The optically thin corona model (see section 2.4.3.3) is valid.

The discussions in sections 1.4, 2.3.2 and 2.4.3 show that for the spectral lines of interest here, and typical coronal conditions, the first three assumptions are likely to be valid, except possibly during flares. The validity of the fourth assumption will be examined later.

Considering the spectral line (energy) intensity I_{ij} due to electron radiative transitions from an excited energy level i to a lower level j in an ion, for constant electron temperature T_e, Equations 2.56 to 2.58 may be combined to give:

$$I'_{ij} = (4\pi L^2)^{-1} B_{ij} E_{ij} \int_V n_g n_e C_{gi} \, dV \qquad (4.1)$$

where: B_{ij}, the radiative branching ratio $= A_{ij} / \sum_{l<i} A_{il}$.

It is assumed that nearly all the ions are in the ground state g (McWhirter, 1965; Gabriel and Jordan, 1972), and therefore the total ion number density

$$n_{Z,z} \approx n_g \ . \qquad (4.2)$$

$n_{Z,z}$ may be expressed as:

$$n_{Z,z} = (n_{Z,z}/n_Z)\ (n_Z/n_H)\ (n_H/n_e)\ n_e \qquad (4.3)$$

or:

$$= A_{Z,z}\ A_Z (n_H/n_e)\ n_e$$

where: n_Z = the total element number density

$(n_{Z,z}/n_Z) = A_{Z,z}$

= the ion abundance relative to the element

$(n_Z/n_H) = A_Z$

= the element abundance relative to hydrogen (assumed to be constant in the corona).

For $T_e \gtrsim 2 \times 10^4$ K both hydrogen and helium are fully ionized and hence:

$$n_H = n_e / \left[1 + 2(n_{He}/n_H)\right] \ . \qquad (4.4)$$

Equations 4.1 to 4.4 may be combined to give:

$$I'_{ij} = (4\pi L^2)^{-1} B_{ij} E_{ij} A_Z \left[1 + 2(n_{He}/n_H)\right]^{-1} \int_V A_{Z,z} n_e^2 C_{gi} \, dV \ . \qquad (4.5)$$

Substituting the following numerical values in Equation 4.5:

$$L = 1 \text{ Astronomical Unit} = 1.496 \times 10^{13} \text{ cm}$$

$$(n_{He}/n_H) \approx 0.1$$

and using the Gaunt factor/oscillator strength approximation for C_{gi} (Equation 2.65):

$$I'_{ij} = 7.75 \times 10^{-43} B_{ij} a_{ij} A_Z f\bar{g} \int_V G(T_e) n_e^2 dV \text{ erg cm}^{-2} \text{ sec}^{-1} \tag{4.6}$$

where: $a_{ij} = E_{ij}/E_{gi} = \lambda_{ig} / \lambda_{ij}$

$G(T_e)$ = the emission function of the spectral line at electron temperature T_e

$$= A_{Z,z} T_e^{-\frac{1}{2}} \exp\left[-E_{gi} /(kT_e)\right] \quad K^{-\frac{1}{2}}$$

$$= A_{Z,z} T_e^{-\frac{1}{2}} \exp\left[-1.439 \times 10^8 /(\lambda_{ig} T_e)\right] K^{-\frac{1}{2}} .$$

The total intensity I_{ij} (erg cm^{-2} sec^{-1}) of the line, is then obtained by integrating I'_{ij} over T_e, i.e.

$$I_{ij} = \int_{T_e} I'_{ij} dT_e$$

$$= 7.75 \times 10^{-43} B_{ij} a_{ij} A_Z f_{gi} \bar{g}_{gi} \int_{T_e} \int_V G(T_e) n_e^2 dV \text{ erg cm}^{-2} \text{sec}^{-1} . \tag{4.7}$$

Assuming that n_e may be expressed as a function of T_e, Equation 4.7 may be rewritten:

$$I_{ij} = 7.75 \times 10^{-43} B_{ij} a_{ij} A_Z f_{gi} \bar{g}_{gi} \int_{T_e} G(T_e) S(T_e) dT_e \tag{4.8}$$

where: $S(T_e)$ = the volume emission measure of the plasma at electron temperature T_e

$$= \frac{d}{dT_e} \int_V n_e^2 \, dV \qquad \text{cm}^{-3} \text{ K}^{-1} .$$

Unless otherwise stated the term "emission measure" will be taken to mean "volume emission measure" (as opposed to "line-of-sight emission measure").

C_{gi} may also be given in terms of the temperature averaged collision strength (Equation 2.68), in which case:

$$I_{ij} = 4.87 \times 10^{-41} B_{ij} \lambda_{ij}^{-1} A_Z \bar{\Omega}_{gi} w_g^{-1} \int_{T_e} G(T_e) S(T_e) dT_e \qquad (4.9)$$

and:

$$\bar{\Omega}_{gi} = 0.0159\, \lambda_{ij} a_{ij} w_g f_{gi} \bar{g}_{gi} \quad . \qquad (4.10)$$

It may be noted that the effective collision strength defined by Tucker and Koren (1971) is:

$$\bar{\Omega}_{eff} = \bar{\Omega}_{gi} B_{ij} / w_g \qquad (4.11)$$

For the spectral lines to be considered here, the lower level j of the transition is the ground level g (thus $a_{ij} = 1$) and the upper level i decays solely by spontaneous radiation to g(i.e. $B_{ij} = 1$), and hence Equations 4.8 to 4.11 reduce to:

$$I = 7.75 \times 10^{-43} A_Z f \bar{g} \int_{T_e} G(T_e) S(T_e) dT_e \qquad (4.12)$$

$$I = 4.87 \times 10^{-41} \lambda^{-1} A_Z \bar{\Omega}_{eff} \int_{T_e} G(T_e) S(T_e) dT_e \qquad (4.13)$$

$$\bar{\Omega}_{eff} = 0.0159 \lambda f \bar{g} \qquad (4.14)$$

and the subscripts i, j, etc. may now be omitted. This simplification of the corona model is known as the two level ion model.

In selecting suitable lines for determination of the emission measure/temperature model the following guidelines are used:

(1) Reliable theoretical models are required for spectral intensities, i.e. in the present case the two level ion model is used.

(2) Reliable atomic data are required.

(3) The observed lines should be as strong as possible to minimise statistical uncertainties in the measured intensities.

(4) The lines should cover, between them, the whole temperature range likely to occur in the observed plasma.

(5) Reliable element abundances are required, and the selected lines should belong to the minimum number of different elements to minimise the effects of uncertainties in the abundances.

The terms 'reliable' and 'strong' used above, must be taken as being relative to the other lines observed in the spectrum. It is found thatthe lines which best fulfil the above criteria are the n = 2 $\rightarrow$ 1 resonance lines of H- and He-like ions, i.e.:

$1s.{}^2S_{\frac{1}{2}} - 2p.{}^2P_{\frac{1}{2},3/2}$ (Lyman α) in H-like ions,

and $1s^2.{}^1S_0 - 1s2p.{}^1P_1$ in He-like ions.

The lines to be used in the present analysis are those from the H-like ions O VIII, Ne X and Mg XII, and the He-like ions O VII, Ne IX and Mg XI.

The $\bar{g}f$ formulation will be used for the calculated intensity (Equation 4.12). The data required by Equation 4.12 and the validity of the two level ion model, for the selected transitions, will now be discussed.

4.2.1 Oscillator Strengths and Gaunt Factors

The oscillator strengths are taken from the compilations of Wiese et al. (1966, 1969), who estimate the uncertainties as $\lesssim$10%. The oscillator strengths are listed in Table 4.1.

For the temperature averaged Gaunt factor, Van Regemorter's (1962) value of $\bar{g} = 0.2$ is used, though this figure was carefully examined, as described below, in the light of improved atomic data, before being accepted. The check on the value of $\bar{g}$ follows the discussion of Parkinson (1975c), with slight differences in some numerical values.

Beigman et al. (1970) have calculated electron collisional excitation cross-sections for H-like ions, using the Coulomb-Born (CB) approximation; their estimated uncertainty is less than 30%. Tucker and Koren (1971) have derived temperature averaged collision strengths from these results and give the following approximate formula for the Lyα transition in H-like ions:

$$\bar{\Omega}_{CB} = 1.5/Z^2 \tag{4.15}$$

which, they estimate, agrees with the values of Beigman et al. to within 30%. Walker (1972) has listed temperature averaged collision strengths for the hydrogenic Lyα transition, derived from the Coulomb-Born-Oppenheimer (CBO) calculations of Burgess et al. (1970). For the ions and temperatures considered in the present work, Walker's results can be approximated by:

$$\bar{\Omega}_{CBO} = 1.9/Z^2 \tag{4.16}$$

to within $\pm$ 10%. Collision strengths $\bar{\Omega}_{gi}$ for higher levels of H-like ions and resonance transitions in He-like ions are obtained by scaling the Lyα collision strength $\bar{\Omega}_{Ly\alpha}$ according to the expression (Tucker and Koren, 1971):

$$\bar{\Omega}_{gi} = \bar{\Omega}_{Ly\alpha}(f_{gi}/f_{Ly\alpha})(E_{ij}/E_{gi}) \quad . \tag{4.17}$$

Equations 4.14 and 4.17 may now be combined with Equation 4.15 or Equation 4.16 to derive a Gaunt factor. For the $n = 2 \rightarrow 1$

resonance lines of H- and He-like ions, both the CB and CBO calculations give a Gaunt factor

$$\bar{g} = 0.2$$

to within $\pm$ 20%, thus supporting Van Regemorter's (1962) estimate.

These results are in close agreement with recent calculations performed, in the CB approximation, directly for He-like ions (Tully, 1974).

4.2.2 Ion Abundances

The ion abundances as a function of electron temperature have been derived by linear interpolation between the tabulated values calculated by Jordan (1969) for the solar atmosphere, (see Section 2.4.3.1). Jordan does not quote any estimated uncertainty for her results, but comparison with other ionization balance calculations (Allen and Dupree, 1969; Landini and Fossi, 1972; Summers, 1974) and reference to the discussion of ionization rates by Bely and Van Regemorter (1970), suggest that her values should be good to at least $\pm$ 50%; the relative values of ion abundance should be more accurate. The derived emission functions $G(T_e)$ are shown in Figure 4.1.

4.2.3 Element Abundances

The element abundances are properties of the coronal plasma itself, and therefore must be deduced either from the data being analysed or from other observations. Examination of the literature (e.g. Flower and Nussbaumer, 1975; Acton et al., 1975; Withbroe, 1971; Pagel, 1973) suggests that suitable values of the O, Ne and Mg abundances are (relative to H):

	A_Z (units of 10^{-5})
O	50
Ne	7
Mg	7

and it is these figures that will be assumed in the present analysis. The subject of element abundances, including the justification of the above values, will be discussed in more detail in Section 4.6.

4.2.4 Validity of the Two Level Ion Model

The two level ion model assumes that the upper level i of the transition (in the ion of net charge z) is populated wholly by collisional excitation from the ground state g and depopulated only by spontaneous radiative decay. Thus, in order to determine the applicability of this model, to the spectral lines being considered, it is necessary to examine the effect of other atomic processes that may be important in the coronal plasma (see e.g. Walker, 1972). Those considered here are radiative and dielectronic recombination, cascade, and spontaneous radiative decay from level i to levels other than g. Resonance line absorption (i.e. photoexcitation from g to i) has already been considered in Section 2.4.3.6, and its effects shown, in general, to be negligible for the transitions in question.

The relative importance of radiative recombination as a population mechanism for level i, may be examined by calculating the ratio R_{rc} of the rates of radiative recombination to direct collisional excitation to level i, i.e.:

$$R_{rc} = n_e n_{z+1} \alpha_{z+1,i} / (n_e n_z C_{z,gi}) \tag{4.18}$$

where the collisional excitation rate coefficient $C_{z,gi}$ is given by Equations 2.65 or 2.68, the radiative recombination rate coefficient $\alpha_{z+1,i}$ is taken from Bates and Dalgarno (1962) and Burgess (1964a), and the relative ion abundance (n_{z+1}/n_z) from Jordan (1969). For the ions, transitions and temperatures of interest here, it is found that R_{rc} is less than 0.02.

For a transition ij in the ion z, the process of dielectronic recombination (to be discussed in greater detail in Chapter 5) from ion z to z-1 may give rise to "satellite" lines near to the "parent" line ij; these satellite lines are due, in effect, to transitions ij in the presence of another outer excited electron. As the principal quantum number n, of this electron increases, the wavelength difference between the satellite and the parent line decreases. Hence, in general, some or all of the satellite lines will not be resolved from the parent line. The ratio R_{dc} of the dielectronic recombination to the collisional excitation contribution to a line is thus:

$$R_{dc} = \sum_{m} (\alpha_{z,i})_m / C_{z,gi} \tag{4.19}$$

where $(\alpha_{z,i})_m$ is the dielectronic recombination rate coefficient for the satellite line m and the summation is over all satellites not resolvable from the parent line. The calculations of Tucker and Koren (1971), Gabriel (1972a) and Bhalla et al. (1975) show that, for the present work $R_{dc} \lesssim 0.1$. In addition, for the SL1101 and SL1206 spectra, the satellite lines $1s^2nl - 1s2pnl$ can generally be resolved from the He-like resonance line $1s^2.{}^1S_0 - 1s2p.{}^1P_1$, for $n \leqslant 4$ (see Chapter 5). Hence, in these cases R_{dc} should be considerably less than 0.1.

The satellite lines to the lines of an ion z, may also be formed by inner-shell excitation in the ion z-1. At present, the only calculations available for the rate coefficients of these inner-shell excitations, are those of Gabriel (1972a) and Bhalla et al. (1975) for the satellites of the type $1s^2 2l - 1s2l'2l$ to the He-like ion lines $1s^2 - 1s2l'$. The results of Bhalla et al. (1975) show that for these satellite lines and the ions of interest here, the total intensity due to inner-shell excitation is about an order of magnitude less than the intensity due to dielectronic recombination.

"Cascade" is the excitation from the ground state to a level i via an intermediate level above i. Bely (1968) and Mewe (1972b) have estimated that for the resonance lines of H- and He-like ions, the ratio of cascade excitation to direct excitation from the ground state is about 6%.

Thus, we have examined the processes that under coronal conditions might be expected to increase the intensities of the H- and He-like resonance lines, above those predicted by the two level ion model; it is seen that the total increase should not exceed 20% and is probably about 10%. The radiative branching ratio for these transitions is effectively unity (see e.g. Wiese et al., 1966, 1969); thus at coronal densities, the upper levels of these transitions are depopulated solely by spontaneous radiative decay to the ground state (Gabriel and Jordan, 1969b, 1972; Hutcheon and McWhirter, 1973).

4.2.5 Calculation of Emission Measure/Temperature Models

The method of Batstone et al. (1970) replaces the integral over electron temperature in Equation 4.12 by a summation over finite temperature intervals ΔT_e. Hence, for a spectral line i, Equation 4.12 becomes:

$$I_i = 7.75 \times 10^{-43} A_{Z,i} f_i \bar{g} \sum_{j=1}^{m} G_i(T_{e,j}) S(T_{e,j}) \qquad (4.20)$$

where: $G_i(T_{e,j}) = A_{Z,z,i} T_{e,j}^{-\frac{1}{2}} \exp\left[-1.439 \times 10^8/(\lambda_i T_{e,j})\right]$

$$S(T_{e,j}) = \Delta T_e^{-1} \int_V n_e^2 \, dV$$

$$\Delta T_e = T_{e,j+1} - T_{e,j}$$

$$i = 1, 2, 3, \ldots\ldots n.$$

Thus, the measured intensities of a set of n lines may be used to derive the emission measure $S(T_{e,j})$ in each of a set of m temperature intervals $(T_{e,j} \pm \frac{1}{2}\Delta T_e)$, where $m \leqslant n$. Equation 4.20 represents a set of n simultaneous equations in m unknowns. A least squares method is used to solve this system of equations. The criterion used to measure the "goodness of fit" between the measured intensities I_m (derived from Equation 3.10) and the calculated intensities I_c (derived from Equation 4.20), is:

$$D^2 = \sum_{i=1}^{n} w_i (I_{m,i} - I_{c,i})^2 \qquad (4.21)$$

where: w_i = weighting factor, in this case = $(\delta I_i)^{-2}$

δI = total uncertainty in intensity

and the goodness of fit parameter D^2 decreases as the fit improves. The physically reasonable constraint that $S(T_{e,j})$ should be zero or positive for all values of electron temperature is imposed to avoid physically absurd solutions. It is not suggested that the final values of $S(T_{e,j})$ which are accepted as a "good" model, correspond to an absolute minimum in D^2 but the individual values of $\left| I_{m,i} - I_{c,i} \right|$ are, in general, within the error limits δI_i .

4.3 The Emission Measure / Temperature Models for Regions 11619, 12628 and 12624

Here, the following values are used:

$T_{e,1} = 2.0 \times 10^6$ K

$\Delta T_e = 1.0 \times 10^6$ K

m = 4 for regions 11619 and 12628

m = 5 for region 12624

n = 6 for regions 12828 and 12624

n = 5 for region 11619 (Mg XII Lyα is not observed).

The minimum temperature interval ($T_{e,1} \pm\frac{1}{2}\Delta T_e$) is chosen so that its lower bound corresponds to the minimum coronal temperature of about 1.5×10^6 K (e.g. Jordan, 1966a; Flower and Nussbaumer, 1975). The maximum temperature interval ($T_{e,m} \pm\frac{1}{2}\Delta T_e$) is established from (1) the minimum value required to explain the observed line intensities, and (2) the maximum value allowed by the absence of emission from the 1s - 2p resonance lines of Si XIV and S XV, and additionally, for region 11619, from Mg XII and Si XIII.

The emission measure/temperature models derived from the SL1101 observations of region 11619 and the SL1206 observations of regions 12624 and 12628 are given in Table 4.2. The measured and calculated intensities of the lines used to construct the models, are listed in Table 4.1.

In all three models the bulk of the emission measure occurs at $T_e \sim (2 \text{ to } 3) \times 10^6$ K, with some material extending up to $T_e \sim 5 \times 10^6$ K. The main difference between these active region models is the presence in region 12624, of material at $T_e \approx 6 \times 10^6$ K. This might be expected in view of the decaying flare. The flare activity is manifested in the enhanced intensities of the higher temperature lines, notably Mg XII, Si XIII, Fe XVIII and Fe XIX.

4.4 Comparison of Active Region Models through Solar Cycle 20

With the analysis of the SL1101 and SL1206 spectra, emission measure/temperature models of coronal active regions, from Leicester observations, are now available covering most of solar activity Cycle 20, from August 1966 to November 1973 (see Table 1.4). Therefore, it may be considered an opportune time to compare these results and attempt to identify any systematic trends.

All the models presented are of non-flaring active regions, with the exception of region 12624 (see Section 3.3.2).

To circumvent possible differences in the instrumental efficiencies, atomic data and element abundances used in the analysis of data from different flights, the present comparison will be concerned only with the gross features of the models, and not with small differences. These remarks apply particularly to the earlier observations (Evans and Pounds, 1968; Batstone et al., 1970; Evans, 1970; Parkinson, 1971a), where the values of crystal integrated reflectivity used, differ by up to a factor ~ 2 from more recent measurements (Leigh and Evans, 1975). However, in the case of the more recent observations, from SL1101 and SL1206, the spectra of regions 11619, 12628 and 12624 have all been analysed in a self-consistent manner (see Sections 4.2 and 4.3 above), and the spectrum of region ~~12628~~ 11621 has been analysed in a very similar way (Parkinson, 1975c).

All the active region models are shown in Figure 4.2. Table 4.3 gives the date and time of each set of observations. The models derived from the SL304 data (Evans and Pounds, 1968) are omitted as the spectral ranges observed did not include lines which would provide a decisive test for the presence of plasma at $T_e \gtrsim 5 \times 10^6$ K.

All the active region spectra obtained by the collimated crystal spectrometers (S69, SL1101, SL1206) are used in Section 4.6 to determine element abundances in the corona. Therefore, the model for region 11060, derived by Parkinson (1971a), is revised here, in the light of the more accurate measurements of crystal integrated reflectivity (Leigh and Evans, 1975), and using the atomic data and element abundances discussed in the preceding Sections. The silicon abundance is required in the analysis; this is taken as $A_Z(Si) = 7 \times 10^{-5}$, and justified in Section 4.6. Both the original and revised models are given in Table 4.5. Table 4.4 lists the spectral lines used in determining the model, together with their recorded counts, and the revised measured and calculated intensities.

When comparing the active region models it should be noted that the spectrometer field-of-view response function (i.e. the collimation) is not the same for all observations (see Table 1.4), and that for SL1101 (regions 11621 and 11619) the centres of the active regions were probably not viewed at maximum collimator transmission efficiency. Also, the X-ray emission is known to be correlated with the stage of development and magnetic configuration of an active region (Parkinson and Pounds, 1971; Parkinson, 1973b), however this may be taken into account, to some extent at least, by comparison of different active regions observed on the same flight.

Figure 4.3 relates the date of each set of observations to the phase of the solar activity cycle, as indicated in this case by the Zurich Sunspot Numbers (Solar Geophysical Data, 1975).

On the basis of the information summarized in Figures 4.2 and 4.3, and subject to the cautionary remarks given above, the following <u>tentative conclusions</u> are drawn, concerning coronal active regions:

(1) The emission measure at a given temperature in a coronal active region appears to increase with the general level of solar activity.

(2) The bulk of the emission for each active region occurs at $T_e \sim (2 \text{ to } 3) \times 10^6$ K.

(3) In all cases, there is significant material up to at least $T_e \sim 5 \times 10^6$ K.

In view of the small number of samples available a more detailed comparison is not felt to be justified. It is hoped that, in the next solar cycle (number 21), X-ray spectra will be obtained frequently, and have at least the quality associated with the SL1101 and SL1206 observations, to provide data for much more detailed study. In order to gain the maximum amount of information, simultaneous high resolution images will also be required (c.f. Section 4.5 below).

4.5 Correlation of the SL1206 Spectra and S-054 Images for Regions 12628 and 12624

4.5.1 Introduction

In order to achieve the maximum sensitivity, observations of the coronal soft X-ray emission have tended to have either high spatial resolution with low spectral resolution or high spectral resolution with a moderate spatial resolution. The instruments normally used have been grazing-incidence telescopes with broadband filters, to obtain the high spatial resolution images with spectral information, and mechanically collimated Bragg crystal spectrometers to give the high resolution spectra.

The separate imaging and spectral data have shown that in order to obtain the maximum information on coronal conditions, simultaneous observations having both high spatial and high spectral resolution are required. Davis, Gerassimenko, Krieger and Vaiana (1975, hereafter referred to as DGKV) have reported the first set of such measurements using the S-054 X-ray telescope and a rocket-borne crystal spectrometer having a field of view of

45 x 45 (arc sec)^2 FWHM. The spectrometer viewed a small portion of an active region; this was shown, both by the spectra and the images, to be nearly isothermal (to within about $\pm$ 0.5 x 10^6 K). DGKV showed that in order to diagnose correctly the coronal plasma parameters and to avoid ambiguities in the interpretation of the data, it was necessary to obtain simultaneous high spectral and high spatial resolution measurements.

Here, new sets of simultaneous soft X-ray spectrometric and imaging observations of the corona, are presented; these measurements are the SL1206 spectra and S-054 images, of regions 12628 and 12624.

4.5.2 The SL1206 Spectra

There were two principal reasons for the choice of spectrometer collimation at 3 x 3 (arc min)^2 FWHM (i.e. 6 x 6 (arc min)^2 full field-of-view); these were (1) to achieve the required sensitivity, and (2) the field-of-view is sufficient to enclose a typically sized active region, thus allowing diagnosis of the temperature structure of the whole coronal active region.

The determination of the emission measure/temperature models for regions 12628 and 12624 has already been discussed in Sections 4.2 and 4.3.

4.5.3 The S-054 Images

The method of analysing the images in terms of effective temperature T_{eff} and line-of-sight emission measure Y as a function of position on the solar disk, has been described in Section 3.4.3.

Figure 4.4 shows X-ray images of the Sun taken by the S-054 telescope at the time of the SL1206 rocket flight and upon which have been superimposed the spectrometer field-of-view. The X-ray images may be compared with Figure 4.5, an Hα photograph taken by Carnarvon Observatory, W. Australia, about five hours earlier. In Figure 4.4 it can be seen that region 12628 consists of a set of low loops connecting the leading and following portions of the region, together with some higher loops connecting with surrounding areas. It appears from Figure 4.5 that the underlying chromospheric network is aligned along the connections. Figure 4.6 is a solar white-light photograph taken at Carnarvon within 15 minutes of the Hα exposure; the leading and following sunspot umbrae and penumbrae are clearly seen for region 12628, while region 12624 shows no visible sunspots. With regard to region 12628, from comparison of the X-ray, Hα and white-light photographs, and photospheric magnetograms (Figure 4.7), it appears that the opposite footpoints of the (X-ray emitting) coronal loops joining the leading and following portions of the active region are (as near as can be judged) coincident with the photospheric sunspots.

The quantitative analysis presented here utilizes S-054 X-ray images taken through two different filters with effective bandpasses of 2 to 17 Å (filter 1), and 2 to 32 and 44 to 54 Å (filter 3) (see Figure 3.15) to obtain values of the deposited energy and hence the SHI. The two energy contour maps of Figure 4.8(a) and (b) show active region 12628 observed through filters 1 and 3, after deconvolution and with the spectrometer's field-of-view superimposed. Figures 4.9(a) and (b) are the effective spectrometer images which result from multiplying the deconvoluted image at each point by the SL1206 collimator directional response function, shown in Figure 4.10. Figures 4.11 and 4.12 are the corresponding energy maps for region 12624.

Figures 4.13 and 4.14 are contour maps of T_{eff} for regions 12628 and 12624, respectively. It is found that over the whole of each active region (i.e. wherever there is significant X-ray emission) there are only relatively small variations of T_{eff} with position. The range of T_{eff} for each active region is:

Active Region No	Range of T_{eff} (10^6 K)
12628	2.7 ± 0.5
12624	5.5 ± 1.5

Using the deconvoluted energy image from one filter and the values of T_{eff}, it is possible to calculate the effective line-of-sight emission measure Y for each picture element, as shown in Figures 4.15 and 4.16 for region 12628. Then, if either (1) the line-of-sight path length l, or (2) a functional relationship between n_e and l, is known, the electron density n_e may be calculated as a function of position in the active region. The latter method was employed by DGKV; here, the first technique is used to derive electron densities for region 12628.

From the X-ray imaging data, region 12628 can be resolved into a number of X-ray emitting loops. These loops are assumed to have a circular cross-section, and hence an r.m.s. value of electron density

$$n_{rms} = \left[l^{-1} \int_l n_e^2 \, dl \right]^{\frac{1}{2}} = (Y/l)^{\frac{1}{2}} \qquad (4.22)$$

can be computed for each cross-section. Since n_{rms} is found to be approximately constant for any given loop, the average value $\bar{n}_{rms}$ for each loop, is computed.

Figure 4.17 shows the model of region 12628 derived from the imaging data. The shaded areas represent the approximate extent of the X-ray emitting loops, and the line along the middle of each loop indicates the approximate position of the maximum intensity. The average electron density $\bar{n}_{rms}$ is given for each loop and the loops are numbered for convenience. The field of view of the SL1206 spectrometer is also marked.

The S-054 data show that the flare which started in region 12628 shortly after the SL1206 observations, occurred in the small loop, # 7, the loop of highest density ($\bar{n}_{rms}$ = 8 x 10^9 cm^{-3}).

The three-dimensional structure of region 12628 (Figure 4.18.ii)has been estimated from S-054 X-ray images obtained between 19 and 27 November, as the region appeared over the Sun's east limb and travelled across the disk (Figure 4.18.i). Neither these observations nor those reported at other wavelengths (Solar Geophysical Data, 1974), indicate any substantial restructuring of the active region from its emergence over the east limb until the 26 November. A qualitative analysis of the limb data indicates that the line-of-sight temperature T_{eff} appears to increase towards the central and lower-lying part of the active region.

4.5.4 Agreement between the Spectral and Imaging Results

In order to relate the results by the two measurement techniques, two effective SHI's are defined:

$$SHI_I = \left[\sum_{x,y} E_3(x,y)C(x,y)\right] / \left[\sum_{x,y} E_1(x,y)C(x,y)\right] \quad (4.23)$$

$$SHI_S = \left[\sum_{T_e} S(T_e)F_3(T_e)\right] / \left[\sum_{T_e} S(T_e)F_1(T_e)\right] \quad (4.24)$$

where $E_n(x,y)$ is the deconvolved energy per picture element obtained through filter n, C(x,y) is the spectrometer collimator response function, $S(T_e)$ is the volume emission measure derived from the spectral intensities and $F_n(T_e)$ is the FSI for filter n.

In order to provide a proper comparison of the two analyses, the same element abundances must be used in both cases. For the present purposes it is adequate, and more convenient, to take the values used in the imaging analysis, namely: $A_Z(O) = 3.1 \times 10^{-4}$, $A_Z(Ne) = 4.0 \times 10^{-5}$, $A_Z(Mg) = 3.1 \times 10^{-5}$. The resulting emission measure/temperature models, from the SL1206 spectra, are given in Table 4.6 (Gerassimenko, 1975). A study of coronal element abundances from Leicester Bragg spectrometer data (Section 4.6) leads to the conclusion that these values should be changed somewhat, but the changes are not large enough to have much effect on the present work.

Under perfect conditions SHI_I and SHI_S would be equal. Thus, their actual values will show the measure of agreement between the imaging and spectral data. The values obtained and the corresponding effective temperatures are:

Active Region No	SHI_I	SHI_S	$T_{eff,I}$	$T_{eff,S}$
			$(10^6$ K)	
12628	12	13	2.85	2.73
12624	6	10	5.6	3.1

After consideration of the uncertainties involved and the temperature dependence of the SHI (Figure 3.17), there is seen to be excellent agreement for region 12628 and acceptable agreement for region 12624.

In order to test fully the consistency between the two types of data, it is necessary to compare, in addition to relative quantities as above, absolute values such as intensity and emission measure. To this end, the following quantities, ('effective recorded energies') are defined:

$$E_{In} = \sum_{x,y} E_n(x,y)\ C(x,y) \qquad (4.25)$$

$$E_{Sn} = A/(4\pi f^2 \ \Delta A') \sum_{T_e} S(T_e)\ F_n(T_e) \qquad (4.26)$$

where A and f are, respectively, the geometrical collecting area and focal length of the telescope, and $\Delta A'$ is the projected area (in cm^2), at the Sun, corresponding to one picture element (i.e. $\Delta A' = 2.11 \times 10^{16}\ cm^2$). As in the case of the effective SHI's, under ideal conditions the 'effective recorded energies' E_{In} and E_{Sn} would be equal, and their actual values will show the measure of agreement between the two data sets. The comparison may also be made in terms of 'effective volume emission measures' derived directly from E_{In} and E_{Sn}, i.e.:

$$S_{In} = (4\pi f^2 \Delta A'/A)\ E_{In} \ /\ F_n(T_I) \qquad (4.27)$$

$$S_{Sn} = (4\pi f^2 \Delta A'/A)\ E_{Sn} \ /\ F_n(T_S) \qquad (4.28)$$

where T_I and T_S are the electron temperatures calculated from SHI_I and SHI_S, respectively. The values obtained for the effective energies and emission measures are, for filter 1:

Active Region No.	E_{I1}	E_{S1}	S_{I1}	S_{S1}
	(10^{-4}erg $cm^{-2}sec^{-1}$)		($10^{48}\ cm^{-3}$)	
12628	2.1	0.43	2.4	0.5
12624	8.6	0.47	1.9	0.4

Thus there is seen to be rather poor agreement when the images and spectra are compared from the point of view of absolute intensities. The thermal analysis of the S-054 images finds more flux (by nearly a factor 5) than can be accounted for by thermal analysis of the SL1206 spectra. This is a somewhat larger difference than is permitted by the most pessimistic view of the combined calibration uncertainty, which might allow a factor 2 discrepancy between E_{In} and E_{Sn}. The discrepancy is in the same direction, and of about the same magnitude, as that found in a similar analysis by DGKV. However in that case the spectrometer field-of-view was much smaller (45 x 45 (arc sec)^2 FWHM) and a small uncertainty in the pointing might have been sufficient explanation. In the present case the spectrometer pointing direction is known (from three independent measurements - the vehicle attitude control unit, the visible light cine camera and the X-ray pin-hole camera array) with an uncertainty of a small fraction of the collimator field, and thus this explanation can be excluded. Similarly, because the spectrometer field is large, the flux comparison is made after integration of the S-054 data over a large area of the image. Because of this, the comparison is almost independent of any plausible error in the deconvolution of the telescope point response function. In this present case this explanation can also be excluded. Indeed, the discrepancy persists even if no deconvolution is made. Two other fundamental explanations may be examined:

The telescope measures the total power in line and continuum spectra. The spectrometer measures the line spectrum only (it is relatively very insensitive to continuum radiation), and the derived emission measure/temperature model must be used to calculate the corresponding continua that must be added to the line flux before comparison with the telescope flux. The Tucker and Koren (1971) model was used for this calculation; but the resulting continuum is only about 20% of the line flux. The tabulations of Mewe (1972a) give approximately the same value. However, there do not appear to be any measurements which explicitly check these calculations. Thus if the Tucker-Koren and Mewe models underestimate the continuum power this would reduce the discrepancy. A direct check is possible with a suitably arranged Bragg spectrometer, and special attention will be given to this matter in future Leicester and ASE coronal observations.

Second, because the entire quantitative interpretation of both sets of data is based on expressions which describe the behaviour of a thermalised plasma, any non-thermal processes in the source are likely to disturb the comparison. There is no clear evidence in the data for significant non-thermal processes in either region 12628 or region 12624 at the time of observation.

Although this discrepancy in recorded flux and hence in emission measure, is a matter of some concern, it is in fact of little significance to the interpretation, that follows, of the (thermalised) coronal conditions in region 12628, since the main significance of the emission measure determination is in the electron densities that may then be derived. The factor 2.2 (from the geometrical mean of S_{I1} and S_{S1}) uncertainty in emission measure corresponds to only a factor 1.5 uncertainty in electron density. This is small compared with other factors, such as the uncertainty in determining the three-dimensional structure of the active region.

4.5.5 Comparison of the Spectral and Imaging Models for Region 12628 and a Combined Model

The emission measure/temperature model for region 12628 (Tables 4.2 or 4.6), derived from the spectral intensities, shows that the X-ray emitting plasma is multi-thermal with most of the emission measure at $T_e \sim (2 \text{ to } 3) \times 10^6$ K but with significant emission measure up to $T_e \sim 5 \times 10^6$ K. This is in contrast to the imaging analysis which gives the effective line-of-sight temperature T_{eff} as approximately (2 to 3) x 10^6 K, over the whole active region, and no values of $T_{eff} \gtrsim 3.2 \times 10^6$ K (Figure 4.13).

Figure 4.15 shows that most ($\sim$90%) of the X-ray emission observed by the SL1206 spectrometers came from the central part of the active region (diameter $\sim$ 2.5 arc min; loops # 2,3,4 and 5 in Figure 4.17). Therefore it is concluded that the hotter ((3 to 5) x 10^6 K) plasma is in the central portion of the active region, either as unresolved structure within the observed loops or as separate hot loops masked by the cooler loops. In addition, the imaging analysis shows that T_{eff} tends to increase towards the centre of the active region.

In order to illustrate the above discussion, the spectral and imaging models have been combined, in a very idealised manner, to form the model shown in Figure 4.19. The important parameters of the model are given in Table 4.7.

This model is tentatively proposed as 'typical' of a bipolar active region near solar cycle minimum and which may be compared with the 'typical' solar maximum model of Parkinson (1973c) (Figure 4.20 and Table 4.8). It is found that the dimensions of the active regions and the temperature range of the plasma are approximately the same in both cases, but the emission measures in the present case are much lower than in Parkinson's model. This implies that in the solar maximum model the numbers or diameters of the X-ray emitting loops are greater or the electron density is higher. However, Parkinson derives values of electron density very similar to those in our own model, but as he had insufficient spatial resolution to observe individual loops, his electron densities represent values averaged over larger volumes than in the present work. Conversely, it is clear from Figure 4.17 that if region 12628 had been observed with a lower resolution, the derived densities would have been less.

4.5.6 Comparison of the Spectral and Imaging Models for Region 12624

The imaging analysis for region 12624 gives line-of-sight temperatures T_{eff} down to $\approx 4 \times 10^6$ K (Figure 4.14), while the spectral line intensities indicate that most of the emission measure is at $T_e \approx (2$ to $3) \times 10^6$ K. Therefore it must be assumed that, as in region 12628, the different temperature components are mixed in the line-of-sight.

Due to its compactness it has not been possible to resolve region 12624 into individual X-ray emitting loops.

4.5.7 Possible Time Variations in the X-ray Emission from Region 12624

Since the SL1206 and S-054 instruments observed region 12624 during the decay phase of a flare, the possible time dependence of the X-ray emission must be examined. Table 4.9 gives the times of important events, for both regions 12624 and 12628, during (and shortly before and after) the SL1206/S-054 observing programme.

From the data recorded in the 8 to 20 Å wavelength band by the Solrad 9 satellite, Gerassimenko (1975) has estimated an e-folding decay time of $\sim$ 3000 sec, for the flare in region 12624. Kahler of ASE has shown that, in general, the X-ray emission recorded through S-054 filter 1 follows very well the 8 to 20 Å Solrad data (Gerassimenko, 1975). This implies a correction of about 12% to the measured SHI, i.e. the measured SHI(= Q_{31}, see Section 3.4.3) must be multiplied by 1.14. This correction is included in the imaging analysis presented here.

If it is assumed that a similar relaxation time of $\approx$3000 sec applies to the intensities of the individual spectral lines observed by SL1206 in the wavelength range $6.5 \lesssim \lambda \lesssim 22$ Å, then the relative change in line intensity during the time taken for a complete spectral scan (i.e. one fast and one slow scan) is $\lesssim 5\%$. This is consistent with two successive observations of the Mg XII Lyα line by the SL1206 ADP spectrometer, where the measured intensity ratio is

$$\frac{I(t = \text{launch} + 408\ \text{s})}{I(t = \text{launch} + 380\ \text{s})} = 1.4 \pm 0.4 \quad .$$

4.5.8 Discussion and Conclusions

Models have been derived for two coronal active regions using simultaneous high spectral and high spatial resolution observations at soft X-ray wavelengths.

It has been shown that measurements having both of these attributes are required in order to be able to study correctly the properties of the solar corona, and of active regions in particular. Observations made only with high spectral resolution or only with high spatial resolution, can lead to misinterpretation of the data, when attempting to derive physical models for the emitting plasma.

The results obtained by the two techniques have been combined to give a model of a coronal active region near to solar minimum. The X-ray emitting plasma is confined to closed loop-like structures by the bipolar magnetic field of the active region. The electron temperature and density are specified as functions of position; they increase towards the centre of the active region (i.e. the smaller, lower lying loops are, in general, hotter and more dense).

The model has been compared with that of Parkinson (1973c) for an active region close to solar maximum, and it is found that the latter model has a much greater emission measure, though the overall spatial extents and temperature are similar in both cases.

The properties of the present active region model are in general agreement with models derived by other workers, both from observations at various wavelengths (reviewed by Jordan, 1975a) and calculations (Jordan, 1975b; Landini and Fossi, 1975).

Region 12628 was also the subject of observation by the Harvard S-055 EUV spectroheliometer on ATM, in emission lines which are characteristic of electron temperatures from about 10^4 K to about 2×10^6 K, i.e. generally cooler than the temperatures to which the SL1206 and S-054 instruments are most sensitive. Foukal (1975) has given a partial description of these measurements, and, while it has not been possible, using that paper, to perform a detailed correlation of the EUV and X-ray data, it is hoped that there will be opportunity for joint study of region 12628 by Leicester, ASE and Harvard.

4.6 Determination of Chemical Element Abundances in the Solar Corona

In the present section, all the Leicester collimated crystal spectrometer observations of solar active regions are used to derive the relative abundances of the elements O, Ne, Na, Mg, Al, Si, Fe and Ni in the corona. The analysis therefore involves the intensities of selected lines of these elements, measured in the spectra of regions 11060, 11619, 11621, 12624 and 12628, by flights S 69, SL1101 and SL1206. The measurements used are restricted to those taken by collimated spectrometers, because of the difficulty with uncollimated observations, in general, of deriving accurate spectral line intensities from the data, which is a convolution of the spectral and spatial intensity distributions for the whole solar disk.

It is assumed that, to within say $\sim \pm 10\%$, the element abundances under consideration are constant in space and time, in the corona, and hence the values derived, for each element, from the various sets of data mentioned above, may be combined to give a 'best estimate' abundance.

It is not possible, from coronal X-ray line intensity measurements alone, to derive the abundance A_Z of an element relative to hydrogen; therefore, the abundances obtained here are strictly values relative to one another, i.e.:

$$O:Ne:Na:Mg:Al:Si:Fe:Ni.$$

Since these abundances will, on occasion (e.g. in the construction of emission measure/temperature models), be required relative to hydrogen, the normalisation

$$A_Z(O) = 5.0 \times 10^{-4}$$

is employed; examination of the literature (e.g. Pottasch, 1967; Withbroe, 1971; Pagel, 1973) suggests that this is a reasonable value to take. In principle, the measured X-ray continuum intensity may be used to derive element abundances relative to hydrogen, but to date, no very satisfactory results have been obtained (Walker, 1972; Walker et al., 1974a,b).

4.6.1 The Abundances of O, Ne, and Mg

The abundance ratios O:Ne and Ne:Mg are derived by a method which is not strongly dependent on the emission measure/temperature model for the observed plasma.

From Equation 4.20, the energy intensity ratio of two spectral lines i and k for which the two-level ion model is valid, is:

$$I_i/I_k=(f_i/f_k)(A_{Zi}/A_{Zk}) \left[\sum_{j=1}^{m} S(T_{ej})G_i(T_{ej})\right] / \left[\sum_{j=1}^{m} S(T_{ej})G_k(T_{ej})\right] \qquad (4.29)$$

If, over the temperature range where lines i and k have significant emission, the ratio of the emission functions

$$G_i(T_e)/G_k(T_e)$$

is approximately constant, then Equation 4.29 may be rewritten:

$$I_i/I_k = (f_i/f_k)(A_{Zi}/A_{Zk}) \left[G_i(T_e)/G_k(T_e)\right]_{eff} \qquad (4.30)$$

or:

$$A_{Zi}/A_{Zk} = (I_i/I_k)(f_k/f_i) \left[G_k(T_e)/G_i(T_e)\right]_{eff} \quad . \qquad (4.31)$$

It is found that suitable pairs of lines are the Lyα line of a H-like ion of nuclear charge Z and the $1s^2.{}^1S_0$ - $1s2p.{}^1P_1$ resonance line of the He-like ion of nuclear charge Z + 2, e.g. O VIII and Ne IX, Ne X and Mg XI, and Mg XII and Si XIII. The ratios of the emission functions for each of these pairs of lines, are plotted in Figure 4.21. It is seen that there exists a plateau - a temperature range over which the variations in emission function ratio are relatively small.

When estimating the temperature range for significant emission, it is the product

$$S(T_e)G(T_e)$$

that is the important quantity, i.e. the upper and lower temperature limits (T_{eu} and T_{el} respectively) for significant emission from a line, are determined from the criterion:

$$\int_{T_{el}}^{T_{eu}} S(T_e)\, G(T_e)\, dT_e \approx \int_0^{\infty} S(T_e)\, G(T_e)\, dT_e \quad . \tag{4.32}$$

In order to estimate these limits, it is noted that:

(1) The minimum coronal temperature is about 1.5×10^6 K (e.g. Jordan, 1966a; Flower and Nussbaumer, 1975).

(2) Published values of abundances relative to hydrogen, for the coronal abundant elements ($A_Z \gtrsim 10^{-5}$), are generally in agreement to within a factor 2 or 3 (e.g. Withbroe, 1971; Pagel, 1973).

Thus, for the measurements considered here, the following values may be determined:

(a) for O VIII Lyα and Ne IX $1s^2.{}^1S_0 - 1s2p.{}^1P_1$
$T_{el} \approx 1.5 \times 10^6$ K, $T_{eu} \approx 6 \times 10^6$ K

(b) for Ne X Lyα and Mg XI $1s^2.{}^1S_0 - 1s2p.{}^1P_1$
$T_{el} \approx 3 \times 10^6$ K, $T_{eu} \approx 7 \times 10^6$ K .

The corresponding ranges of emission function ratios $G(T_e$, H-like): $G(T_e$, He-like), are:

1.64 ± 0.69 for O VIII : Ne IX,

1.12 ± 0.22 for Ne X : Mg XI.

Equation 4.31 then gives the element abundance ratios O:Ne and Ne:Mg to within about $\pm$ 40% and $\pm$ 20% respectively; these ratios are approximately:

O:Ne:Mg 7:1:1.

Hence, with corresponding uncertainties, an emission measure/ temperature model may be determined for each set of observations. This model permits a more precise calculation of

$$S(T_e)\, G(T_e)$$

as a function of T_e, and thus the most appropriate temperature at which to evaluate

$$\left[G_i(T_e) \,/\, G_k(T_e)\right]_{eff}$$

may be chosen.

The intensity ratios and the abundance ratios derived from them, for each set of observations, are listed in Table 4.10. The uncertainty quoted for each abundance ratio is the standard deviation in the value, taking account only of the Poissonian counting errors on the measured spectrum. Table 4.10 also gives the arithmetic mean of the abundance ratio for each pair of elements, O/Ne and Ne/Mg. The mean abundance ratios, i.e.:

$$\mathrm{O:Ne} = 6.0 \pm 0.8$$

$$\mathrm{Ne:Mg} = 0.65 \pm 0.14$$

are taken as the best estimated values from the observations. These figures are in reasonably close agreement with the element abundances used in Sections 4.2 and 4.3 to derive active region emission measure/temperature models.

It should be noted that the abundance ratio Mg:Si cannot, for the measurements presented here, be derived by a method similar to that described above, because the "plateau" in the emission function ratio of Mg XII Lyα to Si XIII $1^1S_0 - 2^1P_1$ (see Figure 4.21), occurs above the high temperature cut-off in emission measure for the active regions observed.

4.6.2 The Abundances of Na, Al, Si, Fe and Ni

For each set of observations, the abundances of Na, Al, Si, Fe and Ni are derived from the emission measure/temperature model and the measured intensity of a resonance line of each of these elements. The spectral lines used are the $1s^2.{}^1S_0 - 1s2p.{}^1P_1$ transition in He-like Na X, Al XII and Si XIII, and the $2p^6.{}^1S_0 - 2p^53d.{}^1P_1$ transition in Ne-like Fe XVII and Ni XIX.

The two-level ion model has been justified for the He-like lines in question (see Section 4.2.4), while Loulergue and Nussbaumer (1973, 1975a) have shown that it is a good approximation for the $2p^6.{}^1S_0 - 2p^53d.{}^1P_1$ resonance lines in Fe XVII and

Ni XIX. Hence, Equation 4.20 may be used to calculate the abundances of the elements concerned. It must be emphasised that the values obtained are relative to the abundances of O, Ne, and Mg used in constructing the emission measure/temperature models. The emission functions are calculated, as in Section 4.2.2, from the ion abundances of Jordan (1969); for Na and Al the ion abundances are derived by isoelectronic interpolation between Jordan's values for Ne and Mg, and Mg and Si, respectively. The oscillator strengths of the $1\,^1S_0 - 2^1P_1$ transitions in Na X, Al XII and Si XIII, are taken from Wiese et al. (1966, 1969), by isoelectronic interpolation/extrapolation in the case of Na and Si. The oscillator strength of the $2p^6.{}^1S_0 - 2p^53d.{}^1P_1$ transition in Fe XVII is taken from Froese (1967), and the corresponding figure for Ni XIX is obtained by isoelectronic interpolation between the tabulated values of Kastner et al. (1967). For this transition in Fe XVII and Ni XIX, the calculated collision strengths of Bely and Bely (1967) and Loulergue and Nussbaumer (1975a) show that a temperature averaged Gaunt factor,

$$\bar{g} = 0.2$$

is appropriate (c.f. Equation 4.14).

The Na X $1s^2.{}^1S_0 - 1s2p.{}^1P_1$ resonance line at 11.003 Å is blended with the Ne IX $1s^2.{}^1S_0 - 1s4p.{}^1P_1$ resonance line at 11.000 Å (the wavelengths are calculated from Ermolaev and Jones, 1974). Therefore, in order to calculate the Na abundance from the intensity of the Na X transition, it is necessary first to subtract the predicted intensity of the Ne IX transition from the total intensity of the blend at 11.00 Å (see Table 4.11 and Section 5.2).

The measured line intensities and the element abundances derived from them, for each set of observations, are listed in Table 4.11, together with the oscillator strength for each spectral line. The uncertainty quoted for each abundance value is the standard deviation, due to the statistical uncertainty in the line intensity; it does not include uncertainties due to any other causes. Table 4.11 also gives the arithmetic mean value of abundance for each element. The mean abundances are taken as the best estimated values from the observations.

4.6.3 Discussion and Conclusions

Solar element abundances have been inferred by various workers using a number of techniques, including the analysis of permitted and forbidden photospheric absorption lines, chromospheric emission lines, permitted XUV and forbidden visible coronal lines, the solar wind, solar cosmic rays, and meteorites. Table 4.12 compares the abundance ratios derived in the present work, from measurements of the coronal X-ray line spectrum, with a representative selection of those obtained by other authors using some of the methods mentioned above.

Table 4.12 shows that there is, in general, reasonable agreement between the various determinations of abundance ratios. In particular, the present results are in good agreement with the values obtained by Pottasch (1967) and Flower and Nussbaumer (1975) from coronal EUV emission line intensities. With the exception of the relative O abundance, the present results are also in good agreement with the coronal abundance values recommended by Withbroe (1971). The relatively low abundances of Na, Al and Ni lead, in general, to correspondingly large uncertainties in the determined abundances of these elements, and thus it is considered that the various sets of measurements are consistent. The most serious discrepancy shown in Table 4.12 is in the abundance of O (relative to Mg and Fe), where the values given by Withbroe (1971), Dupree (1972), Withbroe and Gurman (1973), and Walker et al.(1974a,b,c) are about a factor of 2 higher than those given in the other sets of data shown, including the present results. However, this discrepancy has now been largely removed by the revised analysis of EUV spectra by Withbroe (1975). The comparatively low abundances of Mg, Si, and Fe relative to O and Ne, found by Bertsch et al.(1972) from solar 'cosmic' rays and by Cameron (1974) from meteorites, may be real.

Three other sets of results directly comparable with the present ones, are those of Acton et al. (1975) Davis et al. (1975), and Rugge and Walker (1976). Acton et al. (1975) have deduced, from measured coronal X-ray line intensities, an O:Ne abundance of 4.7 $\pm$ 1.5 using, what they term "a relatively model independent" method, and somewhat similar, in principle, to the technique used in the present work in Section 4.6.1. Rugge and Walker (1976), also using coronal X-ray line intensities and a similar technique to that of Section 4.6.1, have derived a Ne:Mg abundance of 1.47 $\pm$ 0.38. Davis et al. (1975) find that, in order to achieve self-consistency between their coronal X-ray imaging and spectral line intensity measurements, it is necessary to assume Pottasch's (1967) relative abundances for O, Ne, and Fe, rather than those of Withbroe (1971) or Walker et al. (1974a,b,c).

Note added in proof:

The validity of plasma emission measure/temperature models determined from measured spectral intensities (as for example in the present work), has recently been called into question by the analysis of Craig and Brown (1976) on the grounds that the problem is 'ill-conditioned'. These authors suggest that, to test the validity of a solution, the line intensities used in the calculation should be perturbed with random noise and the resulting variations in the emission measure solutions examined. In order to check the results presented in Chapter 4, this procedure has been carried out using a least squares fitting method and the data for active region 12628. A computer program (CORONA) was written and the fitting process performed $\sim 10^3$ times with randomized values of the line intensities. Each time, the intensity of a given line was taken as a random value from a normal distribution having a mean equal to the measured line intensity and standard deviation equal to the standard deviation of the measured line intensity.

The main conclusions which may be drawn from these tests are:

(1) The solution for the emission measure as a function of electron temperature is stable against realistic perturbations of the line intensities used in the analysis.

(2) There are no qualitative changes and no significant quantitative changes required to the results and conclusions presented in Chapter 4.

(3) Craig and Brown find large oscillations in their solutions even for relatively small ($\sim$5 - 10%) noise levels on their input data. It appears that two of the reasons for this behaviour are their omission of (i) a 'low temperature' line such as O VII $1s^2.{}^1S_0 - 1s2p.{}^1P_1$ (needed to give a good

determination of the low temperature end of the emission measure model, $T_e \sim 2 \times 10^6$ K), and (ii) a 'high temperature' line such as S XV $1s^2.{}^1S_0 - 1s2p.{}^1P_1$ (to be included as an upper limit to the measured intensity, and needed to define properly the high temperature cut-off in the model). In addition, in their example, Craig and Brown solved an exactly determined system of simultaneous equations (i.e. n line intensities and n temperature steps) rather than an over-determined system (i.e. more line intensities than temperature steps), the latter being the more usual and appropriate method when dealing with data known to be subject to uncertainties.

It should be noted that, in accordance with Craig and Brown (1976), the present model fitting procedure no longer imposes the constraint of allowing only non-negative emission measures in the solution.

Table 4.1a Measured and calculated spectral line intensities used in the determination of the coronal model for active region 11619

Ion	Transition	Recorded Counts	Intensity (10^{-6} erg cm^{-2} s^{-1})					
			Measured	Calculated				
					$T_e(10^6 K)$			
					1.5–2.5	2.5–3.5	3.5–4.5	4.5–5.5
O VII	$1s^2.{}^1S_o - 1s2p.{}^1P_1$	963	40.6±3.2	40.4	30.9	8.6	0.6	0.2
Ne IX	"	1232	5.88±0.21	5.56	1.29	2.82	0.93	0.53
Mg XI	"	684	3.30±0.14	2.77	0.11	0.73	0.74	1.19
O VIII	$1s.{}^2S_{\frac{1}{2}} - 2p.{}^2P_{\frac{1}{2},\frac{3}{2}}$	190	22.1±2.7	34.3	12.3	16.0	3.6	2.3
Ne X	"	29	0.79±0.17	1.7	0.01	0.37	0.56	0.79

<u>Table 4.1b</u> Measured and calculated spectral line intensities used in the determination of the coronal model for active region 12628

Ion	Transition	Recorded Counts	Intensity (10^{-6} erg cm^{-2} s^{-1})					
			Measured	Calculated				
					$T_e (10^6 K)$			
					1.5–2.5	2.5–3.5	3.5–4.5	4.5–5.5
O VII	$1s^2.{}^1S_0 - 1s2p.{}^1P_1$	4789	136.2 ± 7.5	132.8	111.3	20.0	1.3	0.2
Ne IX	"	4365	13.63 ± 0.34	13.59	4.63	6.58	1.85	0.53
Mg XI	"	1191	3.59 ± 0.13	4.77	0.38	1.71	1.49	1.19
O VIII	$1s.{}^2S_{\frac{1}{2}} - 2p.{}^2P_{\frac{1}{2},\frac{3}{2}}$	795	96.8 ± 6.7	91.3	44.3	37.4	7.3	2.3
Ne X	"	105	3.00 ± 0.33	2.79	0.03	0.86	1.11	0.79
Mg XII	"	14	0.45 ± 0.16	0.21	0.00	0.01	0.05	0.15

Table 4.1c Measured and calculated spectral line intensities used in the determination of the coronal model for active region 12624

Ion	Transition	Recorded Counts	Intensity (10^{-6} erg cm^{-2} s^{-1})						
			Measured	Calculated					
					$T_e(10^6$ K)				
					1.5–2.5	2.5–3.5	3.5–4.5	4.5–5.5	5.5–6.5
O VII	$1s^2.{}^1S_0-1s2p.{}^1P_1$	3415	97.1±6.7	96.0	80.4	14.3	1.0	0.2	0.1
Ne IX	"	3031	9.47±0.26	10.26	3.34	4.70	1.39	0.53	0.3
Mg XI	"	1384	4.17±0.14	5.12	0.28	1.22	1.12	1.19	1.32
O VIII	$1s.{}^2S_{\frac{1}{2}}-2p.{}^2P_{\frac{1}{2},\frac{3}{2}}$	700	85.3±6.7	68.1	32.0	26.7	5.4	2.3	1.6
Ne X	"	66	1.89±0.25	2.98	0.02	0.62	0.83	0.79	0.72
Mg XII	"	32	1.02±0.20	0.59	0.00	0.01	0.04	0.15	0.40

Table 4.1d Three sigma upper limits to measured spectral line intensities

Active region no.	Ion	Transition	3σ upper limit: Recorded Counts	3σ upper limit: Measured Intensity (10^{-6} erg $cm^{-2}s^{-1}$)
11619	Mg XII	$1s.^2S_{\frac{1}{2}} - 2p.^2P_{\frac{1}{2},\frac{3}{2}}$	4.9	0.15
"	Si XIII	$1s^2.^1S_o - 1s2p.^1P_1$	4.1	0.31
12628	Si XIV	$1s.^2S_{\frac{1}{2}} - 2p.^2P_{\frac{1}{2},\frac{3}{2}}$	6.3	0.52
12624	"	"	5.0	0.41
12628	S XV	$1s^2.^1S_o - 1s2p.^1P_1$	6.3	1.00
12624	"	"	5.0	0.79

<u>Table 4.1e</u> Wavelengths and oscillator strengths of the transitions in Tables 4.1a - d

Ion	Transition	Wavelength (Å)[a]	Oscillator strength
O VII	$1s^2.{}^1S_0 - 1s2p.{}^1P_1$	21.601	0.69[b]
Ne IX	"	13.447	0.72[b]
Mg XI	"	9.169	0.75[b]
Si XIII	"	6.648	0.75[c]
S XV	"	5.038	0.76[c]
O VIII	$1s.{}^2S_{\frac{1}{2}} - 2p.{}^2P_{\frac{1}{2},\frac{3}{2}}$	18.969	0.42[b]
Ne X	"	12.134	"
Mg XII	"	8.421	"
Si XIV	"	6.182	"

a) calculated : H-like ions, Garcia and Mack (1965); He-like ions, Ermolaev and Jones (1974).
b) Wiese et al. (1966, 1969).
c) Mewe (1972a); isoelectronic interpolation/extrapolation from Wiese et al. (1966, 1969).

Table 4.2 The coronal active region models for regions 11621, 11619, 12628 and 12624, derived from the X-ray spectral line intensities.

Active Region no.	Emission measure, $\Delta T_e^{-1} \int_V n_e^2 \, dV$ (10^{47} cm^{-3}(10^6 K)$^{-1}$)				
	T_e (10^6 K)				
	1.5-2.5	2.5-3.5	3.5-4.5	4.5-5.5	5.5-6.5
11621[a)]	0.8	1.5	0.6	0.1	
11619	0.5	0.3	0.1	0.1	
12628	1.8	0.7	0.2	0.1	
12624	1.3	0.5	0.15	0.1	0.1

a) Parkinson (1975c)

Table 4.3 Leicester Bragg spectrometer flights - active region observations

Experiment serial no.	Date (day/mth/yr)	Time (hr.min.,UT)	Active regions observed (McMath no.)
SL304	5/5/1966	0414	8278,8279
SL305	8/8/1967	0356	8914,8921,8926
S41	22/11/1968		9772,9780
S69	6/12/1970	1113	11060
SL1101	30/11/1971	0529	11619,11621
SL1206	26/11/1973	0535	12624,12628

Table 4.4 Measured and calculated spectral line intensities used in the determination of the (revised) coronal model for active region 11060

Ion	Transition	Recorded[a] Counts	Intensity (10^{-6} erg cm^{-2} s^{-1})	
			Measured	Calculated
O VII	$1s^2.{}^1S_0 - 1s2p.{}^1P_1$	180	336 ± 25	381
Ne IX	"	201	131 ± 9	93
Mg XI	"	399	43.7 ± 2.2	37.3
Si XIII	"	?	8.75[a]	7.63
O VIII	$1s.{}^2S_{\frac{1}{2}} - 2p.{}^2P_{\frac{1}{2},\frac{3}{2}}$	125	407 ± 36	522
Ne X	"	40	19.6 ± 3.1	22.9

a) Parkinson (1971a)

Table 4.5 Coronal model for active region 11060, from the S69 spectra

Original (Parkinson, 1971a)		Revised (Present work)	
$T_e (10^6 K)$	$\Delta T_e^{-1} \int_V n_e^2 dV$ $(10^{47}\ cm^{-3} (10^6 K)^{-1})$	$T_e (10^6 K)$	$\Delta T_e^{-1} \int_V n_e^2 dV$ $(10^{47}\ cm^{-3} (10^6 K)^{-1})$
1.0-2.0	10	1.5-2.5	2.7
2.0-3.0	16	2.5-3.5	7.0
3.0-4.0	5	3.5-4.5	2.0
4.0-5.0	0.5	4.5-5.5	0.4

Table 4.6 The SL1206 coronal model for active region 12628, derived from the X-ray spectral line intensities, using the same theoretical X-ray spectrum as the S-054 imaging analysis (Gerassimenko, 1975)

T_e (10^6K)	Emission measure, $\Delta T_e^{-1} \int_V n_e^2 \, dV$ (10^{47} cm^{-3} (10^6K)$^{-1}$)
1.5-2.5	3.2
2.5-3.5	1.6
3.5-4.5	0.2
4.5-5.5	0.2

Table 4.7 Parameters of the 'solar minimum' coronal active region model

$T_e (10^6 K)$	Emission measure $\Delta T_e^{-1} \int_V n_e^2 dV$ $(10^{47} cm^{-3} (10^6 K)^{-1})$	Volume, V $(10^{27} cm^3)$	Electron density, n_e $(10^9 cm^{-3})$	Thermal kinetic energy density, $3 n_e k T_e$ (erg cm^{-3})	Equipartition magnetic field, $B_{min} = (24 \pi n_e k T_e)^{\frac{1}{2}}$ (gauss)
1.5-2.5	4.0	100	1-3	1.7	6.5
2.5-3.5	1.4	9	3-5	5.0	11.2
3.5-4.5	0.4	1	5-7	9.9	15.8
4.5-5.5	0.2	0.3	7-9	16.6	20.4

Table 4.8 Parameters of a 'solar maximum' coronal active region model (Parkinson, 1973c).

$T_e \times 10^6$ K	$N_e^2 V$(cms^{-3})	V(cms^3)	N_e(cms^{-3})	Kinetic energy (ergs)	B_{min} (G)
2–3	5.5×10^{48}	10^{30}	2.3×10^{9}	1.2×10^{30}	5.5
3–4	1.8×10^{48}	10^{29}	4.3×10^{9}	3.1×10^{29}	8.8
4–5	4×10^{47}	10^{28}	6.3×10^{9}	5.9×10^{28}	12.2
5–6	1×10^{47}	10^{27}	10^{10}	1.1×10^{28}	16.6

Table 4.9 Time sequence of events for active regions 12624 and 12628, and experiments S-054 and SL1206

26 Nov 1973 Time, UT (hr.min.sec.)	Active region (Solar Geophysical Data, 1974)		Experiment	
	12628	12624	S-054	SL1206
		Flare(importance-N, class C0):		
0436		Hα start		
0442		Hα max.		
0450		X-ray(8-20 Å) max.		
0517		Hα end		
0535			Filter 1, 4s exposure	Launch
			16	
0536			64	
053653				Start fast scan,rgn.12628
053748				End " " " "
0538			256	Start slow " " "
053910				End " " " "
				Apogee (=238 km)
				Start slow scan,rgn.12624
054037				End " " " "
				Start fast " " "
0541			3, 1	
054131				End " " " "
				Start(2nd)fast scan,rgn.12624
0542			4	
			16	
054209				Re-entry
0543			64	
0545			256	
0550			2, 16	
0551			64	
0552	Flare(importance 1B):			
	Hα start			
0553	X-ray start(from S-054)		256	
0556	Hα max.			
0605	Hα end			

Table 4.10 Measured line intensity ratios and derived element abundance ratios O:Ne, Ne:Mg

Active region No.	Measured energy intensity ratio He-like$(1s^2.{}^1S_0-1s2p.{}^1P_1)$: H-like$(1s.{}^2S_{\frac{1}{2}}-2p.{}^2P_{\frac{1}{2},\frac{3}{2}})$		Element abundance ratio	
	Ne IX : O VIII	Mg XI : Ne X	O : Ne	Ne : Mg
11060	0.322 ± 0.037	2.23 ± 0.37	3.90 ± 0.44	0.69 ± 0.12
11619	0.266 ± 0.034	4.18 ± 0.92	4.72 ± 0.60	0.32 ± 0.07
11621	0.203 ± 0.012	1.74 ± 0.22	7.0 ± 0.3	0.83 ± 0.07
12624	0.1110 ± 0.0092	2.21 ± 0.30	8.04 ± 0.67	0.65 ± 0.09
12628	0.141 ± 0.010	1.20 ± 0.14	6.33 ± 0.45	1.11 ± 0.13
		Mean:	6.02 ± 0.78	0.65 ± 0.14

Table 4.11a Wavelengths, measured intensities and oscillator strengths for the spectral lines used in the element abundance analysis

Ion	Transition	Wavelength, λ[a] (Å)	Measured line intensity, I (10^{-6} erg cm^{-2}s^{-1}) Active region no. 11060[b]	11619	11621[c]	12624	12628	Oscillator strength, f
O VIII	$1s.{}^2S_{\frac{1}{2}}-2p.{}^2P_{\frac{1}{2},\frac{3}{2}}$	18.969	407 ± 36	22.1 ± 2.7	119.9 ± 5.2	85.3 ± 6.7	96.8 ± 6.7	0.42[d]
Ne X	"	12.134	19.6 ± 3.1	0.79 ± 0.17	4.72 ± 0.52	1.89 ± 0.25	3.00 ± 0.33	0.42[d]
Mg XII	"	8.421				1.02 ± 0.20	0.45 ± 0.16	0.42[d]
O VII	$1s^2.{}^1S_0-1s2p.{}^1P_1$	21.601	336 ± 25	40.6 ± 3.2	90.9 ± 2.7	97.1 ± 6.7	136.2 ± 7.5	0.69[d]
Ne IX	"	13.447	131 ± 9	5.88 ± 0.21	24.43 ± 0.90	9.47 ± 0.26	13.63 ± 0.34	0.72[d]
Na X	"	11.003 }		0.33 ± 0.13	1.26 ± 0.14	0.48 ± 0.16	1.05 ± 0.22	{ 0.73[e]
Ne IX	$1s^2.{}^1S_0-1s4p.{}^1P_1$	11.000 }						{ 0.056[f]
Mg XI	$1s^2.{}^1S_0-1s2p.{}^1P_1$	9.169	43.7 ± 2.2	3.30 ± 0.14	8.13 ± 0.51	4.17 ± 0.14	3.59 ± 0.13	0.75[d]
Al XII	"	7.757				0.29 ± 0.15	0.36 ± 0.18	0.75[d]
Si XIII	"	6.648	8.75			1.49 ± 0.37	0.78 ± 0.31	0.75[e]
Fe XVII	$2p^6.{}^1S_0-2p^5 3d.{}^1P_1$	15.013	385 ± 19	31.3 ± 1.5	111.26 ± 3.06	133.3 ± 4.4	74.5 ± 3.4	2.24[g]
Ni XIX	"	12.430		0.39 ± 0.12	3.1 ± 0.3	0.97 ± 0.18	0.56 ± 0.16	2.43[h]

Footnotes to Table 4.11a

a) H-like ions, Garcia and Mack (1965), calculated ; He-like ions, Ermolaev and Jones (1974), calculated ; Ne-like ions, present work (Ch. 6), measured.

b) calculated from recorded counts given by Parkinson (1971a).

c) Parkinson (1975c). Uncertainties are calculated from his quoted recorded counts.

d) Wiese et al. (1966, 1969).

e) Mewe (1972a) ; isoelectronic interpolation from Wiese et al. (1966, 1969).

f) Dalgarno and Parkinson (1967).

g) Froese (1967).

h) isoelectronic interpolation from Kastner et al. (1967).

Table 4.11b The derived relative element abundances for Al, Si, Fe, Ni

Active region no.	Derived element abundance, A_z (units of 10^{-5})			
	Al	Si	Fe	Ni
11060			4.9 ± 0.2	
11619			5.9 ± 0.3	0.14 ± 0.04
11621			6.4 ± 0.2	0.36 ± 0.03
12624	0.69 ± 0.36	6.1 ± 1.5	13.8 ± 0.5	0.18 ± 0.03
12628	1.13 ± 0.57	5.2 ± 2.1	7.4 ± 0.3	0.12 ± 0.03
Mean:	0.82 ± 0.37	5.8 ± 1.3	6.4 ± 1.6	0.21 ± 0.06

Table 4.11c The relative element abundance of Na, derived from the Na X/Ne IX line blend at λ11.00 Å

Active region no.	Intensity (10^{-6} erg cm^{-2} s^{-1})			Element abundance, A_z(Na) (units of 10^{-5})
	Measured Na X+Ne IX	Calculated Ne IX	Calculated Na X	
11060				
11619	0.33 ± 0.13	0.20	0.13	0.23 ± 0.23
11621	1.26 ± 0.14[a]	0.81	0.45	0.21 ± 0.07
12624	0.48 ± 0.16	0.35	0.48	0.46 ± 0.15
12628	1.05 ± 0.22	0.45	0.60	0.53 ± 0.19
			Mean:	0.28 ± 0.10

a) Intensity of Parkinson's (1975c) line no. 18 (his Table I). Parkinson assigns the Na X and Ne IX transitions to two separate features in his spectrum 0.02 Å apart. The present author believes (see text) that the λ11.00 Å feature is the stated blend.

Table 4.12 Comparison of solar relative element abundance determinations

Element	Abundance relative to Ne												
	(1)	(2)	(3)	(4)	(5)	(6)	(7)	(8)	(9)	(10)	(11)	(12)	(13)
O	6.0 ± 0.8	9 ± 3	12.9	16.5	21.5	16.1	7.1	13.0	4.7 ± 1.5		6.3	6.3	19.3
Ne	1	1	1	1	1	1	1	1	1	1	1	1	
Na	0.04 ± 0.01		0.1	0.09	0.07	0.08		0.03				0.02	0.05
Mg	1.5 ± 0.3	1.7 ± 0.8	2.0	1.3	1.1	1.3	0.9	0.6		0.68 ± 0.18	0.35	0.31	1
Al	0.12 ± 0.05		0.1	0.08	0.13	0.08	0.06	0.05				0.03	0.07
Si	0.8 ± 0.2		2.0	1.3	1.3	1.3	1.4	0.6			0.18	0.29	1.0
Fe	0.9 ± 0.2		1.7		0.7	1.3	1.4	0.5				0.24	0.7
Ni	0.03 ± 0.01					0.08	0.13					0.01	

Referances and type of measurement:
(1) Present work, corona, X-ray
(2) Flower and Nussbaumer (1975), corona, EUV
(3) Withbroe (1975), corona, EUV
(4) Withbroe and Gurman (1973), corona, EUV
(5) Dupree (1972), corona, EUV
(6) Withbroe (1971), corona, EUV
(7) Pottasch (1967), corona, EUV
(8) Walker et al. (1974a,b,c,), corona, X-ray
(9) Acton et al. (1975), corona, X-ray
(10) Rugge and Walker (1976), corona, X-ray
(11) Bertsch et al. (1972), solar flare 'cosmic' rays
(12) Cameron (1974), solar system, meteorites and solar flare cosmic rays
(13) Withbroe (1971), photosphere, visible (N.B. : normalised to Mg)

FIGURES

Chapter 4

4.1 Emission functions $G(T_e)$ of spectral lines.

a H-like ions, transition $1s.^2S_{\frac{1}{2}} - 2p.^2P_{\frac{1}{2},\frac{3}{2}}$

b He-like ions, transition $1s^2.^1S_0 - 1s2p.^1P_1$

c Ne-like ions, transition $2p^6.^1S_0 - 2p^5 3d.^1P_1$.

4.2 Active region coronal models through solar cycle 20.

4.3 Solar activity cycle 20, as shown by sunspot numbers (Solar Geophysical Data, 1975), with the dates of the Leicester Bragg spectrometer flights.

4.4 X-ray photographs of the solar corona obtained by S-054 on 26 November 1973. North is at the top, east is to the left.

a 16 s exposure, filter 1, time 0535 UT

b 4 s exposure, filter 3, time 0542 UT.

The full field of view (6 x 6 arc min^2) of the SL1206 spectrometer is indicated (by the square outlines) at the positions to which it was pointed, i.e. McMath active regions 12628 (east of disk centre) and 12624 (west of disk centre).*

4.5 Hα photograph of the solar chromosphere at 0016 UT, 26 November 1976 (courtesy of Carnarvon Observatory, W. Australia).

4.6 White light photograph of the solar photosphere at 0030 UT, 26 November 1976 (courtesy of Carnarvon Observatory).

4.7 Magnetograms showing the magnitude of the longitudinal component of the photospheric magnetic field (Mt. Wilson Observatory, in Solar Geophysical Data, 1974).

a 25 November 1973, 1809-1855 UT

b 27 November 1973, 1650-1820 UT.

4.8 The X-ray intensity distribution of the Sun in the neighbourhood of McMath region 12628, as observed by S-054 near 0535 UT 26 November 1973, in the bandpass of (a) filter 1, (b) filter 3. The contours are labelled in relative energy units. The square shows the position of the SL1206 full field of view during its observations. The axes are graduated at 1 arc min intervals.*

4.9 a and b show Fig. 5a and b respectively convolved with the SL1206 spectrometer field of view function.*

4.10 The (relative) field response function (transmission) of the SL1206 spectrometer.

4.11 a and b. As Fig. 4.8, for McMath region 12624.*

4.12 a and b. As Fig. 4.9, for McMath region 12624.*

4.13 Line-of-sight averaged temperature map of McMath region 12628, derived from the intensity maps of fig. 4.8. The contours are labelled in units of 10^6 K.*

4.14 As Fig. 4.13, for McMath region 12624 (derived from Fig. 4.11).*

4.15 Line-of-sight emission measure $\int_l n_e^2 dl$ map, for McMath region 12628, calculated to fit point by point to the measured brightness map of Fig. 4.8a using temperatures as shown on Fig. 4.13. The contours are labelled in relative units (of cm^{-5}).*

4.16 shows Fig. 4.15 convolved with the SL1206 field of view function.*

4.17 A simplified description of the hot loop system in McMath region 12628, derived from the S-054 data. The numbers close to each loop are the (arbitrary) loop reference number (prefixed by #) and the mean electron density n_e in units of 10^9 cm^{-3}.

4.18 i S-054 X-ray images of the Sun, 4s exposure in the bandpass of filter 3, 21-26 November 1973. McMath region 12628 is arrowed.*

Upper left,	21 November,	2125 UT.
Upper right,	23 November,	1502 UT.
Lower left,	25 November,	1218 UT.
Lower right,	26 November,	1258 UT.

ii Idealized sketch of the geometry of the hot loop system in McMath region 12628.

4.19 Schematic solar minimum coronal active region model, based on the S-054 and SL1206 observations of McMath 12628.

4.20 Schematic solar maximum coronal active region model of Parkinson (1973b).

4.21 Ratio of the emission functions $G(T_e)$ of the H-like line Lyα and the He-like line $1s^2.{}^1S_0 - 1s2p.{}^1P_1$.

---

* Reproduced by courtesy of the Solar Physics Group, ASE.

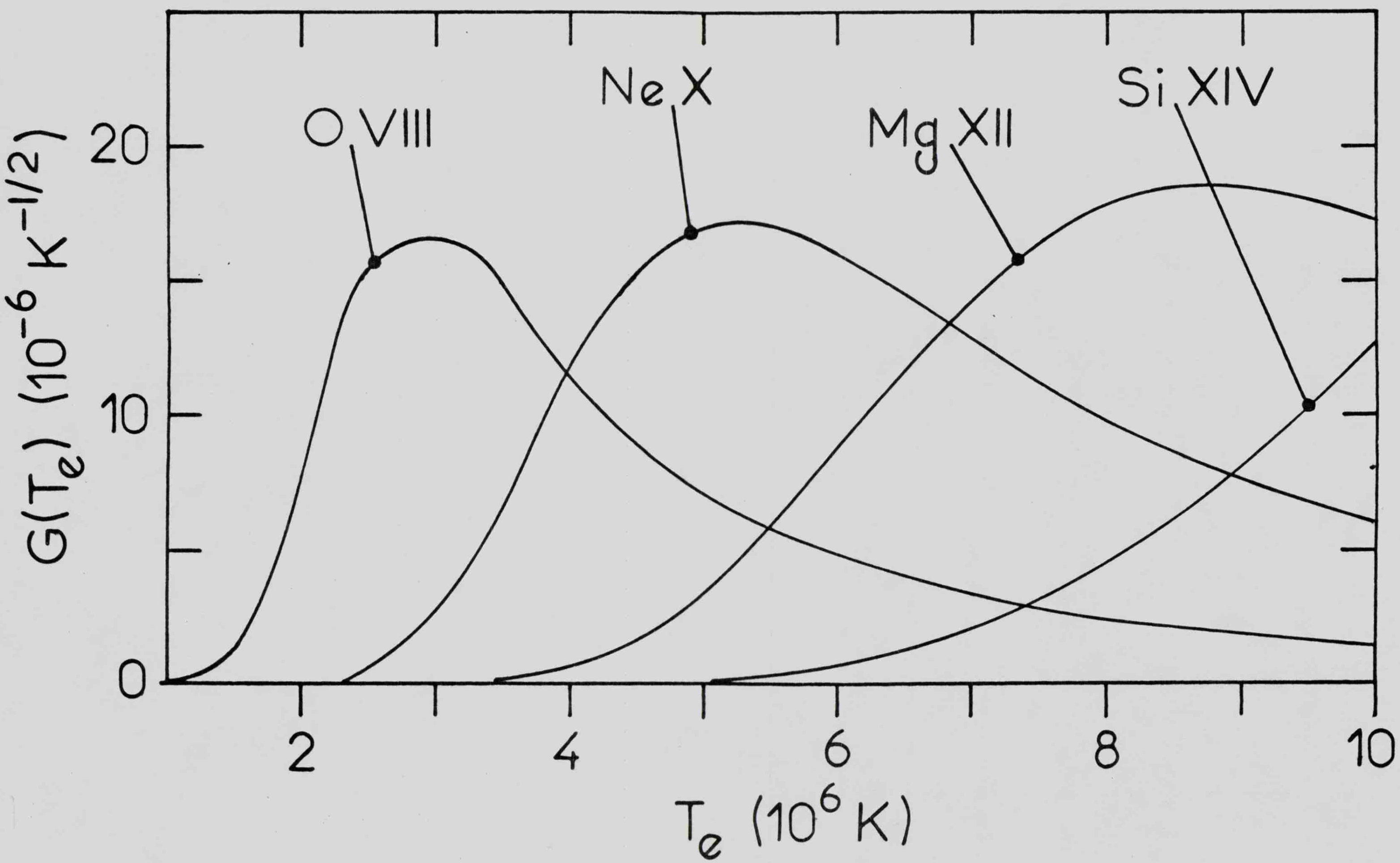

Fig. 4.1.a.

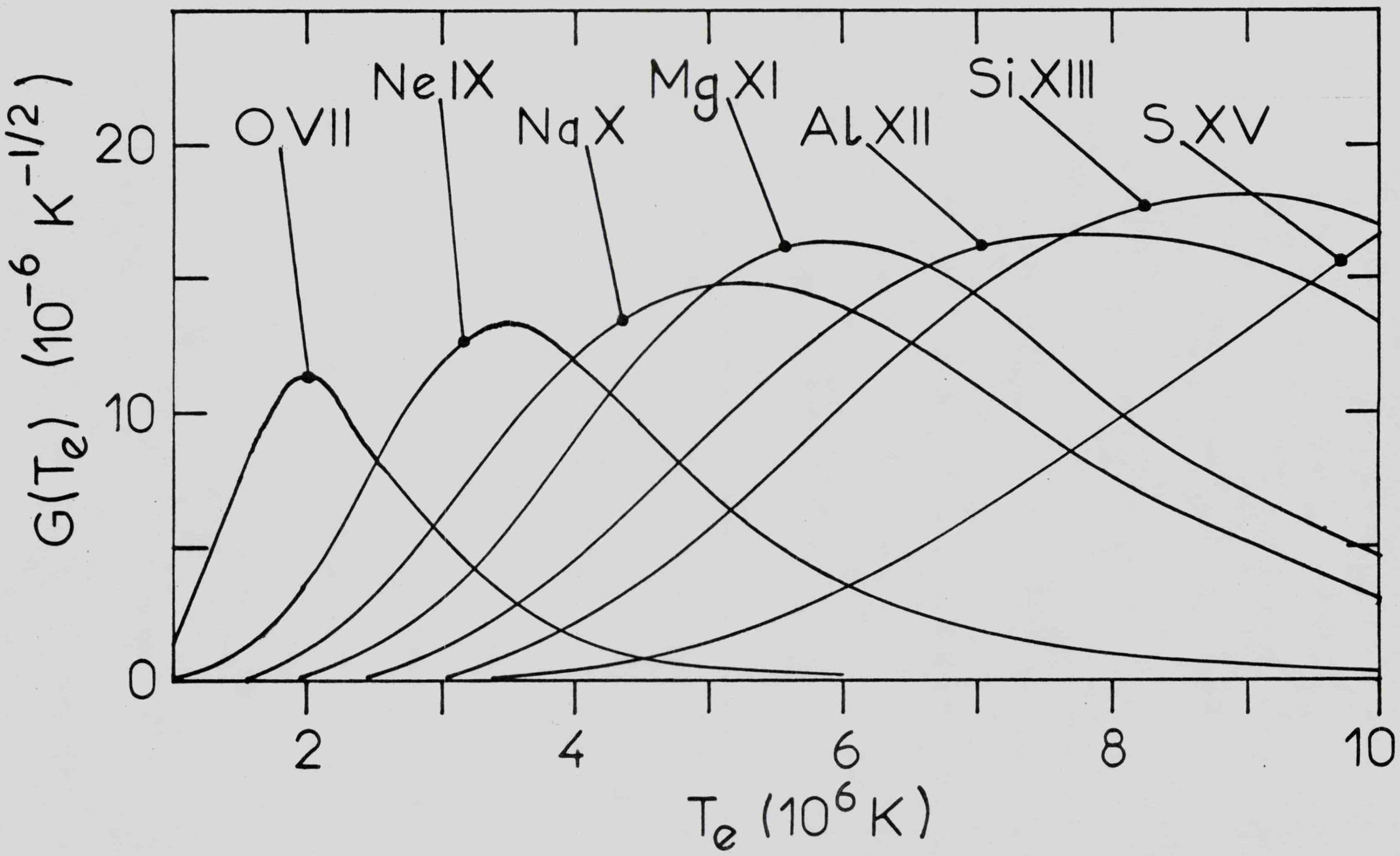
O VII
Ne IX
Na X
Mg XI
Al XII
Si XIII
S XV
20
10
0
2
4
6
8
10
$G(T_e)$ $(10^{-6}\ K^{-1/2})$
T_e $(10^6 K)$

Fig. 4.1.b.

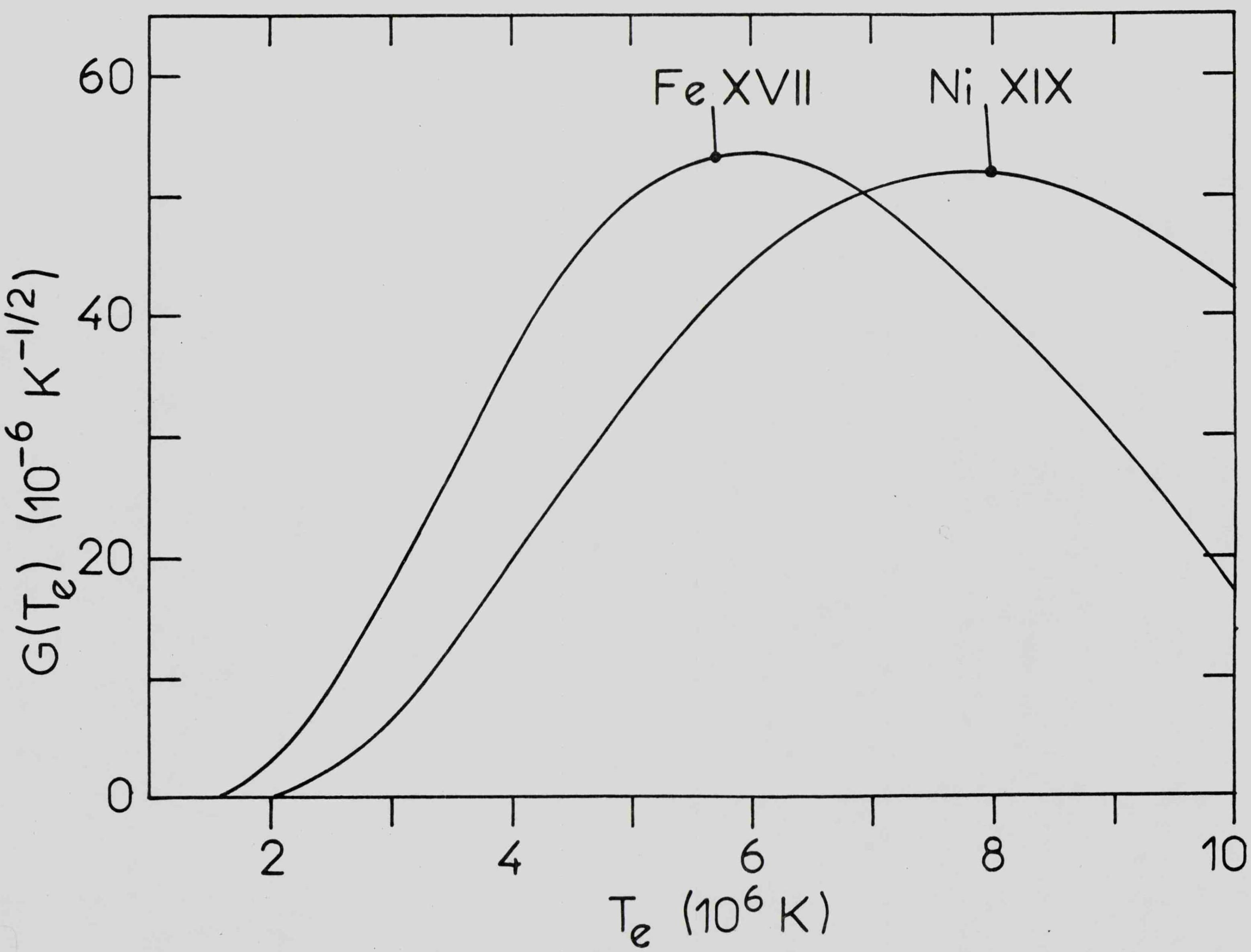

Fig. 4.1.c.

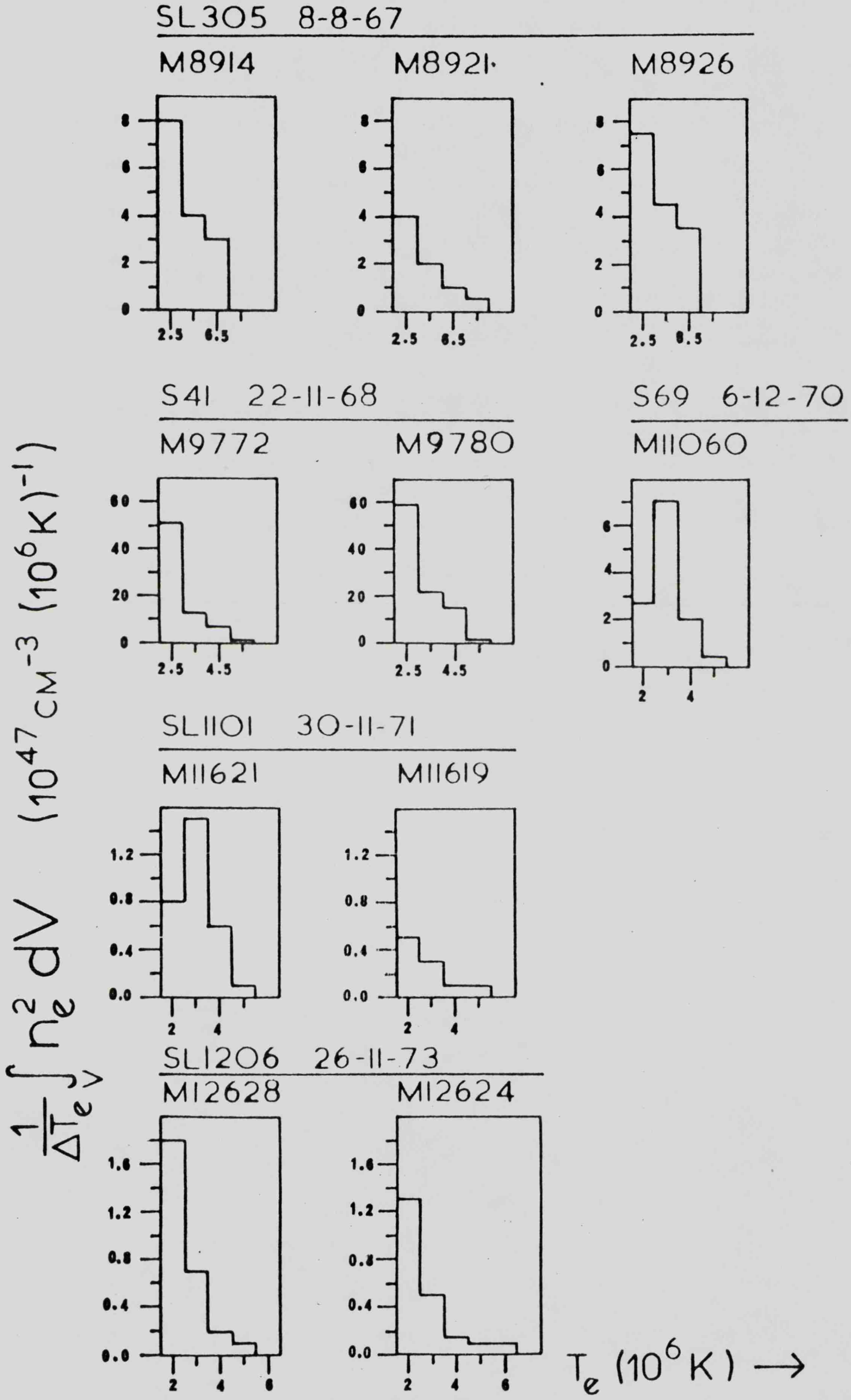

SL305 8-8-67
M8914
M8921
M8926
S41 22-11-68
M9772
M9780
S69 6-12-70
M11060
SL1101 30-11-71
M11621
M11619
SL1206 26-11-73
M12628
M12624
$\frac{1}{\Delta T_e}\int_V n_e^2\,dV$ $(10^{47}\,\mathrm{CM}^{-3}\,(10^6\,\mathrm{K})^{-1})$
$T_e\ (10^6\,\mathrm{K}) \longrightarrow$

Fig. 4.2.

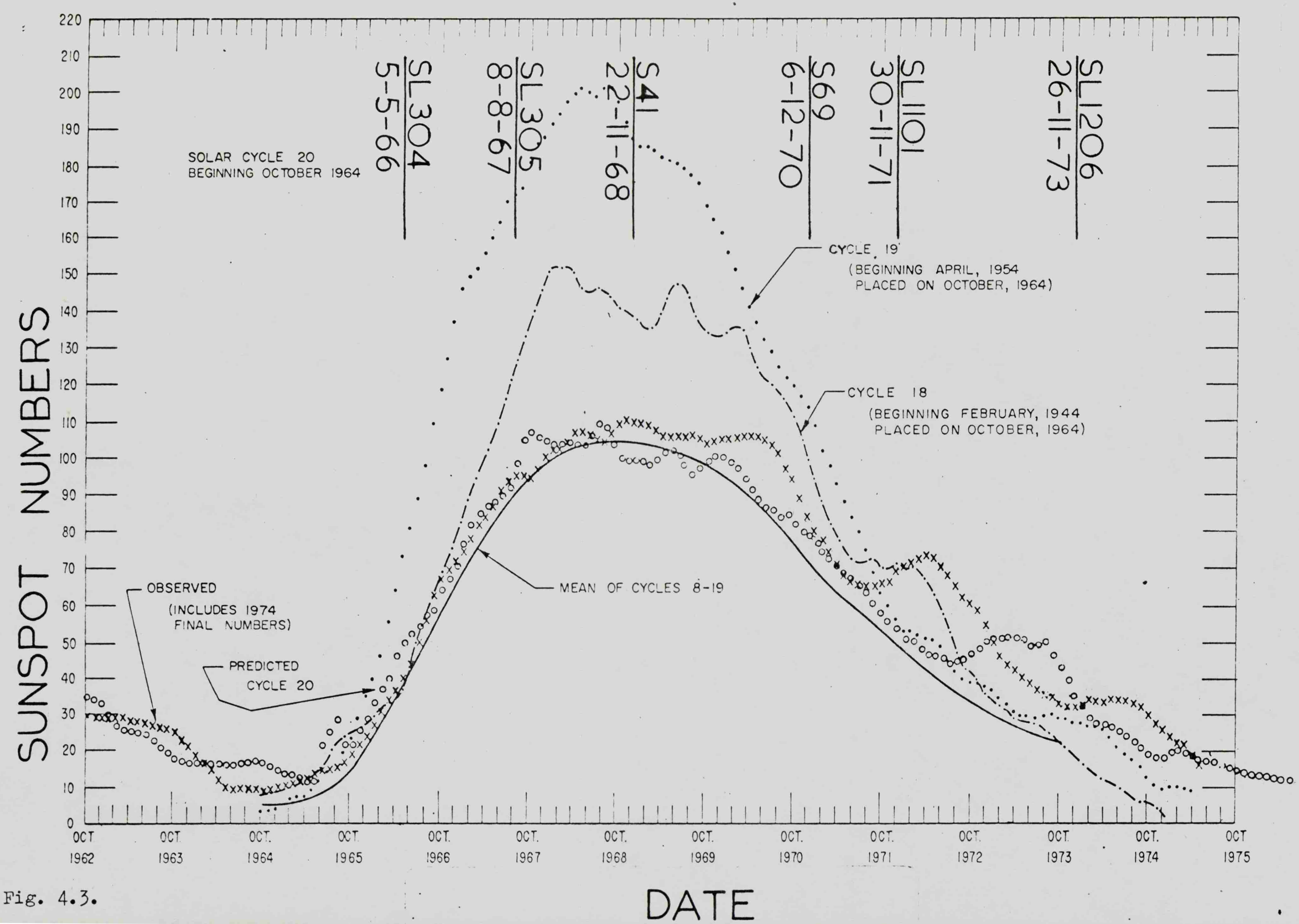
SUNSPOT NUMBERS
DATE
SOLAR CYCLE 20
BEGINNING OCTOBER 1964
SL304
5-5-66
SL305
8-8-67
S41
22-11-68
S69
6-12-70
SL1101
30-11-71
SL1206
26-11-73
CYCLE 19
(BEGINNING APRIL, 1954
PLACED ON OCTOBER, 1964)
CYCLE 18
(BEGINNING FEBRUARY, 1944
PLACED ON OCTOBER, 1964)
MEAN OF CYCLES 8-19
OBSERVED
(INCLUDES 1974
FINAL NUMBERS)
PREDICTED
CYCLE 20
0
10
20
30
40
50
60
70
80
90
100
110
120
130
140
150
160
170
180
190
200
210
220
OCT 1962
OCT. 1963
OCT. 1964
OCT. 1965
OCT. 1966
OCT. 1967
OCT. 1968
OCT. 1969
OCT. 1970
OCT. 1971
OCT. 1972
OCT. 1973
OCT. 1974
OCT 1975

Fig. 4.3.

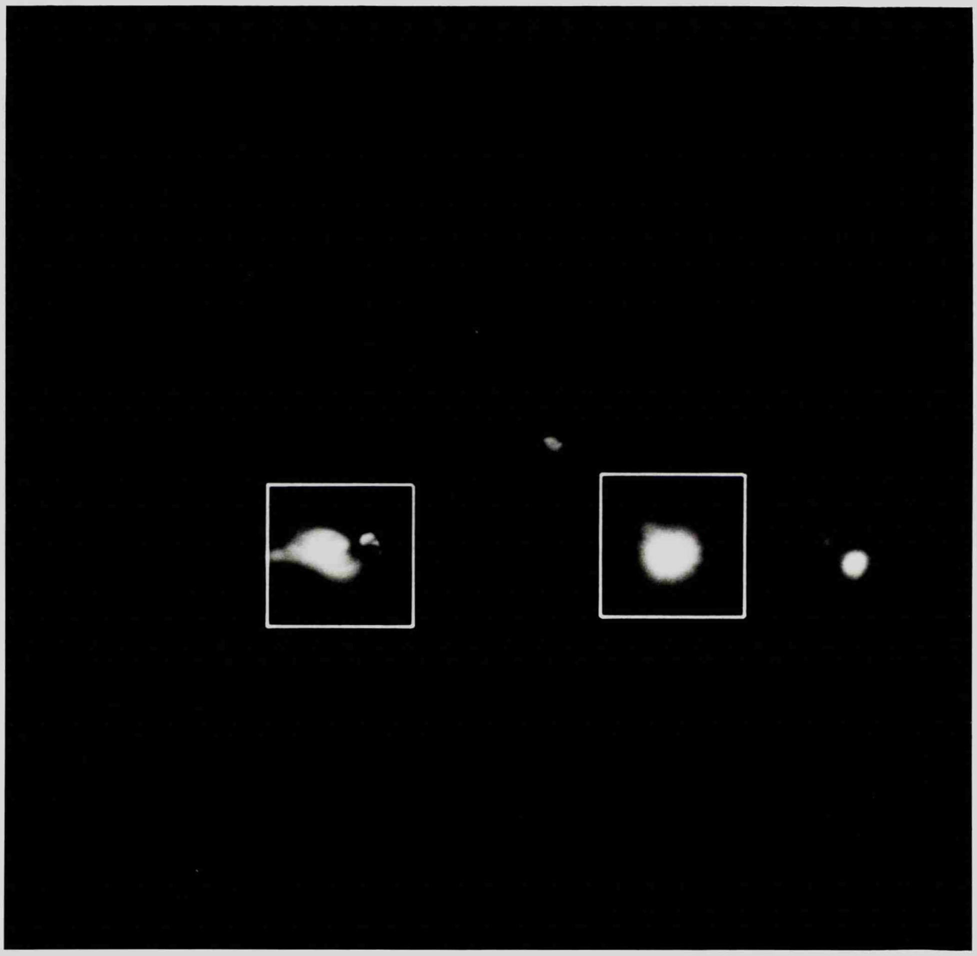

Fig. 4.4.a.

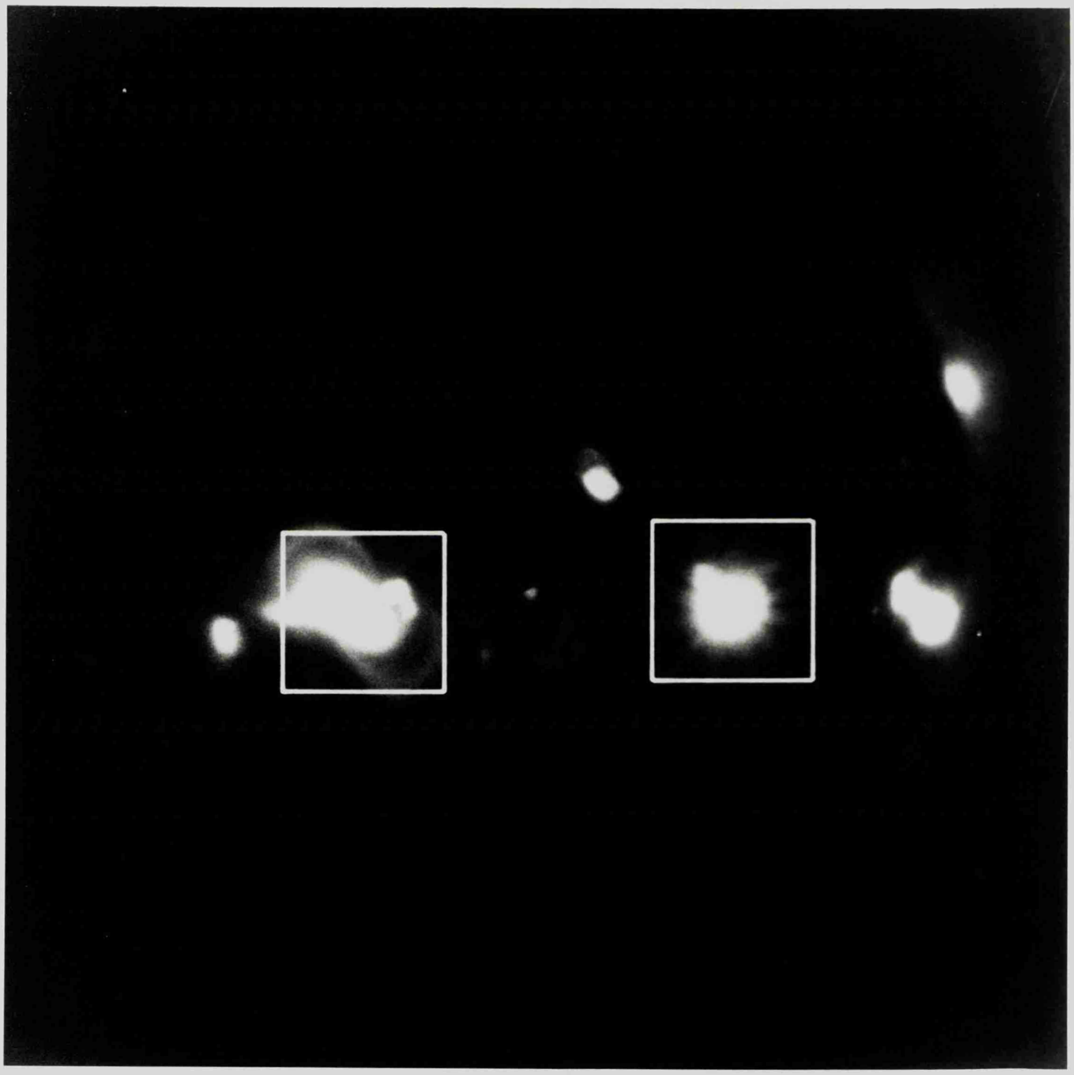

Fig. 4.4.b.

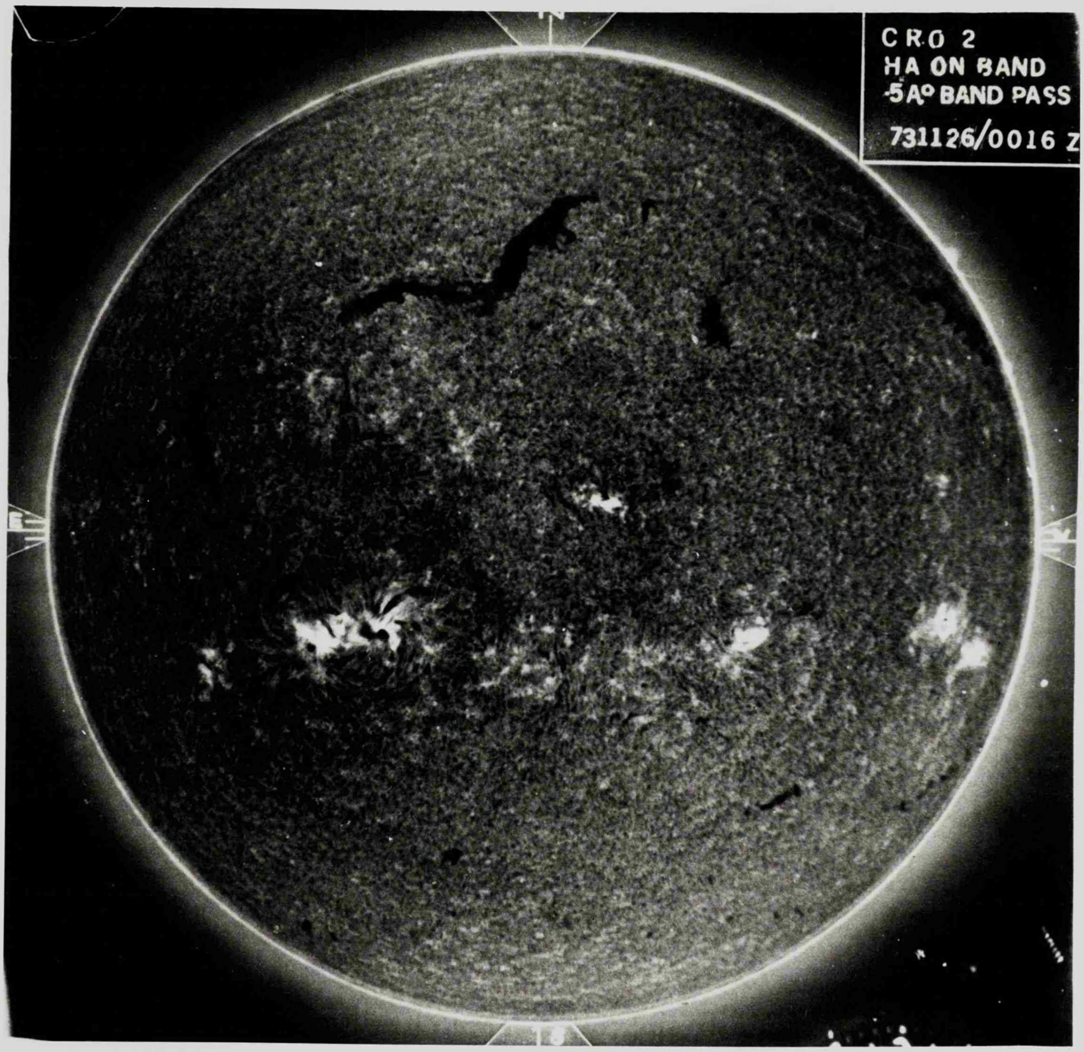

Fig. 4.5.

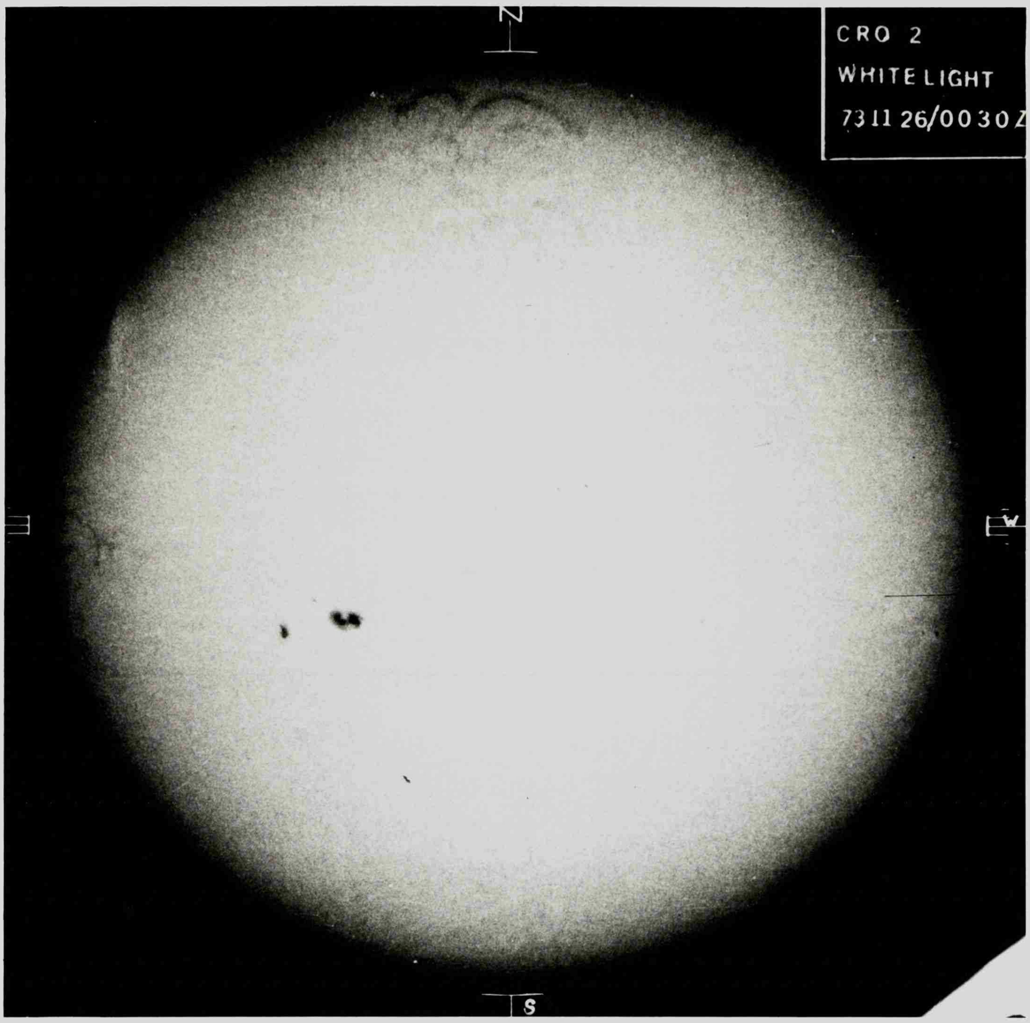

Fig. 4.6.

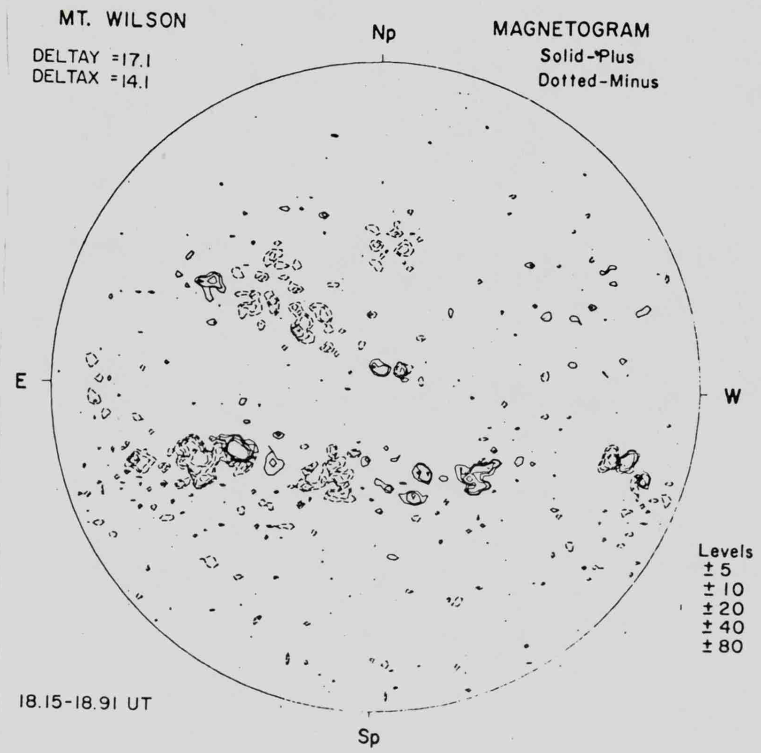
MT. WILSON
DELTAY =17.1
DELTAX =14.1
Np
MAGNETOGRAM
Solid-Plus
Dotted-Minus
E
W
Levels
±5
±10
±20
±40
±80
18.15-18.91 UT
Sp

(a)

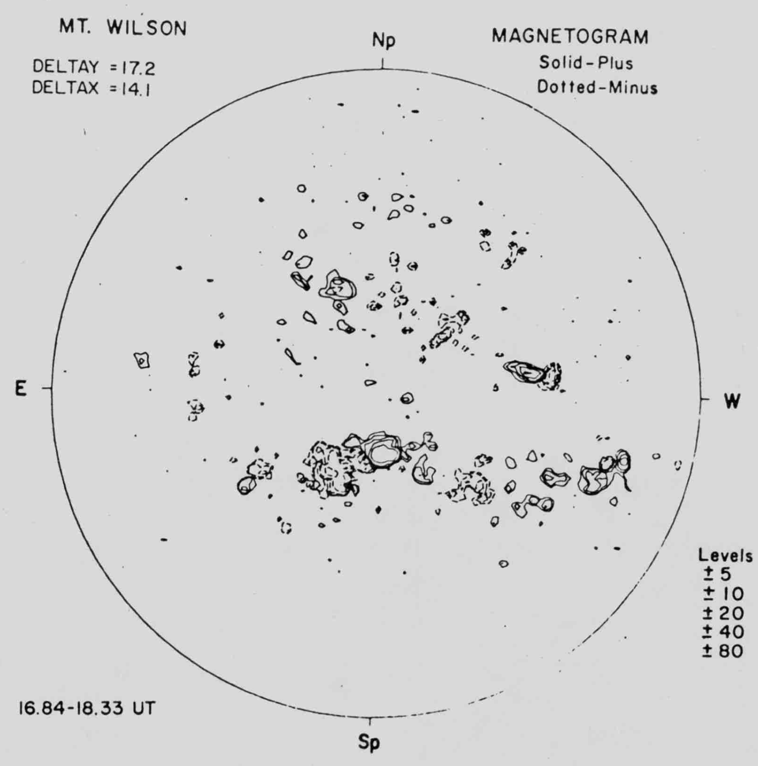
MT. WILSON
DELTAY =17.2
DELTAX =14.1
Np
MAGNETOGRAM
Solid-Plus
Dotted-Minus
E
W
Levels
±5
±10
±20
±40
±80
16.84-18.33 UT
Sp

(b)

Fig. 4.7.

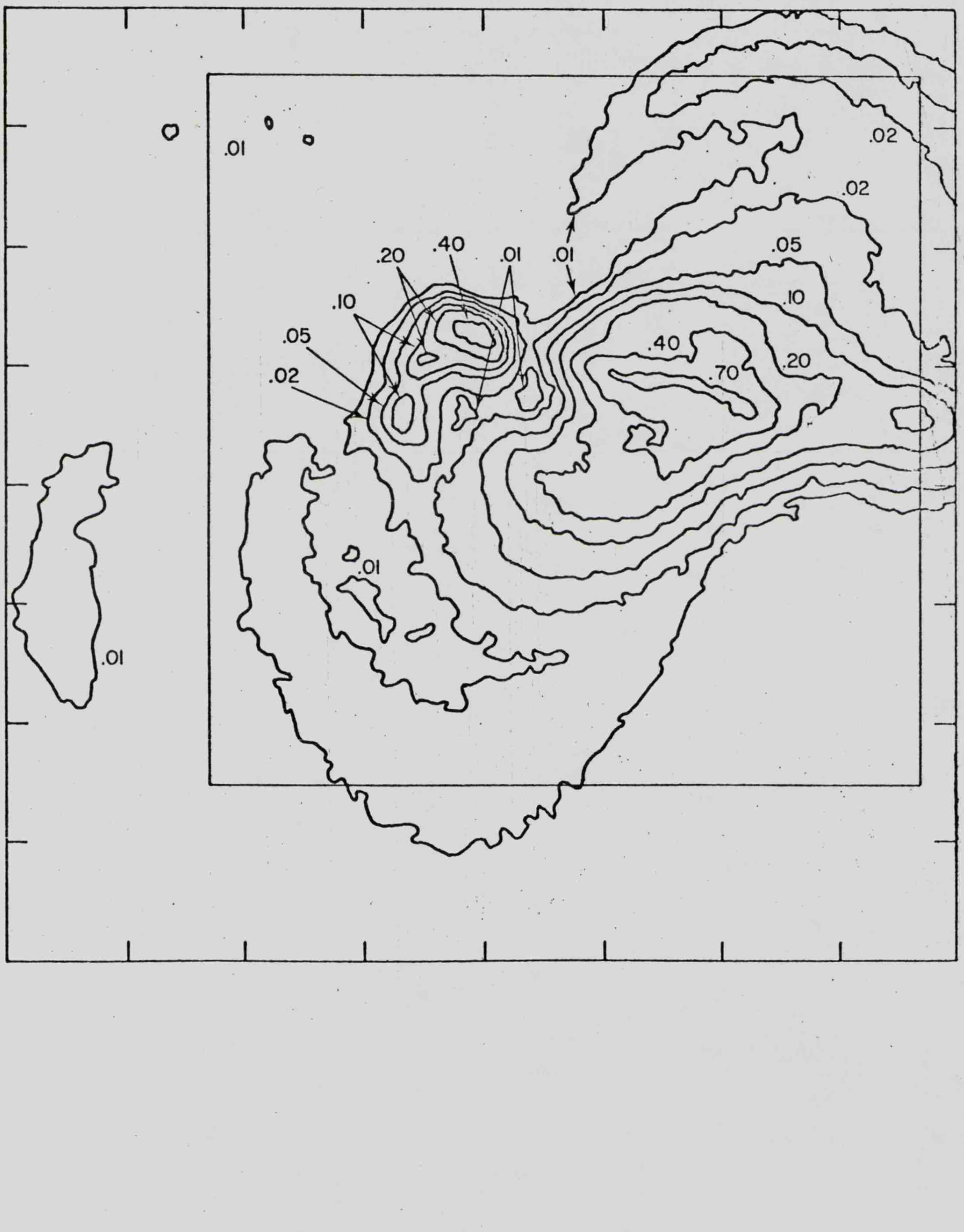

Fig. 4.8.a.

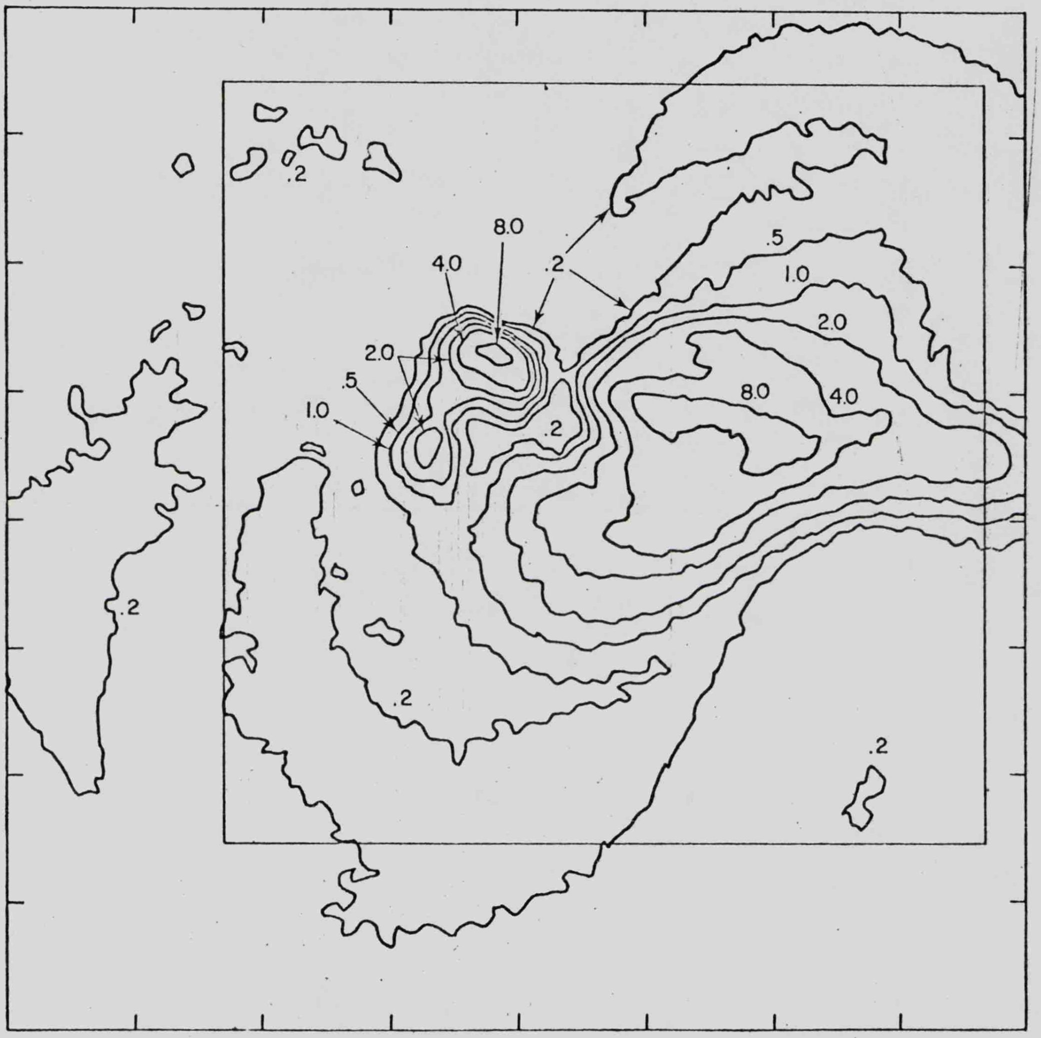

Fig. 4.8.b.

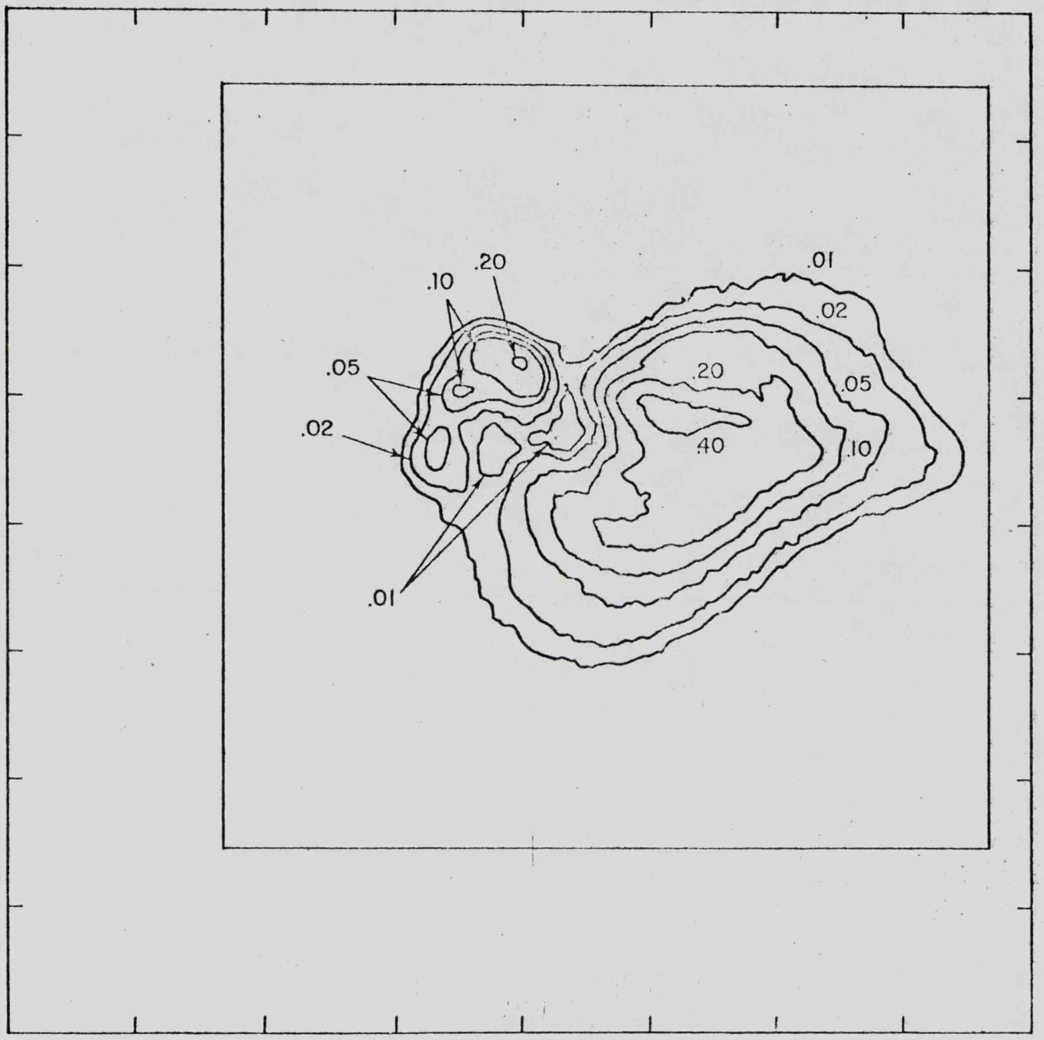

Fig. 4.9.a.

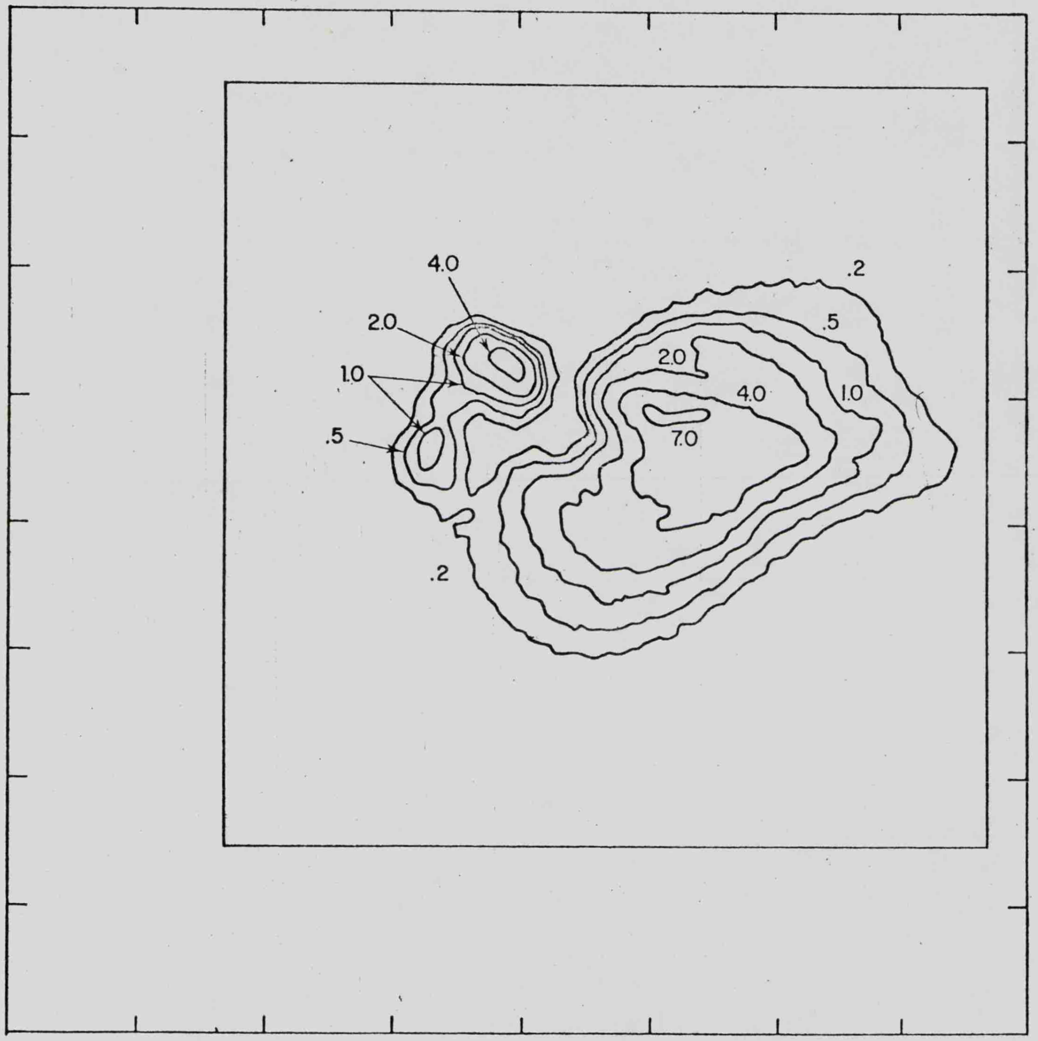

Fig. 4.9.b.

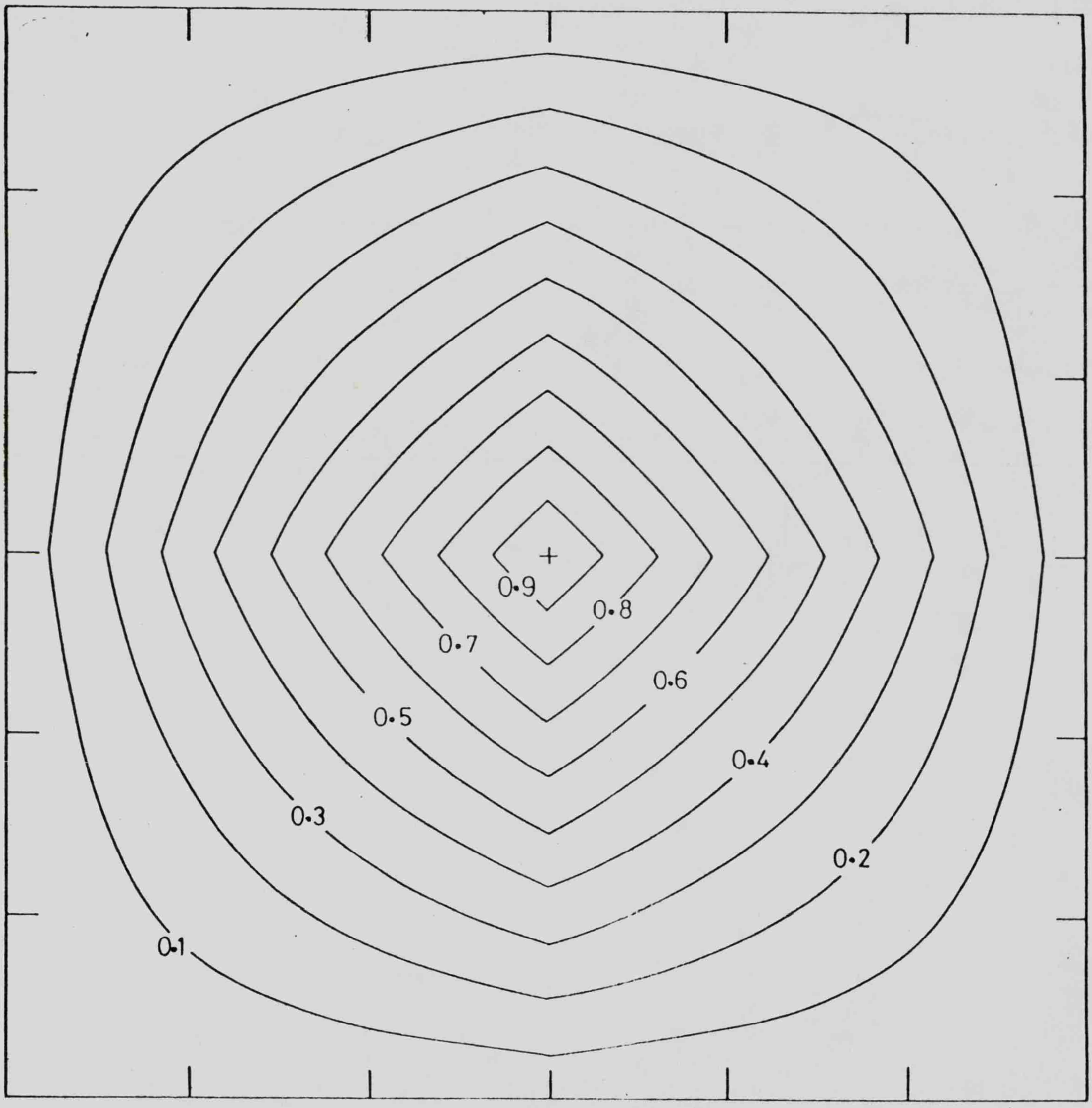

Fig. 4.10.

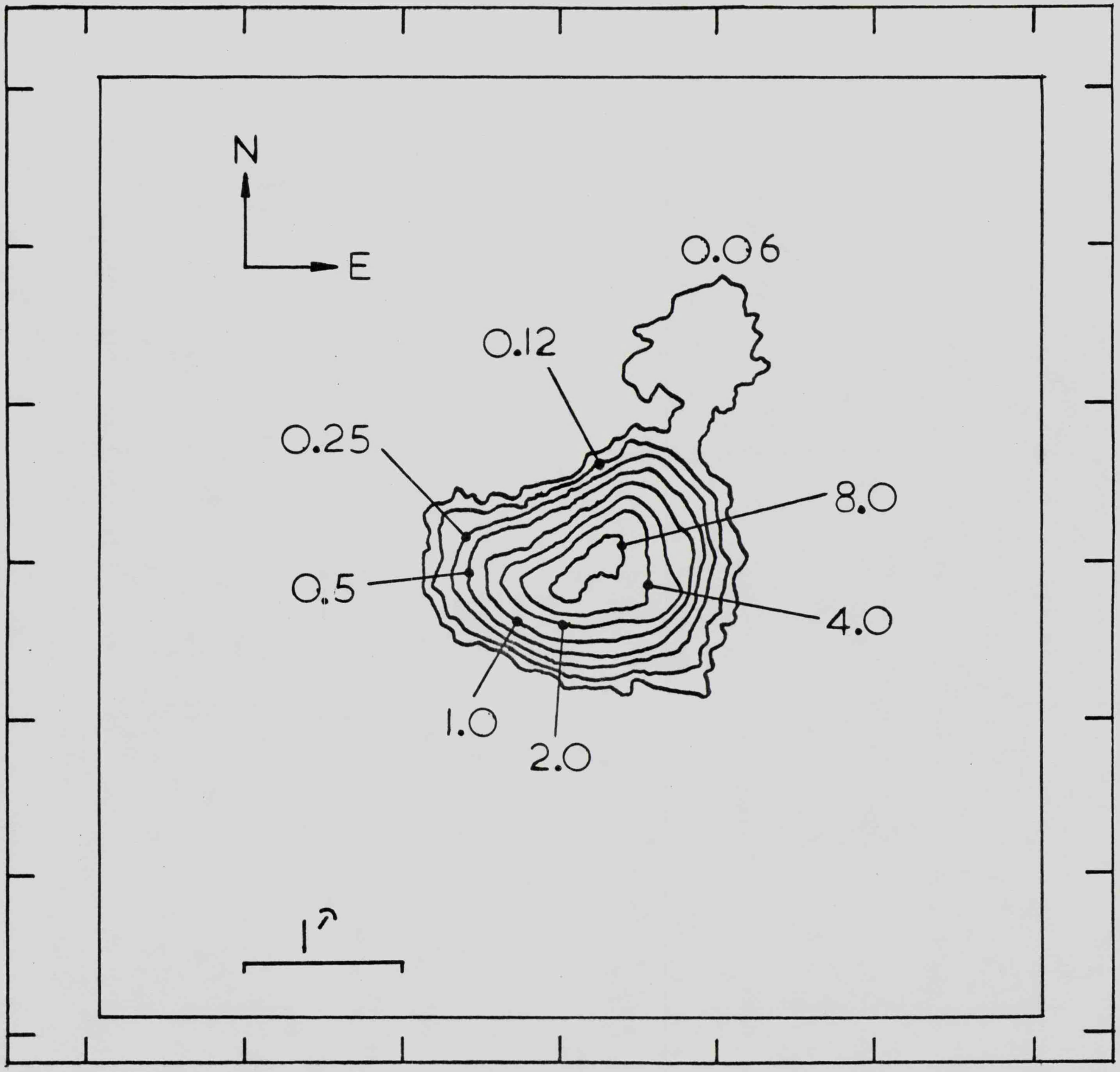

Fig. 4.11.a.

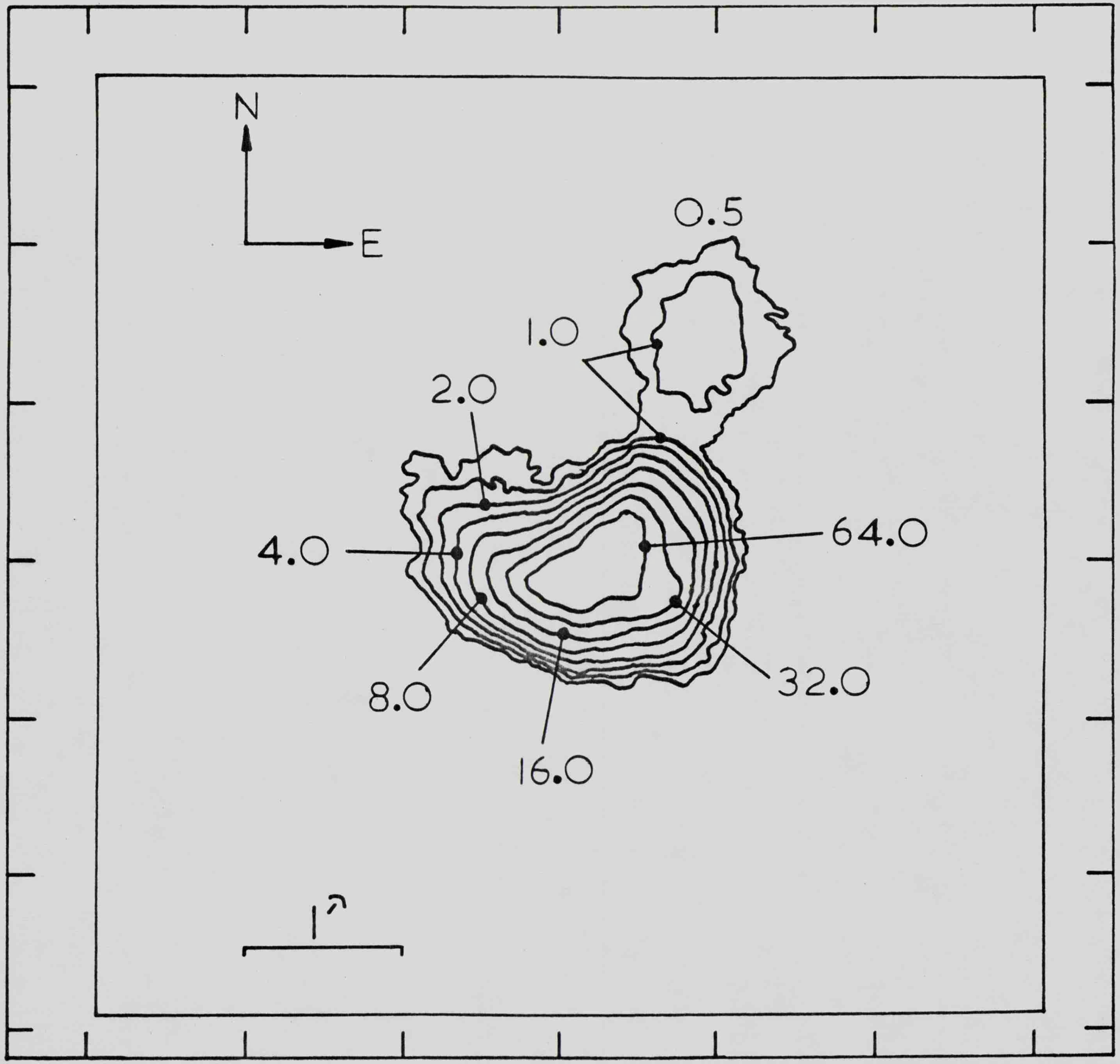

Fig. 4.11.b.

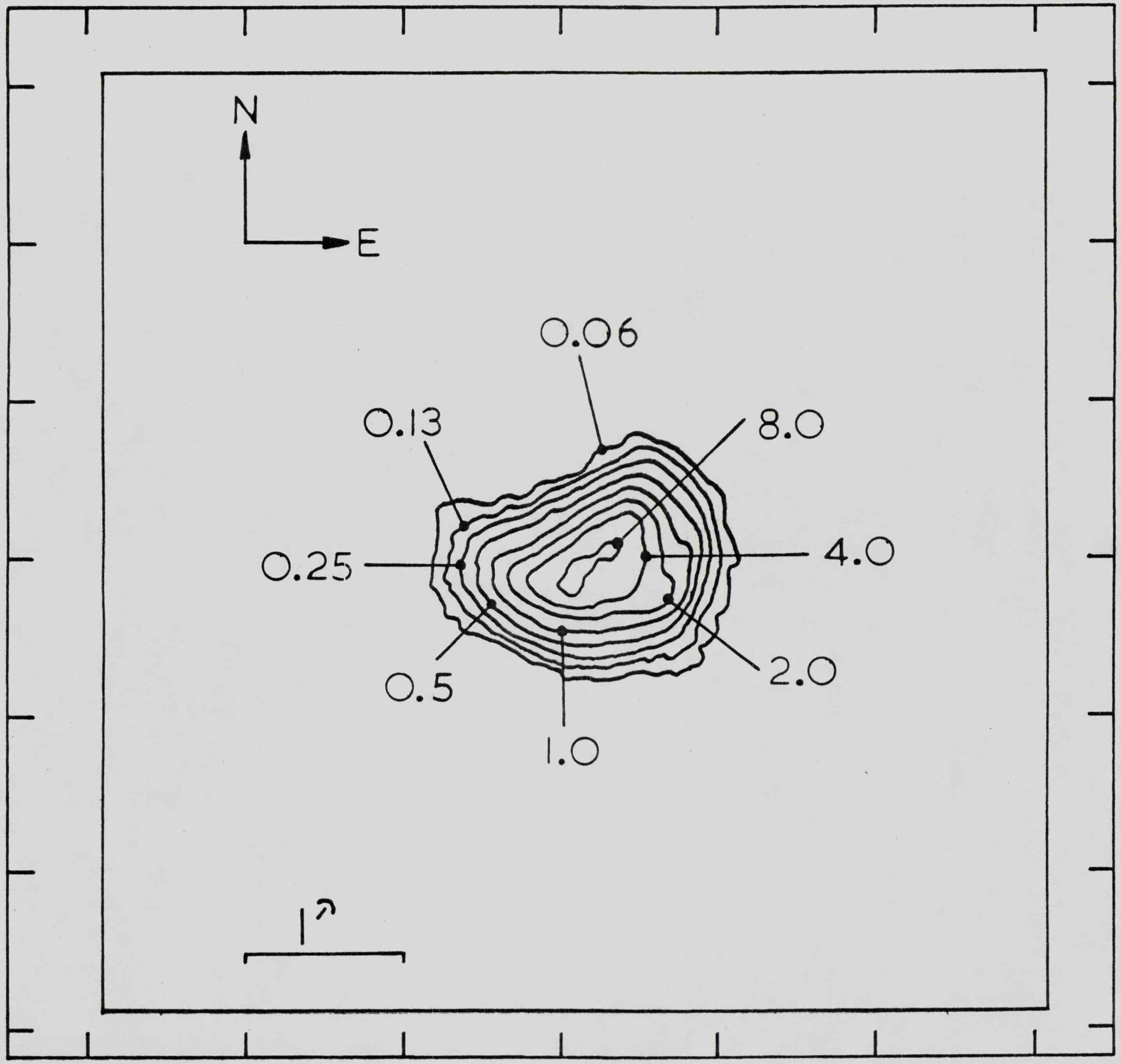

Fig. 4.12.a.

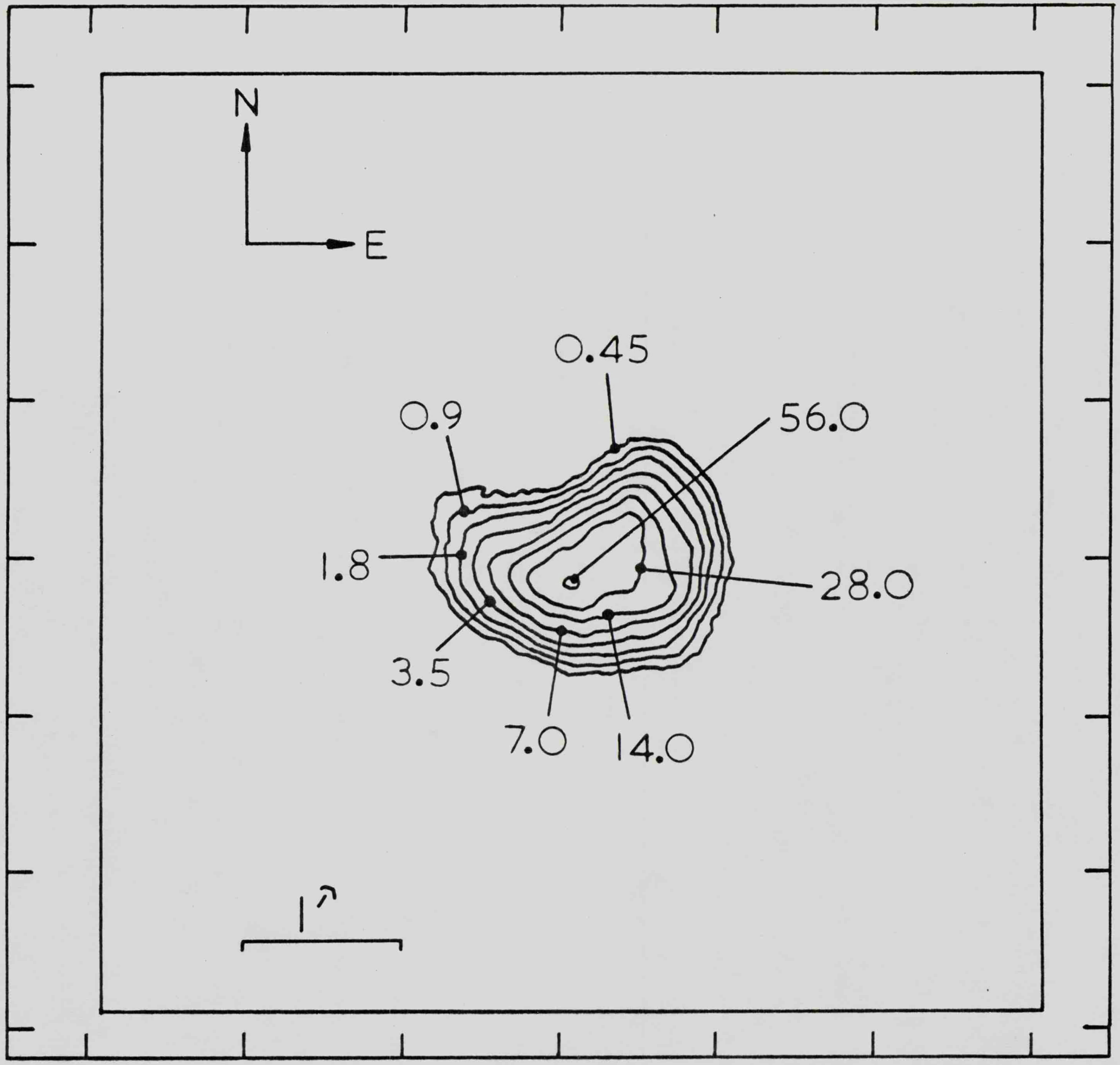

Fig. 4.12.b.

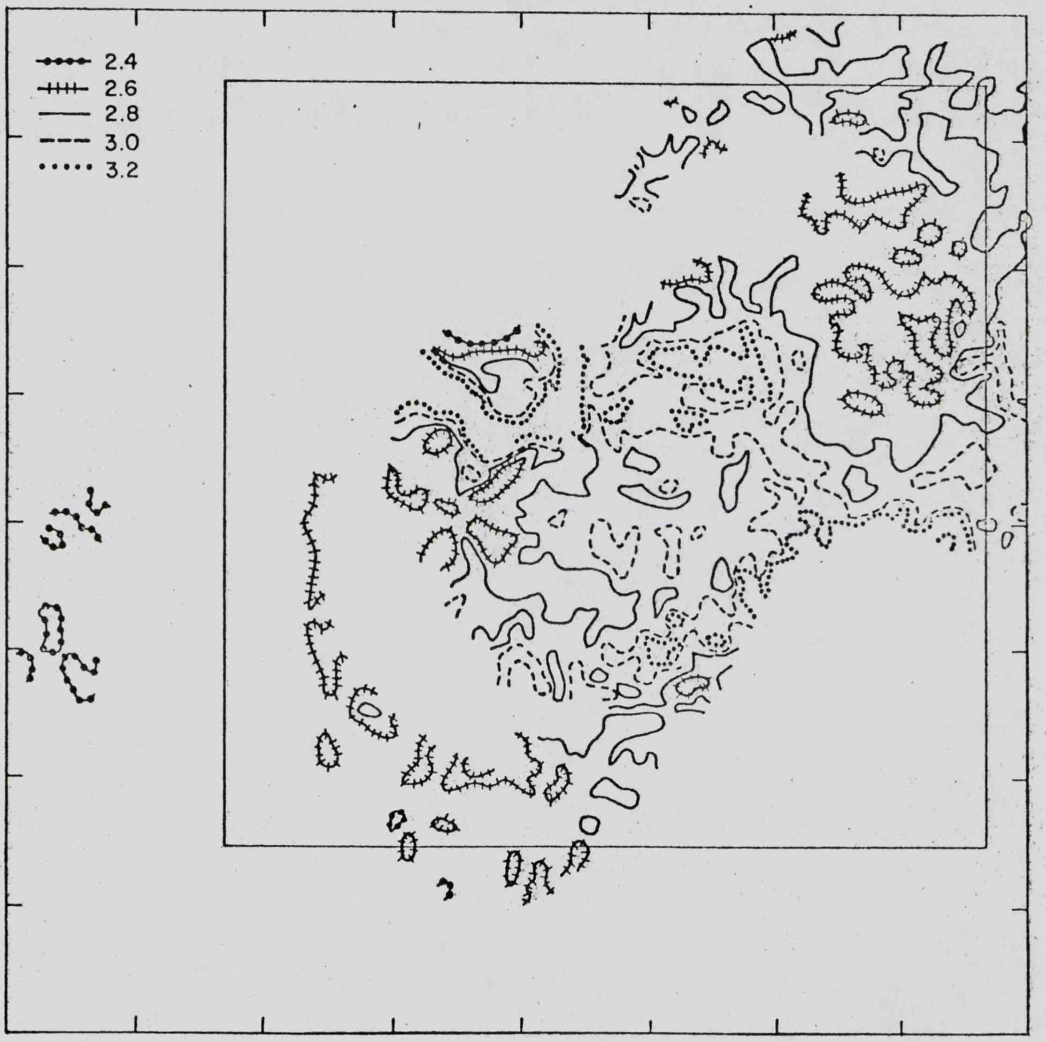

Fig. 4.13.

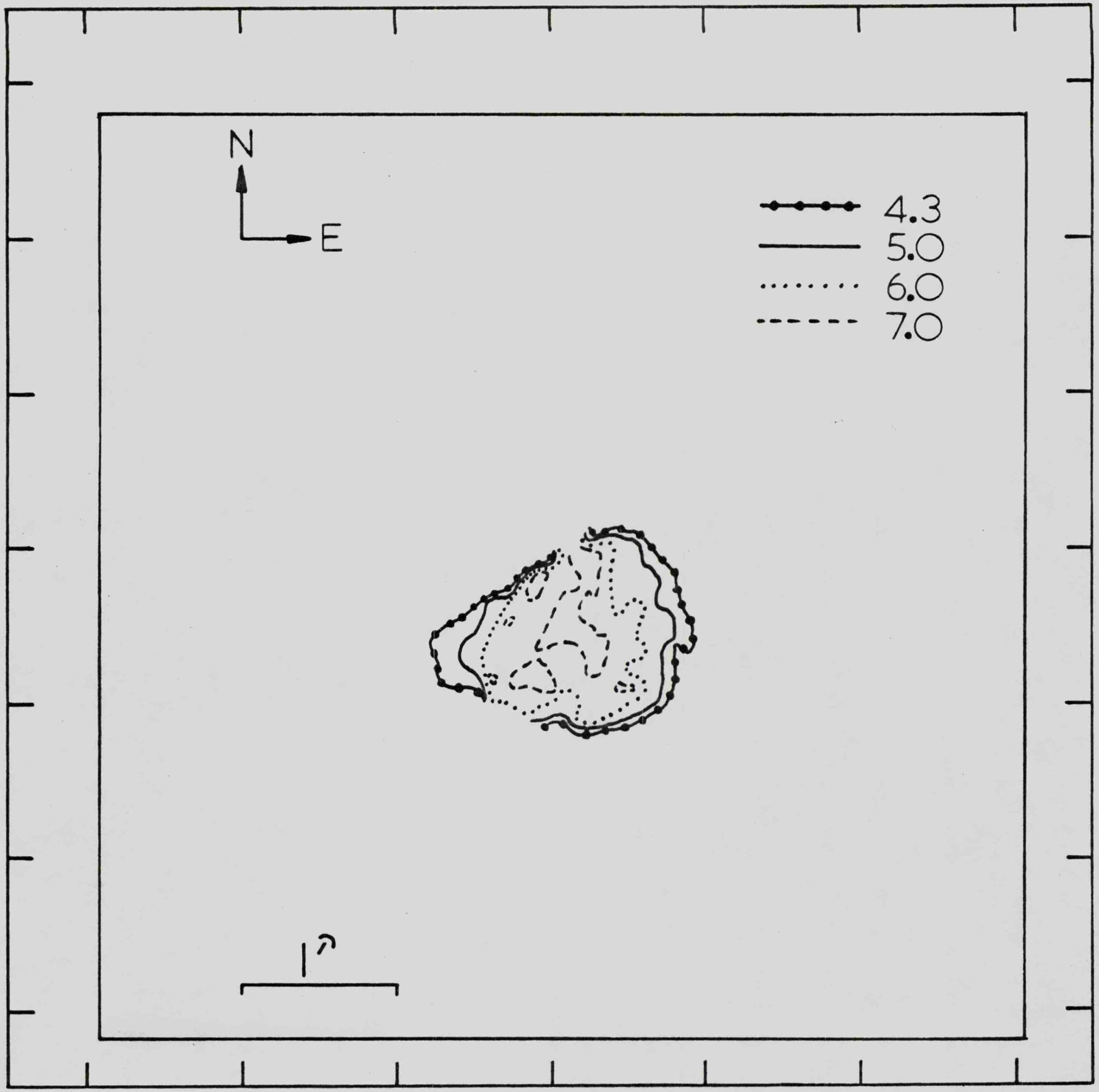

Fig. 4.14.

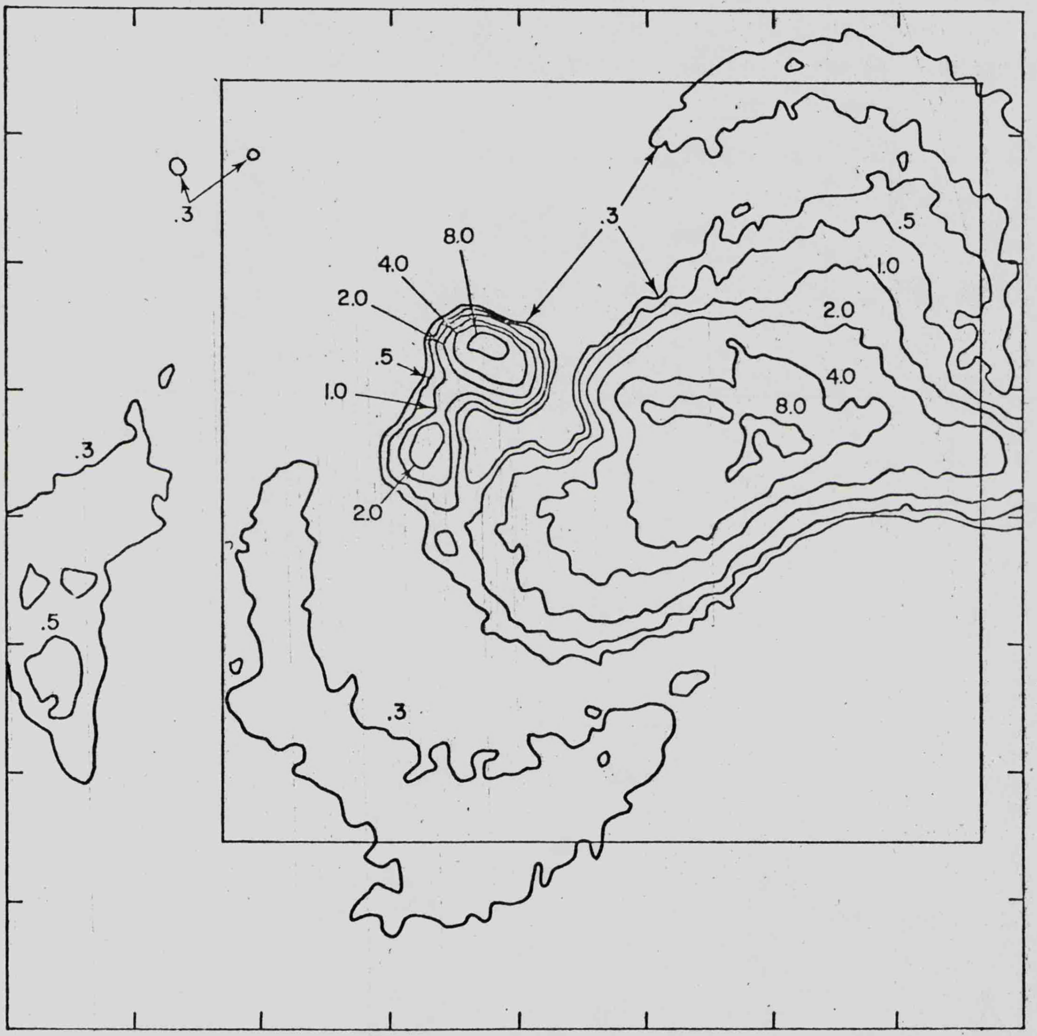

Fig. 4.15.

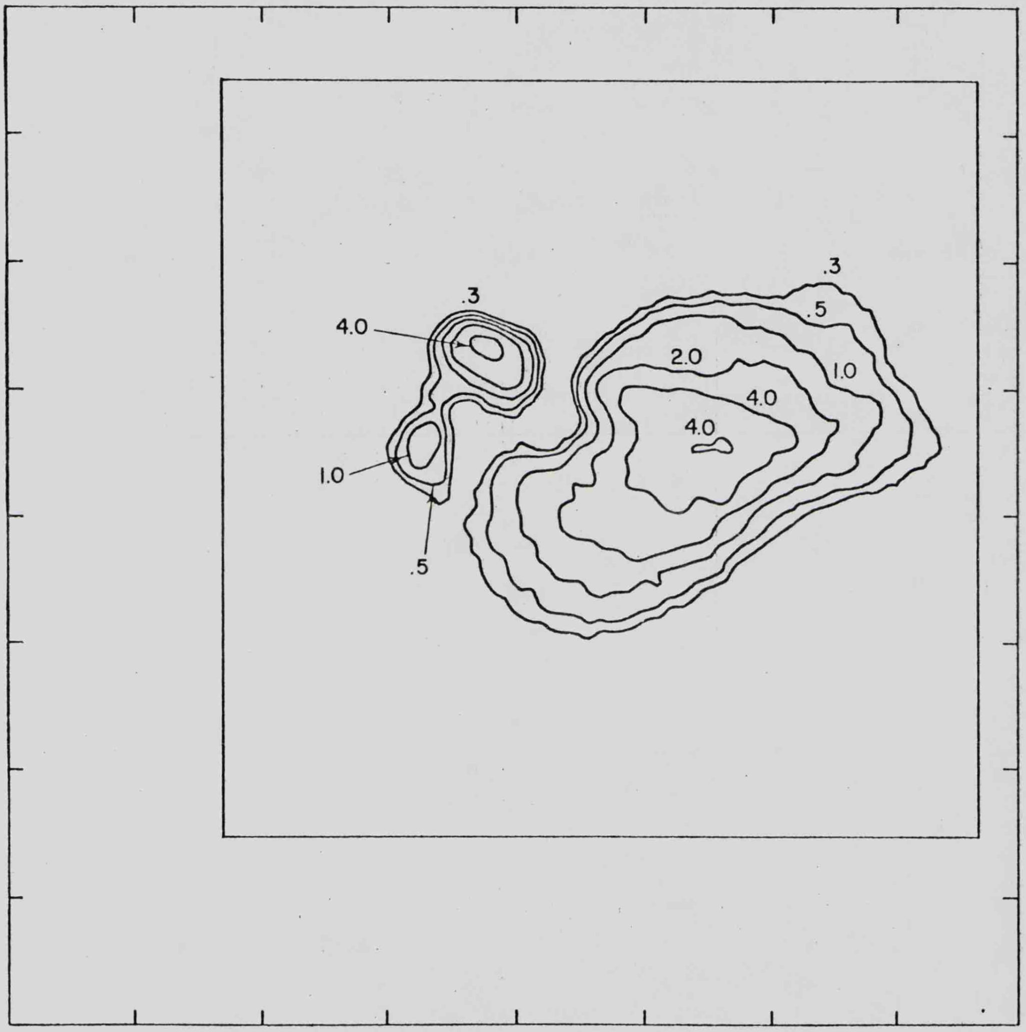

Fig. 4.16.

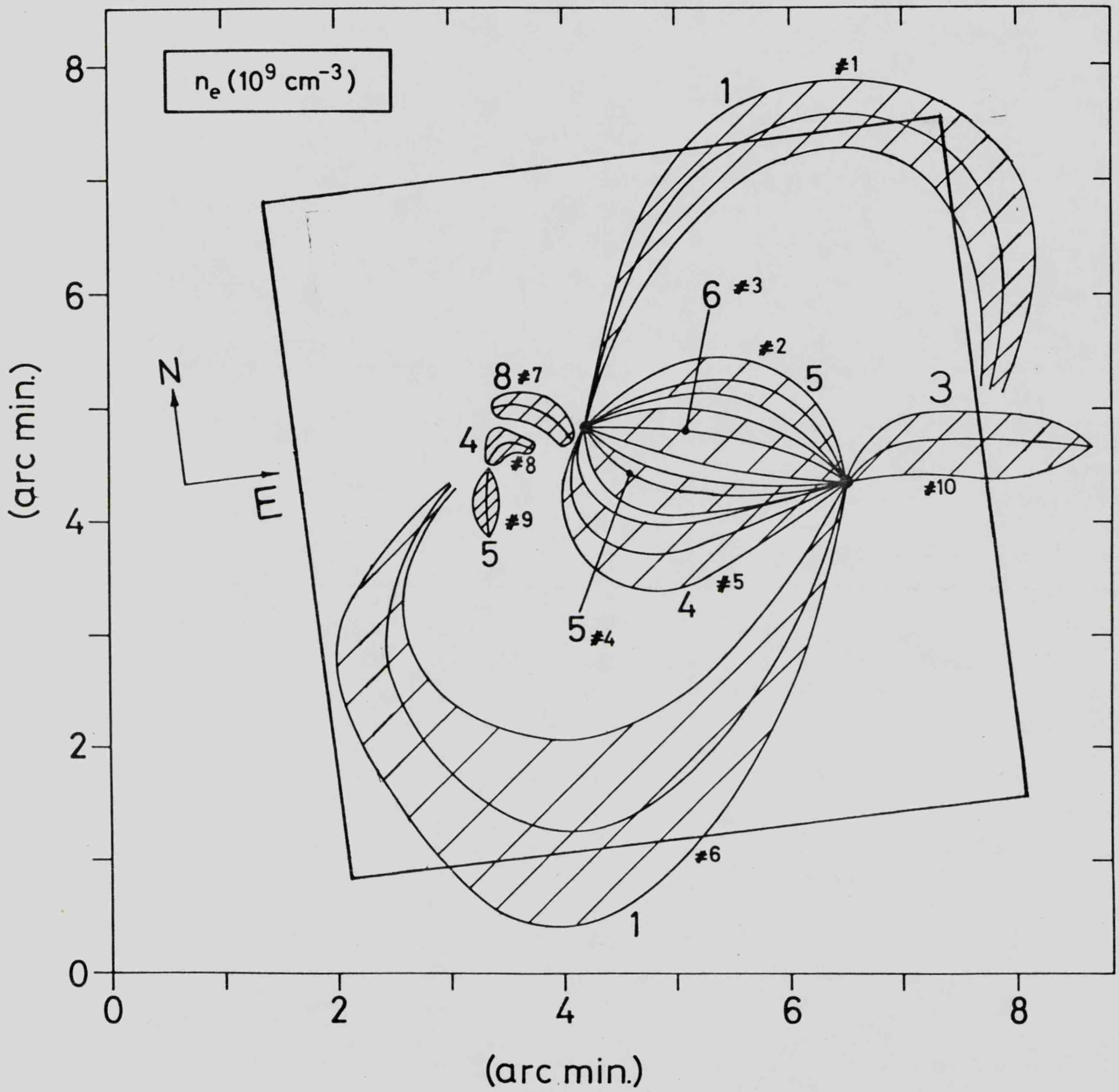

Fig. 4.17.

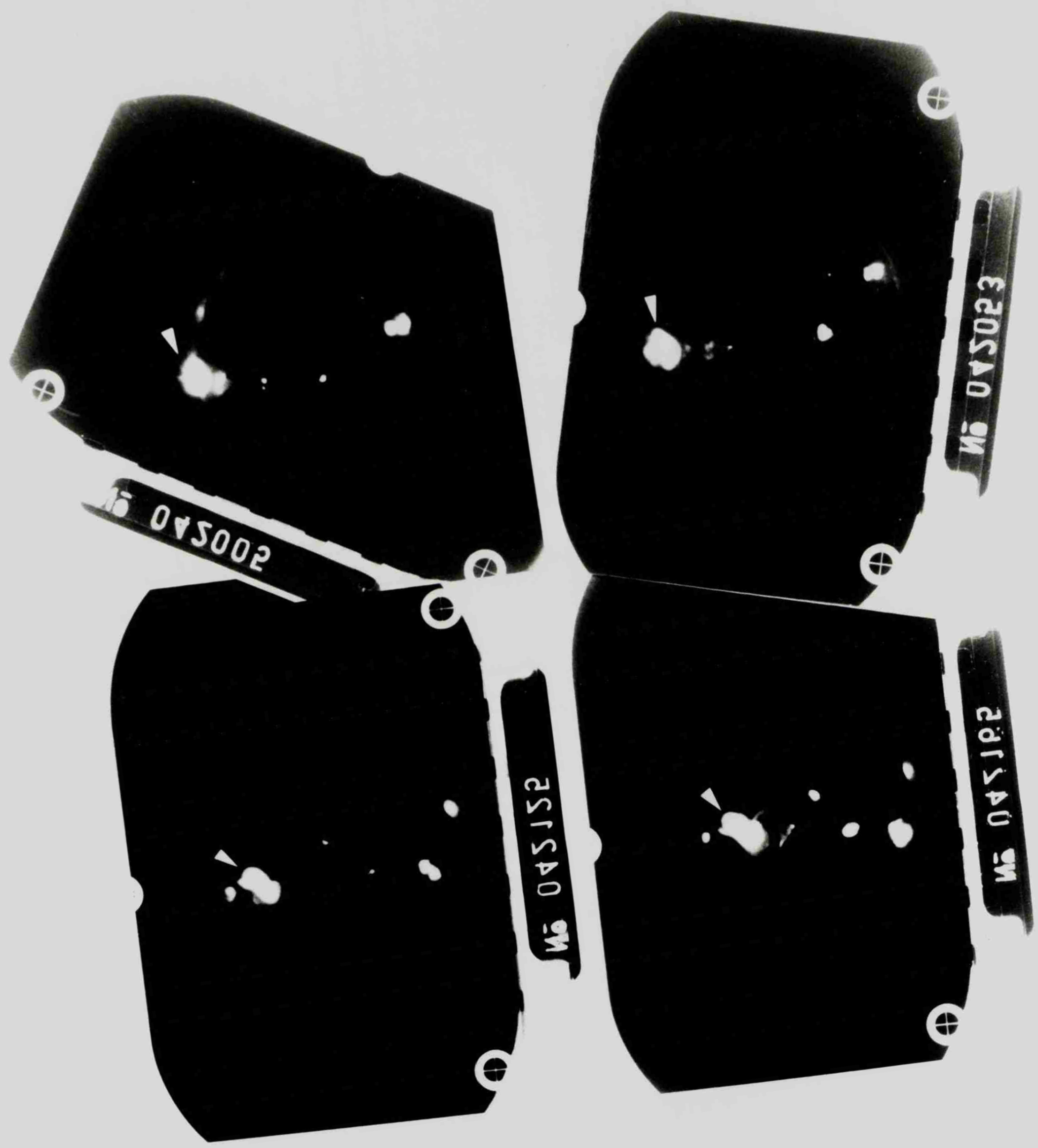

Fig. 4.18.i.

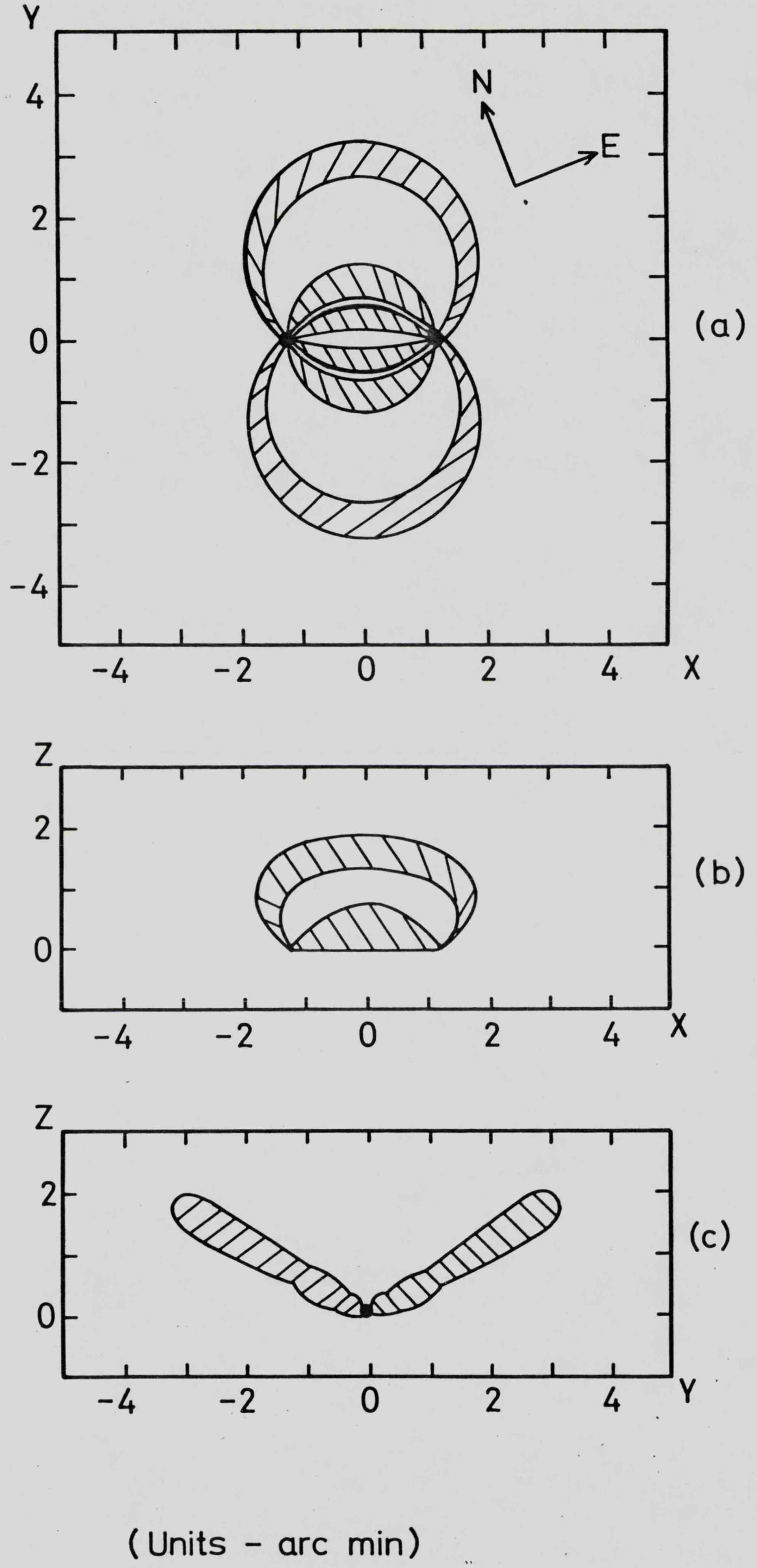

Fig. 4.18.ii.

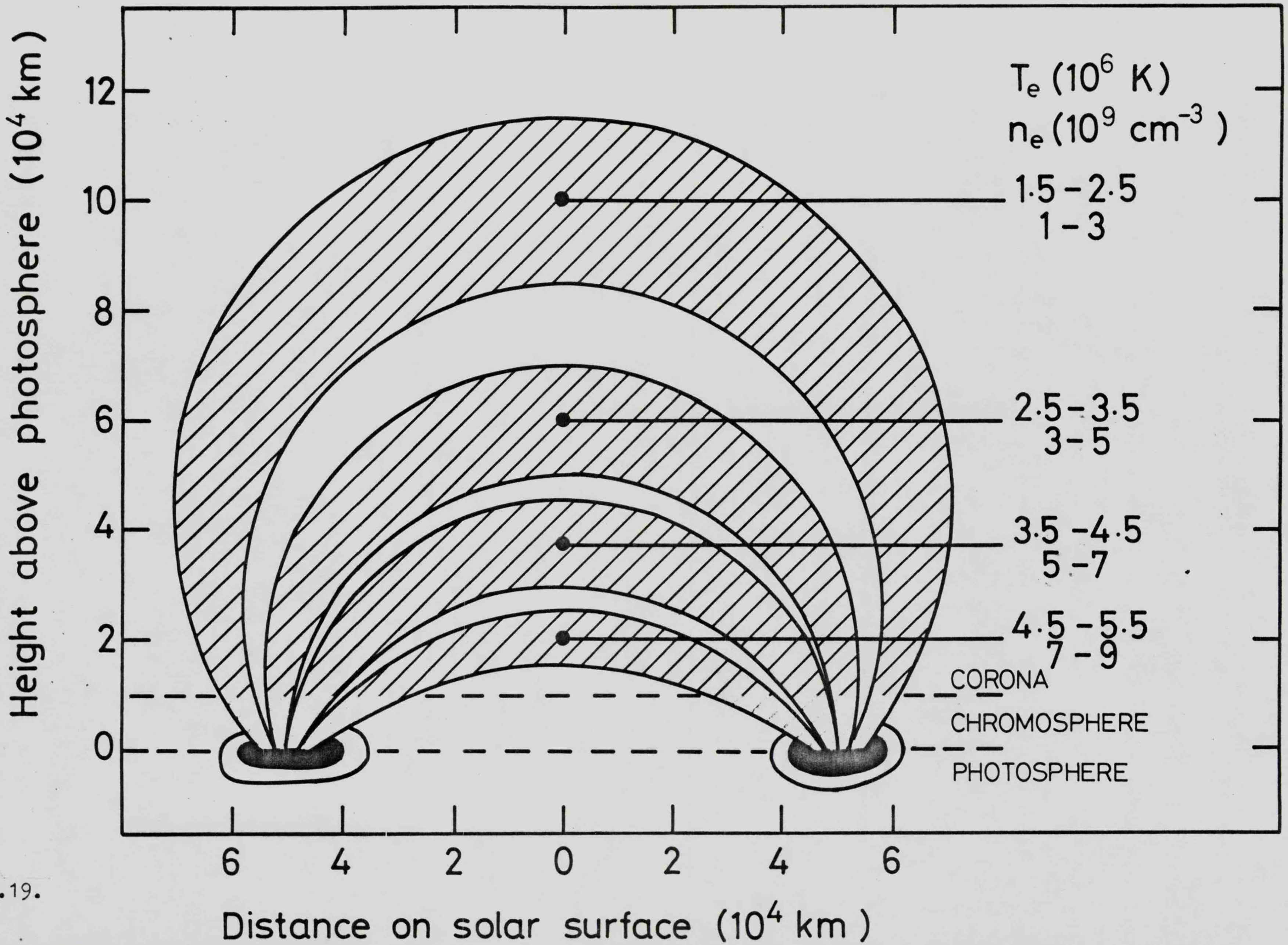

Height above photosphere (10^4 km)
Distance on solar surface (10^4 km)
T_e (10^6 K)
n_e (10^9 cm^{-3})
1.5 – 2.5
1 – 3
2.5 – 3.5
3 – 5
3.5 – 4.5
5 – 7
4.5 – 5.5
7 – 9
CORONA
CHROMOSPHERE
PHOTOSPHERE

Fig. 4.19.

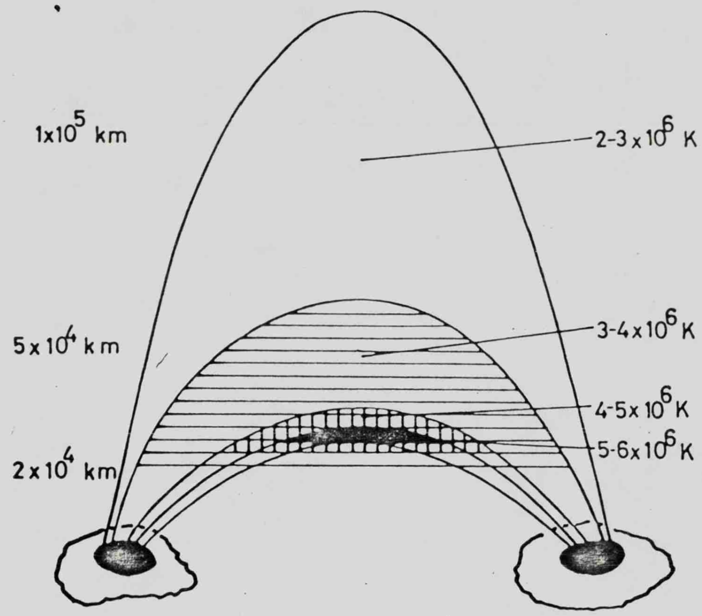

Fig. 4.20.

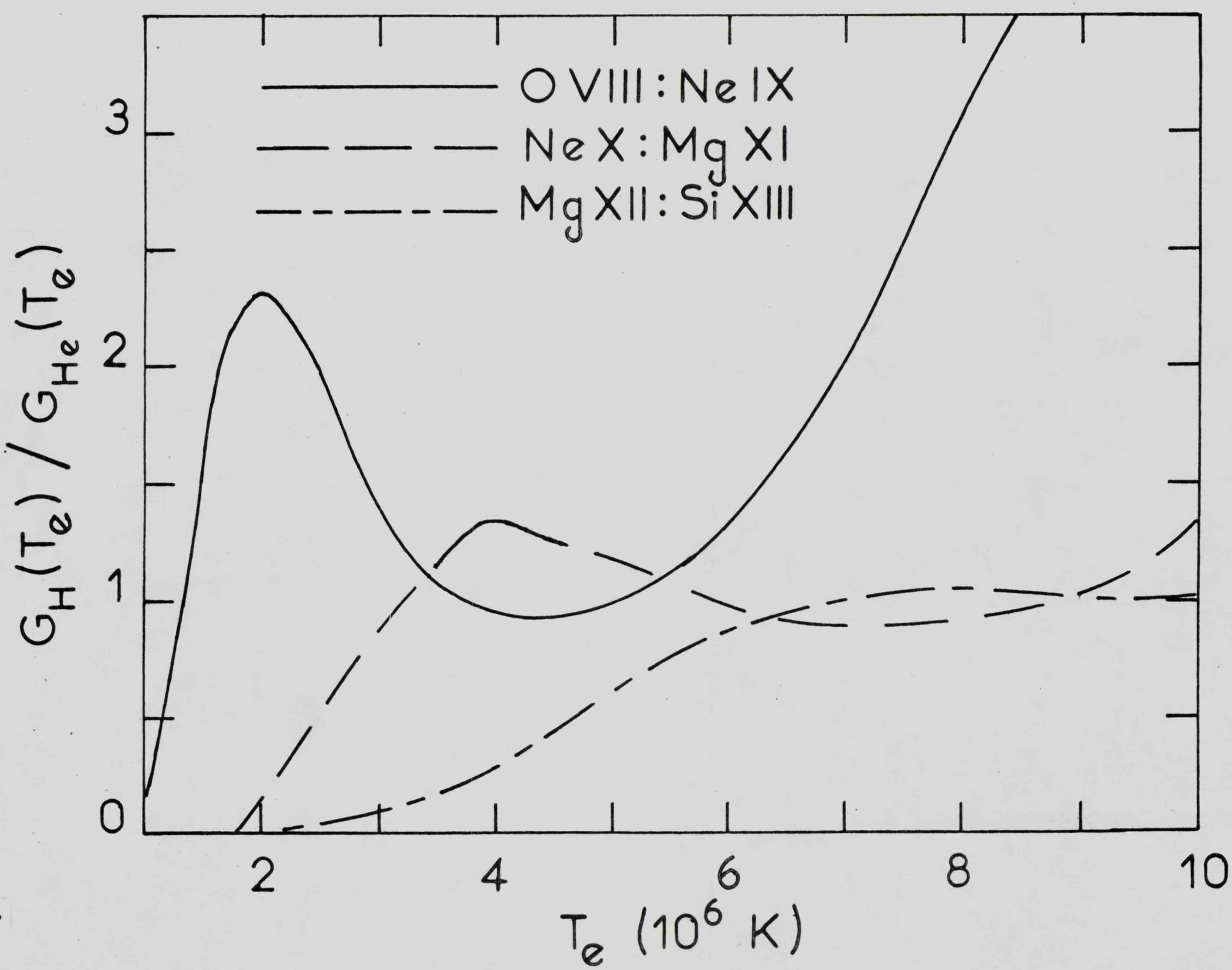
O VIII : Ne IX
Ne X : Mg XI
Mg XII : Si XIII
$G_H(T_e) / G_{He}(T_e)$
0
1
2
3
2
4
6
8
10
T_e (10^6 K)

Fig. 4.21.

Chapter 5

HELIUM-LIKE IONS

5.1 Introduction

The lines of He-like ions make a substantial contribution to the solar X-ray spectrum. In particular, for $\lambda < 25$ Å, the lines of O VII, Ne IX and Mg XI are among the most prominent lines in the spectra of non-flaring active regions. Weaker lines which have been observed include those from Na X, Al XII and Si XIII. The atomic physics of He-like ions is now relatively well understood, and many of the He-like lines are useful for plasma diagnosis (see Chapter 4 and below).

Figure 5.1 is a simplified term diagram of a He-like ion, showing the four n = 2 terms and their main radiative decay processes, together with the approximate radiative transition probabilities. Due to the particularly stable nature of the completed electron shell structure (as in the 'inert' gases such as He itself), the 1s electrons have a high ionisation potential and a high excitation potential to the first excited n = 2 terms. The first excitation potential is over 75% of the ionisation energy (Gabriel and Jordan, 1972; Gabriel, 1972c).

Most observations of the solar soft X-ray line spectrum have shown at least the stronger of the He-like lines (e.g. $1s^2.{}^1S_0 - 1s2p.{}^1P_1$ transition in O VII, Ne IX and Mg XI). Solar and laboratory observations of the He-like lines and their satellites have been reviewed by Doschek (1972), Gabriel (1972b), Jordan (1972), Walker (1972), Fawcett (1974) and Parkinson (1975a). Results of particular interest and more recent observations will be discussed in the appropriate sections of the present chapter.

It is convenient to discuss the He-like lines and their satellites under three headings:

(1) The (resonance) line series $1s^2.^1S_0 - 1snp.^1P_1$.

(2) The $n = 2 \rightarrow 1$ resonance, intercombination and forbidden lines.

(3) The satellite lines.

The data presented here are from SL1101 and SL1206 observations of regions 11619, 12628 and 12624, and are restricted to the relatively abundant ions O VII, Ne IX and Mg XI.

5.2 The Resonance Line Series $1s^2.^1S_0 - 1snp.^1P_1$

The resonance line $1s^2.^1S_0 - 1snp.^1P_1$ will be referred to as the 'nR' line (except that the first line of the series, '2R', will be called 'R').

Several lines in the nR series are observed, for O VII up to n = 3, for Ne IX up to n = 6, and for Mg XI up to n = 3. Table 5.1 lists the theoretical wavelengths (Ermolaev and Jones, 1974, see Section 3.3.3.2), and the measured and predicted intensities. The latter were calculated using the two level ion model and the atomic data and element abundances discussed in Section 4.2. It may be shown, by arguments similar to those in Section 4.2, that the two level ion model is a reasonable approximation for these members of the nR series.

There are two cases where blending is believed to be significant. The Ne IX 4R line at 11.000 Å is blended with the Na X R line at 11.003 Å (see Section 4.6.2), and the Ne IX 5R line at 10.764 Å is blended with the Fe XVII $2p^6.^1S_0 - 2p^5 6d.^3D_1$ line at 10.768 Å (see Section 6.3).

It may be seen from Table 5.1 that there is reasonably good agreement between the measured and calculated intensities, thus supporting the emission measure/temperature models and the use of the two level ion model with the Gaunt factor/oscillator strength approximation.

5.3 The n = 2 → 1 lines $1s^2.{}^1S_0 - 1s2p.{}^1P_1, {}^3P_{1,2}, 1s2s.{}^3S_1$

Figure 5.2 is a term diagram showing the ground and n = 2 terms of the He-like ion. The solid lines indicate collisional transitions and the dashed lines radiative transitions. The radiative transitions from n = 2 to the ground state are:

$1s^2.{}^1S_0 - 1s2p.{}^1P_1$	which forms the resonance line,
$1s^2.{}^1S_0 - 1s2p.{}^3P_1$	which forms the intercombination line,
$1s^2.{}^1S_0 - 1s2p.{}^3P_2$	which is a magnetic quadrupole line transition,
$1s^2.{}^1S_0 - 1s2s.{}^3S_1$	which forms the forbidden line (it is a magnetic dipole transition),
$1s^2.{}^1S_0 - 1s2s.{}^1S_0$	which is a two-photon transition (see Section 2.4.3.2).

In many observations, including the present ones, the magnetic quadrupole line is unresolvable from the intercombination line. For Z $\lesssim$ 12, the magnetic quadrupole transition is expected to contribute less than 10% to the total intensity of the blend (Gabriel, 1972a).

For convenience, the spectral lines will be referred to by key letters, as follows:

R = resonance line (as in Section 5.2 above)

I = intercombination line (and is taken to include the magnetic quadrupole transition, unless otherwise stated),

F = forbidden line.

5.3.1 Theory for the Relative Intensities

The theory for the relative intensities of the R, I and F lines was first worked out by Gabriel and Jordan (1969b), following their identification of the F line in the solar X-ray spectrum (Gabriel and Jordan, 1969a). Gabriel and Jordan (1969b) solved the equations of statistical equilibrium for the ground state and the six n = 2 levels, and showed that the photon intensity ratio $\mathcal{R}$ of the F to I line intensities is given by:

$$\mathcal{R} = A(2^3S \rightarrow 1^1S) \left[\frac{1 + \mathcal{F}}{B} - 1\right] \times \left[A(2^3S \rightarrow 1^1S) + (1 + \mathcal{F}) \left\{ n_e C(2^3S \rightarrow 2^3P) + \phi \right\}\right]^{-1} \tag{5.1}$$

where:

$$\mathcal{F} = C(1^1S \rightarrow 2^3S)/C(1^1S \rightarrow 2^3P) \tag{5.2}$$

and the effective branching ratio:

$$B = \frac{1}{3} \frac{A(2^3P_1 \rightarrow 1^1S)}{A(2^3P_1 \rightarrow 1^1S) + A(2^3P \rightarrow 2^3S)} + \frac{5}{9} \frac{A(2^3P_2 \rightarrow 1^1S)}{A(2^3P_2 \rightarrow 1^1S) + A(2^3P \rightarrow 2^3S)} \quad . \tag{5.3}$$

$A(i \rightarrow j)$ is the spontaneous transition probability and $C(i \rightarrow j)$ the collisional excitation rate coefficient. ϕ is the photo-excitation rate (in sec^{-1}) from 2^3S to 2^3P; it is important only for ions of $Z \leqslant 7$ (Gabriel and Jordan, 1973) and thus may be neglected in the present work. $\mathcal{F}$ is an effective rate ratio which includes all processes populating 2^3S and 2^3P, in particular cascades from higher levels.

It can be seen from Equation 5.1 that there will be a range of electron densities over which $\mathcal{R}$ will be sensitive to, and may be used to measure, the electron density n_e. For the limiting case of $n_e = 0$, $\mathcal{R}$ has a value $\mathcal{R}_0$ given by:

$$\mathcal{R}_0 = \frac{1 + \mathcal{F}}{B} - 1 \ . \qquad (5.4)$$

Equation 5.1 may be rewritten as:

$$n_e = \frac{A(2^3S \rightarrow 1^1S) \left[(\mathcal{R}_0/\mathcal{R}) - 1 \right]}{C(2^3S \rightarrow 2^3P)(1 + \mathcal{F})} \ . \qquad (5.5)$$

In order to allow for uncertainties in the atomic data and in the observed intensity ratios, Gabriel and Jordan (1969b) have defined an upper limit to the range of $\mathcal{R}$ that can be used to derive significant values of n_e. This limit is arbitrarily taken as $\mathcal{R} = 0.9\,\mathcal{R}_0$. The corresponding lower limit critical density n_e^* is thus given by (from Equation 5.5):

$$n_e^* = \frac{A(2^3S \rightarrow 1^1S)}{9\ C(2^3S \rightarrow 2^3P)\ (1 + \mathcal{F})} \ . \qquad (5.6)$$

Hence, a measured value of $\mathcal{R} \geqslant 0.9\mathcal{R}_0$ is taken to imply that $n_e \leqslant n_e^*$.

Since the original paper of Gabriel and Jordan (1969b), there have been significant improvements in the accuracy of some of the atomic data required in the theory outlined above (see Gabriel and Jordan, 1970; Freeman et al.,1971; Gabriel and Jordan, 1972; Blumenthal et al., 1972; Gabriel, 1972c; Gabriel and Jordan, 1973). The present status of the atomic data is summarized by Gabriel and Jordan (1973); their recommended values are adopted in the present work and are given in Table 5.2 for ions of $6 \leqslant Z \leqslant 26$. The value of $\mathcal{F}$ used is 0.35. The collisional rate coefficients $C(i \rightarrow j)$, and hence $\mathcal{F}$, $\mathcal{R}$, $\mathcal{R}_0$ and n_e^*, are evaluated at the electron temperature T_{em} at which the emission function $G(T_e)$ of the ion is a maximum; however, Gabriel and Jordan (1973) have shown that temperature variations will usually have only a small effect. In quantitative terms, for $8 \leqslant Z \leqslant 14$ and T_e such that $G(T_e) \geqslant 0.5G(T_{em})$, the temperature dependence of $\mathcal{F}$ causes changes of less than $\pm$ 10% to the value of $\mathcal{R}$.

It is the variation of $\mathcal{R}$ between observations, rather than its absolute value, that should be used to test whether $\mathcal{R} < \mathcal{R}_0$ (and hence $n_e > n_e^*$), thus guarding against possible errors in the atomic data (Gabriel and Jordan, 1972).

It is useful to define a quantity $\mathcal{G}$, the ratio of the sum of the photon intensities of the F and I lines to the photon intensity of the R line. It can be seen from Figure 5.2 that:

$$\mathcal{G} = (I_F + I_I)/I_R$$

$$= \left[C(1^1S \rightarrow 2^3S) + C(1^1S \rightarrow 2^3P)\right] / C(1^1S \rightarrow 2^1P) \qquad (5.7)$$

and is independent of n_e. As with $\mathcal{F}$, $\mathcal{G}$ is an effective rate ratio which includes all processes populating 2^3S, 2^3P and 2^1P, in particular cascades from higher levels. Gabriel and Jordan (1969b) have shown that over a wide range of solar observations, $\mathcal{G} \approx 1.1$, thus supporting the assumption that ratios of ground state excitation rates are insensitive to T_e or Z.

The theory outlined above applies to a plasma in ionization equilibrium or to an ionizing plasma. For a recombining plasma the spectra may be produced primarily by radiative recombination, and under these conditions it is expected that there should be little change in the interpretation of $\mathcal{R}$, though $\mathcal{G}$ would tend to 3.0 (Gabriel and Jordan, 1969b).

5.3.2 Previous Solar Measurements

Most coronal measurements of the relative intensities of the lines R, I and F have shown no significant variations of the observed ratio $\mathcal{R}$, either between individual measurements, or from the low density limit $\mathcal{R}_0$ predicted by the theory, when account is taken of the experimental uncertainties and an additional variation of $\pm$ 10% allowed to cover the possible temperature dependence of $\mathcal{R}$ (see e.g. Batstone et al. 1970; Rugge and Walker, 1970; Parkinson, 1971b, 1972, 1975c; Acton et al. 1972; Bonnelle et al. 1973).

To date, the best evidence for significant variations in $\mathcal{R}$ is the observation of the coronal O VII emission by Acton and Catura (1975), who obtained one dimensional X-ray spectroheliograms with a spatial resolution of 1.3 arc min FWHM, using a collimated crystal spectrometer. From these results and the calculations of Gabriel and Jordan (1973), Acton and Catura infer electron densities (averaged over the spectrometer field-of-view) of up to $n_e \approx 7 \times 10^9 cm^{-3}$.

5.3.3 The Present Measurements

Table 5.3 lists the measured wavelengths and photon intensities of the R, I and F lines of O VII, Ne IX and Mg XI from the SL1101 and SL1206 observations of regions 11621 (Parkinson, 1975c), 11619, 12628 and 12624, together with the theoretical wavelengths of Ermolaev and Jones (1974). Table 5.4 gives the corresponding (photon) intensity ratios $\mathcal{R}$, $\mathcal{G}$, I/R, F/R, and their mean values. Figures 5.3 to 5.5 show examples of the observations. All the data presented in these Tables and Figures were obtained in the slow scan mode of the spectrometer, giving a very high sensitivity and wavelength resolution (see Chapter 3).

For regions 11619, 12628 and 12624, the measured wavelengths in Table 5.3 have been derived by using the theoretical wavelength λ_R (Ermolaev and Jones, 1974) and measured Bragg angle θ_R of each R line to calibrate the corresponding spectra; i.e. for any line i (with measured Bragg angle θ_i) on a given scan the measured wavelength λ_i is taken as (see Section 3.3.3.2):

$$\lambda_i = 2d_{eff} \sin \theta_i \qquad (5.8)$$

where: $$2d_{eff} = \lambda_R / \sin \theta_R , \qquad (5.9)$$

since the variation of $2d_{eff}$ over the interval $|\lambda_i - \lambda_R|$ is expected to be negligible. The generally close agreement between the measured and theoretical wavelengths of the I and F lines justifies this assumption, and the spread in values reflects the accuracy with which a measured wavelength may be assigned to a feature (via λ_R, θ_R and θ_i). This discussion is of particular relevance to the next section, where measured wavelengths are presented for the satellite lines which occur close to the R, I and F lines.

The criterion given in Section 5.3.2 for a significant departure of the ratio $\mathcal{R}$ from the mean value $\bar{\mathcal{R}}$, may be formalised as:

$$\frac{|\mathcal{R} - \bar{\mathcal{R}}|}{\delta\mathcal{R} + 0.1\bar{\mathcal{R}}} > 1 . \tag{5.10}$$

Applying this condition to the results in Table 5.4, it is seen that, for O VII at least, there are no significant variations in $\mathcal{R}$, and that $\mathcal{G} \approx 1.1$ in accordance with theory. In Ne IX and Mg XI there are significant variations in $\mathcal{R}$ according to the above criteria; however, they are not interpreted here as indicating the presence of electron densities greater than n_e, as there are also significant variations in $\mathcal{G}$ (using a similar criterion to Formula 5.10), which are not predicted by the calculations summarized in Section 5.3.1 above. Although from the present measurements it is not possible to determine exactly the cause of the discrepancies, it is interesting to note that the relative intensity F:R appears to show greater variability than the ratio I:R (see Table 5.4).

Acton and Catura (1975) have discussed the variations in $\mathcal{G}$ observed in their own coronal measurements, and have interpreted them as variations in the optical depth of the R line. However, Acton and Catura have treated the radiative transfer problem purely as an absorption effect, whereas it is shown below that under coronal conditions, the radiative transfer of the R line is much closer to being a scattering process.

Under coronal conditions, the ratio of the spontaneous radiative decay rate for the transition $1s2p.^1P_1 \rightarrow 1s^2.^1S_0$ (giving rise to the R line) to the total depopulation rate from the $1s2p.^1P_1$ level, is practically unity (see Section 4.2.4), and hence an R line photon which undergoes resonance line absorption is simply re-emitted, though its direction may be changed (see Section 2.4.3.6). However, from consideration of the coronal active region structures observed on high resolution X-ray images (see e.g. Vaiana et al. 1973a, b; present work, Section 4.5.3), it appears unlikely that the plasma geometry could provide a satisfactory explanation of variations in $\mathcal{G}$ of the magnitude observed in the present data and that of Acton and Catura (1975). It may be that the atomic model for the He-like ions requires slight revisions.

5.4 The Satellites to the He-like Lines

The satellite lines considered here are systems of lines that appear close to the members of the resonance series ($1s^2.^1S_0$ - $1sn'p.^1P_1$) of highly ionized He-like ions. These satellites are due to transitions with the same configurations as the parent line, but with an additional electron in some outer orbit nl, i.e.

$$1s^2nl - 1sn'l'nl \quad .$$

Thus the upper level is a doubly excited state. As n increases, the satellite spectra become closer in wavelength to the parent line, until finally they are unresolvable from it (see Section 4.2.4).

These satellites were first reported from a laboratory carbon vacuum spark source by Edlén and Tyrén (1939), who proposed the above configurations. Gabriel and Jordan (1969a) classified the terms responsible. Figure 5.6 is a schematic energy level diagram showing the He-like and satellite transitions.

For the upper levels of the satellite transitions there are four populating mechanisms which may be considered, though some may not be permitted. These processes are (Gabriel and Jordan, 1972):

(1) dielectronic recombination of the He-like ion,

(2) inner-shell excitation of the Li-like ion,

(3) inner-shell ionization of the Be-like ion,

(4) simultaneous impact excitation of two electrons in the Li-like ion.

Gabriel and his co-workers (Gabriel and Jordan, 1969a; Gabriel et al. 1969; Gabriel and Paget, 1972; Gabriel, 1972a; Bhalla et al. 1975) have shown that the dominant mechanisms are (1) and (2), with (1) being generally the more important, except in transient plasmas.

We shall be concerned here mainly with satellite lines of the type

$$1s^2nl - 1s2l'nl.$$

Many of the satellites including all those with n = 2, occur on the long-wavelength side of the corresponding resonance line, though this is fortuitous (Summers, 1973).

5.4.1 Calculated Wavelengths

The wavelengths of the satellites with n = 2 have been calculated independently by Gabriel (1972a), Goldsmith (1974) and Vainshtein and Safronova (1972). These results agree with each other and with laboratory (e.g. Peacock et al. 1973; Feldman et al. 1974; Golts et al. 1974) and solar measurements (e.g. Parkinson, 1972, 1975c; Grineva et al., 1973) generally to within 0.02 to 0.05%, for elements of $6 \lesssim Z \lesssim 29$. The possible transitions are listed in Table 5.5, and following Gabriel (1972) each transition is given a key letter for ease of reference.

Summers (1973) has calculated energy levels for the satellite lines with n = 2, 3 and 4. The derived wavelengths agree with those of Gabriel (1972) to within about 0.1 to 0.2% for n = 2 and Z = 10 (Ne). For the n = 3 and 4 satellites the wavelengths are expected to be somewhat more accurate than for n = 2. The wavelength difference between a satellite and the parent resonance line is expected to be more accurate than the absolute wavelengths, due to cancellation of systematic errors (see e.g. Gabriel and Jordan, 1969a; Gabriel, 1972a; Summers, 1973).

A short description of dielectronic recombination is now in order, and is, of course, not restricted to He-like ions.

5.4.2 Dielectronic Recombination

Dielectronic Recombination may be considered as a three-part process (Burgess, 1964b, 1965; Gabriel and Jordan, 1972):

(1) The colliding electron (at below threshold energy) excites an ion to a resonance transition, but is itself trapped in an outer orbital. If autoionization now occurs, the system returns to its initial state and no recombination has taken place.

(2) Alternatively, the doubly excited ion stabilizes by radiative decay of the inner excited electron, emitting a photon of resonance radiation of the recombining ion, shifted slightly in wavelength (usually to longer wavelength) by the influence of the additional outer electron.

(3) The ion is now singly excited and cascades to its ground state.

Autoionization is the inverse process to dielectronic recombination.

5.4.3 Calculated Intensities

The theory for the intensities of the n = 2 satellite spectra has been developed by Gabriel and his co-workers (Gabriel et al., 1969; Gabriel and Paget, 1972; Gabriel, 1972a; Bhalla et al. 1975), the current status being given by Bhalla et al. At present there are no detailed calculations available for the intensities of the individual satellite lines with $n \geqslant 3$.

The following discussion of the theoretical satellite line intensities follows the references cited above.

5.4.3.1 Dielectronic Recombination.

The intensity (in photons per unit volume) of a satellite line due to dielectronic recombination of the He-like ion is (c.f. Figure 5.6):

$$I_s = 4\pi^{3/2} a_o^3 \frac{g_s}{g_1} \frac{A_r A_a}{(A_a + \sum A_r)} n_{He} n_e \frac{\exp(-E_s/T_e)}{T_e^{3/2}} \qquad (5.11)$$

where: a_o = Bohr radius,

n_{He} = number density of He-like ions,

n_e = number density of electrons,

g_s = statistical weight of the satellite level,

g_1 = statistical weight of the He-like ground state,

A_a = transition probability for decay by autoionization,

A_r = transition probability for decay by radiation,

E_s = energy of the satellite level above the He-like ground state (Rydberg).

T_e = electron temperature (Rydberg),

and the summation $\sum A_r$ is over all possible radiative transitions from the satellite level.

Equation 5.11 may be rewritten

$$I_s = 2.06 \times 10^{-16} \frac{g_s}{g_1} \frac{A_r A_a}{(A_a + \sum A_r)} n_{He} n_e \frac{\exp\left[-E_s/(kT_e)\right]}{T_e^{3/2}} \qquad (5.12)$$

where T_e is now in K.

The intensity (in photons per unit volume) of the He-like ion resonance line is:

$$I = n_{He} n_e C(1 + \alpha) \tag{5.13}$$

where: C = collisional excitation rate coefficient,

and α is a correction for the contribution to the resonance line intensity from dielectronic recombination, i.e. it is the sum over all satellites which cannot be resolved spectroscopically from the resonance line. In their computations Gabriel (1972a) and Bhalla et al. (1975) have taken this to include all satellites with $n \geqslant 3$. Then

$$\alpha = D/C \tag{5.14}$$

where D is that fraction of the dielectronic recombination rate coefficient responsible for this contribution.

Combining Equations 5.12 to 5.14, the ratio of a satellite's intensity due to dielectronic recombination, to the resonance line intensity is:

$$I_s/I = (1 + \alpha)^{-1} \; F_1(T_e) \; \times \; F_2(s) \tag{5.15}$$

where: $F_1(T_e) = 1.2 \times 10^{-13} \dfrac{E_o}{\bar{g} \, f \, T_e} \exp\left[(E_o - E_s)/(kT_e)\right]$,

$$F_2(s) = \frac{g_s}{g_1} \frac{A_r A_a}{(A_a + \sum A_r)} \; ,$$

and $g_1 = 1.$

E_o is the energy of the resonance line (eV) and T_e is in K.

$\bar{g}$ is the temperature averaged Gaunt factor, taken as 0.2.

f is the effective oscillator strength for the resonance line transition, and is taken semi-empirically as f = 0.55 for astrophysical plasmas, in which $1s2s.\,^1S$ decays by two-photon emission.

α may be calculated from the dielectronic recombination rate coefficient (Burgess, 1965; Gabriel, 1972a), and is $\sim 0.0 \rightarrow 0.1$.

The intensity ratio can thus be separated into a function of electron temperature, $F_1(T_e)/(1+\alpha)$, and a function of the individual satellite line, $F_2(s)$.

5.4.3.2 Inner-shell Excitation

The intensity (in photons per unit volume) of a satellite line due to inner-shell excitation of the Li-like ion is:

$$I'_s = n_{Li}\, n_e\, C' \quad \frac{A_r}{(A_a + \sum A_r)} \tag{5.16}$$

where: C' = inner-shell collisional excitation rate coefficient,

n_{Li} = number density of Li-like ions.

Since $E_s \approx E_o$:

$$C'/C \approx f'/f,$$

where f' is the effective oscillator strength for the inner shell excitation, and has been computed by Bhalla et al. (1975). Combining Equations 5.13, 5.14 and 5.16, the ratio of a satellite's intensity due to inner-shell excitation, to the resonance line intensity is:

$$I'_s/I = (1+\alpha)^{-1} \quad F'_1(T_z) \quad \times \quad F'_2(s) \ , \tag{5.17}$$

where: $F'_1(T_z) = n_{Li}/n_{He}$,

$$F_2(s) = \frac{f'}{f} \quad \frac{A_r}{(A_a + \sum A_r)} \ .$$

The ion abundance n_{Li}/n_{He} is a function both of electron temperature T_e and of the departure from ionization equilibrium. An "ionization temperature" T_z is defined, which is the temperature at which the actual ratio n_{Li}/n_{He} would exist in ionization equilibrium. Then n_{Li}/n_{He} is a function only of T_z, and:

$T_z = T_e$ for ionization equilibrium,

$T_z < T_e$ for transient ionizing conditions,

$T_z > T_e$ for transient recombining conditions.

Thus again the intensity ratio can be separated into a function of temperature, $F_1'(T_z)/(1+\alpha)$, and a function of the individual satellite line, $F_2'(s)$.

It may be noted from Equations 5.15 and 5.17 that the relative intensities (I_s/I) and (I_s'/I) are independent of electron density and element abundance. The relative importance of dielectronic recombination and inner-shell excitation varies between the different satellite transitions, and hence a suitable choice of spectra will yield diagnostic information on both the electron temperature and ionization conditions in the X-ray emitting plasma. Bhalla et al. (1975) have tabulated the data required to calculate (I_s/I) and (I_s'/I) as functions of T_e and T_z respectively, for the n = 2 satellites of elements $6 \leqslant Z \leqslant 26$.

5.4.4 The Present Measurements

The observations were made in the slow-scan mode of the SL1101/SL1206 spectrometers, with the ADP, gypsum and KAP crystals viewing the Mg XI, Ne IX and O VII spectra, respectively (see Figures 5.3 to 5.5).

5.4.4.1 The n = 2 Satellite Spectra.

Table 5.6 lists the measured wavelengths of the n = 2 satellites for Ne IX and Mg XI, from regions 11619, 12628 and 12624, together with the mean values. These figures are compared with Parkinson's (1972, 1975c) measured wavelengths for region 11621 and with the computed wavelengths of Gabriel (1972a) and Goldsmith (1974). It is seen that all the sets of wavelengths are in close agreement, generally to within 0.002 Å. The n = 2 satellites for O VII are too weak to be observed in the present data.

In Table 5.7 the measured intensities for Ne and Mg are compared with those predicted by using the calculations of Bhalla et al. (1975) together with the active region emission measure/temperature models (Section 4.3) and assuming (since this appears reasonable from the observational evidence in Chapter 4) that $T_z = T_e$; i.e. the predicted satellite line intensity (relative to the resonance line R) is taken as:

$$I_s/I = \frac{\sum_{T_e} \left[(I_s/I)(T_e)\right] I(T_e)}{\sum_{T_e} I(T_e)} \tag{5.18}$$

where: $(I_s/I)(T_e)$ = the total calculated intensity (due to dielectronic recombination and inner-shell excitation; Bhalla et al., 1975) of the satellites relative to the resonance line R, at electron temperature T_e, assuming $T_z = T_e$.

$I(T_e)$ = the intensity of the resonance line R, at electron temperature T_e, predicted by the active region emission measure/temperature model (Table 4.1).

It is seen from Table 5.7 that there is generally good agreement between the measured and predicted intensities. In particular, for the comparatively strong and well resolved multiplet q, r in Mg, it is interesting to note the significantly lower observed relative intensity for region 12624 (compared with the other regions), in accordance with the theory, and due to the presence in that active region of hotter material than in the other regions.

In all cases the measured intensity of the multiplet k, j, l in Mg is lower than predicted by about a factor of two. These lines are barely resolved from the forbidden line F, but at the worst, the measured intensities quoted provide upper limits. Thus, as discussed by Bhalla et al. (1975) and Parkinson (1975c), if the observed intensities for the multiplets q, r and k, j, l in Mg are taken at face value then the calculations of Bhalla et al. imply an ionizing plasma, which is somewhat at variance with the rest of the observations and which would be rather unexpected in stable active regions or the decay phase of a flare.

The only clear observation (either in the present data or in the literature) of a feature corresponding in wavelength to the Ne multiplet n, m, occurs in the spectrum of region 11619 at 13.530 Å (see Figure 5.4a). Its measured intensity is rather higher than the predicted value; however, it is a very weak feature (statistical significance about 5σ), and though well resolved from the Ne IX intercombination line at 13.553 Å it may suffer some blending with the broad wings of the instrumental profile of that line.

5.4.4.2 The Satellite Spectra with n $\geqslant$ 3.

Feldman et al. (1974) have studied the He-like and satellite spectra of elements 11 $\leqslant$ Z $\leqslant$ 22, obtained from laboratory laser-produced plasmas. Using the energy level calculations of Summers (1973), they have classified a feature observed close to the long-wavelength side of the corresponding $1s^2.{}^1S_0$ - $1s2p.{}^1P_1$ resonance line, as a blend of several n = 3 satellites, namely $1s^23p$ - $1s2p({}^1P)3p.{}^2D$, ${}^2P$ and $1s^23s.{}^2S$ - $1s2p({}^1P)3s.{}^2P$. Pospieszczyk (1975) has reported, from spectra of a laboratory theta-pinch plasma, a feature at 21.71 Å in O, which he identifies with the n = 3 satellite transitions $1s^23p$ - $1s2p3p$. In a Mg spectrum from a laser-produced plasma, Peacock et al. (1973) have noted features at λ 9.181, λ9.187 and λ9.195 Å, which they assign simply to $1s^2nl$ - $1s2pnl$, n $\geqslant$ 3.

In the spectra of coronal active regions 11060 and 11621 Parkinson (1971a,b; 1972; 1975c) has reported two features just to the long-wavelength side of the 1s-2p resonance line, for O VII (Parkinson, 1971a, b), Ne IX (Parkinson, 1971a,b, 1975c) and Mg XI (Parkinson, 1971a,b, 1972, 1975c). From the calculations of Summers, Parkinson (1975c) has partially classified these features, for Ne and Mg, as the n = 3 and 4 satellite transitions, $1s^2 3l$ - 1s2p3l (Ne λ13.488 Å, Mg λ9.193 Å) and $1s^2 4l$ - 1s2p4l (Ne λ13.469 Å, Mg λ9.180 Å).

The present author has used the calculations of Summers to predict satellite wavelengths for n = 3 and 4 in O, Ne and Mg. The energy levels have been adjusted (as suggested by Summers) to take account of the best available theoretical energy levels for the He-like ions (Ermolaev and Jones, 1974); i.e. (since the transition energy = hc/λ) the final predicted satellite wavelength λ_s, is given by:

$$\lambda_s^{-1} = \lambda_{sS}^{-1} + (\lambda_R^{-1} - \lambda_{RS}^{-1}) \qquad (5.19)$$

where:

λ_{sS} = predicted satellite wavelength, from Summers (1973)

λ_R = predicted 1s - 2p resonance line wavelength, from Ermolaev and Jones (1974)

λ_{RS} = predicted 1s - 2p resonance line wavelength, from Summers (1973).

Table 5.8 compares the present measured wavelengths for the n $\geqslant$ 3 satellite spectra in O, Ne and Mg, with predicted and previous measured wavelengths. The calculated wavelengths were derived as described above; the measured wavelengths are from laboratory spectra of Feldman et al. (1974) and Pospieszczyk (1975), and from the solar observations of active regions 11621 (Parkinson, 1972, 1975c) and 11619, 12628 and 12624 (present work). For Ne and Mg, the different sets of wavelengths are in reasonably good agreement (to about 0.005 Å). There are rather larger variations in O; however, for the present measurements at least, these may be largely attributed to the low signal to noise ratio in this portion of the data (see Figure 5.5, and note the scatter in the measured O VII wavelengths in Table 5.3).

Table 5.9 gives the measured intensity of each satellite line relative to that of the He-like resonance line $1s^2.{}^1S_0 - 1s2p.{}^1P_1$ (no resolvable satellites are included in the resonance line intensity), for the present observations of regions 11619, 12628 and 12624 and Parkinson's (1975c) results for region 11621. Any interpretation of these figures (e.g. in terms of the plasma parameters) must await a detailed theoretical model for the intensities of the satellite spectra with $n \geq 3$. It is worthwhile noting however that Gabriel (1972a) calculates a maximum intensity (relative to the corresponding resonance line) of $\sim$ 0.1 for the sum of all satellites with $n \geq 3$, whereas Table 5.9 shows that, in some cases, the sum of the measured values for the n = 3 and 4 satellites is about 0.2 to 0.3.

In the spectrum of region 11619 the Mg satellite at $\lambda \approx$ 9.180 Å is absent, and a new feature at λ = 9.176 Å is just resolvable from the Mg XI resonance line λ 9.169 Å. Although no calculated wavelengths are available for satellite spectra with $n \geq 5$, the feature λ9.176 Å is probably due to satellite transitions where n = 5, with a possible contribution from the satellite $1s^24s.{}^2S - 1s2p({}^1P)4s.{}^2P$ (see Table 5.8).

Unlike the spectra of regions 11619, 12628 (see Figure 5.4) and 11621 (see Parkinson, 1975c), the data for region 12624 requires at least two lines to be present in the wavelength interval 13.46 - 13.47 Å (see Figure 5.4c). In the latter case, the best fit to the observations is obtained with lines at λ13.464 and λ13.473 Å, as shown in Figure 5.4c and Table 7.3. As may be seen from Figure 5.4, the spectrum of the (decaying flare) active region 12624 shows about a dozen lines in the wavelength interval 13 - 14 Å, which are additional to those normally observed from non-flaring active regions such as 11619, 11621 and 12628. Hence it seems likely that, for region12624, the Ne n = 3 satellite λ13.469 Å may be blended with one or more lines from another ion. The "flare" lines from region 12624 will be discussed further, in Chapter 7.

Table 5.1 Theoretical wavelengths, and measured and calculated intensities of the resonance line series $1s^2.{}^1S_0-1snp.{}^1P_1$ in the He-like ions O VII, Ne IX and Mg XI

n	Theoretical wavelength[a] (Å)	Oscillator strength[f]	Intensity (10^{-7} erg cm^{-2} s^{-1}), Active region no. 11619: Measured	11619: Calculated	12628: Measured	12628: Calculated	12624: Measured	12624: Calculated
O VII:								
2	21.601	0.69	406±32 [e]	404	1362±75 [e]	1328	971±67 [e]	960
3	18.628	0.15			261±50	174.3	213±49	126.0
Ne IX:								
2	13.447	0.72	58.8±2.1 [e]	55.6	136.3±3.4 [e]	135.9	94.7±2.6 [e]	102.6
3	11.547	0.15	4.9±1.4	6.4	12.7±2.3	14.8	10.9±2.1	11.4
4	11.000	0.056	3.3±1.3 [c]	1.9	10.5±2.2 [c]	4.4	4.8±1.6 [c]	3.4
5	10.764	0.027	2.1±1.1 [d]	0.9	9.2±2.0 [d]	1.9	7.9±1.9 [d]	1.5
6	10.640 [b]	0.015					2.5±1.3	0.8
Mg XI:								
2	9.169	0.75	33.0±1.4 [e]	27.7	35.9±1.3 [e]	47.7	41.7±1.4 [e]	51.2
3	7.850	0.15	2.1±1.2	2.9	5.1±1.9	4.6	4.0±1.6	5.5

a) Ermolaev and Jones (1974).
b) Hutcheon (1975b), Rydberg series extrapolation from (a).
c) Blended with the Na X $1s^2.{}^1S_0-1s2p.{}^1P_1$ transition at 11.003 Å (see Section 4.6.2).
d) Blended with the Fe XVII $2p^6.{}^1S_0-2p^5 6d.{}^3D_1$ transition at 10.768 Å (see Section 6.3).
e) Used in calculation of active region emission measure/temperature model.
f) Dalgarno and Parkinson (1967), Wiese et al. (1966, 1969).

Table 5.2 He-like ions: the atomic coefficients, and limiting values of ratios and densities, used in the analysis of low density plasmas (for explanation of symbols, see Section 5.3)

Ion	$T_{em}(10^6 K)$ [a]	$A(2^3S \rightarrow 1^1S)$ [b] (s^{-1})	$C(2^3S \rightarrow 2^3P)$ [c,d] $(10^{-9}\ cm^3 s^{-1})$	B [e]	$\mathcal{R}_o$	$n_e^*\ (cm^{-3})$
C V	1.0	4.86×10^1	53.0	0.111	11.16	7.5×10^7
N VI	1.25	2.53×10^2	31.0	0.225	5.00	6.7×10^8
O VII	1.95	1.04×10^3	21.24	0.293	3.61	4.0×10^9
Ne IX	3.5	1.09×10^4	11.82	0.338	2.99	7.6×10^{10}
Mg XI	5.8	7.24×10^4	7.44	0.370	2.65	8.0×10^{11}
Al XII	7.4	1.66×10^5	6.7	0.391	2.45	2.0×10^{12}
Si XIII	8.9	3.56×10^5	6.31	0.425	2.18	4.6×10^{12}
S XV	1.55	1.41×10^6	4.9	0.506	1.67	2.4×10^{13}
Ca XIX	22	1.38×10^7	4.15	0.675	1.00	2.7×10^{14}
Fe XXV	40	2.00×10^8	2.7	0.801	0.69	6.1×10^{15}

a) Gabriel and Jordan (1972)
b) Drake (1971)
c) Blaha (1971)
d) Blaha, private communication to Blumenthal et al. (1972)
e) Blumenthal et al. (1972)

Table 5.3 Wavelengths and measured intensities of the $n = 2 \rightarrow 1$ lines of O VII, Ne IX and Mg XI

Key letter	Transition	Theoretical wavelength[a] (Å)	Measured wavelength (Å)				Measured photon intensity (10^2 ph cm^{-2}s^{-1})			
			Active region no.				Active region no.			
			11621[b]	11619	12628	12624	11621[b]	11619	12628	12624
O VII:										
R	$1s^2.{}^1S_0 - 1s2p.{}^1P_1$	21.601	21.58	21.601[c]	21.601[c]	21.601[c]	988±29	441±34	1480±81	1056±73
I	$-1s2p.{}^3P_2$, ${}^3P_1$	21.801, 21.803	21.78	21.777	21.806	21.801	304±17	114±31	409±65	278±67
F	$-1s2s.{}^3S_1$	22.098	22.07	22.094	22.098	22.104	812±29	271±38	958±87	1045±89
Ne IX:										
R		13.447	13.445	13.447[c]	13.447[c]	13.447[c]	124.6±2.8	39.8±1.4	92.3±2.3	64.1±1.7
I		13.550, 13.553	13.552	13.552	13.552	13.553	25.8±1.2	8.57±0.64	19.13±0.77	12.16±0.64
F		13.699	13.697	13.697	13.699	13.700	83.7±2.3	21.4±0.10	64.9±1.7	48.7±1.4
Mg XI:										
R		9.169	9.169[d]	9.169[d]	9.169[d]	9.167[d]	28.71±0.97	15.23±0.64	16.57±0.58	19.25±0.64
I		9.228, 9.231	9.232[d]	9.231[d]	9.231[d]	9.231[d]	7.53±0.49	3.74±0.33	3.68±0.28	2.81±0.24
F		9.314	9.315[d]	9.315[d]	9.314[d]	9.314[d]	22.69±0.85	8.02±0.47	10.12±0.45	10.39±0.45

a) Ermolaev and Jones (1974)
b) Parkinson (1975c). Uncertainties are calculated from his quoted recorded counts.
c) Reference wavelength (see Section 5.3.3).
d) Assumes 2d(ADP) = 10.648 Å.

Table 5.4 Measured intensity ratios for the n = 2 → 1 lines of O VII, Ne IX and Mg XI (for explanation of symbols see Section 5.3)

	Measured photon intensity ratio				
	Active region no.				
Quantity	11621[a)]	11619	12628	12624	Mean
O VII:					
$\mathcal{R}$	2.67 ± 0.18	2.39 ± 0.73	2.34 ± 0.43	3.76 ± 0.96	2.64 ± 0.16
G	1.13 ± 0.05	0.87 ± 0.13	0.92 ± 0.089	1.25 ± 0.14	1.08 ± 0.04
I/R	0.308 ± 0.019	0.257 ± 0.072	0.276 ± 0.047	0.263 ± 0.066	0.298 ± 0.017
F/R	0.821 ± 0.038	0.615 ± 0.099	0.647 ± 0.069	0.99 ± 0.11	0.781 ± 0.030
Ne IX:					
$\mathcal{R}$	3.25 ± 0.18	2.50 ± 0.22	3.39 ± 0.16	4.01 ± 0.24	3.22 ± 0.12
G	0.88 ± 0.03	0.75 ± 0.04	0.91 ± 0.03	0.95 ± 0.04	0.88 ± 0.02
I/R	0.207 ± 0.011	0.215 ± 0.017	0.207 ± 0.010	0.189 ± 0.011	0.203 ± 0.006
F/R	0.672 ± 0.023	0.537 ± 0.031	0.703 ± 0.025	0.760 ± 0.030	0.673 ± 0.013
Mg XI:					
$\mathcal{R}$	3.0 ± 0.2	2.14 ± 0.22	2.74 ± 0.23	3.70 ± 0.35	2.77 ± 0.12
G	1.04 ± 0.05	0.77 ± 0.16	0.83 ± 0.04	0.69 ± 0.03	0.81 ± 0.02
I/R	0.261 ± 0.018	0.246 ± 0.024	0.222 ± 0.018	0.146 ± 0.014	0.203 ± 0.009
F/R	0.782 ± 0.036	0.526 ± 0.038	0.611 ± 0.034	0.540 ± 0.029	0.608 ± 0.017

a) Parkinson (1972), Mg XI; Parkinson (1975c), O VII, Ne IX (see present work Table 5.3).

Table 5.5 Helium-like and satellite transitions (Gabriel, 1972a)

Array	Multiplet	Line	Key letter
$1s^2 2p - 1s 2p^2$	$^2P^0 - ^2P$	$1\frac{1}{2} - 1\frac{1}{2}$	a
		$\frac{1}{2} - 1\frac{1}{2}$	b
		$1\frac{1}{2} - \frac{1}{2}$	c
		$\frac{1}{2} - \frac{1}{2}$	d
	$^2P^0 - ^4P$	$1\frac{1}{2} - 2\frac{1}{2}$	e
		$1\frac{1}{2} - 1\frac{1}{2}$	f
		$\frac{1}{2} - 1\frac{1}{2}$	g
		$1\frac{1}{2} - \frac{1}{2}$	h
		$\frac{1}{2} - \frac{1}{2}$	i
	$^2P^0 - ^2D$	$1\frac{1}{2} - 2\frac{1}{2}$	j
		$\frac{1}{2} - 1\frac{1}{2}$	k
		$1\frac{1}{2} - 1\frac{1}{2}$	l
	$^2P^0 - ^2S$	$1\frac{1}{2} - \frac{1}{2}$	m
		$\frac{1}{2} - \frac{1}{2}$	n
$1s^2 2p - 1s 2s^2$	$^2P^0 - ^2S$	$1\frac{1}{2} - \frac{1}{2}$	o
		$\frac{1}{2} - \frac{1}{2}$	p
$1s^2 2s - 1s 2p 2s$	$^2S - (^1P)\, ^2P^0$	$\frac{1}{2} - 1\frac{1}{2}$	q
		$\frac{1}{2} - \frac{1}{2}$	r
	$^2S - (^3P)\, ^2P^0$	$\frac{1}{2} - 1\frac{1}{2}$	s
		$\frac{1}{2} - \frac{1}{2}$	t
	$^2S - ^4P^0$	$\frac{1}{2} - 1\frac{1}{2}$	u
		$\frac{1}{2} - \frac{1}{2}$	v
$1s^2 - 1s 2p$	$^1S - ^1P^0$	$0 - 1$	w
	$^1S - ^3P^0$	$0 - 2$	x
		$0 - 1$	y
$1s^2 - 1s 2s$	$^1S - ^3S$	$0 - 1$	z

Table 5.6 Measured and predicted wavelengths for n = 2 satellites to Ne IX and Mg XI

Transition key letter[a]	Predicted wavelength (Å)		Measured wavelength (Å)				
			Active region no.				
	Gabriel(1972a)	Goldsmith(1974)	11619	12628	12624	Mean[b]	11621[c]
Mg XI:							
n	9.218	9.218	9.223			9.223	9.223
m	9.221	9.221					
s	9.235	9.235	9.237			9.237	9.237
t	9.236	9.234					
q	9.284	9.283	9.283	9.282	9.284	9.282	9.284
r	9.286	9.285		9.286		9.286	9.286
k	9.318	9.316	9.318			9.318	9.319
j	9.321	9.319	9.321			9.321	9.323
l	9.322	9.318					
Ne IX:							
n	13.532	13.536	13.530			13.530	
m	13.535	13.538					
s	13.562	13.564					
t	13.563	13.565					
q	13.652	13.652		13.653		13.653	13.648
r	13.654	13.654					
k	13.708	13.707					
j	13.711	13.711					
l	13.711	13.710					

a) see Table 5.5.
b) mean of measurements for regions 11619, 12628, 12624.
c) Parkinson (1975c).

Table 5.7 Measured and calculated intensities for n = 2 satellites to Ne IX and Mg XI

Transition key letter[a]	Photon intensity relative to resonance line[b,c,e] — Active region no. 11621: Calculated	11621: Measured[d]	11619: Calculated	11619: Measured	12628: Calculated	12628: Measured	12624: Calculated	12624: Measured
Mg XI:								
n,m	0.014	0.020	0.013	0.024 ± 0.009	0.016	$\leq 0.018\pm0.008$	0.013	$\leq 0.017\pm0.007$
s,t	0.016	0.025	0.015	0.024 ± 0.009	0.019	$\leq 0.014\pm0.008$	0.014	$\leq 0.013\pm0.007$
q	0.026	0.048	0.024	0.056 ± 0.011	0.029	0.043 ± 0.009	0.023	0.038 ± 0.008
r	0.016	0.025	0.014		0.018	0.024 ± 0.009	0.014	
k	0.045	0.028	0.040	0.025 ± 0.009	0.051	$\leq 0.024\pm0.009$	0.040	$\leq 0.017\pm0.019$
j,l	0.076	0.046	0.068	0.033 ± 0.010	0.086	$\leq 0.033\pm0.009$	0.067	$\leq 0.024\pm0.007$
Ne IX:								
n,m			0.0055	0.025 ± 0.008	0.0063	$\leq 0.021\pm0.003$	0.0061	
s,t			0.0048	$\leq 0.014\pm0.008$	0.0056	$\leq 0.014\pm0.003$	0.0054	
q,r	0.018	0.015	0.020	$\leq 0.013\pm0.008$	0.023	$\leq 0.019\pm0.003$	0.023	
k	0.033	< 0.02	0.014	$\leq 0.019\pm0.008$	0.016	$\leq 0.020\pm0.004$	0.015	$\leq 0.038\pm0.007$
j,l			0.025	$\leq 0.038\pm0.010$	0.029	$\leq 0.039\pm0.004$	0.028	$\leq 0.077\pm0.008$

a) see Table 5.5.
b) calculated intensities are derived from Bhalla et al.(1975), via the emission measure/temperature models in Table 4.2 (see Section 5.4.4.1).
c) The measured upper limits quoted, for regions 11619, 12628 and 12624, are the recorded intensities at the expected wavelengths of the lines.
d) Parkinson (1975c).
e) The close ($n \geq 3$) satellites are included with the resonance line.

Table 5.8 Measured and predicted wavelengths for n ≥ 3 satellites to O VII, Ne IX and Mg XI

Key Letter	Transition[c)]	Wavelength (Å)							
		Predicted[a)]	Measured[b)]						
			(1)	(2)	(3)	(4)	(5)	(6)	(7)
Mg XI:									
S1	$1s^2 3p.\,^2P - 1s2p(^1P)3p.\,^2D$	9.190	9.190		9.193	9.193	9.191	9.191	9.192
	^2P	9.189							
	$1s^2 3s.\,^2S - 1s2p(^1P)3s.\,^2P$	9.186							
S2	$1s^2 4p.\,^2P - 1s2p(^1P)4p.\,^2D$	9.179			9.180		9.179	9.181	9.180
	^2P	9.179							
		9.176							
S3	$1s^2 4s.\,^2S - 1s2p(^1P)4s.\,^2P$	9.176				9.176			9.176
Ne IX:									
S1	$1s^2 3p.\,^2P - 1s2p(^1P)3p.\,^2D$	13.484			13.488	13.488	13.489	13.491	13.489
	^2P	13.483							
	$1s^2 3s.\,^2S - 1s2p(^1P)3s.\,^2P$	13.478							
S2	$1s^2 4p.\,^2P - 1s2p(^1P)4p.\,^2D$	13.466			13.469	13.470	13.467		13.469
	^2P	13.465							
	$1s^2 4s.\,^2S - 1s2p(^1P)4s.\,^2P$	13.460							
O VII:									
S1	$1s^2 3p.\,^2P - 1s2p(^1P)3p.\,^2D$	21.673		21.71		21.711	21.720		21.716
	^2P	21.672							
	$1s^2 3s.\,^2S - 1s2p(^1P)3s.\,^2P$	21.662							
S2	$1s^2 4p.\,^2P - 1s2p(^1P)4p.\,^2D$	21.637				21.642	21.650		21.646
	^2P	21.636							
	$1s^2 4s.\,^2S - 1s2p(^1P)4s.\,^2P$	21.626							

Footnotes to Table 5.8

a) From Summers (1973) (see present work Section 5.4.4.2)

b) References:

(1) Laboratory, Feldman et al. (1974)

(2) Laboratory, Pospieszczyk (1975)

(3) Solar, active region 11621, Parkinson (1975c)

(4) " " " 11619, present work

(5) " " " 12628, " "

(6) " " " 12624, " "

(7) Mean of (4), (5), (6).

c) Classifications for the n = 3 satellites are taken from Feldman et al. (1974). For n = 4 they are given by analogy with n = 3. The measured features (i.e. S1, S2, S3) may contain contributions from other satellite transitions (see Section 5.4.4.2)

Table 5.9 Measured intensities for $n \geqslant 3$ satellites to O VII, Ne IX, Mg XI

Line key letter[a]	Measured photon intensity relative to resonance line[b]			
	Active region no.			
	11621[c]	11619	12628	12624
Mg XI:				
S3		0.111 ± 0.016		
S2	0.165 ± 0.015		0.091 ± 0.013	0.051 ± 0.009
S1	0.129 ± 0.012	0.075 ± 0.014	0.075 ± 0.012	0.059 ± 0.010
Ne IX:				
S2	0.0926 ± 0.0071	0.103 ± 0.013	0.084 ± 0.006	
S1	0.0458 ± 0.0048	0.038 ± 0.010	0.042 ± 0.004	0.022 ± 0.006
O VII:				
S2		0.16 ± 0.07	0.32 ± 0.05	
S1		0.17 ± 0.07	0.22 ± 0.05	

a) See Table 5.8
b) All resolvable satellites are excluded from the resonance line intensity
c) Parkinson (1975c), Ne IX (see footnote (b), Table 5.3); Parkinson (1972), Mg XI.

FIGURES

Chapter 5

5.1 Energy level diagram showing the ground and first four excited states of a helium-like ion. Radiative decay mechanisms are shown with their approximate Z-scaling. Z-1 is the net ionic charge and A is the transition probability for spontaneous radiative decay (Gabriel, 1972c).

5.2 Energy level diagram showing the ground and first four excited states of a helium-like ion, together with the individual levels in each state. Also indicated are those processes taken into account in the analysis of low density plasmas (see text). The solid arrowed lines denote collisional transitions, the dashed lines radiative transitions. The wavelengths refer to the O VII ion (Gabriel and Jordan, 1972).

5.3 High resolution slow scans showing the $n = 2 \rightarrow 1$ spectral lines of the He-like ion Mg XI and dielectronic satellites (see text for explanation of transition key letters).

a McMath region 12628 (flight SL1206)

b McMath region 12624 (flight SL1206)

c McMath region 11619 (flight SL1101).

5.4 As Fig. 5.3 for Ne IX.

5.5 As Fig. 5.4 for O VII.

5.6 Energy level diagram showing the helium-like and satellite transitions (Gabriel, 1972b).

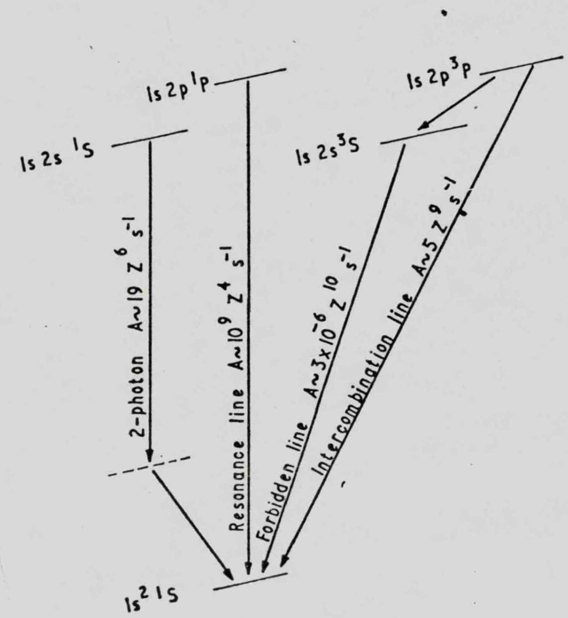
1s 2s ^{1}S
1s 2p ^{1}P
1s 2s ^{3}S
1s 2p ^{3}P
2-photon A∼19 Z^6 s^{-1}
Resonance line A∼10^9 Z^4 s^{-1}
Forbidden line A∼3×10^{-6} Z^{10} s^{-1}
Intercombination line A∼5 Z^9 s^{-1}
1s^2 ^{1}S

Fig. 5.1.

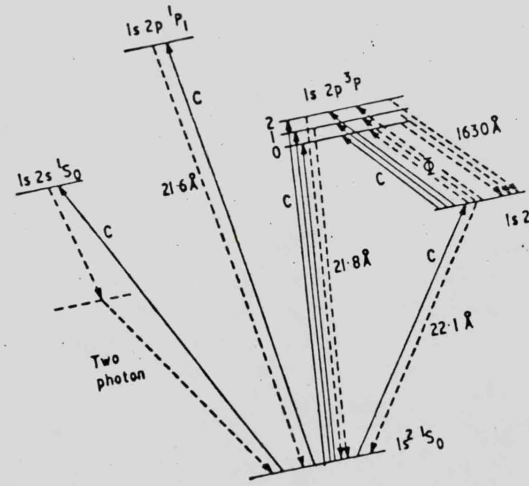
1s 2p ^{1}P$_1$
1s 2s ^{1}S$_0$
1s 2p ^{3}P
2
1
0
1630 Å
1s 2s ^{3}S$_1$
C
21·6 Å
21·8 Å
22·1 Å
Two photon
1s^2 ^{1}S$_0$

Fig. 5.2.

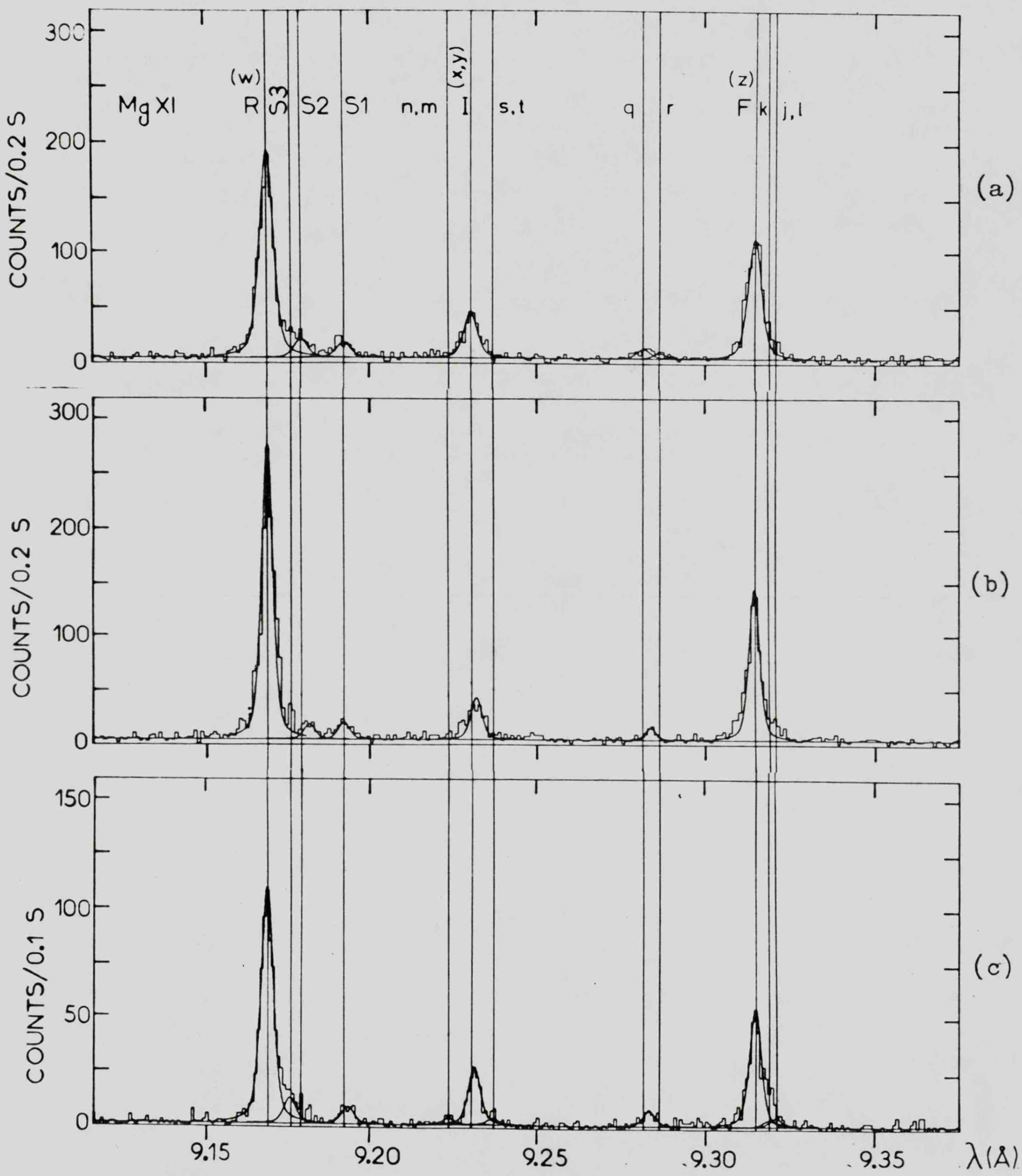

Mg XI
(w)
R
S3
S2
S1
n,m
(x,y)
I
s,t
q
r
(z)
F
k
j,l
COUNTS/0.2 S
COUNTS/0.1 S
(a)
(b)
(c)
9.15
9.20
9.25
9.30
9.35
λ(Å)

Fig. 5.3.

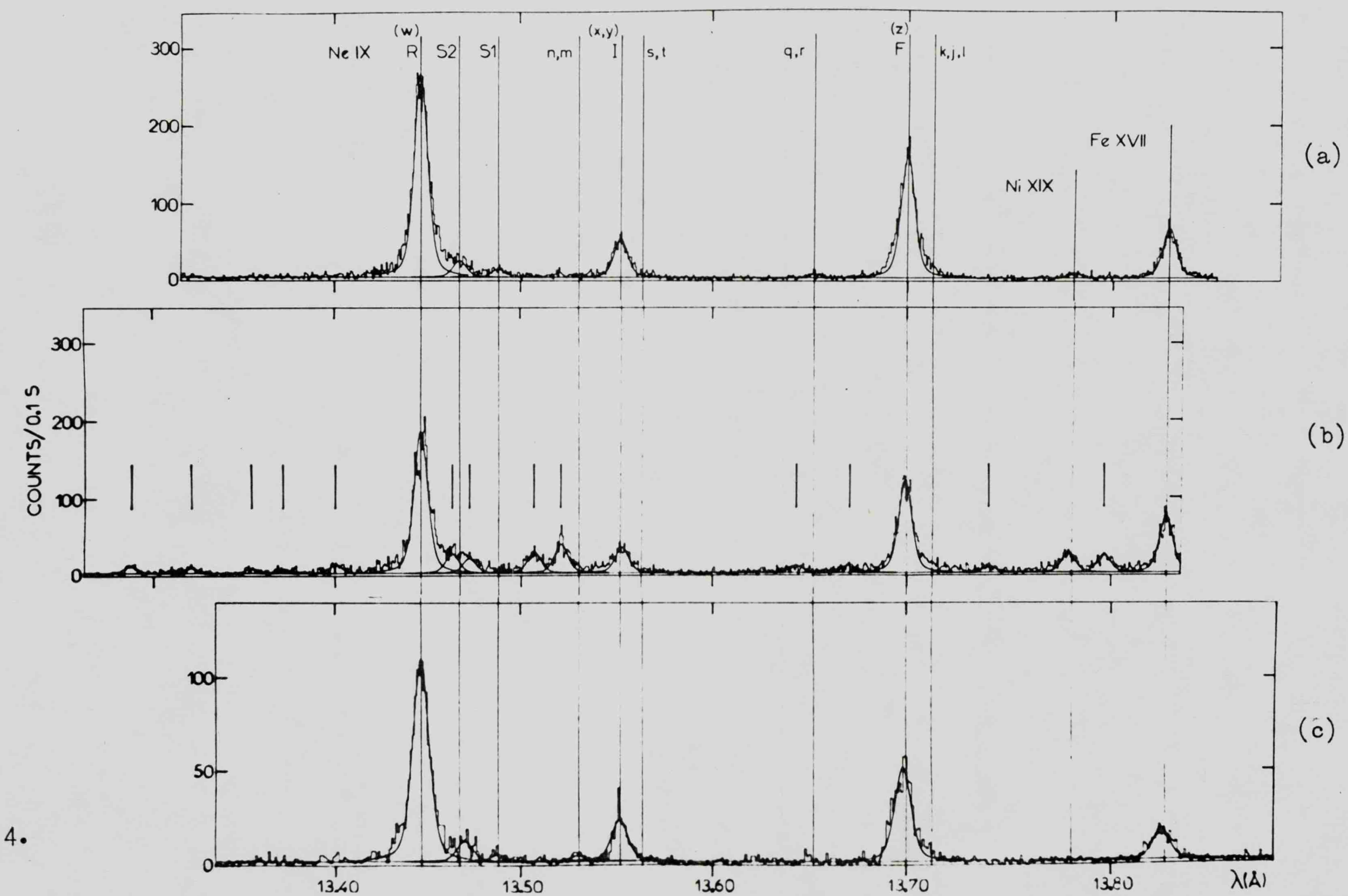

Ne IX
(w)
R
S2
S1
n,m
(x,y)
I
s,t
q,r
(z)
F
k,j,l
Ni XIX
Fe XVII
(a)
(b)
(c)
COUNTS/0.1 S
300
200
100
0
50
13.40
13.50
13.60
13.70
13.80
λ(Å)

Fig. 5.4.

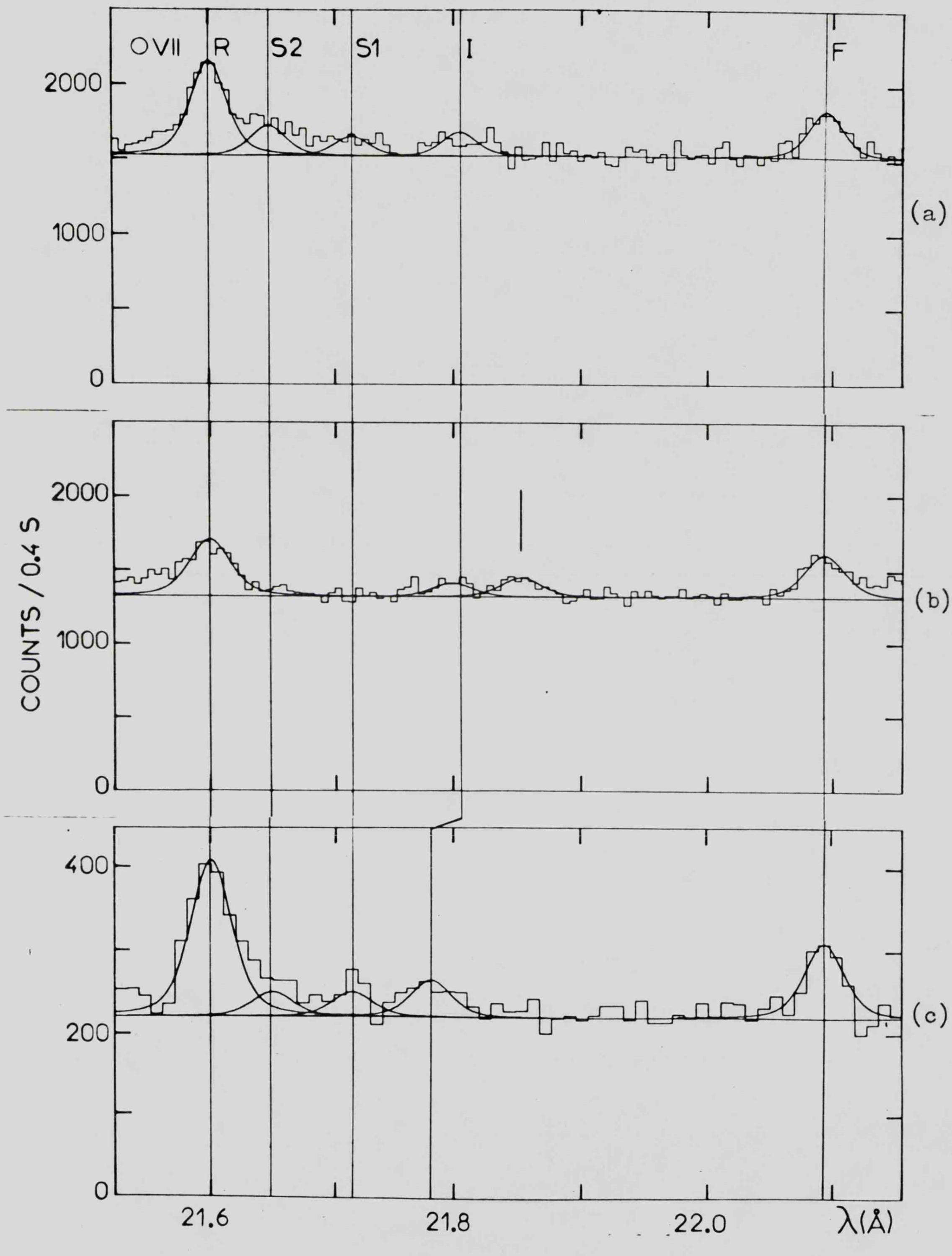

Fig. 5.5.

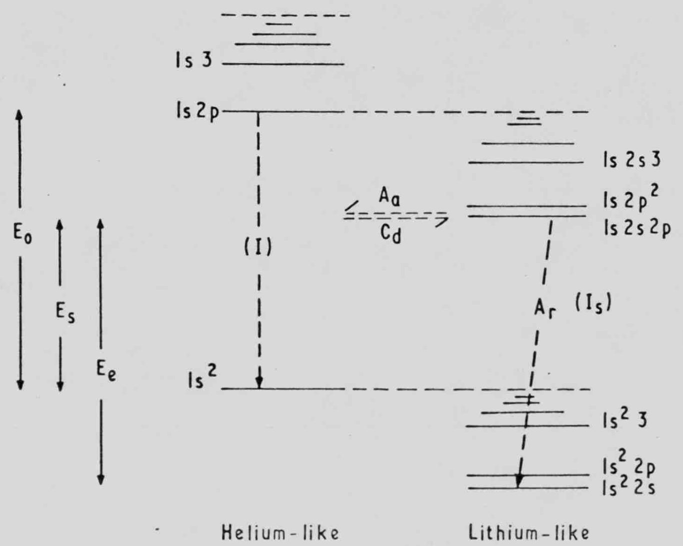
ls 3
ls 2p
ls 2s 3
ls 2p²
ls 2s 2p
Aa
Cd
Eo
Es
Ee
(I)
Ar (Is)
ls²
ls² 3
ls² 2p
ls² 2s
Helium-like
Lithium-like

Fig. 5.6.

Chapter 6

THE Ne-LIKE IONS Fe XVII AND Ni XIX

The soft X-ray emission spectra of solar active regions show transitions of the Ne-like ions Fe XVII and Ni XIX. In particular some of the Fe XVII transitions are among the most prominent coronal soft X-ray transitions and a detailed knowledge of these lines is therefore of great interest. This chapter describes accurate measurements of the wavelengths and relative intensities of most of the $n = 3 \rightarrow 2$ and $n = 4 \rightarrow 2$ transitions in Fe XVII and some of these transitions in Ni XIX (n is the principal quantum number), and a search for weaker lines due to higher transitions, $n = 5, 6, 7, 8 \rightarrow 2$, in Fe XVII. In the case of iron the spectrum of Fe XVII is very strong at active region temperatures and higher stages are observable also (see Chapter 7). In the case of nickel the spectrum of Ni XIX is significant but spectra of higher ions are not observed mostly because of the much lower abundance of nickel relative to that of iron (see Section 4.6) and partly because of the higher ionization potentials.

The results reported here are from SL1101 observations of region 11619 and SL1206 observations of regions 12628 and 12624. The data were obtained with the gypsum and KAP spectrometers.

6.1 The Fe XVII Lines, $n = 3, 4 \rightarrow 2$

Until recently the spectrum of Ne-like Fe XVII has not been well understood. However, Loulergue and Nussbaumer (1973) gave results of comprehensive calculations of the relative intensities of $n = 3 \rightarrow 2$ transitions in the coronal Fe XVII spectrum. Parkinson (1973a) showed that these results are consistent with his measurements of this spectrum. Loulergue and Nussbaumer (1975a) have now extended their calculations to include n = 4 → 2 transitions also and this provides an opportunity to interpret the complex group of lines observed in the coronal spectrum between 11.0 and 12.7 Å by critical comparison with their calculations. The present Chapter describes intensity measurements for all currently known coronal Fe XVII n = 3 → 2 and n = 4 → 2 transitions. The wavelengths of these lines are known with varying degrees of precision and it was considered worthwhile to remeasure all of them as accurately as possible. The values obtained agree closely with previous measurements for well-established Fe XVII lines (e.g. Tyrén, 1938) but lead to corrected wavelengths of improved accuracy for other Fe XVII lines.

Samples of the spectra (for region 12624) used in the present analysis are shown in Figures 6.1 and 6.2. Those lines which are discussed below are shown fitted with an approximation to the instrument spectral response function (see Section 3.3.3.1). Figures 6.1 and 6.2 show data taken with the instrument in spectral survey (fast scan) mode.

6.1.1 The Fe XVII Term System

Currently known coronal Fe XVII transitions which terminate on the $2s^2 2p^6 . {}^1S_0$ ground level belong to eight Rydberg series. These are the two groups of $\Delta l = 1$ series, $2s^2 2p^6 . {}^1S_0 - 2s^2 2p^5 ns . {}^1P_1$, ${}^3P_1$, ${}^3P_2$ and $2s^2 2p^6 . {}^1S_0 - 2s^2 2p^5 nd . {}^1P_1$, ${}^3D_1$, ${}^3P_1$ and the group of inner shell transition series $2s^2 2p^6 . {}^1S_0 - 2s 2p^6 np . {}^1P_1$, ${}^3P_1$. The $2p^5 3s . {}^3P_2$ level decays through a magnetic quadrupole transition to $2p^6 . {}^1S_0$. For ease of reference, the lines will be designated by key letters. Table 6.1 relates the key letters to the spectroscopic classifications.

6.1.2 Calculated Line Intensities

Loulergue and Nussbaumer (1973) gave results of calculations of the relative intensities of the eight known coronal Fe XVII n = 3 → 2 transitions, based on a 37-level ion model (the ground level and the 36 n = 3 levels). Loulergue and Nussbaumer (1975a) subsequently extended the calculations to include the corresponding n = 4 → 2 transitions, modified their earlier results for n = 3 → 2 transitions and included results for the isoelectronic Ni XIX. The calculations consider transitions between 52 of the lowest 57 levels, i.e. those in the $2p^6$ (ground state), $2p^5 3l$, $2s2p^6 3l$ (l = 0, 1, 2), $2p^5 4s$, $2p^5 4d$ and $2s2p^6 4p$ configurations. The population processes included are collisional excitation from the ground level and the metastable $2p^5 3s.{}^3P_2$ levels and all significant radiative processes between the 52 levels. They show that ionization and recombination need not be included. Their results are expressed as energy intensities relative to the 'resonance' line $2p^6.{}^1S_0 - 2p^5 3d.{}^1P_1$ and are included in Table 6.1. Where comparison is possible their results are substantially in agreement with those of Beigman & Urnov (1969). Both papers conclude that the relative intensities of the n = 3 → 2 transitions are largely independent of temperature and density. Loulergue and Nussbaumer (1975a) predict that although the n = 4 → 2 transitions become easier to excite as the temperature is increased, the power in these n = 4 → 2 transitions relative to the resonance line is not very sensitive to temperature. Both papers note that the $2p^5 3s$ configuration is mainly populated indirectly from the ground state by radiative cascade from higher levels, via the path $2s2p^6 3d \rightarrow 2s^2 2p^5 3d \rightarrow 2s^2 2p^5 3p \rightarrow 2s^2 2p^5 3s$. Table 6.2 shows the population mechanisms for the $2p^5 3d$ and

$2p^5 3s$ levels, from the 37-level ion model of Loulergue and Nussbaumer (1973); the extension to 57 levels modifies these figures by only a few percent (Loulergue and Nussbaumer, 1975a). Figure 6.3 is an energy level diagram for Fe XVII, showing the principal decay paths for the first 36 excited levels. As this illustration is rather complicated, a reduced version is given in Figure 6.4, which shows only the strongest lines (i.e. $2p^6 - 2p^5 3d, s.$) and the corresponding paths of the main population and depopulation processes.

Two other recent calculations of coronal Fe XVII relative intensities should be noted. That of Neupert et al. (1973) is commented on below. Beigman et al. (1974) gave limited calculations for the relative strengths of $2p^6 - 2p^5 3d.{}^1P_1$ and $2p^6 - 2p^5 nd.{}^3D_1$ for n = 4 to 8. They predict for example, the relative intensity $I(2p^6 - 2p^5.{}^3D_1)/I(2p^6 - 2p^5 3d.{}^1P_1)$ at 0.2 for a coronal temperature of 5×10^6 K and state that this ratio does 'not depend strongly on the plasma emitting temperature'. This result is substantially larger than the authors' own observed value (0.09), the present values (0.056, 0.043 and 0.021; see Table 6.1), the value observed by Neupert et al. (0.13) and the calculated result (0.05) by Loulergue and Nussbaumer. It appears that the calculations of Loulergue and Nussbaumer are generally closer to presently measured values than are the results of Beigman et al.

6.1.3 Previous Observations

Most previous observers have given more comment on $n = 3 \rightarrow 2$ transitions than on higher transitions. Loulergue and Nussbaumer (1973) collated measurements prior to 1972 and found broad agreement with their calculations but only when allowance was made for the fact that two blends were not resolved in data published prior to 1972. These two blends were $2s^2 2p^6 . ^1S_0$ - $2s2p^6 3p . ^1P_1$ and $^3P_1$; and $2p^6 . ^1S_0 - 2p^5 3s . ^3P_1$ and $^3P_2$.

The first published observations in which all eight known coronal Fe XVII $n = 3 \rightarrow 2$ transitions were clearly resolved are those of Parkinson (1973a) (from the SL1101 data of region 11621). His relative intensities for transitions from the $2p^5 3s$ and $2p^5 3d$ configurations again broadly agree with the values predicted by Loulergue and Nussbaumer (1975a). Walker et al. (1974c) have also reported observations of the same eight lines, together with theoretical intensity ratios calculated using a model similar in approach to that of Loulergue and Nussbaumer (1973a). Walker et al. find general agreement between their own measured and predicted relative intensities, the observations of Parkinson (1973a) and the calculations of Loulergue and Nussbaumer (1973a). The average discrepancy between the theoretical relative intensities of Loulergue and Nussbaumer (1973a) and the other theoretical and experimental values is about 25%. The largest discrepancy occurs for the inner shell $2s^2 2p^6 - 2s2p^6 3p$ transitions, where it amounts to about 70%.

This broadly satisfactory situation was challenged by Neupert et al. (1973), hereafter referred to as NSK. These authors compare the Fe XVII $n = 3 \rightarrow 2$ spectra of two solar flares (measured with the OSO-5 spacecraft) with their own intensity calculations which include 16 excited levels. They find serious discrepancies and conclude that some additional temperature or density effect must be allowed for in calculation. However, NSK quote measured intensities relative to the feature at 17.05 Å which they identify with $2p^6 - 2p^5 3s . ^3P_1$ only, apparently neglecting the blend with the equally strong $2p^6 - 2p^5 3s . ^3P_2$. The anomalous strength of $2p^6 - 2p^5 3d . ^3P_1$ listed (but not commented upon) by NSK may be due to incorrect identification. Finally NSK's theoretical model neglects an important population process for the $2p^5 3s$ configuration ($2p^6 \rightarrow 2p^5 3d \rightarrow 2p^5 3p \rightarrow 2p^5 3s$). If allowance is made for these matters there appears to be no remaining difficulty.

Previous measurements for the $n = 4 \rightarrow 2$ transitions are confined to the $2p^6 . {}^1S_0 - 2p^5 4d . {}^1P_1$, ${}^3D_1$ lines (Evans and Pounds, 1968; Walker and Rugge, 1969). The ratios obtained by Evans and Pounds (average values 0.041 and 0.039 for the ${}^1P_1$, ${}^3D_1$ transitions respectively) are in fair agreement with calculation. However, the two values for $2p^6 . {}^1S_0 - 2p^5 4d . {}^3D_1$ given by Walker and Rugge exceed the calculated value by factors of 2 and 5. This discrepancy has not been resolved.

6.1.4 Analysis of the Present Observations

The data used in the present analysis were obtained with much greater sensitivity and substantially better resolution and wavelength calibration (see Chapter 3) than most previous observations. The assignment of features to the spectrum of Fe XVII was guided by the improved wavelength calibration and by use of the higher temperature spectrum of the flaring region 12624 to exclude the possibility of misidentification of transitions in higher ion stages.

All but three of the $n = 3 \rightarrow 2$ and $n = 4 \rightarrow 2$ transitions in the eight known Rydberg series have been found previously and good wavelengths were available (Tyrén, 1938; Swartz et al., 1971; Parkinson, 1973a). There was no difficulty in assigning features in the present spectra to these transitions. The three missing transitions were all $n = 4 \rightarrow 2$ lines, namely the inner shell and magnetic quadrupole transitions. The search for these lines in the present data was guided by the following considerations.

(a) THE INNER SHELL ($2s^2 2p^6 . ^1S_0 - 2s2p^6 np . ^1P_1, ^3P_1$) TRANSITIONS.

These lines, with $n \geqslant 4$, have been previously found only for three low members of the Ne-like isoelectronic sequence (Ne I: Codling et al. 1967; Mg III: Esteva and Mehlman, 1974; Al IV: Carillon et al. 1972). Thus it has not been possible to predict accurate wavelengths for the corresponding Fe XVII lines by either isoelectronic or Rydberg series extrapolation. However, an approximate prediction is possible on the basis that quantum defects vary only slowly along Rydberg series. Hutcheon (1975b) has performed such a calculation. Thus comparison of the quantum defects of Ne I, Mg III and Al IV with those of Fe XVII, and considering the dependence of the quantum defect on multiplet splitting and on n, yields the values 11.022 and 11.040 Å respectively for the wavelengths of Fe XVII $2s^2 2p^6 . ^1S_0 - 2s2p^6 4p . ^1P_1, ^3P_1$. The uncertainties on these absolute values are estimated at less than 0.02 Å and that on the difference is perhaps a few milliangstroms (Hutcheon, 1975b).

A feature consistently appears in the present spectra at 11.029 $\pm$ 0.004 Å with statistical significance of about 8σ on each of three independent measurements. Others have found features in their spectra consistent with this wavelength but have offered different classifications.

Swartz et al. (1971) found a line at 11.021 $\pm$ 0.005 Å in measurements of an iron plasma in a vacuum spark, which they partially classify as a Fe XVIII $2p^5 - 2p^4(^1S)4d$ line. However, Hutcheon (1975b) has extrapolated along the Rydberg series using the known energy levels of the corresponding $2p^5 - 2p^4(^1S)3d$ transitions (from Feldman et al. 1973), and this calculation indicates that the proposed identification of Swartz et al. is somewhat unlikely.

Neupert et al. (1973) classify a feature at 11.03 Å in the laboratory spectrum of Feldman and Cohen (1968) as a Fe XIX $2p^4(^3P) - 2p^34s(^3D)$ line whose predicted wavelength is 10.99 Å. This transition could perhaps contribute to the feature observed by Swartz et al. but not to our 11.029 Å feature. Thus the most intense coronal Fe XIX lines should be various $2p^5 - 2p^43d$ transitions (Fawcett et al. 1974) but these do not appear on the spectra of regions 11619 and 12628. Several of them are tentatively identified in the (flaring) region 12624 spectrum (see Chapter 7) but the 11.029 Å intensity is not there increased in proportion, as could be expected if it contained a significant Fe XIX contribution.

It is concluded therefore that the present 11.029 Å feature may not be ascribed either to Fe XVIII or Fe XIX transitions. In contrast ascribing the feature to a blend of the two Fe XVII $2s^22p^6 - 2s2p^64p$ transitions, as suggested by the coincidence of predicted and measured wavelengths, is supported by the intensity calculations of Loulergue and Nussbaumer. The total intensity they predict for the two lines is close to the strength of the measured feature. Note that Loulergue and Nussbaumer predict the $2s^22p^6.{}^1S_0 - 2s2p^64p.{}^1P_1$ line about five times stronger than the corresponding $4p.{}^3P_1$ line.

(b) THE MAGNETIC QUADRUPOLE TRANSITION, $2p^6.{}^1S_0 - 2p^54s.{}^3P_2$.

It is now believed (contrary to the suggestion of Hutcheon (1975a)) that this transition is unlikely to be observable since the $2p^54s.{}^3P_2$ state may decay by allowed electric dipole transitions, mainly to $2p^53p.{}^3S_1$, ${}^3D_3$, ${}^3P_2$, as pointed out by Loulergue and Nussbaumer (1975a). An unidentified line at 12.700 ± 0.003 Å occurs in the present spectra very close to the predicted wavelength (Hutcheon, 1975b) of the magnetic quadrupole transition at 12.691 $\pm$ 0.011 Å but the identification cannot now be accepted.

Table 6.1 gives the measured values, for each of the three observed active regions, of the strengths of the Fe XVII $n = 3 \rightarrow 2$ and $n = 4 \rightarrow 2$ transitions normalized to the strength of the resonance line $2p^6.{}^1S_0 - 2p^5 3d.{}^1P_1$ (in conformity with Loulergue and Nussbaumer). Also included is the absolute intensity of this reference line for each region.

According to Loulergue and Nussbaumer's figures, also given in Table 6.1, the $2p^6.{}^1S_0 - 2p^5 4d.{}^3P_1$ transition (found in a vacuum spark spectrum at 12.319 Å by Swartz et al. 1971) should be too weak to appear in the present data. This is the case and the recorded intensity at 12.319 Å is listed as the upper limit for the strength of that line.

6.1.5 Discussion

Table 6.1 shows broad agreement between the measured and calculated intensities for $n = 3 \rightarrow 2$ and $n = 4 \rightarrow 2$ transitions. Consistency is particularly good for the $2p^6 - 2p^5 3d$, 4d transitions. Some difficulties are apparent for the $2p^6 - 2p^5 3s$ lines; thus some of the calculated values are consistent with measurement, some diverge by up to 50% and for some lines different measurements of the same line are inconsistent by much more than the known measurement error. Nevertheless, for each region observed, the sum of the measured intensities of the $2p^6 - 2p^5 3s$ transitions agrees considerably better with the calculated sum, i.e. to within 20%. This may indicate the presence of processes, not yet included in the calculations, which affect the distribution of the populations of the $2p^5 3s$ levels. For the $2p^6 - 2p^5 4s$ transitions the measured strengths somewhat exceed the calculated values.

It is interesting to note that the (summed) relative intensities of both the $2p^6 - 2p^5 3s$ and $2p^5 4s$ lines is lowest in the spectrum of the (hotter) decaying flare region.

Where previous laboratory wavelengths exist (Tyrén, 1938; Cohen and Feldman, 1970; Connerade et al. 1970; Swartz et al. 1971) the new measurements agree to within $\pm$ 0.0035 Å of the average of previous values. This consistency is improved if the average of previous values is calculated by weighting each value according to the inverse of its uncertainty (Hutcheon, 1975b). This, together with the broadly satisfactory understanding of the relative intensities observed in three separate scans, leaves little room for doubt of the assignment of features in the present spectra to the correct Fe XVII transitions. The wavelengths listed in Table 6.1 are the average of values found from the three scans. The quoted uncertainty represents the spread in the three individual values plus an added $\pm$ 0.001 Å to allow for systematic error due to the uncertainty in some wavelength standards. The uncertainties given in Table 6.1 are in general substantially smaller than those previously given and, as a consequence, some of the wavelengths given are shifted slightly (though by less than 0.0035 Å) from previous values. The present wavelengths for the $2p^6 - 2p^5 3s$ transitions differ from those of Parkinson (1973a, 1975c) by larger amounts (0.006 - 0.011 Å) but Parkinson's uncertainty was up to $\pm$ 0.008 Å.

As always the measured results for intensities and wavelengths are given on the assumption that no undetected blends exist in the lines discussed. For the $n = 3 \rightarrow 2$ transitions this was discussed by Walker et al. (1974c) who pointed out the risk of weak Fe XIX lines blending with the $2p^6 - 2p^5 3d.{}^3D_1$, ${}^3P_1$ lines. However, they argue that this is not significant in their measurements and similar arguments apply to the present ones also. Of the $n = 4 \rightarrow 2$ transitions, $2p^6.{}^1S_0 - 2p^5 4d.{}^1P_1$ at 12.124 Å is partially blended with Ne X Lyα at 12.134 Å. This blend has been deconvolved in the present analysis and the quoted results for the Fe XVII transition intensity and wavelength allow for this. There are no other known blends with $n = 3 \rightarrow 2$, $n = 4 \rightarrow 2$ transitions, and there is no evidence of undue broadening in any of the line profiles. Finally, many of the lines discussed are among the strongest lines in the coronal X-ray spectrum. Undetected blends can only now occur with weak lines so that, at least for the stronger lines, the vulnerability to error, either in wavelength or intensity, is very small.

6.2 The Ni XIX Lines

The preceding study has also been extended to the more highly charged Ne-like ion Ni XIX. However, the Ni XIX lines are comparatively weak due to the low solar abundance of nickel (at least an order of magnitude less than iron; see Section 4.6) and the higher temperature required to produce and excite Ni XIX efficiently (e.g. Jordan, 1969, 1970). Hence observations are much more limited. A further difficulty is that the uncertainty in the known wavelengths of the Ni XIX lines is considerably greater than for the corresponding Fe XVII lines. This, together with the low intensity, complicates the problem of correctly identifying a Ni XIX transition, especially in the vicinity of other weak lines.

6.2.1 Previous Observations

Feldman and Cohen (1967) give laboratory wavelengths of seven $n = 3 \rightarrow 2$ transitions to two decimal places (in Ångstroms) but do not mention uncertainties. Feldman et al. (1967) give the wavelengths of two n = 4 $\rightarrow$ 2 transitions to $\pm$ 0.01 Å. Swartz et al. (1971) give wavelengths for all the lines previously reported and also for two further n = 4 $\rightarrow$ 2 transitions, nominally to three decimal places in Ångstroms. However, for the lines discussed here, the nearest wavelength calibration standards used by Swartz et al. are some of the Ni XIX transitions reported by Feldman et al. and Feldman and Cohen, and this makes the third decimal place very uncertain.

Swartz et al. (1971) observe in their spectrum of a nickel electrode vacuum spark a transition at 10.306 Å which they classify as Ni XIX $2p^6.{}^1S_0 - 2p^5 4s.{}^1P_1$ and a slightly weaker transition at 10.261 Å. Hutcheon (1975b) has performed a quantum defect analysis which indicates that the 10.261 Å feature is a much more likely candidate for this transition.

Some of these Ni XIX transitions have been reported in solar active region spectra by Evans and Pounds (1968), Rugge and Walker (1968), Walker and Rugge (1969) and Parkinson (1971a). However, their data had only moderate spectral resolution and some of the Ni XIX lines recorded were badly blended with other much stronger lines. For this reason the relative intensities of coronal Ni XIX lines have not previously received close study.

Parkinson (1975c) has reported several Ni XIX n = 3 $\rightarrow$ 2 transitions in the spectrum of region 11621 obtained by SL1101. However, he has not presented any detailed investigation of these lines, and as mentioned earlier, his wavelength uncertainties are, in general, somewhat greater than for the present work.

6.2.2 Interpretation of the Present Spectra

The spectra were searched for features that could be assigned to the Ni XIX spectrum according to three criteria. The wavelength of such a candidate was required to be in reasonable agreement with previous laboratory measurements - though in view of the remarks above (Section 6.2.1) rather greater discrepancies were tolerated than in the case of the analysis of the Fe XVII spectrum. Second, the intensities of the candidate (relative to the Fe XVII lines), as measured from the three active regions, were required to vary in the appropriate manner. Thus, Ni XIX lines could be expected to be stronger relative to Fe XVII for the case of the (hotter) region 12624. Finally, the relative intensities of the Ni XIX lines should be distributed in approximate agreement with the calculated results of Loulergue and Nussbaumer (1975a). This condition is imposed in view of the general success of their results in predicting the corresponding relative intensities for Fe XVII (see Section 6.1).

Application of these conditions to the data leads one to believe that detailed discussion of three Ni XIX $n = 3 \rightarrow 2$ transitions is possible. One other $n = 3 \rightarrow 2$ transition may contribute to a blend. It is convenient to discuss these in turn, starting with the 'resonance' line.

Samples of the spectra (for region 12624) used in the present analysis are shown in Figures 6.1 and 6.5.

6.2.2.1 The $2p^6.{}^1S_0 - 2p^53d.{}^1P_1$ Line.

Feldman et al. (1967) give the laboratory wavelength of this line at 12.42 Å and this value was used as a calibration standard by Swartz et al. (1971). In the present data a group of partially blended lines occurs around 12.4 Å, Lines are observed at 12.406, 12.418, 12.430 and 12.450 Å. Only the 12.430 Å line shows a temperature dependence consistent with assignment to Ni XIX. Thus this feature is much the strongest of the group in the spectrum of the decaying subflare region (12624). The intensity of this line is least in the cool region 11619, greatest in the hot region 12624, and varies in step with the corresponding Fe XVII resonance line. The 12.418 Å line although closer to the laboratory wavelength, is unlikely to be Ni XIX $2p^6.{}^1S_0 - 2p^53d.{}^1P_1$ as it is too weak even to be observed in the subflare region. The 12.430 Å feature is thus tentatively identified with the resonance transition. The proposed identification is supported by good agreement between the measured wavelength of the feature and the value (12.428 ± 0.005 Å) predicted by Hutcheon (1975b) from isoelectronic extrapolation.

6.2.2.2 The $2p^6.{}^1S_0 - 2p^53d.{}^3D_1$ Line

The laboratory wavelength for this line is 12.641 Å (Swartz et al. 1971) (note the caution given in Section 6.2.1 above regarding uncertainty in the last decimal place). The value predicted by Hutcheon (1975b) from isoelectronic extrapolation is 12.649 Å. The candidate feature in the present data is at 12.651 Å.

6.2.2.3 The $2p^6.{}^1S_0 - 2p^53s.{}^1P_1$ Line

The wavelength given by Swartz et al, (1971) is 13.768 Å. The isoelectronic extrapolation procedure (Hutcheon, 1975b) predicts 13.778 ± 0.005 Å. In the present data a feature appears in the spectra of regions 12628 and 12624 at 13.780 Å. The feature fits the other criteria for identification with Ni XIX $2p^6.{}^1S_0 - 2p^53s.{}^1P_1$.

6.2.2.4 The $2s^22p^6.{}^1S_0 - 2s2p^63p.{}^1P_1$ Line.

The wavelength from Feldman et al. (1967) is 11.53 Å, that of Swartz et al. (1971) is 11.522 Å. The isoelectronic extrapolation (Hutcheon, 1975b) predicts 11.525 ± 0.005 Å. The spectra of regions 12624 and 12628 show a feature at 11.526 ± 0.001 Å with an (energy) intensity relative to the resonance line of 0.8 ± 0.2 and 0.6 ± 0.3 respectively. However, this feature is thought to be a blend for the following reasons. First, Cohen and Feldman (1970) and Swartz et al. (1971) observe an unclassified iron line for which they give measured wavelengths of 11.524 and 11.521 Å respectively. (Hutcheon (1975b) has suggested that this iron line is most likely to be a member of the Fe XVIII $2p^5 - 2p^4 4d$ array. A complete analysis of this array would greatly help the interpretation of hot active region and flare spectra.) Secondly, the observed relative intensity is considerably higher than the theoretical value of about 0.2 predicted by Loulergue and Nussbaumer (1975a).

6.2.2.5 The $n = 4 \rightarrow 2$ Transitions.

For the case of the isoelectronic Fe XVII spectrum, the stronger $n = 4 \rightarrow 2$ transitions are found in the present data. For Ni XIX these transitions are all too weak to appear in the present data, according to the calculations of Loulergue and Nussbaumer (1975a). The strongest transition should be $2p^6.{}^1S_0 - 2p^5 4d.{}^1P_1$ (λ 9.97 Å according to Feldman and Cohen (1967)). In the present spectra, the 4σ sensitivity limit at this wavelength is an order of magnitude above the predicted line intensity, and no feature is in fact present.

6.2.3 Discussion

Table 6.3 lists the average measured wavelengths, measured intensities and calculated (by Loulergue and Nussbaumer) intensities of the observed Ni XIX lines, and the upper limit for the $n = 4 \rightarrow 2$ line discussed. Note that the intensity normalisation for the measured data assumes that the resonance line is at 12.430 Å as discussed above, and that it is assumed that the data is not affected by blending other than as discussed above. The measured wavelengths listed for the three $n = 3 \rightarrow 2$ lines are thought to be correct to an uncertainty of about $\pm$ 0.002 Å based upon the spread of measurements from the separate scans and knowledge of the wavelength calibration (see Section 3.3.3.2). The new wavelengths are about 0.01 Å longer than laboratory measurements but they agree much more closely with the values predicted by Hutcheon (1975b) from isoelectronic extrapolation.

The coronal Ni XIX spectrum is weaker than that of Fe XVII and does not therefore provide such a good test of the Loulergue and Nussbaumer model. However, the measured and predicted intensity ratios for the three active regions are consistent and show reasonable agreement, with one exception. The discrepancy, as in the case of Fe XVII, arises (perhaps fortuitously) from a $2p^6 - 2p^5 3s$ transition, namely $^1S_0 - {}^1P_1$, where the relative intensity observed from region 12624 is well above the theoretical value. Unfortunately the Ni XIX $3s.{}^3P_{1,2}$ lines are not available for comparison due to the higher background level on the KAP spectra. The possibility of blending of the Ni XIX line with an unknown transition cannot be eliminated, but such a transition would have to have significant intensity only at $T_e \gtrsim 5 \times 10^6$ K (the discrepancy occurs only for region 12624), and its wavelength separation from the Ni XIX line must be $\lesssim 0.002$ Å (there is no measurable broadening of the $\lambda 13.780$ Å line profile). The upper limits on the intensities of those Ni XIX $n = 3 \rightarrow 2$ and $n = 4 \rightarrow 2$ transitions too weak to be observed are consistent with the predictions.

6.3 The Fe XVII Lines, $n \geq 5 \rightarrow n = 2$

The Fe XVII $n \geq 5 \rightarrow n = 2$ transitions lie in the wavelength region 10 to 12 Å. All of the coronal active region X-ray spectra recorded by the Leicester University Bragg spectrometers since 1966 have shown the presence of many emission lines in this wavelength band. However, until recently neither the resolution nor the sensitivity of available spectra have been good enough for interpretation of most of the features recorded. The complexity of the interval was noted also by Neupert et al. (1973), Beigman et al. (1974) and Parkinson (1975c).

Table 6.4 lists the upper levels of the eight Fe XVII Rydberg series known to be significantly radiated under coronal conditions. Following the convention adopted in Section 6.1, Table 6.4 also gives a key letter to each series so that, for conciseness, any Fe XVII transition may be fully specified by the key letter of its series preceded by the principal quantum number of its upper level.

6.3.1 Previously Available Wavelengths

The wavelengths shown without underlining in Table 6.4 were obtained by Hutcheon (1975b) from a critical survey of previously available measured values (Tyrén, 1938; Cohen and Feldman, 1970; Connerade et al. 1970; Swartz et al. 1971; Parkinson, 1973a, 1975c). The values listed are the averages of the published values weighted according to the inverse of their uncertainties. Only measurements whose third decimal place (in Ångstroms) was significant were included. The r.m.s. deviation of the published values about these averaged values is about 0.002 Å for the n = 3, 4, 5 $\rightarrow$ 2 transitions and about 0.004 Å for n = 6 $\rightarrow$ 2 transitions. These figures are thus conservative estimates of the uncertainty on the average values assuming there were no blends in the measurements used. It has previously been argued, in Section 6.1, that blends with Fe XVII n = 3, 4 $\rightarrow$ 2 lines are unlikely in the present data. It can similarly be shown that blending is unlikely to affect other observations of both these and the n = 5 $\rightarrow$ 2 lines. The one exception is the frequent partial blending of the 4C line, at 12.123 Å, with Ne X Lyα at 12.134 Å, as already discussed in Section 6.1. With regard to the two previously known n = 6 $\rightarrow$ 2 transitions, the 6C line at 10.659 Å is not known to blend with any other line; the 6D line at 10.768 Å is blended in the present data with Ne IX $1s^2.{}^1S_0 - 1s5p.{}^1P_1$ at 10.764 Å.

6.3.2 Predicted Wavelengths

In Table 6.4 required wavelengths whose values were not previously known are shown underlined. They were calculated by Hutcheon (1975b) by extrapolation using the best (averaged) wavelengths of lower members of the same Rydberg series. For the series C, D, E, F and G, the wavelength predictions should have an uncertainty comparable with that of the largest uncertainty in the base wavelengths (i.e. about $\pm$ 0.004 Å). Extrapolation for the A and B series is less accurate because only one term is known in each case (see Section 6.1) and the uncertainties in the absolute predicted wavelengths are then much bigger (about $\pm$ 0.02 Å) though the uncertainties on the differences between calculated wavelengths (in the same configuration) are still quite good. The wavelengths for the H series for n $\geq$ 4 are omitted from Table 6.4 because the power radiated in these magnetic quadrupole transitions is predicted to be too small, by many orders of magnitude, to appear on the present spectra due to depopulation of the $2p^5ns.{}^3P_2$, n $\geq$ 4 levels by allowed electric dipole transitions, as discussed in Section 6.1.4.

The wavelength predictions are given on the assumption that the base wavelength values are not distorted by unknown line blends. Their accuracy is limited by the small number of terms known in each Rydberg series and by the uncertainties in their wavelengths.

6.3.3 Predicted Intensities

No comprehensive calculation of the relative intensities of Fe XVII n $\geqslant$ 5 $\rightarrow$ n = 2 transitions is presently available. Limited results were given by Beigman et al. (1974) but their results for n = 3, 4 $\rightarrow$ 2 were at variance both with measured values and with other calculations (see Section 6.1.2). However, it may be noted that Loulergue and Nussbaumer's (1975a) detailed calculations of the n = 3, 4 $\rightarrow$ 2 transition intensities reveal that the intensities of the n = 4 $\rightarrow$ 2 lines are reasonably well predicted by the two level ion model (see e.g. Section 4.2, and Pottasch (1964)) when Crance's (1973) calculated oscillator strengths are used in that model. (Note that this simple approach does not work for the 2p - 3s lines, cf. Section 6.1). From Section 6.1 it is found that the measured 2p - 4d intensities are smaller by a factor 2 than the Pottasch-Crance predictions, and the measured 2p - 4s intensities larger by a factor 2 than the Pottasch-Crance values. For the present purposes this level of agreement is tolerable for such a simple and convenient calculation. There is no reason to suppose that the Pottasch-Crance calculations will be much less successful for n > 4 $\rightarrow$ 2 transitions; in fact it may be expected that some improvement in the calculated intensities can be made by taking the measured n = 4 $\rightarrow$ 2 intensities as a guide. Thus the Pottasch formula can be forced to fit the measured n = 4 $\rightarrow$ 2 intensities by solution for "empirical oscillator strengths". These latter are to be taken as effective oscillator strengths whose use modifies the two level ion model so as just to compensate for neglect of interactions with other levels. With this approach Hutcheon (1975b) and the present author have used the Pottasch model to predict the intensities of n $\geqslant$ 5 $\rightarrow$ 2 lines by using the empirical $n = 4 \rightarrow 2$ effective oscillator strengths scaled along each Rydberg series in the same ratios as those of Crance where they are available (i.e. up to $n = 6 \rightarrow 2$) or like the asymptotic hydrogenic n^{-3} where they are not. This procedure requires the source emission measure/temperature model (see Sections 4.2 and 4.3, and Equation 4.20). The temperature averaged Gaunt factor was taken as 0.2. The results of these (rather crude) intensity calculations are included in Table 6.5 and discussed below.

6.3.4 The Present Measurements

The present analysis utilizes the data obtained by the SL1101 and SL1206 gypsum spectrometer operating in the fast scan "spectral survey" mode. An example of these observations (for region 12624) is shown in Figure 6.6. The presence (already discussed in Chapter 4 and the present chapter) in the cooling flare region 12624 of hotter material than in regions 11619 and 12628, was most convenient for the present purposes. In particular, the intensities of lines from Fe XVIII and higher Fe ions, relative to the Fe XVII spectrum, are sensitive to the temperature difference between the flaring and non-flaring regions. These trends in the three data sets were used to help discriminate against incorrect assignments to Fe XVII, of observed features which may in fact be poorly known transitions in higher Fe ion stages.

In the present analysis the following convention is adopted: a feature tentatively assigned to an Fe XVII transition is called an "Fe XVII feature"; after confirmation of the assignment the feature is referred to as an "Fe XVII line".

6.3.5 Assignments to Fe XVII

Table 6.5 lists all the features in the present data which occur within 0.01 Å of wavelengths predicted (see Table 6.4) for the C, D, F and G series. The E series is not discussed because the 4E transition is too weak (Section 6.1) to appear in the data and this is also expected to be true for higher E series members. The criterion of wavelength coincidence to $\pm$ 0.01 Å allows for $\pm$ 0.004 Å uncertainty in predicted wavelength, $\pm$ 0.003 Å measurement uncertainty and a somewhat arbitrary $\pm$ 0.003 Å safety margin.

As discussed above (Section 6.3.2) the uncertainty in the wavelength predictions is larger, at $\pm$ 0.02 Å, for the A and B series. This requires relaxation of the coincidence criterion in the search of the data for possible assignments to these series. Agreements similar to those used for the other series suggest a tolerance of $\pm$ 0.03 Å. From Table 6.4 the predicted wavelengths for the 5A and 5B transitions are 10.120 $\pm$ 0.02 Å and 10.127 $\pm$ 0.02 Å respectively. Noting that the uncertainty on their wavelength separation is much less than the quoted absolute uncertainty, it is expected that the two lines should blend in the present data (though if the 5A to 5B intensity ratio follows that for 4A, 4B and 3A, 3B then the 5B line would be very weak in the present spectra). A feature occurs in the data (for the subflare region 12624) at 10.123 $\pm$ 0.003 Å. Its intensity is about one-quarter that of the combined intensity of the 4A and 4B transitions; comparison with the predicted intensities (Table 6.5) thus supports this feature as a candidate for those transitions. Further, by arguments similar to those of Sections 6.3.6 and 6.3.7 below, this feature cannot be assigned to any ion other than Fe XVII. The scans show no other feature within $\pm$ 0.05 Å of the predicted wavelength. The predicted wavelengths of the 6A and 6B transitions are 9.699 $\pm$ 0.02 Å and 9.703 $\pm$ 0.02 Å respectively. The subflare spectrum contains a weak broad feature at about 9.70 Å which may contain a contribution from these lines. It does not occur in the spectra of the other regions. None of the scans shows A or B series transitions for n $\geq$ 7. Hutcheon (1975b) has pointed out that the predicted $2s2p^6np$ levels with n $\geq$ 6 lie above the first ionisation limit for Fe XVII and are autoionising. The intensities of direct transitions from these levels to the ground state may thus be substantially reduced.

All these features in Table 6.5 coincide with the predicted wavelengths to well within the adopted tolerances; conversely only one feature (at 10.320 Å) would be added to the table by allowing a slight (as opposed to substantial) relaxation of tolerances. That these two facts should be true throughout a relatively large and complete set of transitions is persuasive evidence that these features may properly be assigned to Fe XVII, or at least that where there are blends then the Fe XVII components are significant. One feature, at 10.221 $\pm$ 0.004 Å, lies close to the predicted 8C line (10.226 Å) and 9D line (10.220 Å). If the intensities of both are significant they would in fact blend in the data.

Table 6.5 includes the intensities of these Fe XVII transitions, for each of the three active regions. For completeness, the measured wavelengths and intensities for the previously known 5C, 5D, 6C, and 6D Fe XVII lines are also included; thus this table and Table 6.1 together give the measured wavelengths and intensities of all features in the present scans which are known or believed to be properly assigned to Fe XVII. In addition, there are present in the scans, several features between the possible 8C/9D blend at 10.221 Å and the series limits of the C and D series (predicted at 9.726 Å and 9.823 Å respectively). These features may coincide with the wavelengths of predicted Fe XVII transitions for n $\geq$ 8.

However, because the intensity of the 10.221 Å feature is already close to the sensitivity limit of the present observations, these identifications have not been pursued.

Table 6.5 includes the calculated intensities of the $n \geqslant 5 \rightarrow 2$ lines predicted as explained in Section 6.3.3 above. In the data compilation for Table 6.5 the previous practice of Sections 6.1 and 6.2 has been followed; i.e. the intensity figures have been normalized, though with some reservations, to the intensity of the resonance line, 3C. The hesitancy in applying this procedure was due to the fact (Section 6.1) that the observed intensities of $n = 4 \rightarrow 2$ lines (relative to the 3C line) are consistent from one active region to another (and with the Loulergue and Nussbaumer 1975a calculations) only to a factor 2 or so. Consequently, since the predicted intensities in Table 6.5 are essentially extrapolations from the measured $n = 4 \rightarrow 2$ intensities, as explained in Section 6.3.3 above, the predicted relative intensities show a variation from one active region to another. For the $n = 3, 4 \rightarrow 2$ transitions there is a systematic tendency for all lines to be weaker relative to the 3C line in the case of the hotter source region (12624). This trend is also apparent in Table 6.5 for the $n \geqslant 5 \rightarrow 2$ transitions. An experiment in orbit, with the same effective aperture and quantum efficiency as the Leicester Mk. 3 instrument, would readily obtain sufficient good scans of a statistically significant number of source regions to clarify this matter. There is no known mechanism whereby the intensity of the $2p^6.{}^1S_0 - 2p^5 3d.{}^1P_1$ line would be enhanced relative to the rest of the Fe XVII spectrum, by the extent shown, by relatively small increases in the source temperature. The possibility of such an effect has been discussed recently by Loulergue and Nussbaumer (1975a,b). Note that the possible effect is in any case relatively modest, only a factor 2 between the subflare and other regions.

From the preceding paragraph the merit of having intensities predicted from the $n = 4 \rightarrow 2$ intensities is now clear, since the possible temperature variation is then included in the extrapolation and one can still look for agreement between predicted and measured intensities despite the possible temperature difficulties. Examination of Table 6.5 in this way shows quite good agreement for all lines observed in regions 11619 and 12628 with the exception of the 6D line in region 12628, which is anomalously strong. In the case of 12624 (the hot region) the C series lines are all weaker than expected, by about a factor 2. If the comparison is made according to the n-value of the upper level then agreement with prediction is quite satisfactory for $n = 5 \rightarrow 2$ transitions, but transitions from higher n-values tend on the whole to be rather stronger than expected. It is noted that the feature very close to the predicted 7F wavelength (for region 12624) is much stronger than expected whilst no feature is found at the expected 6F wavelength. On these grounds, the validity of that one assignment must be doubted. If there is another line there, it is likely to be an Fe XVIII $2p^5 - 2p^4 5s$ or 5d transition (Hutcheon, 1975b).

6.3.6 The Possibility of Erroneous Assignments in the Present Work

From the presently available knowledge of ionic energy levels and solar element abundances it may be concluded that the only ions whose spectra could confuse the present work are Ne IX, X; Na X, XI; Mg XI, XII; Al XII, XIII; Fe XVIII, XIX and Ni XIX, XX. The calculated energy levels of Garcia and Mack (1965) and Ermplaev and Jones (1974), for the well established term diagrams of H-like and He-like ions respectively, are sufficient to show that, with the exception of Ne IX, X, none of the H-like or He-like ions can be confused with the Fe XVII spectrum. The remaining ions are now considered in turn.

(a) Ne IX. Ermolaev and Jones' wavelength for Ne IX $1s^2.^1S_0 - 1s5p.^1P_1$ is 10.764 Å and it must be accepted that this line blends with the presently observed 6D feature at 10.766 Å. This is the only Fe XVII feature, in Table 6.5, definitely known to be blended with a line of another ion. The matter is of some importance because if the intensity in the Ne IX line is significant then the listed wavelength for the 6D transition has increased uncertainty as also will those predicted (from the measured 6D wavelength) for the 7D and 8D transitions. The intensity of the Ne IX line can be estimated by the Pottasch method as described above for the case of Fe XVII. Taking the source emission measure/temperature model, and using oscillator strengths from Dalgarno and Parkinson (1967), the Ne IX contribution to the blend is found to be about 25%. This extrapolation was checked by comparing similarly predicted intensities with the measured intensities for other non-blended members of the same Ne IX series (e.g. $1s^2.^1S_0 - 1s3p.^1P_1$, see Section 5.2). Agreement was found to within 20%. These data for the wavelength and intensity of the Ne IX line indicate that the proper wavelength for Fe XVII 6D is only 0.001 Å longer than the peak wavelength of the measured blend.

Extrapolation of Ermolaev and Jones' wavelengths to higher members of the Rydberg series (Hutcheon, 1975b) shows that Ne IX $1s^2.^1S_0 - 1snp.^1P_1$, $n \geq 9$, transitions occur in the waveband

10.368 to 10.487 Å. However, the intensity of these lines calculated as described above shows that no significant contribution can be made to the intensity of any of the features observed in the present data.

It is noted that Parkinson's (1975c) measured wavelength of 10.742 Å for the Ne IX transition $1s^2.{}^1S_0 - 1s5p.{}^1P_1$, is believed to be in error due to his mistaking his feature no. 16 (his Table I) for the Ne IX line. It is believed that this Ne IX transition is in fact blended with his recorded Fe XVII 6D feature, as in the present data, and therefore his feature 16 at 10.742 Å should be regarded as unidentified.

(b) Ne X. Figure 6.6 shows the well established Ne X Lyβ line at 10.239 Å easily resolved from the Fe XVII 8C feature at 10.221 Å. Note that Ne X Lyβ certainly blends with Fe XVII 9G at 10.241 Å but this latter transition is not discussed because its intensity must be negligible, as can be seen from the intensities of lower members of the G series (Table 6.5).

(c) Ni XIX. The spectrum of Ni XIX has already been discussed in Section 6.2. The nearest coincidence between any feature listed in Table 6.5 and any known Ni XIX transition, is that between Fe XVII 7F at 10.436 Å and Ni XIX 4G at 10.417 $\pm$ 0.004 Å (Swartz et al. 1971). This near blend should be resolved in the present data. Further, from the calculations of Loulergue and Nussbaumer (1975a), Ni XIX 4G should be an order of magnitude weaker than Ni XIX 4C, and from the discussion of the coronal Ni XIX spectrum, in Section 6.2, the 4C line should itself be an order of magnitude too weak to appear on the present scans.

(d) Ni XX. This ion is expected to have a very low population (e.g. Jordan, 1969, 1970) at the source temperatures calculated for all the present active region spectra (Section 4.3). Further, the strongest Ni XX transition arrays are thought to be $2p^5 - 2p^4ns$, nd. From the classifications of Swartz et al. (1971), and by extrapolation (Hutcheon,1975b) of those of Feldman et al. (1973) for Fe XVIII, it is concluded that these arrays do not overlap the band of the Table 6.5 wavelengths.

(e) Fe XVIII. The possibility of confusion with lines of this ion cannot be dismissed by wavelength arguments alone. The spectrum is rich; the $2p^5 - 2p^4 3s,3d$ arrays together contain over 30 classified transitions (Feldman et al. 1973), and this presumably applies to the corresponding $n \geqslant 4$ arrays. The $2p^5 - 2p^4 3s$, 3d arrays occur at 14 to 16 Å. The corresponding $n \geqslant 4$ arrays have not been analysed beyond the first few members of the F-like sequence (Edlén,1973; Artru and Brillet, 1974). Using the Fe XVIII $n = 3$ energy levels given by Feldman et al. (1973), Hutcheon (1975b) has extrapolated along the Rydberg series to find the wavelength ranges within which the $n = 4 \rightarrow 2$ transition arrays are expected to lie. He has compared the predicted wavebands of the Fe XVIII spectrum with the many probable Fe XVIII lines that do appear in the present spectra. One result of his study was that the Fe XVIII $2p^5 - 2p^4 4d$ array overlaps the Fe XVII $n = 5 \rightarrow 2$ transition wavelengths, and that the Fe XVIII $2p^5 - 2p^4 5s$, 5d arrays overlap with the Fe XVII $n = 6, 7, 8 \rightarrow 2$ wavelengths. In particular it is believed (on the grounds of anomalously high intensity) that the Fe XVII 5G and 7F, 7G features in the present scans may be especially liable to Fe XVIII blends. Nevertheless, as already noted, one of the active regions (12624) contained a significant amount of hot flare residue material. Known Fe XVIII lines are much stronger in the scans of that region than in those of the others (Section 7.1), as is to be expected. Thus, this source temperature difference in the scans, could be used to discrininate against many Fe XVIII lines.

(f) Fe XIX. The risk of confusion with the lines of this ion is perhaps lower. Thus, Jordan's (1969, 1970) calculated ionisation equilibria indicate a much lower (than Fe XVIII) population of this ion stage even at the active region 12624 temperatures. In fact to date, only a few tentative identifications of Fe XIX lines have been made in the scans (in those for region 12624, as might be expected) and then only in a special high sensitivity scan obtained near 13.5 Å (Section 7.2). From these lines it is believed that the spectrum of Fe XIX is too weak in the present scans to interfere with the assignments made to Fe XVII.

6.3.7 Discussion

The present section has discussed the higher members of all eight Rydberg series known to be significantly radiated by Fe XVII under coronal conditions. Comparison of the present coronal X-ray spectra with known and predicted wavelengths, and with simple intensity calculations, has shown a set of observed emission lines whose wavelengths are consistent with the previously known and predicted wavelengths. The measured intensities are broadly as expected, and the intensity discrepancies have been commented upon. The present data give improved wavelengths for many of the observed higher transitions in Fe XVII.

While one can largely exclude the possibility of erroneous identification from most of the measured Fe XVII features, it is not possible to exclude totally the possibility of confusion of the listed transitions with (as yet little known) transitions of Fe XVIII or transitions involving double excited states in Fe XVI. This, together with the fact that there are still a number of unidentified features in the 10 - 12 Å waveband of the present data, indicates that further laboratory study of the spectrum of highly ionized Fe (especially Fe XVIII, XIX) would be of great assistance in the interpretation of the solar X-ray spectrum.* However, the existence of coronal spectra for different source temperatures has, as noted above, provided a powerful technique for avoiding confusion with the spectra of F-like and higher ions of Fe. Note that, because of this latter point, although it is expected that others may be able to apply the analysis given in this section to gain an understanding of their coronal active region spectra, much greater care will be required in using the present results to interpret flare spectra. In those cases there is a high risk of confusing Fe XVII transitions with the little known spectra of more highly charged Fe ions. High resolution flare spectra in this waveband are likely to be very rich. It is likely that equipment having at least the resolution and sensitivity of the Leicester Mk. 3 instrument will be operated in orbit during the next few years and will achieve much better quality data than the present, just due to the order of magnitude longer exposure per spectrum. Even for non-flaring regions many more weak lines will then be observed and the problem of identification will still be severe. It is expected that the above analysis will be of assistance to this task.

---

* Note added in proof: Recent classifications in the transition arrays Fe XVIII $2p^5 - 2p^4 4d$, Fe XIX $2p^4 - 2p^3 4d$ (Bromage et al. 1976) and Fe XIX $2p^4 - 2p^3 3d$ (Bromage and Fawcett, 1976, see present work Section 7.2), have now greatly clarified the situation.

Table 6.1 Measured wavelengths and comparison of measured and calculated intensity ratios for Fe XVII n = 3, 4 $\rightarrow$ 2 lines.

Key letter	Transition (Lower level is $2s^2 2p^6 . {}^1S_0$) Upper level		Measured wavelength (Å)	Relative energy intensity (3C = 1)					
				Measured d)			Calculated a)		
				Active region no.			$T_e (10^6$ K)		
				11619	12628	12624	2	5	8
3A	$2s2p^6 3p.$	${}^1P_1$	13.825 ± 0.002	0.12 ± 0.02	0.08 ± 0.02	0.11 ± 0.01	0.088	0.11	0.12
3B		${}^3P_1$	13.890 ± 0.003	0.09 ± 0.02	0.05 ± 0.02	0.03 ± 0.01	0.011	0.014	0.015
3C	$2s^2 2p^5 3d.$	${}^1P_1$	15.013 ± 0.002	1	1	1	1	1	1
3D		${}^3D_1$	15.262 ± 0.002	0.41 ± 0.04	0.44 ± 0.04	0.38 ± 0.02	0.37	0.37	0.37
3E		${}^3P_1$	15.455 ± 0.003	0.14 ± 0.03	0.07 ± 0.03	0.09 ± 0.01	0.11	0.12	0.13
3F	$2s^2 2p^5 3s.$	${}^1P_1$	16.775 ± 0.003	0.85 ± 0.07	0.77 ± 0.06	0.54 ± 0.03	0.53	0.55	0.56
3G		${}^3P_1$	17.051 ± 0.002	0.68 ± 0.06	1.02 ± 0.07	0.67 ± 0.04	0.88	0.97	1.00
3H		${}^3P_2$	17.097 ± 0.002	1.14 ± 0.09	0.86 ± 0.07	0.69 ± 0.04	0.65	0.75	0.79
4A	$2s2p^6 4p.$	${}^1P_1$	11.029 ± 0.004	0.012 ± 0.004	0.009 ± 0.003	0.004 ± 0.001	0.003	0.0078	0.01
4B		${}^3P_1$					0.0005	0.0013	0.002
4C	$2s^2 2p^5 4d.$	${}^1P_1$	12.124 ± 0.002 b)	0.060 ± 0.008	0.059 ± 0.006	0.041 ± 0.003	0.033	0.063	0.073
4D		${}^3D_1$	12.264 ± 0.002	0.056 ± 0.008	0.043 ± 0.005	0.021 ± 0.002	0.028	0.051	0.059
4E		${}^3P_1$	12.319 c)	$\leqslant 0.002 \pm 0.002$	$\leqslant 0.001 \pm 0.001$	$\leqslant 0.001 \pm 0.001$	0.0006	0.0010	0.0012
4F	$2s^2 2p^5 4s.$	${}^1P_1$	12.521 ± 0.002	0.007 ± 0.003	0.008 ± 0.002	0.004 ± 0.001	0.0017	0.0029	0.003
4G		${}^3P_1$	12.680 ± 0.002	0.008 ± 0.003	0.008 ± 0.002	0.004 ± 0.001	0.0026	0.0043	0.005
Measured absolute intensity of 3C reference line (10^{-6} erg cm^{-2} s^{-1})				31 ± 2	75 ± 3	133 ± 4			

Footnotes to Table 6.1

a) Loulergue and Nussbaumer (1975a)

b) Partially blended (see text)

c) Swartz et al (1971)

d) Upper limits are recorded intensities at the expected wavelengths of the lines.

Table 6.2 Population mechanisms for upper levels of observed lines $2p^6\,{}^1S_0 - 2p^5 3d,s$ in Fe XVII (Loulergue and Nussbaumer, 1973).

Excited level	Excitation or cascade from	$2p^6\,{}^1S_0$ (in %)		$2p^5 3s\,{}^3P_0$ (in %)		$2p^5 3p$ (in %)		$2s\,2p^6 3s$ (in %)	$2s\,2p^6 3d$ (in %)
		(1)	(2)	(1)	(2)	(1)	(2)	(2)	(2)
$2p^5 3s$	${}^3P_2^0$	10	2			90	88	10	
	${}^3P_1^0$	5	2	15	15	80	70	13	
	${}^3P_0^0$	6	2			94	88	10	
	${}^1P_1^0$	5	2			95	83	15	
$2p^5 3d$	${}^3P_1^0$		15						85
	${}^3D_1^0$		80						20
	${}^1P_1^0$		90						10

Model of the ion includes 26 levels for (1) and 36 levels for (2)

Table 6.3 Measured wavelengths and comparison of measured and calculated intensity ratios for Ni XIX lines

Key Letter	Transition (Lower level is $2s^2 2p^6 . {}^1S_o$) Upper level	Measured wavelength (Å)	Relative energy intensity				
			Measured[c]			Calculated[a]	
			Active region no.			T_e (10^6 K)	
			11619	12628	12624	3	8
3C	$2s^2 2p^5 3d . {}^1P_1$	12.430 ± 0.002	1	1	1	1	1
3D	${}^3D_1$	12.651 ± 0.002	$\leqslant 0.2 \pm 0.2$	1.0 ± 0.4	0.4 ± 0.2	0.42	0.42
3F	$2s^2 2p^5 3s . {}^1P_1$	13.780 ± 0.001	$\leqslant 0.1 \pm 0.1$	0.6 ± 0.2	1.6 ± 0.3	0.60	0.61
4C	$2s^2 2p^5 4d . {}^1P_1$	9.97[b]	$\leqslant 0.2 \pm 0.2$	$\leqslant 0.6 \pm 0.3$	$\leqslant 0.3 \pm 0.1$	0.04	0.07
Measured absolute intensity of 3C reference line (10^{-6} erg $cm^{-2} s^{-1}$)			0.39 ± 0.12	0.56 ± 0.16	0.97 ± 0.18		

a) Loulergue and Nussbaumer (1975a)
b) Feldman and Cohen (1967)
c) Upper limits are recorded intensities at the expected wavelengths of the lines.

Table 6.4 Predicted (underlined) and known transitions in Fe XVII (Hutcheon, 1975b)

Rydberg series key letter	Transition upper level[a]	Wavelength (Å) n = 3	= 4	= 5	= 6	= 7	= 8	Series limit
A	$2s\,2p^6np.\,^1P_1$	13.824	<u>11.025</u>	<u>10.120</u>	<u>9.699</u>	<u>9.466</u>	<u>9.322</u>	<u>8.893</u>
B	$^3P_1$	13.890	<u>11.041</u>	<u>10.127</u>	<u>9.703</u>	<u>9.486</u>	<u>9.324</u>	<u>8.893</u>
C	$2s^22p^5nd.\,^1P_1$	15.012	12.123	11.129	10.659	<u>10.391</u>	<u>10.226</u>[b]	<u>9.726</u>
D	$^3D_1$	15.260	12.263	11.250	10.768	<u>10.499</u>	<u>10.331</u>	<u>9.823</u>
E	$^3P_1$	15.452	12.319	<u>11.274</u>	<u>10.782</u>	<u>10.507</u>	<u>10.337</u>	<u>9.726</u>
F	$2s^22p^5ns.\,^1P_1$	16.775	12.521	<u>11.288</u>	<u>10.737</u>	<u>10.438</u>	<u>10.255</u>	<u>9.823</u>
G	$^3P_1$	17.051	12.681	<u>11.419</u>	<u>10.856</u>	<u>10.550</u>	<u>10.364</u>	<u>9.823</u>
H	$^3P_2$	17.094						

a) Lower level is $2s^22p^6.\,^1S_0$ for all transitions.

b) Note that this value is close to the predicted wavelength for the 9D line at 10.220 Å.

Table 6.5 Predicted and measured wavelengths and intensities for Fe XVII n $\geqslant$ 5 $\rightarrow$ 2 transitions

Transition	Wavelength (Å)				Relative energy intensity (3C = 1000)					
					Active region no.					
					11619		12628		12624	
	previously known	predicted[a]	measured	uncertainty (mÅ)	predicted	measured	predicted	measured	predicted	measured
5A 5B		10.120 10.127	10.123	3					1.7	2.2 $\pm$ 1
5C	11.129		11.129	1½	20	17 $\pm$ 5	19	20 $\pm$ 4	14	8 $\pm$ 2
6C	10.659		10.655	3	10	6 $\pm$ 3	9	6 $\pm$ 2	6	3 $\pm$ 1
7C		10.391	10.386	3	5	7 $\pm$ 4	5.2	3.4 $\pm$ 2	3.9	1.4 $\pm$ 1
8C 9D		10.226 10.220	10.221	4			3.3 1.1	3 $\pm$ 2	2.5 0.6	1.4 $\pm$ 1
5D	11.250		11.250	1½	15	10 $\pm$ 4	11	11 $\pm$ 3	6	7 $\pm$ 2
6D	10.768		10.766[b]	4	6	7 $\pm$ 4[b]	4	12 $\pm$ 3[b]	2.3	6 $\pm$ 1[b]
7D		10.499	10.501	2			2.5	4.7 $\pm$ 2	1.3	3.3 $\pm$ 1
8D		10.331	10.332[c]	3			1.6	4.7 $\pm$ 2	0.85	1.9 $\pm$ 0.9
9D										
5F		11.288	11.287	2			1.9	3.7 $\pm$ 2	1.1	2.1 $\pm$ 1
6F		10.737	-							$<$1.6[d]
7F		10.438	10.436	1					0.26	1.7 $\pm$ 1
5G		11.419	11.420	3			2.2	2.5 $\pm$ 2	1.1	2.5 $\pm$ 1
6G		10.856	10.851	6			0.93	3.4 $\pm$ 2	0.45	1.2 $\pm$ 0.9
7G		10.550	10.550	1					0.26	1.7 $\pm$ 1

a) Hutcheon (1975b).
b) Includes Ne IX $1s^2.{}^1S_0 - 1s5p.{}^1P_1$ transition (see text).
c) There is another recorded feature at 10.320 Å (see Section 6.3.5).
d) 3σ upper limit.

FIGURES

Chapter 6

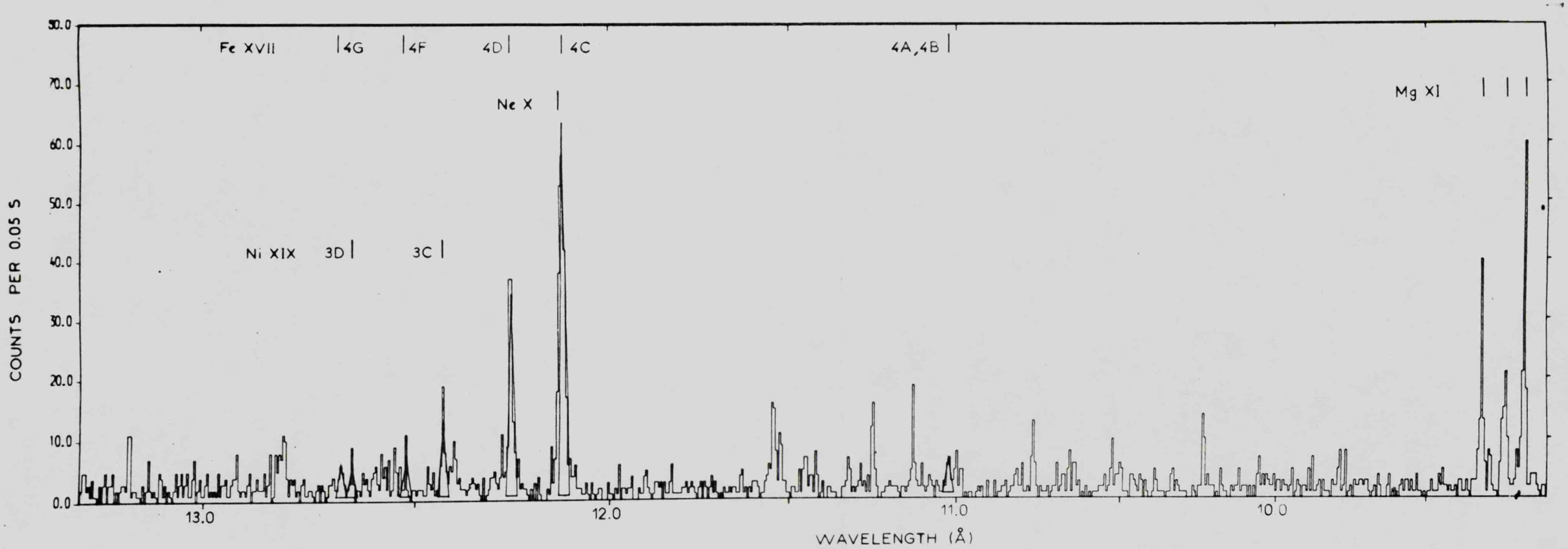
Fe XVII
4G
4F
4D
4C
4A,4B
Ne X
Mg XI
Ni XIX
3D
3C
COUNTS PER 0.05 S
WAVELENGTH (Å)
13.0
12.0
11.0
10.0
0.0
10.0
20.0
30.0
40.0
50.0
60.0
70.0
80.0

Fig. 6.1.

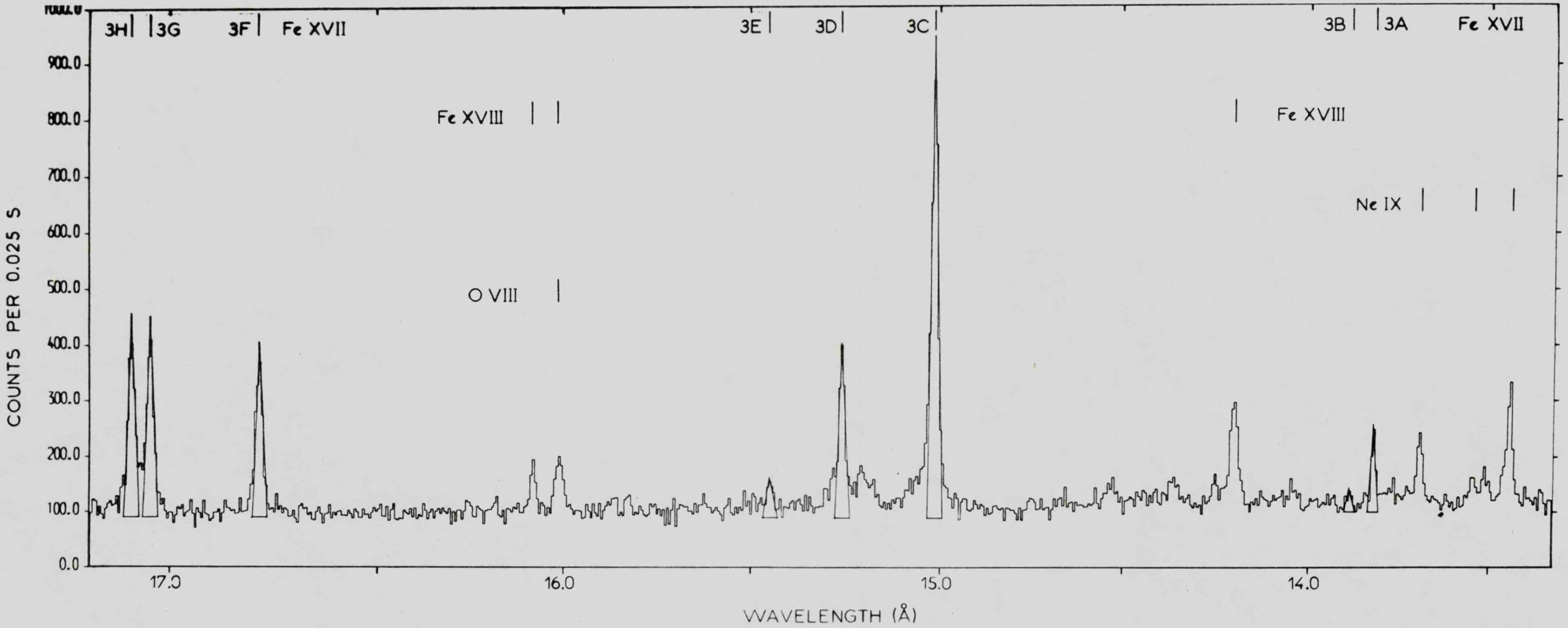
3H
3G
3F
Fe XVII
3E
3D
3C
3B
3A
Fe XVII
Fe XVIII
Fe XVIII
Ne IX
O VIII
COUNTS PER 0.025 S
900.0
800.0
700.0
600.0
500.0
400.0
300.0
200.0
100.0
0.0
17.0
16.0
15.0
14.0
WAVELENGTH (Å)

Fig. 6.2.

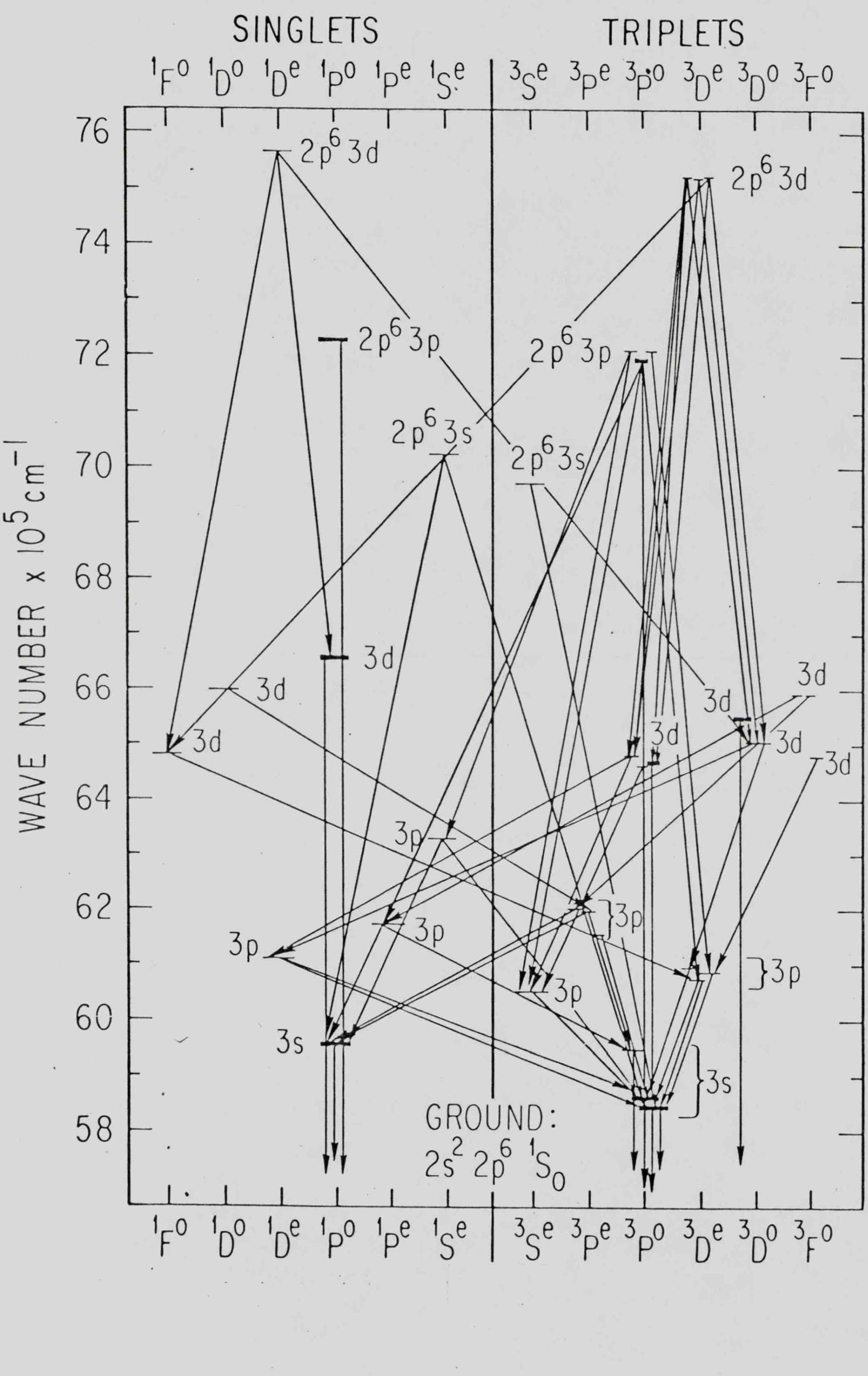

SINGLETS
TRIPLETS
1F0 1D0 1De 1P0 1Pe 1Se
3Se 3Pe 3P0 3De 3D0 3F0
WAVE NUMBER x 10^5 cm^-1
76
74
72
70
68
66
64
62
60
58
2p6 3d
2p6 3p
2p6 3s
3d
3p
3s
GROUND:
2s2 2p6 1S0

Fig. 6.3.

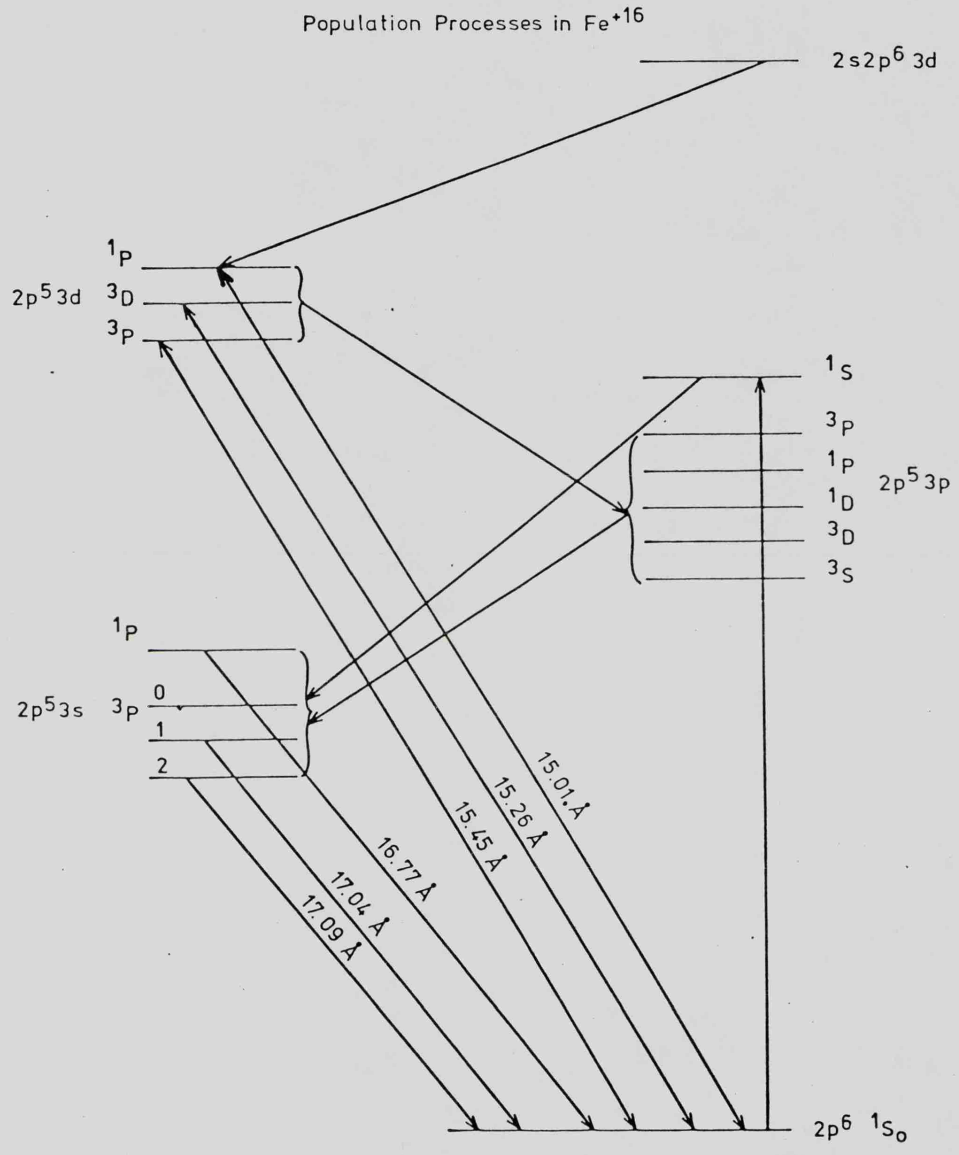

Population Processes in Fe+16
2s2p6 3d
1P
2p5 3d 3D
3P
1S
3P
1P
2p5 3p
1D
3D
3S
1P
2p5 3s 3P 0
1
2
15.01 Å
15.26 Å
15.45 Å
16.77 Å
17.04 Å
17.09 Å
2p6 1So

Fig. 6.4.

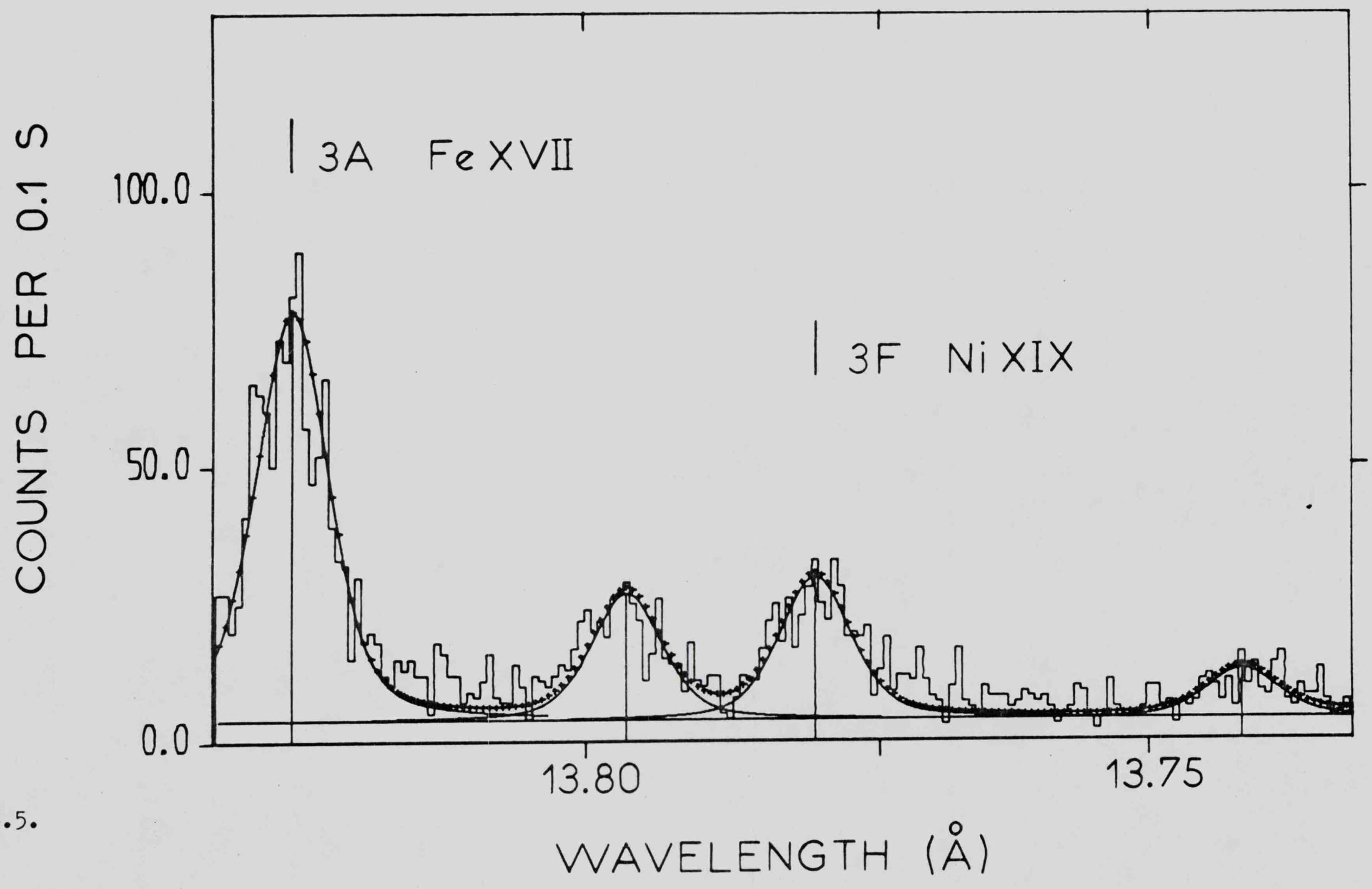
3A Fe XVII
3F Ni XIX
COUNTS PER 0.1 S
100.0
50.0
0.0
13.80
13.75
WAVELENGTH (Å)

Fig. 6.5.

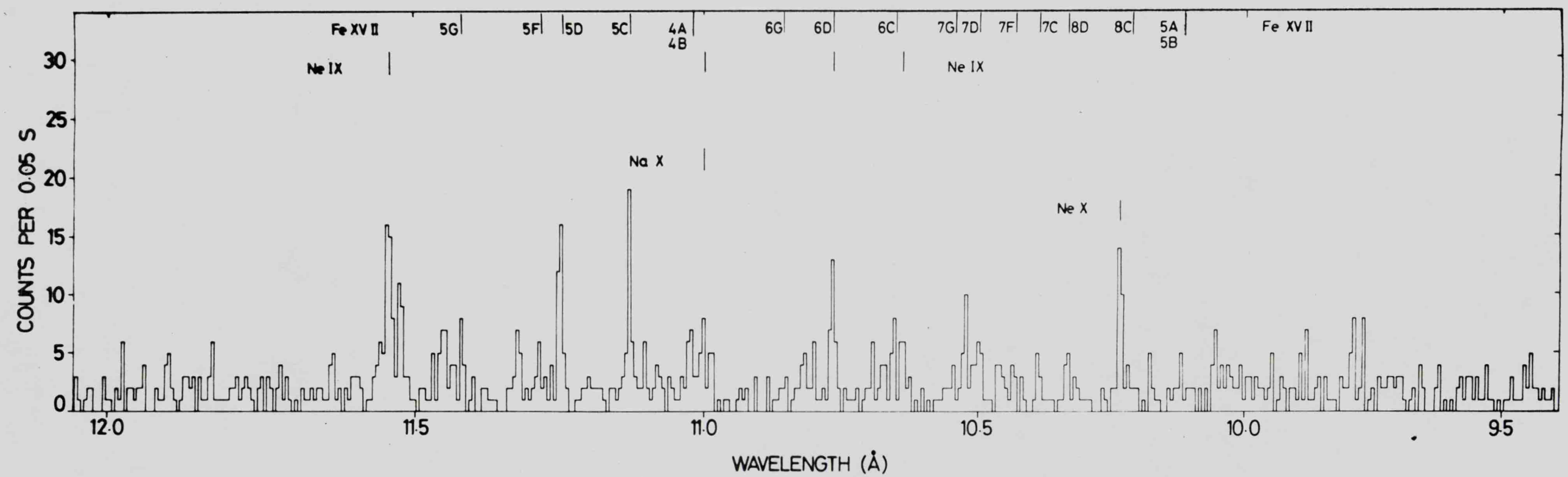

Fe XVII
Ne IX
5G
5F
5D
5C
4A
4B
Na X
6G
6D
6C
7G
7D
7F
7C
8D
8C
5A
5B
Ne IX
Ne X
Fe XVII
COUNTS PER 0·05 S
0
5
10
15
20
25
30
12·0
11·5
11·0
10·5
10·0
9·5
WAVELENGTH (Å)

Fig. 6.6.

Chapter 7

Fe XVIII, Fe XIX AND OTHER 'HIGH TEMPERATURE' LINES

The spectrum of the decaying flare region 12624 shows, quite clearly, a number (~ 20) of lines which are very weak or absent in the spectra of regions 11621 (Parkinson, 1975c), 11619 and 12628. It has already been shown in Chapter 4 that the main difference between region 12624 and the other three active regions (11619, 11621 and 12628), as regards the distribution of emission measure with temperature, is the presence in region 12624 of a significant quantity of plasma at $T_e \approx 6 \times 10^6$K. Thus it appears quite reasonable to assume that the enhancements in the spectrum of region 12624 are due to lines which are produced more efficiently at temperatures above 5×10^6 K, and in fact it will be shown below that ten of these 'high temperature' lines between $\lambda\lambda$14 and 16 Å agree very well in wavelength with lines classified in laboratory spectra, by Feldman et al. (1973), as F-like Fe XVIII $n = 3 \rightarrow 2$ transitions.

It is convenient, for reasons which will become clear later, to divide the discussion of the 'high temperature' lines, into two parts, covering the wavelength intervals 14 - 16 Å and 13 - 14 Å. There are a number of features in the region 10 to 13 Å which might properly be termed 'high temperature' lines, however these features are, in general, much less prominent than those occurring between 13 and 16 Å. Hutcheon (1975b) has pointed out that the Fe XVIII $n \geqslant 4 \rightarrow n = 2$ transitions are expected to fall in the region 10 - 13 Å, and that the wavelengths of most of these transitions are not known with any accuracy (see Section 6.3.6). Therefore, the interval 10 - 13 Å will not be discussed further in this Chapter.

7.1 The Fe XVIII Lines, $\lambda\lambda$14 - 16 Å

To date, the most complete analysis of the energy levels in F-like ions is that of Feldman et al. (1973), who have used laboratory spectra in order to classify n = 3 → 2 transitions in the F-like isoelectronic sequence up to Z = 27 (Co). Feldman et al. have identified 27 features in their Fe spectrum as due to Fe XVIII n = 3 → 2 transitions. It is the wavelengths given by Feldman et al. that have been used to search the present solar spectra for possible Fe XVIII lines.

Lines of Fe XVIII have previously been reported in the solar X-ray spectrum by Evans and Pounds (1968), Walker and Rugge (1969), Neupert et al. (1973), Brabban and Glencross (1973), Beigman et al. (1974) and Parkinson (1975c). However, with the exception of Parkinson's results (for region 11621), these observations had a much lower resolution than the present spectra of regions 11619, 12628 and 12624. Thus, the high resolution and sensitivity of the present data, combined with the favourable temperature conditions in region 12624, allow for the first time, clear observations of many Fe XVIII lines in the solar X-ray spectrum.

7.1.1 The Fe XVIII Term System

The ground state configuration of a F-like ion is $1s^2 2s^2 2p^5$, the incomplete $2p^5$ shell giving the two levels $2p^5 . ^2P_{\frac{1}{2},3/2}$. Ordinary excited terms (as distinct from inner-shell transitions) are formed by the addition of an orbiting electron to a core with configuration $2p^4$. This core gives the terms ^1S, ^3P, ^1D. Each of the core terms can combine with the configuration nl of the orbiting electron. Only an excited level where l = 0 or 2 can decay by an optically allowed (i.e. electric dipole) radiative transition to the ground configuration, and thus there are 28 such transitions for n = 3. They are listed in Table 7.1. Feldman et al. (1973) have assigned laboratory measured wavelengths to 27 n = 3 $\rightarrow$ 2 transitions in Fe XVIII, of which 17 are optically allowed.

7.1.2 Analysis of the Present Observations

The data used in the present analysis of the Fe XVIII spectrum were obtained in the fast scan mode of the SL1101/SL1206 KAP spectrometer. Examples of these observations are shown in Figure 7.1. The spectra were searched for features that could be assigned to the Fe XVIII spectrum according to two criteria. First, the wavelength of a candidate feature was required to be in reasonable agreement with the laboratory measurements of Feldman et al. (1973). Second, the intensities of the candidate (relative to the lines of the lower temperature ion Fe XVII), as measured from the three active regions, were required to vary in the appropriate manner. Thus Fe XVIII lines could be expected to be stronger relative to Fe XVII for the (hotter) region 12624.

According to these conditions, ten features in the present spectra can be identified with Fe XVIII transitions. Table 7.2 lists the measured wavelengths and intensities of these features, together with the corresponding wavelengths and classifications from Feldman et al. Results are presented only for regions 11619 and 12624; for region 12628 a 4σ upper limit of about 7 x 10^{-6} erg cm^{-2} sec^{-1} may be placed on the intensity of any of the features listed in Table 7.2. For all the observed features which have been assigned to Fe XVIII in the present spectra, there are no other features within about 0.04 Å that could be offered as alternative candidates. Table 7.2 shows the good agreement between the present measured wavelengths and those of Feldman et al.

Several of the presently reported features have profile widths significantly greater than those of nearby lines, and hence it must be assumed that these broader features contain contributions from two or more transitions. In several cases, reference to the wavelengths of Feldman et al. shows that a blend is probably due to two Fe XVIII transitions. The wide feature observed at λ16.00 Å in the solar spectra is a blend of the Fe XVIII transition $2p^5.{}^2P_{3/2} - 2p^4({}^3P)3s.{}^4P_{3/2}$ at 16.003 Å (Feldman et al. 1973) and O VIII Lyβ at 16.006 Å (Garcia and Mack, 1965). The case of the λ14.20 Å feature is of particular interest. Feldman et al. predict that the $2p^5.{}^2P_{3/2} - 2p^4({}^1D)3d.{}^2P_{3/2}, {}^2D_{5/2}$ lines should lie within 0.009 Å of each other from K XI to Fe XVIII, and state that this wavelength difference is less than the accuracy of their calculations and less than the resolution of their observations for blended lines. In addition, they say that both lines are predicted to be among the most intense F-like lines observed, the ${}^2P_{3/2} - {}^2P_{3/2}$ line being predicted to be about half the intensity of ${}^2P_{3/2} - {}^2D_{5/2}$. Feldman et al. are thus unable to exclude the possibility that their observed feature which they classify as ${}^2D_{5/2}$ may be a blend of two lines; stating however, that two distinct lines are not observed in the spectra of any ion along the isoelectronic sequence. The present spectra of both regions 11619 and 12624 clearly show that the λ14.20 Å feature is broadened relative to a single line profile (as estimated from nearby features believed to be unblended; see Figure 7.1), i.e.:

FWHM (λ14.20 Å feature) $\approx$ 0.027 Å,

FWHM (single line) $\approx$ 0.016 Å.

At present, there are no detailed calculations available for the spectral line intensities of F-like ions. Several authors

(Cohen et al. 1968; Gruzdev, 1971; Chapman and Shadmi, 1973) have calculated oscillator strengths for transitions in highly charged F-like ions, however, there appear to be some serious discrepancies between these results. Walker (1975) has noted that the $2p^4 3p$ levels decay by cascade to the $2p^4 3s$ levels, a somewhat similar situation to that already encountered in Ne-like ions (see Chapter 6). Thus it seems likely that accurate predictions of F-like line intensities will require a many-level ion model of the type calculated by Loulergue and Nussbaumer (1973, 1975a) for the Ne-like ions Fe XVII and Ni XIX. Indeed, the model for the F-like ion may well turn out to be even more complex than the Ne-like case, due to the larger number of energy levels and possible transitions in the F-like ion.

7.2 λλ13 - 14 Å

The SL1101 and SL1206 gypsum spectrometers covered the wavelength interval 13 to 14 Å in the high sensitivity, high resolution slow-scan mode. The data are shown in Figure 7.2 (and 5.4). All the spectral lines observed from the quiescent active regions11621 (Parkinson, 1975c), 11619 (Figure 5.4c) and 12628 (Figure 7.2b) are now well established transitions, namely: the Ne IX $n = 2 \longrightarrow 1$ and satellite lines, Fe XVII $2s^2 2p^6.{}^1S_0 - 2s2p^6 3p.{}^1P_1$ and Ni XIX $2p^6.{}^1S_0 - 2p^5 3s.{}^1P_1$. However, the spectrum of the (decaying flare) region 12624 (Figure 7.2a) shows, in addition, about a dozen new lines, and it is these that are the subject of the present Section. Little progress was made in the classification of these new lines until the recent calculation, by Bromage and Fawcett (1976), of the wavelengths and oscillator strengths of the Fe XIX 2p - 3d lines in this waveband.

Table 7.3 lists the features found in Figure 7.2a together with their measured wavelengths and intensities.

7.2.1 Classification of the Lines

In the first column of Table 7.3 lines which are regarded as well established in the solar spectrum by previous observation are distinguished by their wavelengths being offset to the left. All of these lines appear on Figure 7.2b and no other lines appear on Figure 7.2b. The new lines which appear on Figure 7.2a, and are not registered on Figure 7.2b, are similarly distinguished by their wavelengths being offset to the right in the first column of Table 7.3. It appears that classification of these lines must be sought among those spectra of medium Z ions ($8 \lesssim Z \lesssim 30$) which are not significantly excited until the temperature reaches about 5×10^6 K and, in this case of the solar atmosphere, that means Fe XVIII to perhaps Fe XXI and, with lower probability (mostly because of the smaller abundance) the isoelectronic nickel spectra. It is believed that lines due to other ions (including other elements) are unlikely and can be ruled out on the grounds of solar element abundance (see e.g. Withbroe, 1971, 1976) and/or wavelength. In particular the wavelengths of transitions in H- and He-like ions are well established (Garcia and Mack, 1965; Ermolaev and Jones, 1974; respectively), as are those in Ne-like Fe XVII and Ni XIX (see Chapter 6).

In Table 7.3, under the heading "classification", the accepted identities of previously observed lines are listed offset to the left. Distinguished by an offset to the right are listed transitions which must be considered as candidate contributors to the features shown on Figure 7.2a. The list contains those transitions for which was noticed a wavelength coincidence between a wavelength of a feature in the first column of Table 7.3 and results of previous theoretical or laboratory plasma studies of spectra considered likely (on grounds as above) to be emitted by coronal material. The list may not be exhaustive since knowledge of the relevant spectra is still fragmentary. Even in the works cited (in the last column of Table 7.3) wavelengths found by direct wave mechanical calculation often have uncertainty of order 0.02 Å and those found by isoelectronic extrapolation are sometimes such large extrapolations (over Z) as to suffer similarly. Some further possibilities, e.g. the calculation of Ni XX wavelengths by Gruzdev (1971), have been omitted either because the wavelength uncertainties are so large as to embrace several previously unobserved lines in the present spectra or else because extrapolations (by Hutcheon, 1975b) from more recent published work do not support the earlier work. Chapman and Shadmi (1973) have calculated the wavelengths of many Fe XVIII inner shell transitions in this waveband and some of these wavelengths also show coincidences with the present features. However, although they find quite large calculated oscillator strengths, their wavelength uncertainty appears to be about $\pm$ 0.07 Å and again this is too large to assess possible assignment in this case. They are absent from even the best laboratory spectra (Fawcett, 1976) and it is doubted that they can be significant at the low density limit. Further wavelength coincidences may be noted between the present features and unidentified wavelengths in the laboratory Fe spectra of Cohen and Feldman (1970). However Fawcett (1976) has pointed out that the Fe XIX $2s2p^5$ - $2s2p^4 3d$ transition array contributes a dense population of lines to the 13.2 to 13.8 Å band and he believes that most of the remaining unidentified lines in this part of the

Cohen and Feldman spectrum are members of this array. The energy levels of the $2s2p^5$ configuration lie well above those of the $2s^2 2p^4$ ground configuration so these lines cannot be expected in the coronal spectrum for reasons discussed below. These lines are not present even in the spectra of θ-pinch machines operated at plasma electron density near 10^{16} cm^{-3} (Fawcett, 1976).

Note that for every previously observed line (wavelength offset to the left in Table 7.3, first column) a previously accepted classification can be found (offset to the left under "classification"). However, it so happens that, for source material above 5×10^6 K, in most of these cases, additional transitions, at very close wavelengths according to previous authors, may blend (at resolution $\Delta\lambda/\lambda \approx$ 1 part in 1000) with the usually accepted classification. Indeed, in two cases, i.e. λ13.464 and λ13.473 Å, it is believed that the previously accepted classification is not the dominant component in the blends in Figure 7.2a and in one further case, λ13.491 Å, it is not known which of the listed transitions is dominant despite the existence of a previously accepted classification at this wavelength.

7.2.1.1 Classification with the Fe XIX 2p - 3d transition array.

Bromage and Fawcett (1976) have found the wavelengths and oscillator strengths of all electric dipole transitions in this array by adjustment to fit laboratory wavelengths (for oxygen-like spectra) of directly calculated energy levels. Their Table V (and the present work, Table 7.4) lists those transitions thus found to have significant oscillator strength. Gabriel et al. (1965) and Fawcett (1974, p 237) have argued that near the low electron density limit, as at coronal densities, the collision rate may be insufficient to maintain, against radiative decay, a thermal distribution of the ion populations among the energy levels of the ground configurations. That is, it can be expected that all terms in the ground configuration except the lowest (in this case ^3P) will have low population. Then, to the extent that collision strengths for electron collisional excitation follow the general trends of the corresponding radiation oscillator strengths, it can be expected that most collisional excitations will be to excited states in those allowed series which end on the lowest ground term. Examination of Table 7.4 shows that some thirteen of these allowed 2p - 3d transitions, ending on the lowest ground term, can be expected to be excited in coronal conditions. To these should be added $^1D_2 - (^2P)^3P_2$ and $^1D_2 - (^2P)^3D_2$ where it is noted that the upper levels may easily be excited and the oscillator strengths for these intercombination transitions are large enough for them to compete with direct decay to the ground level. Of these fifteen predicted transitions one, $^3P_1 - (^4S)^2D_2$ at λ14.039 Å, lies outside the limits of Figure 7.2a; of the remaining 14, Bromage and Fawcett consider that 10 clearly resolved features in Figure 7.2a may be assigned as in their Table V consistently with the uncertainty in their wavelength calculations. Of the remaining 4, three (λ13.442, λ13.554, λ13.563 Å; see next paragraph) appear to be hopelessly blended with strong Ne IX lines and the remaining one, the intercombination line λ13.712 Å, may be just visible in the wing of the strong Ne IX line λ13.699 Å. The best estimate of wavelength for this apparent line is 13.708 Å. The intercombination line Fe XIX $2p^4.{}^1D_2 - 2p^3(^2P)3d.{}^3P_2$ thus appears to be a good candidate classification for it.

λ13.442 Å is a transition from the $(^2P)^3D_1$ upper level (to the level $^3P_0$) which must compete with the transition at

λ13.469 Å from the same upper level (to the level $^3P_1$). This latter transition is observed and the ratio of the two oscillator strengths then allows estimation of the power in $^3P_0 - (^2P)^3D_1$ at λ13.442 Å. Reference to Tables 7.3 and 7.4 then shows λ13.442 Å to be probably very weak. Similarly the intercombination line $^1D_2 - (^2P)^3D_2$ at λ13.554 Å must compete with the direct decay $^3P_1 - (^2P)^3D_2$ at λ13.409 Å. This latter transition is observed and the oscillator strength ratio suggests significant power in $^1D_2 - (^2P)^3D_2$ at λ13.554 Å blended with the Ne IX intercombination line. Again the line at λ13.563 Å $^3P_1 - (^2P)^3P_2$ is competed with by the intercombination line $^1D_2 - (^2P)^3P_2$ at λ13.712 Å. This latter line is discussed above as possibly detected in the wing of the Ne IX forbidden line. This suggests that some flux from the line at λ13.563 Å probably is blended into the Ne IX intercombination line at λ13.553 Å.

The arguments in favour of these assignments to Fe XIX may now be assembled:

a) The new lines are very probably iron lines (see above).

b) They are not lines of Fe XVII (c.f. Chapter 6).

c) Though knowledge of its spectra is not complete they are probably not lines of Fe XVIII (see above, also Section 7.1, and Feldman et al. 1973; Bromage et al. 1976).

d) Their temperature dependence is about right for Fe XIX.

e) Their wavelength coincidence with the calculated values of Bromage and Fawcett, <u>and throughout a relatively large set</u>, is somewhat persuasive.

f) Of the set of transitions predicted with reasonable oscillator strengths ($\dot{f}$) by Bromage and Fawcett, the <u>complete</u> set is accounted for (except for one line not scanned and three expected to be blended with much stronger lines). Not one can be said to be missing in such a way as to challenge the completeness of the set.

g) Although the two-level ion model may well prove inadequate for accurate description of the intensities of such complex spectra, nevertheless the lines with strongest f-values are markedly strongest in the coronal spectrum and the general trend of coronal intensities follows the trends in predicted f-values.

7.2.1.2 Still unidentified lines.

Note that four features on Figure 7.2a, λ13.321, λ13.356, λ13.373, λ13.644 Å remain unidentified.

7.2.1.3 Blending with particular attention to Ne IX.

The intensities of the Ne IX $n = 2 \rightarrow 1$ transitions are much used in plasma diagnostics. It has been noted above and can be seen in Table 7.3 that the resonance line is probably blended with an Fe XIX line (predicted separation 0.005 Å) and the inter-combination line is blended with two contaminants (separations 0.001 Å and 0.01 Å). Also noted was the presence of an Fe XIX line in the wing of the Ne IX forbidden line, λ13.699 Å. In the case of use of much lower (than the present 1 part in 1000) resolution equipment the Ne IX lines cannot be used for diagnosis of plasma containing much material above about 5×10^6 K. The point is made clear by comparison of Figure 7.2a with the corresponding data from any of the presently reported satellite instruments e.g. Neupert et al. (1973) (they were aware of the difficulty, see their Section 4.1).

The situation with regard to the Ne IX satellites requires careful interpretation. Thus Figure 7.2b, a spectrum of rather cooler material than that of Figure 7.2a, shows the three usually reported neon satellites (i.e. Ne VIII $1s^2nl - 1s2pnl$ where n = 4, 3 and 2). In Figure 7.2a the satellite Ne VIII $1s^2 2s.\,^2S_{1/2} - 1s2p(^1P)2s.\,^2P_{1/2,\ 3/2}$ is definitely absent. Two new lines appear closely on either side of this satellite wavelength and, with only slightly less resolving power, might be mistaken for the satellite. Similarly, Figure 7.2a shows very little power at the wavelength of the Ne VIII $1s^2 3l - 1s2p3l$ transitions. In Figure 7.2a very little power can be allowed for Ne VIII $1s^2 4l$ - $1s2p4l$ either, though there is lower confidence in this case because the two new lines now required to fit the data between λ13.45 and λ13.48 Å would be blended with any small residual flux in this line. Detailed study of the satellites Ne VIII $1s^2 nl - 1s2pnl$, n = 4, 3, 2, in the presence of material above 4×10^6 K will require equipment much more powerful, in respect of both resolution and sensitivity, than any reported to date.

Table 7.1 The 28 optically allowed transitions $n = n' \rightarrow 2$ (excluding inner-shell transitons) in a F-like ion (Hutcheon, 1975b)

Lower level	Upper level
$2p^5.\,^2P_{\frac{1}{2}}$	$2p^4(^1S)n's.\,^2S_{\frac{1}{2}}$
$^2P_{\frac{3}{2}}$	$^2S_{\frac{1}{2}}$
$2p^5.\,^2P_{\frac{1}{2}}$	$2p^4(^3P)n's.\,^2P_{\frac{1}{2}}$
$^2P_{\frac{1}{2}}$	$^2P_{\frac{3}{2}}$
$^2P_{\frac{3}{2}}$	$^2P_{\frac{1}{2}}$
$^2P_{\frac{3}{2}}$	$^2P_{\frac{3}{2}}$
$2p^5.\,^2P_{\frac{1}{2}}$	$2p^4(^1D)n's.\,^2D_{\frac{3}{2}}$
$^2P_{\frac{3}{2}}$	$^2D_{\frac{3}{2}}$
$^2P_{\frac{3}{2}}$	$^2D_{\frac{5}{2}}$
$2p^5.\,^2P_{\frac{1}{2}}$	$2p^4(^1S)n'd.\,^2D_{\frac{3}{2}}$
$^2P_{\frac{3}{2}}$	$^2D_{\frac{3}{2}}$
$^2P_{\frac{3}{2}}$	$^2D_{\frac{5}{2}}$
$^2P_{\frac{1}{2}}$	$2p^4(^3P)n'd.\,^2P_{\frac{1}{2}}$
$^2P_{\frac{1}{2}}$	$^2P_{\frac{3}{2}}$
$^2P_{\frac{3}{2}}$	$^2P_{\frac{1}{2}}$
$^2P_{\frac{1}{2}}$	$^2P_{\frac{3}{2}}$
$^2P_{\frac{1}{2}}$	$^2D_{\frac{3}{2}}$
$^2P_{\frac{3}{2}}$	$^2D_{\frac{3}{2}}$
$^2P_{\frac{3}{2}}$	$^2D_{\frac{5}{2}}$
$2p^5.\,^2P_{\frac{1}{2}}$	$2p^4(^1D)n'd.\,^2S_{\frac{1}{2}}$
$^2P_{\frac{3}{2}}$	$^2S_{\frac{1}{2}}$
$^2P_{\frac{1}{2}}$	$^2P_{\frac{1}{2}}$
$^2P_{\frac{1}{2}}$	$^2P_{\frac{3}{2}}$
$^2P_{\frac{3}{2}}$	$^2P_{\frac{1}{2}}$
$^2P_{\frac{3}{2}}$	$^2P_{\frac{3}{2}}$
$^2P_{\frac{1}{2}}$	$^2D_{\frac{3}{2}}$
$^2P_{\frac{3}{2}}$	$^2D_{\frac{3}{2}}$
$^2P_{\frac{3}{2}}$	$^2D_{\frac{5}{2}}$

Table 7.2 Measured wavelengths and intensities for Fe XVIII n = 3 → 2 lines

Line no.	Transition[a)]	Measured Wavelength (Å): Laboratory (Feldman et al., 1973)	Present work, solar active region no.: 11619	12624	Mean	Measured intensity (10^{-6} erg cm^{-2} s^{-1}), active region no.: 11619	12624
1	$2p^5\,{}^2P_{\frac{1}{2}} - 2p^4(^1S)3d\,{}^2D_{\frac{3}{2}}$	14.121		14.132	14.132		4.7±1.4
2	$^2P_{\frac{3}{2}} - 2p^4(^1D)3d\,{}^2D_{\frac{5}{2}}$, $^2P_{\frac{3}{2}}$	14.20	14.210[e)]	14.205[e)]	14.207	6.95±0.83	38.8±2.4
3	$^2S_{\frac{1}{2}}$	14.255	14.258	14.257	14.257	1.85±0.59	7.8±1.5
	$^2P_{\frac{1}{2}} - {}^2D_{\frac{3}{2}}$	14.361[b)]					
4	$^2P_{\frac{3}{2}} - 2p^4(^3P)3d\,{}^2D_{\frac{5}{2}}$	14.373	14.380	14.369[e)]	14.374	2.83±0.65	11.2±1.7
5	$^4F_{\frac{5}{2}}$	14.536		14.535[e)]	14.535		13.3±2.0
	$^4P_{\frac{3}{2}}$	14.551[c)]					
6	$2p^4(^1D)3s\,{}^2D_{\frac{5}{2}}$	15.623	15.629	15.627	15.628	2.64±0.84	8.1±2.0
7	$2p^4(^3P)3s\,{}^2P_{\frac{3}{2}}$	15.826		15.826	15.826		7.4±2.0
8	$^2P_{\frac{1}{2}} - 2p^4(^1D)3s\,{}^2D_{\frac{3}{2}}$	15.869	15.875	15.873[e)]	15.874	3.16±0.88	10.2±2.0
9	$^2P_{\frac{3}{2}} - 2p^4(^3P)3s\,{}^4P_{\frac{3}{2}}$	16.003	16.009[d,e)]	16.003[d,e)]	16.006[d)]	8.79±1.23[d)]	28.4±2.4[d)]
10	$^4P_{\frac{5}{2}}$	16.073	16.080	16.072	16.076	2.70±0.89	19.8±2.4

a) Classification from Feldman et al., (1973)
b) May contribute to line no. 4.
c) May contribute to line no. 5.
d) Blended with O VIII Lyβ, λ16.006 Å (see text). Quoted figures refer to whole blend.
e) 'Wide' feature (see text).

Table 7.3 Wavelengths of all emission lines observed in Figures 7.2a and b

Measured Wavelength (Å)	Measured Intensity (10^{-6} erg $cm^{-2}s^{-1}$)	Uncertainty	Statistical Significance of the Measurement	Candidate	Classification	(Previous) Wavelength	Reference
13.288	0.44	0.06	14.9	* Fe XIX	$2p^4.{}^3P_2-2p^3({}^2P)3d.{}^3D_3$	13.289	d
13.321	0.34	0.06	11.6				
13.356	0.30	0.05	9.9				
13.373	0.30	0.05	9.9				
13.402	0.56	0.06	18.2	* Fe XIX	$2p^4.{}^3P_1-2p^3({}^2P)3d.{}^3D_2$	13.409	d
13.447 +	9.47	0.26	large	+x* Ne IX	$1s^2.{}^1S_o-1s2p.{}^1P_1$	13.447	a
				Fe XIX	$2p^4.{}^3P_o-2p^3({}^2P)3d.{}^3D_1$	13.442	d
13.464	1.30	0.08	large	* Fe XIX	$2p^4.{}^3P_1-2p^3({}^2P)3d.{}^3D_1$	13.469	d
(13.467)	(this feature recorded on Fig. 7.2b but not on Fig.7.2a,see text)			x Ne VIII	$1s^2 4l-1s2p4l$	13.46	c
13.473	0.99	0.07	large	* Fe XIX	$2p^4.{}^3P_2-2p^3({}^2D)3d.{}^3S_1$	13.488	d
13.491	0.21	0.05	6.6	Fe XIX	$2p^4.{}^3P_o-2p^3({}^2P)3d.{}^3P_1$	13.499	d
(13.489)	(on the spectrum of Fig. 7.2b)			x Ne VIII	$1s^2 3l-1s2p3l$	13.48	c
13.507	1.43	0.09	large	* Fe XIX	$2p^4.{}^3P_2-2p^3({}^2D)3d.{}^3P_2$	13.525	d
13.521	1.97	0.10	large	* Fe XIX	$2p^4.{}^3P_2-2p^3({}^2D)3d.{}^3D_3$	13.536	d
13.553	1.78	0.09	large	Ne IX	$1s^2.{}^1S_o-1s2p.{}^3P_2$	13.550	a
				x* Ne IX	$1s^2.{}^1S_o-1s2p.{}^3P_1$	13.553	a
				Fe XIX	$2p^4.{}^1D_2-2p^3({}^2P)3d.{}^3D_2$	13.554	d
				Fe XIX	$2p^4.{}^3P_1-2p^3({}^2P)3d.{}^3P_2$	13.563	d

13.644	0.57	0.07	16.6			
13.653	present only on Fig. 7.2b			× Ne VIII $1s^2 2s.\,^2S_{\frac{1}{2}}-1s2p(^1P)2s.\,^2P_{\frac{1}{2},\frac{3}{2}}$	$(\frac{3}{2})$13.652 $(\frac{1}{2})$13.654	b b
13.671	0.58	0.07	16.6	*Fe XIX $2p^4.\,^3P_1-2p^3(^2D)3d.\,^3P_1$	13.693	d
13.700	7.07	0.20	large	×*Ne IX $1s^2.\,^1S_o-1s2s.\,^3S_1$	13.699	e
13.708	0.5	factor 2	-	*Fe XIX $2p^4.\,^1D_2-2p^3(^2P)3d.\,^3P_2$	13.712	d
13.742	0.55	0.07	14.9	*Fe XIX $2p^4.\,^3P_1-2p^3(^2D)3d.\,^3D_2$	13.748	d
13.780	1.63	0.10	large	×*Ni XIX $2p^6.\,^1S_o-2p^5 3s.\,^1P_1$	13.780	e
				Fe XX $2p^3.\,^4S_{\frac{3}{2}}-2p^2(^3P)3s.\,^4P_{\frac{5}{2}}$	13.78	f
13.797	1.46	0.10	large	*Fe XIX $2p^4.\,^3P_2-2p^3(^4S)3d.\,^3D_3$	13.818	d
13.827	4.80	0.17	large	×*Fe XVII $2s^2 2p^6.\,^1S_o-2s2p^6 3p.\,^1P_1$	13.825	e

Footnote:
In the first column, lines which have previously been reported are signified by their wavelengths offset to the left. They all appear on Fig. 7.2b. New lines recorded for the first time on Fig. 7.2a are signified by wavelengths to the right of the first column. The measured intensities, for all lines, are those recorded on Fig. 7.2a. For the spectrum recorded in Fig. 7.2a that candidate transition which is believed to be the dominant contribution to each recorded line is marked with an asterisk (*). For the spectrum of Fig. 7.2b the believed dominant transition is marked with a cross(×). Previously accepted classifications are distinguished by an offset to the left under the 'classification' column. The references for previous wavelengths are as follows: a, Ermolaev and Jones (1974); b, Gabriel (1972a); c, Summers (1973); d, Bromage and Fawcett (1976); e, present work, Chapter 6; f, Fawcett et al. (1974).

+ Reference wavelength (see Chapter 5).

Table 7.4 Calculated wavelengths and weighted oscillator strengths (gf) in Fe XIX for $2p^4$-$2p^3 3d$ transitions (Bromage and Fawcett, 1976)

Transition	gf	Wavelength (Å)
$^3P_2 - (^2P)^3D_3$	0.17	13.289
$^3P_1 - (^2P)^3D_2$	0.80	13.409
$^3P_2 - (^2P)^3F_3$	0.01	13.428
$^3P_0 - (^2P)^3D_1$	0.08	13.442
$^3P_2 - (^2D)^1F_3$	1.06	13.451
$^3P_1 - (^2P)^3D_1$	1.22	13.469
$^3P_1 - (^2P)^1D_2$	0.29	13.484
$^3P_2 - (^2D)^3S_1$	1.22	13.488
$^3P_0 - (^2P)^3P_1$	1.48	13.499
$^3P_2 - (^2D)^3P_2$	2.14	13.525
$^3P_2 - (^2D)^3D_3$	3.61	13.536
$^1D_2 - (^2P)^1F_3$	5.44	13.546
$^1D_2 - (^2P)^3D_2$	1.68	13.554
$^3P_1 - (^2P)^3P_2$	1.32	13.563
$^3P_1 - (^2D)^3P_1$	0.61	13.693
$^1D_2 - (^2P)^3P_2$	0.86	13.712
$^1S_o - (^2P)^1P_1$	2.21	13.737
$^1D_2 - (^2P)^3F_3$	0.72	13.739
$^2P_1 - (^2D)^3D_2$	1.27	13.748
$^1D_2 - (^2D)^1F_3$	1.07	13.763
$^3P_2 - (^4S)^3D_3$	1.25	13.818
$^1D_2 - (^2D)^1D_2$	0.53	13.821
$^3P_1 - (^4S)^3D_2$	0.20	14.039

gf = statistical weight of lower level x absorption oscillator strength

The calculated energy levels of the Fe XIX ground configuration $2s^2 2p^4$ are (Fawcett et al. 1974, in units of cm^{-1} above the lowest ground term $^3P_2$): $^3P_2(0)$, $^3P_1(89,316)$, $^3P_o(73,823)$, $^1D_2(159,268)$, $^1S_o(323,831)$.

FIGURES

Chapter 7

7.1 Active region X-ray spectra, 13 - 17 Å, recorded with a KAP Bragg spectrometer (scan rate 0.01 rad s^{-1}). The numbered (Fe XVIII) spectral lines are identified in Table 7.2.

- a McMath region 12624, flight SL1206 (during late stages of a small flare)
- b McMath region 12628, flight SL1206
- c McMath region 11619, flight SL1101.

7.2 Active region X-ray spectra, 13.3 - 13.8 Å, recorded with the SL1206 gypsum spectrometer (scan rate 0.001 rad s^{-1}).

- a McMath region 12624 (during late stages of a small flare)
- b McMath region 12628.

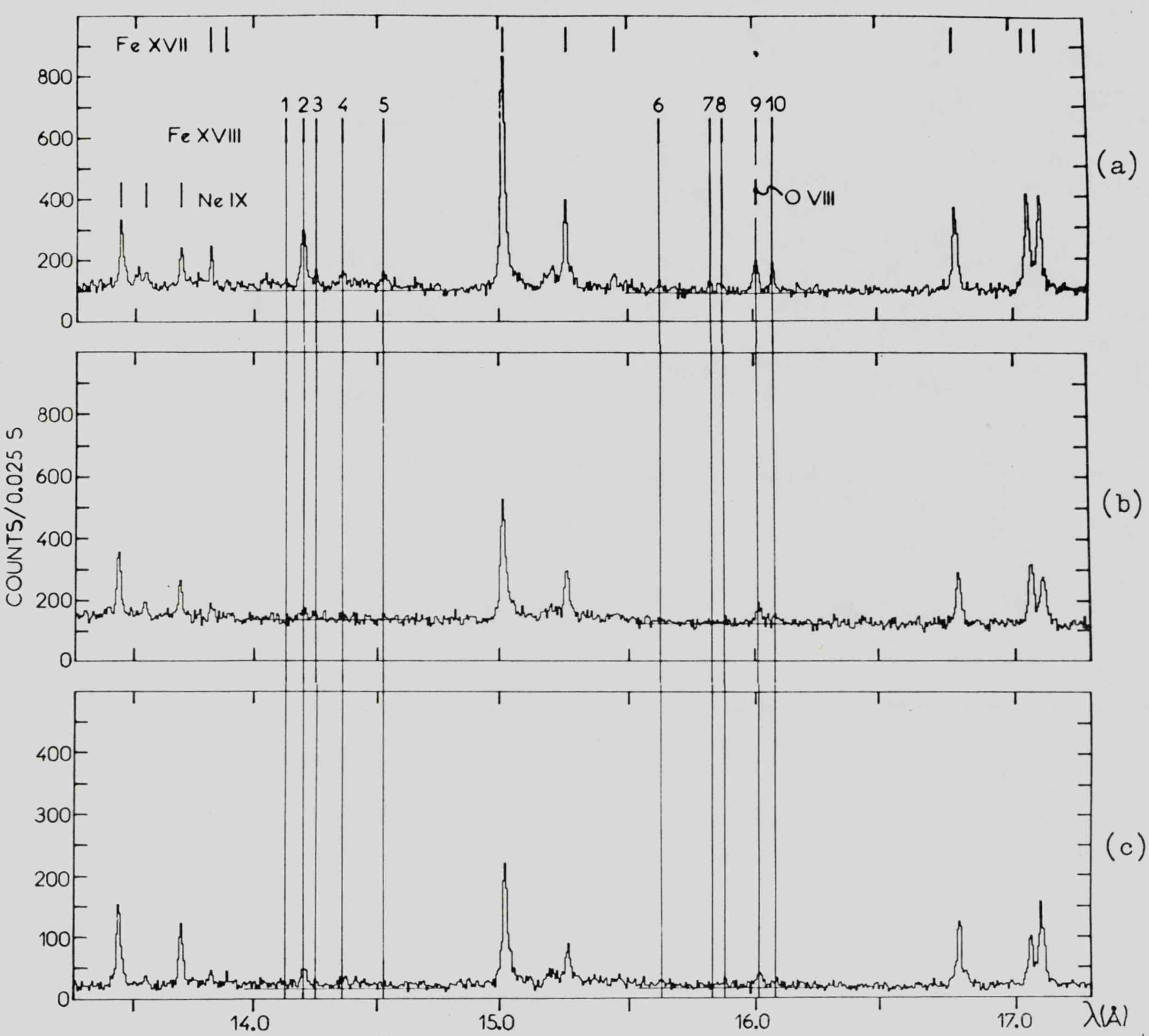

Fe XVII
800
600
400
200
0
Fe XVIII
Ne IX
1 2 3 4 5
6
7 8 9 10
O VIII
(a)
COUNTS/0.025 S
(b)
300
100
(c)
14.0
15.0
16.0
17.0
λ(Å)

Fig. 7.1.

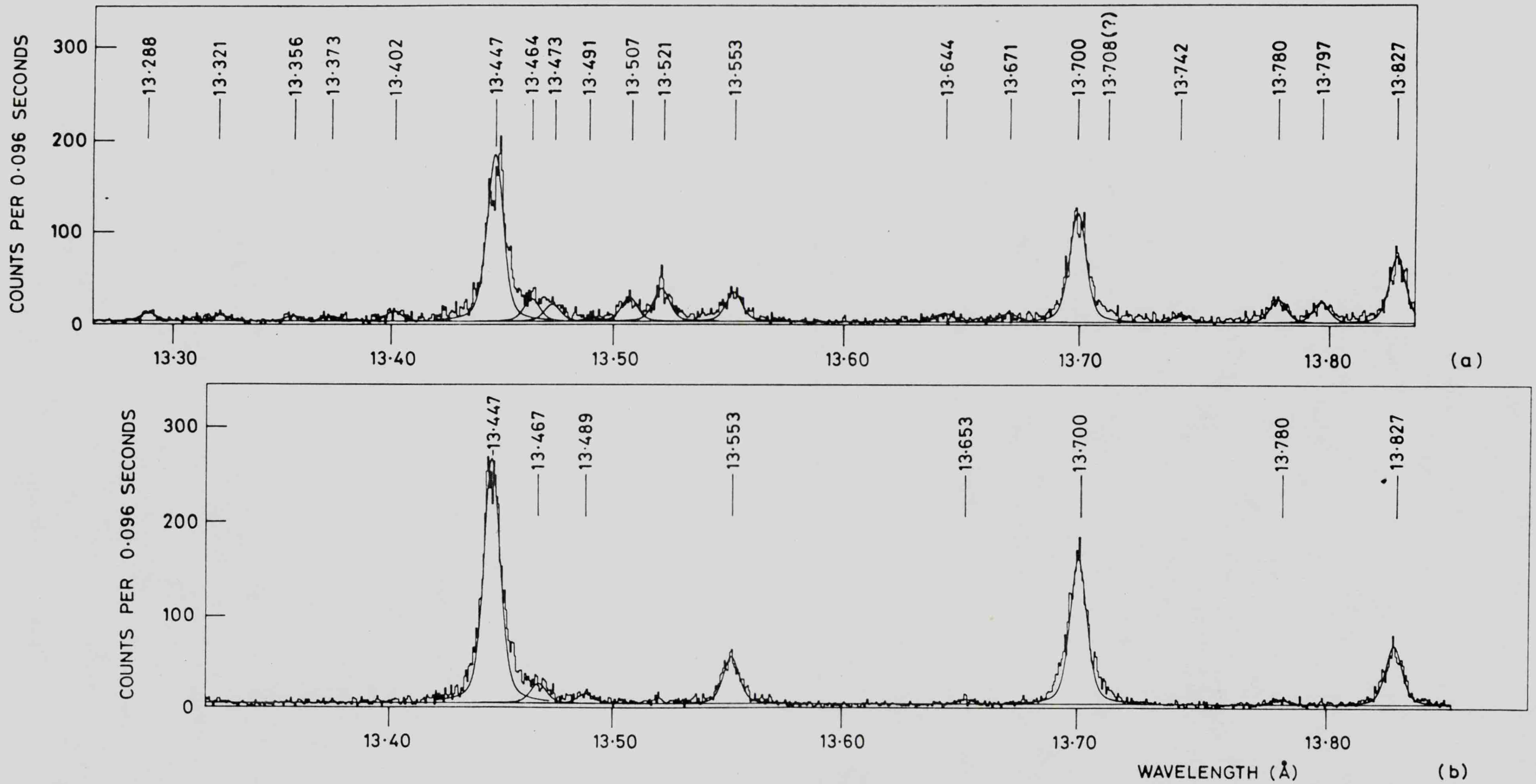

COUNTS PER 0·096 SECONDS
300
200
100
0
13·288
13·321
13·356
13·373
13·402
13·447
13·464
13·473
13·491
13·507
13·521
13·553
13·644
13·671
13·700
13·708(?)
13·742
13·780
13·797
13·827
13·30
13·40
13·50
13·60
13·70
13·80
(a)
COUNTS PER 0·096 SECONDS
300
200
100
0
13·447
13·467
13·489
13·553
13·653
13·700
13·780
13·827
13·40
13·50
13·60
13·70
13·80
WAVELENGTH (Å)
(b)

Fig. 7.2.

FINAL DISCUSSION AND FUTURE WORK

Spectra and images of solar coronal active regions have been presented. These observations have been interpreted as thermal emission from an optically thin plasma, and thus used to determine electron temperature, electron density, emission measure ($n_e^2 \Delta V$), spatial structure and element abundances of the active region plasma. The most detailed model to date, of the density and temperature distribution within a high temperature ($T_e \gtrsim 10^6$ K) active region loop system, has been derived. The present active region models have been compared with each other and with previous models to examine possible variations with the solar activity cycle. Element abundances, together with estimates of their uncertainties, have been derived for oxygen, neon, sodium, magnesium, aluminium, silicon, iron and nickel.

The measurements of spectral line wavelengths and intensities have yielded new information on the spectra of highly stripped ions. The observation and interpretation, have been discussed, of spectra of ions in particular isoelectronic sequences, namely: Helium-like O VII , Ne IX and Mg XI, Neon-like Fe XVII and Ni XIX, Fluorine-like Fe XVIII and Oxygen-like Fe XIX. Many new spectral line identifications have been made; improved wavelengths have been given for previously known lines, and where possible, the measured intensities have been compared with calculated values.

Future work using the present data will include:

(1) Study of energy balance in active regions.

(2) Comparison of images obtained in different wavebands

(from visible to X-ray), and hence corresponding to different temperatures and heights in the solar atmosphere. This information will be used to derive a complete active region model.

(3) Study of growth and time evolution of active regions, and in particular, changes associated with flares.

(4) Further investigation of the spectra of the ions mentioned above, especially Fe XVIII.

Looking to future observations of the Sun from space vehicles, planned projects include the NASA "Solar Maximum Mission" satellite, and solar instruments to be flown on the NASA "Space Shuttle" and associated ESA (European Space Agency) "Spacelab".

Appendix I

PREDICTION OF SPECTRAL LINE WAVELENGTHS BY EXTRAPOLATION

The following is an outline of the extrapolation methods used by Hutcheon (1975b) to predict spectral line wavelengths. This summary is freely adapted from a private communication from Dr. R.J. Hutcheon to the present author. The techniques are based on those discussed by Edlén (1964). The term "extrapolation" will be used here to cover both the processes of interpolation and extrapolation.

I.1 Extrapolation Along a Rydberg Series

From the Bohr formula for the energy difference between two energy levels in an ion (e.g. Herzberg, 1944):

$$\delta = n - \left[Rz^2/(W_I + W_S - 10^8 \lambda^{-1})\right]^{\frac{1}{2}} \qquad (I.1)$$

where: δ = quantum defect = n - n'

n = principal quantum number of the upper level of the transition

n' = effective principal quantum number of the upper level of the transition

R = Rydberg constant (cm^{-1})

z = net charge of the ionic core, i.e. z-1 is the net ionic charge (e.g. z = 17 for Fe XVII)

W_I = ionization potential of the ground level (cm^{-1})

W_S = energy gap between ionization potential and appropriate series limit (determined by the energy state of the ionic core as the orbiting electron tends to the series limit) (cm^{-1})

λ = wavelength of the transition to the ground state (Å).

A "Ritz plot" is a graph of the quantum defect against the "reduced term value" t, where t is the energy gap between the relevant upper level and the appropriate series limit in units of the z-scaled Rydberg, i.e.:

$$t = (W_I + W_S - 10^8 \lambda^{-1})/(Rz^2) . \tag{I.2}$$

From Equations I.1 and I.2 it follows that:

$$t = (n - \delta)^{-2} . \tag{I.3}$$

"Ritz Law" states that the Ritz plot should be linear, i.e.:

$$\delta = a + bt \tag{I.4}$$

where a and b are constants. Using known values of λ, the ionization potential W_I is derived, by iteration, by finding that value of W_I which produces a linear Ritz plot. Wavelengths can then be extrapolated by producing the Ritz plot towards higher n (i.e. towards t = 0) and reading the appropriate values of δ from the graph; sometimes an iterative process (using Equation I.3) may be required.

I.2 Extrapolation along an Isoelectronic Sequence

Wavelengths may be extrapolated along an isoelectronic sequence by calculating the quantity

$$Q = \frac{10^8 \lambda^{-1} - Rz^2(n_1^{-2} - n_2^{-2})}{z} \tag{I.5}$$

where: λ = wavelength of the transition (Å)

n_1 = principal quantum number of the lower level of the transition

n_2 = principal quantum number of the upper level of the transition.

Q has the property of smooth, slowly varying, and often nearly linear, dependence on z (e.g. Fawcett et al. 1974).

References

Acton, L.W.: 1975, Space Sci. Instr., in press.

Acton, L.W., Catura, R.C.: 1975, Phil. Trans. R.S., A281, 383 (published 1976).

Acton, L.W., Catura, R.C., Meyerott, A.J., Wolfson, C.J., Culhane,J.L.: 1972, Solar Phys., 26, 183.

Acton, L.W., Catura, R.C., Joki, E.G.: 1975, Ap. J., 195, L93.

Adler, I.: 1967, in E.F. Kaelble (ed.), Handbook of X-rays, McGraw-Hill, New York, Vol. 31, p.18.

Allen, C.W.: 1973, Astrophysical Quantities, Athlone Press, London.

Allen, J.W., Dupree, A.K.: 1969, Ap. J., 155, 27.

Artru, M.C., Brillet, W.L.: 1974, J.O.S.A., 64, 1063.

Babcock, H.W.: 1960, Ap. J., 133, 572.

Bates, D.R., Dalgarno, A.: 1962, in D.R. Bates (ed.), Atomic and Molecular Processes, Academic Press, London, p.245.

Batstone, R.M., Evans, K., Parkinson, J.H., Pounds, K.A.: 1970, Solar Phys., 13, 389.

Bearden, A.J., Huffman, F.N.: 1962, Rev. Sci. Instr., 34, 1233 (published 1963).

Beigman, I.L., Urnov, A.M.: 1969, Opt. Spect., 27, 203.

Beigman, I.L., Vainstein, L.A.: 1971, Soviet Astron., 14, 825.

Beigman, I.L., Vainstein, L.A., Vinogradova, A.: 1970, Soviet Astron. 13, 775.

Beigman, I.L., Grineva, Yu. I., Korneev, V.V., Krutov, V.V., Mandelstam, S.L., Vainstein, L.A., Vasilyev, B.N., Zhitnik, I.A.: 1974, Preprint No. 67, P.N. Lebedev Physical Institute, Moscow.

Bely, O.: 1968, Phys. Lett., 26A, 408.

Bely, O., Bely, F.: 1967, Solar Phys., 2, 285.

Bely, O., Van Regemorter, H.: 1970, Ann. Rev. Astron. Ap., 8, 329.

Bertin, E.P.: 1970, Principles and Practice of X-ray Spectrometric Analysis, Plenum Press, New York.

Bertsch, D.L., Fichtel, C.E., Reames, D.V. : 1972, Ap. J., 171, 169.

Bhalla, C.P., Gabriel, A.H., Presnyakov, L.P.: 1975, M.N.R.A.S., 172, 359.

Blaha, M.: 1971, B.A.A.S., 3, 246.

Blake, R.L.: 1970, Adv. X-ray Anal., 13, 352.

Blake, R.L., Wick, W.D.: 1973, Rev. Sci. Instr., 44, 985.

Blumenthal, G.R., Tucker, W.H.: 1974, in R. Giacconi and H. Gursky (eds.), X-Ray Astronomy, Reidel, Dordrecht, p.99.

Blumenthal, G.R., Drake, G.W.F., Tucker, W.H.: 1972, Ap. J., 172, 205.

Bonnelle, C., Senemaud, C., Senemaud, G., Chambe, G., Guionnet, M., Henoux, J.C., Michard, R.: 1973, Solar Phys., 29, 341.

Brabban, D.H., Glencross, W.M.: 1973, Nature Phys. Sci., 244, 67.

Brandt, J.C.: 1966, The Sun and Stars, McGraw-Hill Inc., New York.

Bromage, G.E, Fawcett, B.C.: 1976, M.N.R.A.S., in press.

Bromage, G.E., Cowan, R.D., Fawcett, B.C.: 1976, M.N.R.A.S., in press.

Burgess, A.: 1964a, Memoirs R.A.S., 69, 1.

Burgess, A.: 1964b, Ap. J., 139, 776.

Burgess, A.: 1965, Ap. J., 141, 1588.

Burgess, A., Hummer, D.G., Tully, J.A.: 1970, Phil. Trans. R.S., A266, 225.

Cameron, A.G.W.: 1974, Space Sci. Rev., 15, 121.

Carillon, A., Jamelot, P., Sureau, A., Jaeglé, P.: 1972, Phys. Lett., 38A, 91.

Chambe, G.: 1971, Astron. Ap., 12, 210.

Chapman, R.D., Shadmi, Y.: 1973, J.O.S.A., 63, 1440.

Codling, K., Madden, R.P., Ederer, D.L.: 1967, Phys. Rev., 155, 26.

Cohen, L., Feldman, U.: 1970, Ap. J. 160, L105.

Connerade, J.P., Peacock, N.J., Speer, R.J.: 1970, Solar Phys., 14, 159.

Cox, D., Tucker, W.: 1969, Ap. J., 157, 1157.

Craig, I.J.D., Brown, J.C.: 1976, Astron. Ap., 49, 239.

Crance, M.: 1974, Atomic Data, 5, 185.

Culhane, J.L. : 1969, M.N.R.A.S., 144, 375.

Culhane, J.L., Acton, L.W. : 1974, Ann. Rev. Astron. Ap., 12, 359.

Culhane, J.L., Vesecky, J.F., Phillips, K.J.H.: 1970, Solar Phys., 15, 394.

Dalgarno, A., Parkinson, E.M.: 1967, Proc. R.S., A301, 253.

Datlowe, D.W., Hudson, H.S., Peterson, L.E.: 1974, Solar Phys., 35, 193.

Davis, J.M.: 1974, Technical Proposal for a Solar X-ray Astronomy Rocket Program: Solar Minimum and Ascending Solar Cycle Phase, ASE-3652-1.

Davis, J.M., Gerassimenko, M., Krieger, A.S., Vaiana, G.S.: 1975, Solar Phys., 45, 393.

Doschek, G.A.: 1972, Space Sci. Rev., 13, 765.

Doschek, G.A.: 1975, in S.R.Kane (ed.), Solar Gamma, X- and EUV-Radiation, Proc. IAU Symp. 68, p.165.

Doschek, G.A., Meekins, J.F.: 1973, in R. Ramaty and R.G. Stone (eds.), High Energy Phenomena on the Sun, NASA SP-342, p.262.

Doschek, G.A., Meekins, J.F., Kreplin, R.W., Chubb, T.A., Friedman, H.: 1971, Ap. J., 164, 165.

Drake, G.W.F.: 1971, Phys. Rev. A, 3, 908.

Dupree, A.K.: 1972, Ap. J., 178, 527.

Eddy, J.: 1975, in P. Stubbs (ed.), New Science in the Solar System, IPC Magazines Ltd., p.9.

Edlén, B.: 1973, Physica Scripta, 7, 93.

Edlén, B., Tyrén, F.: 1939, Nature, 143, 940.

Elwert, G.: 1952, Z.F.Nat., 7a, 432.

Elwert, G.: 1961, J.G.R., 66, 391.

Ermolaev, A.M., Jones, M.: 1974, J. Phys. B, 7, 199.

Esteva, J.M., Mehlman, G.: 1974, Ap. J., 193, 747.

Evans, K.D.: 1970, A Programme of X-ray Spectrometric Studies of the Solar Corona, Ph.D. Thesis, Leicester University.

Evans, K.D.: 1975, Private communication.

Evans, K., Pounds, K.A.: 1968, Ap. J., 152, 319.

Evans, K., Pounds, K.A., Culhane, J.L.: 1967, Nature, 214, 41.

Fawcett, B.C.: 1974, Adv. At. Mol. Phys., 10, 233.

Fawcett, B.C.: 1976, Private communication.

Fawcett, B.C., Cowan, R.D., Hayes, R.W.: 1974, Ap. J., 187, 377.

Feldman, U., Cohen, L.: 1967, Ap. J., 149, 265.

Feldman, U., Cohen, L.: 1968, Ap. J., 151, L55.

Feldman, U., Cohen, L., Swartz, M.: 1967, Ap. J., 148, 585.

Feldman, U., Doschek, G.A., Cowan, R.D., Cohen, L.: 1973, J.O.S.A., 63, 1445.

Feldman, U., Doschek, G.A., Nagel, D.J., Cowan, R.D., Whitlock, R.R.: 1974, Ap. J., 192, 213.

Flemberg, H.: 1942, A.J.M.A.F., 28A, No. 18.

Flower, D.R., Nussbaumer, H.: 1975, Astron. Ap., 39, 295.

Foukal, P.: 1975, Solar Phys., 43, 327.

Fraser, R.D.B., Suzuki, E.: 1970, in J.A. Blackburn (ed.), Spectral Analysis, Marcel Dekker Inc., New York, p. 171.

Freeman, F.F., Gabriel, A.H., Jones, B.B., Jordan, C.: 1971, Phil. Trans. R.S., A270, 127.

Froese, C.: 1967, B.A.I.N., 19, 86.

Gabriel, A.H.: 1972a, M.N.R.A.S., 160, 99.

Gabriel, A.H.: 1972b, Space Sci. Rev., 13, 655.

Gabriel, A.H.: 1972c, in T.R. Carson and M.J. Roberts (eds.), Atoms and Molecules in Astrophysics, Academic Press, New York, p. 311.

Gabriel, A.H., Jordan, C.: 1969a, Nature, 221, 947.

Gabriel, A.H., Jordan, C.: 1969b, M.N.R.A.S., 145, 241.

Gabriel, A.H., Jordan, C.: 1972, in E. McDaniel and M.McDowell (eds.), Case Studies in Atomic Collision Physics II, North-Holland, Amsterdam, p. 209.

Gabriel, A.H., Jordan, C.: 1973, Ap. J., 186, 327.

Gabriel, A.H., Paget, T.M.: 1972, J. Phys. B, 5, 673.

Gabriel, A.H., Niblett, G.B.F., Peacock, N.J.: 1962, J.Q.S.R.T., 2, 491.

Gabriel, A.H., Fawcett, B.C., Jordan, C.: 1965, Nature, 206, 390.

Gabriel, A.H., Jordan, C., Paget, T.M.: 1969, in Proc. 6th Int. Conf. on Physics of Electronic and Atomic Collisions, M.I.T. Press, Massachusetts, p. 558.

Garcia, J.D., Mack, J.E.: J.O.S.A., 55, 654.

Gerassimenko, M.: 1975, Private communication.

Giacconi, R., Reidy, W., Vaiana, G.S., Van Speybroeck, L., Zehnpfennig,T.: 1969, Space Sci. Rev., 9, 3.

Gibson, E.G.: 1973, The Quiet Sun, NASA SP-303.

Goldberg, L.: 1974, Ap. J., 191, 1.

Goldsmith, S.: 1974, J. Phys. B, 7, 2315.

Golts, E. Ya., Zhitnik, I.A., Kononov, E. Ya., Mandelstam, S.L., Sidelnikov, Yn. V.: 1974, Report No. 4 of the Spectroscopy Institute, USSR Academy of Sciences (to be published in Soviet Physics, Doklady).

Griem, H.R.: 1964, Plasma Spectroscopy, McGraw-Hill Inc., New York.

Grineva, Yu. I., Karev, V.I., Korneyev, V.V., Krutov, V.V., Mandelstam, S.L., Vainstein, L.A., Vasilyev, B.N., Zhitnik, I.A.: 1973, Solar Phys., 29, 441.

Gruzdev, P.F.: 1971, Opt. Spect., 30, 319.

Gursky, H.: 1970, in L. Gratton (ed.), Non-Solar X- and Gamma-Ray Astronomy, Proc. IAU Symp. No. 37, Reidel, Dordrecht, p.5.

Gursky, H., Schwartz, D.: 1974, in R. Giacconi and H. Gursky (eds.), X-Ray Astronomy, Reidel, Dordrecht, p. 25.

Hall, R., Evans, K.D.: 1975, Private communication.

Henke, B.L., Elgin, R.L.: 1970, Adv. X-ray Anal., 13, 639.

Herzberg, G.: 1944, Atomic Spectra and Atomic Structure, Dover Publ. Inc., New York.

Howard, R.: 1972, Science, 177, 1157.

Hutcheon, R.J.: 1975a, in S.R. Kane (ed.), Solar Gamma-, X-, and EUV-Radiation, Proc. IAU Symp. No. 68, Reidel, Dordrecht, p.69.

Hutcheon, R.J.: 1975b, Private communication.

Hutcheon, R.J., McWhirter, R.W.P.: 1973, J. Phys. B, 6, 2668.

Hynek, J.A.: 1951, Astrophysics, McGraw-Hill, New York.

Jordan, C.: 1966a, M.N.R.A.S., 132, 463.

Jordan, C.: 1966b, M.N.R.A.S., 132, 515.

Jordan, C.: 1969, M.N.R.A.S., 142, 501.

Jordan, C.: 1970, M.N.R.A.S., 148, 17.

Jordan, C.: 1972, Space Sci. Rev., 13, 595.

Jordan, C.: 1975a, in S.R. Kane (ed.), Solar Gamma-, X-, and EUV-Radiation, Proc. IAU Symp. 68, Reidel, Dordrecht, p. 109.

Jordan, C.: 1975b, Phil. Trans. R.S., A281, 391 (published 1976).

Jordan, C., Wilson, R.: 1971, in C.J. Macris (ed.), Physics of the Solar Corona, Reidel, Dordrecht, p. 219.

Kafatos, M.C., Tucker, W.H.: 1972, Ap. J., 175, 837.

Kahler, S.: 1972, Solar Phys., 22, 2.

Kane, S.R.: 1974, in G.A. Newkirk (ed.), Coronal Disturbances, Proc. IAU Symp. No. 57, p. 105.

Kaplan, S.A., Pikel'ner, S.B., Tsytovich, V.N.: 1974, Physics Reports, 15, 1.

Kastner, S.O., Omidvar, K., Underwood, J.H.: 1967, Ap. J., 148, 269.

Kiepenheuer, K.: 1959, The Sun, Univ. of Michigan Press, Ann Arbor.

Kuperus, M.: 1974, in Contopoulos (ed.), Highlights of Astronomy, p. 133.

Landini, M., Fossi, B.C.: 1970, Astron. Ap., 6, 468.

Landini, M., Fossi, B.C.: 1972, Astron. Ap. Suppl., 7, 291.

Landini, M., Fossi, B.C.: 1975, Astron. Ap., 42, 213.

Landini, M., Fossi, B.C., Pallavicini, R.: 1973, Solar Phys., 29, 93.

Leigh, B., Evans, K.D.: 1975, Private communication.

Leighton, R.B.: 1969, Ap. J., 156, 1.

Leroux, J.: 1963, in G.L. Clark (ed.), Encyclopaedia of X-rays and Gamma-rays, Reinhold Publ. Corp., New York, p. 9.

Livingston, W.C.: 1966, Scientific American, 215, 107.

Loulergue, M., Nussbaumer, H.: 1973, Astron. Ap., 24, 209.

Loulergue, M., Nussbaumer, H.: 1974, Astron. Ap., 34, 225.

Loulergue, M., Nussbaumer, H.: 1975a, Astron. Ap., 45, 125.

Loulergue, M., Nussbaumer, H: 1975b, Ap. Space Sci., 38, 365.

Macris, C.J. (ed.): 1971, Physics of the Solar Corona, Reidel, Dordrecht.

McWhirter, R.W.P.: 1965, in R.H. Huddlestone and S.L. Leonard (eds.), Plasma Diagnostic Techniques, Academic Press, New York, p. 201.

McWhirter, R.W.P., Wilson, R.: 1974, J. Phys. B, 7, 1588.

Mewe, R.: 1972a, Solar Phys., 22, 459.

Mewe, R.: 1972b, Astron. Ap., 20, 215.

Meyer, F.: 1971, in C.J. Macris (ed.), Physics of the Solar Corona, Reidel, Dordrecht, p. 29.

Moiseiwitsch, B.L., Smith, S.J.: 1968, Rev. Mod. Phys., 40, 238.

NASA-GSFC: 1974, Report of the OSO-K/Solar Flare Mission Study Group, X-680-74-66.

NASA-GSFC: 1975, Interim Report of the Astronomy Spacelab Payloads Study, Volume 1, Solar Physics.

Neupert, W.M.: 1969, Ann. Rev. Astron. Ap., 7, 121.

Neupert, W.M.: 1971, in C.J. Macris (ed.), Physics of the Solar Corona, Reidel, Dordrecht, p. 237.

Neupert, W.M., Swartz, M., Kastner, S.O.: 1973, Solar Phys., 31, 171.

Pagel, B.E.J.: 1973, in A.G.W. Cameron (ed.), Cosmochemistry, Reidel, Dordrecht, p. 1.

Parker, E.N.: 1970, Ann. Rev. Astron. Ap., 8, 1.

Parkinson, J.H.: 1971a, X-Rays from Solar Active Regions, Ph.D. Thesis, Leicester University.

Parkinson, J.H.: 1971b, Nature Phys. Sci., 233, 44.

Parkinson, J.H.: 1972, Nature Phys. Sci., 236, 68.

Parkinson, J.H. : 1973a, Astron. Ap., 24, 215.

Parkinson, J.H.: 1973b, Solar Phys., 28, 137.

Parkinson, J.H.: 1973c, Solar Phys., 28, 487.

Parkinson, J.H.: 1975a, in S.R. Kane (ed.), Solar Gamma-, X-, and EUV-Radiation, Proc. IAU Symp. 68, p. 45.

Parkinson, J.H.: 1975b, Phil. Trans. R.S., A281, 375 (published 1976).

Parkinson, J.H.: 1975c, Solar Phys., 42, 183.

Parkinson, J.H., Pounds, K.A.: 1971, Solar Phys., 17, 146.

Parkinson, J.H., Evans, K., Pounds, K.A.: 1972, Space Sci. Rev., 13, 740.

Peacock, N.J., Hobby, M.G., Galanti, M.: 1973, J. Phys. B, 6, L298.

Phillips, K.J.H.: 1975, Ap. J., 199, 247.

Phillips, K.J.H., Neupert, W.M., Thomas, R.J.: 1974, Solar Phys., 36, 383.

Pospieszczyk, A.: 1975, Astron. Ap., 39, 357.

Pottasch, S.R.: 1964, Space Sci. Rev., 3, 816.

Pottasch, S.R.: 1967, B.A.I.N., 19, 113.

Pounds, K.A.: 1970, Ann. Geophys., 26, 555.

Rugge, H.R., Walker, A.B.C.: 1968, Space Research, 8, 439.

Rugge, H.R., Walker, A.B.C.: 1971a, Solar Phys., 15, 372.

Rugge, H.R., Walker, A.B.C.: 1971b, Solar Phys., 18, 244.

Rugge, H.R., Walker, A.B.C.: 1976, Ap. J., 203, L139.

Schnopper, H.W.: 1962, Research Report No. 13, to U.S. Airforce, Contract No. AF 49 (638)-402.

Smith A.G.: 1967, Radio Exploration of the Sun, Van Nostrand Reinhold, New York.

Solar Geophysical Data: 1974, No. 353, Part I, No. 357, Part II.

Solar Geophysical Data: 1975, No. 376, Part I.

Spitzer, L, Jr.: 1962, Physics of Fully Ionized Gases, Wiley, New York.

Stein, R.F., Leibacher, J.: 1974, Ann. Rev. Astron. Ap., 12, 407.

Stevens, G.A.: 1974, Astron. Ap., 31, 157.

Sturrock, P.A.: 1973, in R. Ramaty and R.G. Stone (eds.), High Energy Phenomena on the Sun, NASA SP-342, p. 3.

Summers, H.P.: 1972, M.N.R.A.S., 158, 255.

Summers, H.P.: 1973, Ap. J., 179, L45.

Summers, H.P.: 1974, M.N.R.A.S., 169, 663.

Swartz, M., Kastner, S., Rothe, E., Neupert, W.: 1971, J. Phys. B, 4, 1747.

Tucker, W.H., Koren, M.: 1971, Ap. J., 168, 283.

Tully, J.A.: 1974, J. Phys. B, 7, 386.

Tyrén, F.: 1938, Z. Physik, 111, 314.

Tyrén, F.: 1940, N.A.R.S.U., Ser. IV 12, No. 1.

Underwood, J.H.: 1974, in P.W. Sanford (ed.), Proceedings of the X-ray Optics Symposium, held at Mullard Space Science Laboratory, University College London, England, April 1973, p. 1.

Vaiana, G.S.: 1975, Phil. Trans. R.S., A281, 365 (published 1976).

Vaiana, G.S., Tucker, W.H.: 1974, in R. Giacconi and H. Gursky (eds.), X-Ray Astronomy, Reidel, Dordrecht, p. 169.

Vaiana, G.S., Davis, J.M., Giacconi, R., Krieger, A.S., Silk, J.K., Timothy, A.F., Zombeck, M.: 1973a, Ap. J., 185, L47.

Vaiana, G.S., Krieger, A.S., Timothy, A.F.: 1973b, Solar Phys., 32, 81.

Vaiana, G.S., Krieger, A.S., Petrasso, R., Silk, J.K., Timothy, A.F.: 1974, Proc. S.P.I.E., 44, 185.

Vainstein, L.A., Safronova, U.I.: 1972, Short Communications in Physics, Lebedev Institute, Moscow, 3, 40.

Van Beek, H.F., de Feiter, L.D., de Jager, C.: 1974, Space Res. XIV, 447.

Van Regemorter, H.: 1962, Ap. J., 136, 906.

Van Speybroeck, L.: 1972, Space Sci. Rev., 13, 845.

Veigele, W.J.: 1973, Atomic Data, 5, 51.

Walker, A.B.C.: 1972, Space Sci. Rev., 13, 672.

Walker, A.B.C.: 1974, Proc. International Conference on X-rays in Space, University of Calgary, Canada, p. 565 (published 1975).

Walker, A.B.C.: 1975, in S.R. Kane (ed,), Solar Gamma-, X-, and EUV-Radiation, Proc. IAU Symp. 68, p. 73.

Walker, A.B.C., Rugge, H.R.: 1969, in C. de Jager and Z. Svestka (eds.), Solar Flares and Space Research, North-Holland Publ. Co., Amsterdam, p. 102.

Walker, A.B.C., Rugge, H.R.: 1970, Astron. Ap., 5, 4.

Walker, A.B.C., Rugge, H.R., Weiss, K.: 1974a, Ap. J., 188, 423.

Walker, A.B.C., Rugge, H.R., Weiss, K.: 1974b, Ap. J., 192, 169.

Walker, A.B.C., Rugge, H.R., Weiss, K.: 1974c, Ap. J., 194, 471.

Watson, D.J.: 1975, Private communication.

Wiese, W.L., Smith, M.W., Glennon, B.M.: 1966, Atomic Transition Probabilities, NSRDS-NBS-4.

Wiese, W.L., Smith, M.W., Miles, B.M.: 1969, Atomic Transition Probabilities, NSRDS-NBS-22.

Wilson, R.: 1962, J.Q.S.R.T., 2, 477.

Withbroe, G.L.: 1971, Proc. Menzel Symp., NBS-353, 127.

Withbroe, G.L.: 1975, Solar Phys., 45, 301.

Withbroe, G.L.: 1976, Solar Phys., in press.

Withbroe, G.L., Gurman, J.B.: 1973, Ap. J., 183, 279.

Wooley, R.V.D.R., Allen, C.W.: 1948, M.N.R.A.S., 108, 292.

Wyckoff, R.W.G.: 1965, Crystal Structures, Wiley & Sons, London, Vols. 1-6.

Zemansky, M.: 1968, Heat and Thermodynamics, McGraw-Hill, New York.

Zirin, H.: 1966, The Solar Atmosphere, Blaisdell, London.

Zirin, H.: 1974, Vistas in Astronomy, 16, 1.

PUBLICATIONS

"X-ray Spectroscopy of Solar Active Regions during the Third Skylab Mission", J.P.Pye, R.J.Hutcheon, J.H.Parkinson and K.A.Pounds. Proc. IAU Symp. No. 68, 65-66 (1975).

"The Spectrum of Fe XVII in the Solar Corona", R.J.Hutcheon, J.P.Pye and K.D.Evans. M.N.R.A.S. (1976) 175, 489-499.

"The Spectrum of Ni XIX in the Solar Corona", R.J.Hutcheon, J.P.Pye and K.D.Evans. Solar Phys. (1976) 46, 171-177.

"Weak Fe XVII Transitions in the Coronal X-ray Spectrum", R.J.Hutcheon, J.P.Pye and K.D.Evans. Astron. Astrophys. (1976) 51, 451-460.

"The Wavelength Calibration and Resolution of the Leicester Solar Coronal Bragg Spectrometer", K.D.Evans, R.J.Hutcheon and J.P.Pye. Space Sci. Instr. (1976) 2, 339-348.

"The Coronal Emission Line Spectrum 13.3 to 13.8 Å", J.P.Pye, K.D.Evans and R.J.Hutcheon. M.N.R.A.S., in press.

"The Structure of the X-ray Bright Corona above Active Region McMath 12628", J.P.Pye, K.D.Evans, R.J.Hutcheon, M.Gerassimenko, A.S.Krieger, J.M.Davies, J.Vesecky. Astron. Astrophys., submitted.

"The Gross Energy Balance of Solar Active Regions", J.Vesecky, J.P.Pye, K.D.Evans, R.J.Hutcheon, A.S.Krieger, M.Gerassimenko. Ap. J. Letters, submitted.

Journal Abbreviations

Adv. At. Mol. Phys.	Advances in Atomic and Molecular Physics
Adv. X-Ray Anal.	Advances in X-Ray Analysis
Ann. Geophys.	Annals de Geophysique
Ann. Rev. Astron. Ap.	Annual Review of Astronomy and Astrophysics
A.J.M.A.F.	Arkiv for Matematic Astronomi ock Fysik
Astron. Ap.	Astronomy and Astrophysics
Ap. J.	Astrophysical Journal
Ap. Space Sci.	Astrophysics and Space Science
B.A.A.S.	Bulletin of the American Astronomical Society
B.A.I.N.	Bulletin of the Astronomical Institute of the Netherlands
J.G.R.	Journal of Geophysical Research
J. Phys. B	Journal of Physics, B, Atomic and Molecular Physics
J.Q.S.R.T.	Journal of Quantitative Spectroscopy and Radiative Transfer
J.O.S.A.	Journal of the Optical Society of America
Memoirs R.A.S.	Memoirs of the Royal Astronomical Society
M.N.R.A.S.	Monthly Notices of the Royal Astronomical Society
Nature Phys. Sci.	Nature Physical Science
N.A.R.S.U.	Nova Acta Reg. Soc. Sci. Upsaliensis
Opt. Spect.	Optics and Spectroscopy
Phil. Trans. R.S.	Philosophical Transactions of the Royal Society of London
Phys. Rep.	Physics Reports
Phys. Rev.	Physics Review
Proc. R.S.	Proceedings of the Royal Society of London
Proc. S.P.I.E.	Proceedings of the Society of Photo-Optical and Instrumentation Engineers
Rev. Mod. Phys.	Review of Modern Physics
Rev. Sci. Instr.	Review of Scientific Instruments
Solar Phys.	Solar Physics

Soviet Astron.	Soviet Astronomy
Space Res.	Space Research
Space Sci. Instr.	Space Science Instrumentation
Space Sci. Rev.	Space Science Review
Z.F. Nat.	Zeitschrift für Physik

ACKNOWLEDGMENTS

This work has been carried out as part of the research programme of the X-ray Astronomy Group in the Department of Physics, University of Leicester. I thank first my supervisor Professor K.A. Pounds for his advice and encouragement, and Professor J.E. Enderby in whose department this work was performed. The receipt of a Science Research Council Research Studentship is gratefully acknowledged.

It is a great pleasure to acknowledge many valuable discussions with Dr's K.D. Evans and R.J. Hutcheon of the X-ray Astronomy Group. I am grateful to Dr's B.C. Fawcett (ARD, Culham), M. Gerassimenko (ASE), M. Loulergue (Meudon Observatory) and H. Nussbaumer (ETH, Zurich) for helpful discussions, D.J. Watson for the preparation and successful operation of the SL1101 and SL1206 spectrometers, Dr. J.H. Parkinson (University College, London, late of Leicester University) as project scientist of the SL1101 flight and for his assistance in the joint S-054/SL1206 observing programme, and Dr. A.S. Krieger (ASE) for the Skylab S-054 data. I was a visiting scientist at ASE during the initial stages of the S-054 data analysis described in Chapter 4.

I thank Mrs. M. Garner for typing this thesis so efficiently. The photographic work for the figures was performed by Mr. J. Kerruish. Mrs. R. Littler and Mr. P. Kirk were responsible for the final tracings of several of the diagrams.

My wife Lydia typed the original draft of this thesis and helped to check the tables. I am most grateful to Lydia, and to my parents, for their support, encouragement and patience.

DECLARATION

I, the undersigned, declare that the work described in this thesis has, except where indicated, been carried out by the author, during the period of registration for the degree of Ph.D. at the University of Leicester. No part of it has been submitted for any other degree.

John P. Pye.

JOHN P. PYE

J.P. PYE Ph.D. THESIS 1976

SUMMARY

A study of the X-ray emission from solar coronal active regions is presented. The observations were made with two instruments: (1) a collimated Bragg crystal spectrometer with high spectral resolution ($400 \lesssim \lambda/\Delta\lambda \lesssim 1000$) and moderate spatial resolution (about 3 arc min), and (2) a grazing incidence telescope which obtained broad wavelength-band images with high spatial resolution (about 2 arc sec). Chapter 1 gives a brief review of the relevant physics, with particular emphasis on the Sun's soft X-ray emission (i.e. $1 \lesssim$ wavelength, $\lambda \lesssim 25$ Å). The plasma and atomic physics required to interpret the X-ray observations are summarised in Chapter 2.

The instruments used in this work were the (sounding) rocket-borne Leicester Mk. 3 Bragg spectrometer, and the American Science and Engineering (ASE) X-ray telescope S-054, aboard the Skylab Apollo Telescope Mount. The instruments and data analysis techniques are described in Chapter 3.

The data are interpreted in terms of thermal emission from an optically thin plasma. In Chapter 4, coronal active region models, are derived, of electron density and emission measure ($n_e^2\Delta V$) as a function of electron temperature and spatial location. Abundances are derived for the elements oxygen, neon, sodium,magnesium,aluminium,silicon, iron and nickel in the solar corona.

Chapters 5, 6 and 7 describe observations and interpretation of spectra of ions belonging to particular isoelectronic sequences, namely: Chapter 5, the Helium-like ions O VII, Ne IX and Mg XI; Chapter 6, the Neon-like ions Fe XVII and Ni XIX, Chapter 7, Fluorine-like Fe XVIII and Oxygen-like Fe XIX.